THE UNIVERSITY OF WARWICK

Library Declaration and Deposit Agreement

1. STUDENT DETAILS

Please complete the following:

Full name: ……

University ID number: ……

2. THESIS DEPOSIT

2.1 I understand that under my registration at the University, I am required to deposit my thesis with the University in BOTH hard copy and in digital format. The digital version should normally be saved as a single pdf file.

2.2 The hard copy will be housed in the University Library. The digital version will be deposited in the University's Institutional Repository (WRAP). Unless otherwise indicated (see 2.3 below) this will be made openly accessible on the Internet and will be supplied to the British Library to be made available online via its Electronic Theses Online Service (EThOS) service.
[At present, theses submitted for a Master's degree by Research (MA, MSc, LLM, MS or MMedSci) are not being deposited in WRAP and not being made available via EthOS. This may change in future.]

2.3 In exceptional circumstances, the Chair of the Board of Graduate Studies may grant permission for an embargo to be placed on public access to the hard copy thesis for a limited period. It is also possible to apply separately for an embargo on the digital version. (Further information is available in the *Guide to Examinations for Higher Degrees by Research*.)

2.4 *If you are depositing a thesis for a Master's degree by Research, please complete section (a) below. For all other research degrees, please complete both sections (a) and (b) below:*

(a) Hard Copy

I hereby deposit a hard copy of my thesis in the University Library to be made publicly available to readers (please delete as appropriate) EITHER immediately OR after an embargo period of ……..... months/years as agreed by the Chair of the Board of Graduate Studies.

I agree that my thesis may be photocopied. YES / NO (*Please delete as appropriate*)

(b) Digital Copy

I hereby deposit a digital copy of my thesis to be held in WRAP and made available via EThOS.

Please choose one of the following options:

EITHER My thesis can be made publicly available online. YES / NO (*Please delete as appropriate*)

OR My thesis can be made publicly available only after…..[date] (Please give date)
YES / NO (*Please delete as appropriate*)

OR My full thesis cannot be made publicly available online but I am submitting a separately identified additional, abridged version that can be made available online.
YES / NO (*Please delete as appropriate*)

OR My thesis cannot be made publicly available online. YES / NO (*Please delete as appropriate*)

3. GRANTING OF NON-EXCLUSIVE RIGHTS

Whether I deposit my Work personally or through an assistant or other agent, I agree to the following:

Rights granted to the University of Warwick and the British Library and the user of the thesis through this agreement are non-exclusive. I retain all rights in the thesis in its present version or future versions. I agree that the institutional repository administrators and the British Library or their agents may, without changing content, digitise and migrate the thesis to any medium or format for the purpose of future preservation and accessibility.

4. DECLARATIONS

(a) I DECLARE THAT:

- I am the author and owner of the copyright in the thesis and/or I have the authority of the authors and owners of the copyright in the thesis to make this agreement. Reproduction of any part of this thesis for teaching or in academic or other forms of publication is subject to the normal limitations on the use of copyrighted materials and to the proper and full acknowledgement of its source.

- The digital version of the thesis I am supplying is the same version as the final, hard-bound copy submitted in completion of my degree, once any minor corrections have been completed.

- I have exercised reasonable care to ensure that the thesis is original, and does not to the best of my knowledge break any UK law or other Intellectual Property Right, or contain any confidential material.

- I understand that, through the medium of the Internet, files will be available to automated agents, and may be searched and copied by, for example, text mining and plagiarism detection software.

(b) IF I HAVE AGREED (in Section 2 above) TO MAKE MY THESIS PUBLICLY AVAILABLE DIGITALLY, I ALSO DECLARE THAT:

- I grant the University of Warwick and the British Library a licence to make available on the Internet the thesis in digitised format through the Institutional Repository and through the British Library via the EThOS service.

- If my thesis does include any substantial subsidiary material owned by third-party copyright holders, I have sought and obtained permission to include it in any version of my thesis available in digital format and that this permission encompasses the rights that I have granted to the University of Warwick and to the British Library.

5. LEGAL INFRINGEMENTS

I understand that neither the University of Warwick nor the British Library have any obligation to take legal action on behalf of myself, or other rights holders, in the event of infringement of intellectual property rights, breach of contract or of any other right, in the thesis.

Please sign this agreement and return it to the Graduate School Office when you submit your thesis.

Student's signature: .....…… Date: .....

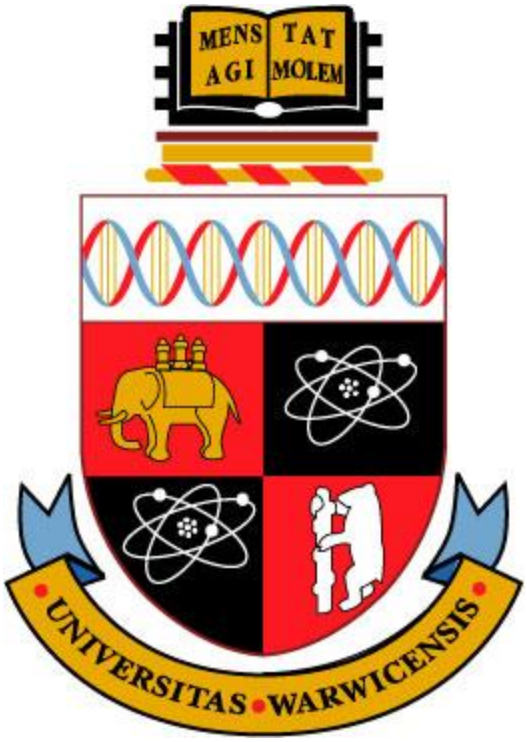

Characterisation of Mixed-Metal Oxides Prepared by Hydrothermal Synthesis

by

Mohammad Hilni Harunsani

A thesis submitted in partial fulfilment of the requirements for the degree of

Doctor of Philosophy in Chemistry

Department of Chemistry, University of Warwick

September 2013

Table of Contents

Acknowledgements

Alhamdulillahi Rabbil 'Alamin. All praises and thanks be to God for giving me everything that I have and allowing me to see the completion of this thesis.

This thesis would not be possible without the assistance and guidance of various people. I would therefore like to offer my sincerest thanks to all of them and may God reward them with success and happiness in this world and in the hereafter.

Firstly, my sincerest appreciation and gratitude to Professor Richard Walton for being such a wonderful supervisor, amazing teacher and also for being a marvellous person to work for. Without his persistent help and guidance, this thesis would not be possible. Thank you for accepting me to join your research group, always providing me with excellent ideas, immensely useful feedback during the write-up of this thesis and for guiding me throughout my time in Warwick.

Thank you to the Ministry of Education in Brunei for giving me the opportunity to study in UK and providing me with a scholarship from the start of my A-levels to the end of my PhD.

Thank you to Dr David Woodward for his help in obtaining neutron diffraction data at ILL, in Grenoble, and for his help with the piezoelectric and ferroelectric measurements and also for proof reading this work. Thank you to Dr Dean Keeble for his help in using the TOPAS software. Thank you to Dr David Walker for his help in obtaining high resolution XRD.

Thank you to Dr Helen Playford for all her help with various matters in the lab and in the office, for organising events, for her useful advice and also for proof reading this work. Thank you also to Dr Alexis Munn for her help throughout my PhD and for always inviting everyone to tea. Thank you to Dr Ben Douglas for training me to use the Raman spectrometer at Milburn house and for being so friendly on my first day visiting the Walton group. Thank you to Dr Deena Modeshia for teaching me how to carry out a hydrothermal reaction and help me settle in when I first joined the group. Thank you to Dr Peter Dunne for his help in obtaining TGA data and the synthesis method for Ce-TiO_2 materials.

Thank you to Craig Hiley for his help in obtaining XANES data at Diamond, help with BET and for all the funny puns he comes up with. Thank you to Matthew Breeze for accompanying me at Diamond for data collection. Thank you to Luke Daniels for his help with obtaining TGA data on numerous samples and for always being so helpful.

Thank you to Dr Syazana Ebil for being my close friend and companion ever since I started studying in UK. Without your constant encouragement, motivation and support, this journey would not be as easy and enjoyable. Thank you Sayang.

Last but not least, Thank you to my parents for raising me up well and providing me with everything I need to succeed in life. Thank you also to my siblings for their support, especially Liz for coming to UK, helping me move houses when I was in the process of writing this thesis and also proof reading my work.

"Surely, with every hardship, there is relief. Surely, with every hardship there is relief" Surah Insyirah, 94:5-6

Declaration

This thesis is submitted to the University of Warwick in support of my application for the degree of Doctor of Philosophy. It has been composed by myself and has not been submitted in any previous application for any degree.

Abstract

Mixed-metal oxides were prepared via hydrothermal synthesis and characterised using various analytical techniques. Three different class of materials were studied, namely perovskites, hexagonal perovskites and doped TiO_2. By using hydrothermal synthesis, control on the crystal size, morphology and phase purity was achieved, which are difficult by conventional methods.

A new titanate perovskite solid solution with nominal composition, $NaCe_{1-x}La_xTi_2O_6$, containing three different metals on the A-site was produced by a single step hydrothermal synthesis. Rietveld analysis of powder X-ray and neutron diffraction data enabled the space group $R\bar{3}c$ to be assigned for the whole series. The particle size and morphology can be changed by varying the solvent and NaOH concentration. ^{23}Na MAS NMR showed that a genuine solid solution was produced, with no A-site ordering present, while ^{2}H MAS NMR of the samples prepared in D_2O showed the inclusion of D_2O in the lattice in place of Na, greatest for the cerium-containing materials, in which oxidation to Ce^{4+} can occur.

The preparation of B-site substituted perovskites was possible via hydrothermal synthesis. The effect of substituting Zr for Ti was studied for two different perovskites namely $NaLaTi_2O_6$ and $NaBiTi_2O_6$. For $NaLaTi_2O_6$, Zr substitution had a drastic effect on the crystal morphology. Other factors that can affect the morphology such as the solvent, reaction time, temperature and NaOH concentrations were also investigated. In the case of $NaBiTi_2O_6$, the effect of Zr substitution on ferroelectric and piezoelectric properties was studied.

Pure hexagonal $YMnO_3$ was achieved by a comproportionation hydrothermal reaction between $KMnO_4$ and $MnCl_2$. The possibility of doping $YMnO_3$ with Fe was investigated. Fe doping up to 10% was possible but above this level, impurity phases were observed. Pure orthorhombic $YFeO_3$ can also be prepared and the Fe^{3+} was replaced by up to 30% Mn^{3+}. The oxidation states of these materials were determined using XANES.

Phase pure rutile TiO_2 was prepared via two different hydrothermal routes. Attempts at doping W into TiO_2 were only achieved at 1% W doping level. With Sn, a rutile Sn-TiO_2 complete solid solution is formed. In contrast, Ce-TiO_2 with up to 15% Ce is formed as the anatase structure with a mixture of Ce^{3+} and Ce^{4+}. The photocatalytic properties of the Ce-TiO_2 materials show promise for high activity hydrogen production by UV splitting of water.

Abbreviations

BET	Brunauer-Emmett-Teller
EDTA	Ethylenediaminetetraacetic acid
EDXA	Energy dispersive X-ray analysis
ICP-OES	Inductively coupled plasma optical emission spectroscopy
IR	Infrared spectroscopy
MAS NMR	Magic-angle spinning nuclear magnetic resonance
MPB	Morphotropic phase boundary
SEM	Scanning electron microscopy
TEM	Transmission electron microscopy
TGA	Thermogravimetric analysis
TiBALD	Titanium Bisammonium Lactato Dihydroxide
XANES	X-ray absorption near-edge structure spectroscopy
XPS	X-ray photoelectron spectroscopy
XRD	X-ray diffraction

Chapter 1 – Introduction

1.1 Introduction

This thesis describes the preparation of known and novel metal oxides by hydrothermal synthesis, the characterisation of their structure using various techniques and, where appropriate, measurement of their properties. The aim of the work was to achieve control over the crystal structure, particle size, morphology and metal oxidation state in mixed metal oxides. The materials studied all have interesting properties and potential applications hence it is important that new synthetic routes are developed to improve these materials for real uses and to provide convenient, efficient methods of preparation. Chapter 1 gives an introduction to the different types of mixed metal oxides studied and provides a literature review on the hydrothermal synthesis of important oxide materials.

1.2 Mixed-Metal Oxides

Mixed-metal oxides are important materials in the world today. They have a vital role in many technological applications. For example, they are used to make capacitors and magnetic components in commonly used electronic devices.[1] They are also used in high temperature solid oxide fuel cells and in the production of materials for energy storage.[2] In catalysis, the majority of catalysts used in industrial applications involve metal oxides being used as the active phase, promoter or catalyst support.[3-4] Some metal oxides are used as photocatalysts in waste-water treatment or for splitting of water.[5-6] They are also widely used as pigments in paints,

in sunscreens where they absorb ultraviolet light and even used as food additives.[7-9] These physical properties generally arise from the crystal structure of these materials so the ability to control the synthesis of these metal oxides to give homogeneous, crystalline phases is crucial.

Multi-element oxide phases are desired for many applications where properties, such as electronic, magnetic or catalysis, can be tuned by partial replacement of one element by another to give solid solutions (where the crystal structure remains unchanged over the whole composition range) or by the addition of dopants which can introduce favourable properties. In this thesis, three different group of mixed-metal oxide materials were studied; perovskites, hexagonal perovskites and doped TiO_2. These each represent examples of important functional materials where synthesis is usually by high temperature methods and where greater control in synthesis could lead to fine control of material properties.

1.3 Perovskites

The mineral perovskite, $CaTiO_3$, was first discovered by Gustav Rose in 1839 and was named after a Russian mineralogist Lev Alexeievich Perovski.[10] Since then, the name 'perovskite' has been applied to the class of compounds that have similar structure and stoichiometry as $CaTiO_3$. Much of the early work on perovskites was carried out by Goldschmidt, who also developed the principal of tolerance factor, which may be used to predict their structures and stability, and will be described further below.[11]

Perovskites are a versatile group of materials that can accommodate a large variety of chemical elements due to the flexibility of the structure. They exhibit a range of interesting physical properties, particularly when an external electrical stimulus is applied to them. These properties such as ferroelectric, piezoelectric, pyroelectric and dielectric behaviour have led to numerous applications in charge storage, non-volatile memory applications, transducers, actuators and infra-red detection.[12-13] These properties are influenced by the structure, as slight changes can alter the symmetry considerations, bond lengths and band energy levels of the material.

The ideal, undistorted perovskite structure is cubic with space group $Pm\bar{3}m$ and has an empirical formula of ABX_3, where A and B are conventionally the cations while X is the anion. However, in the case of anti-perovskites such as Li_3OCl and K_3OBr, the A and B sites are occupied by anions and the X sites are occupied by cations instead. Typically, the A-cation is a large cation with low valency, often an alkali or alkaline earth metal. In contrast, the B-cation,tends to be smaller and usually a transition metal. The anion is usually an oxide but it may be another chalcogenide or a halide. Nearly every element in the Periodic Table, apart from the noble gases, has been incorporated into the perovskite structure.

The ideal perovskite structure consists of the A-cation being surrounded by 12 anions (Fig. 1.1a) and the B cations are surrounded by 6 anions (Fig. 1.1b). Another way of describing the perovskite structure is as a network of corner sharing $[BX_6]$ octahedra with the vacancies between them occupied by A-cations (Fig. 1.1c).

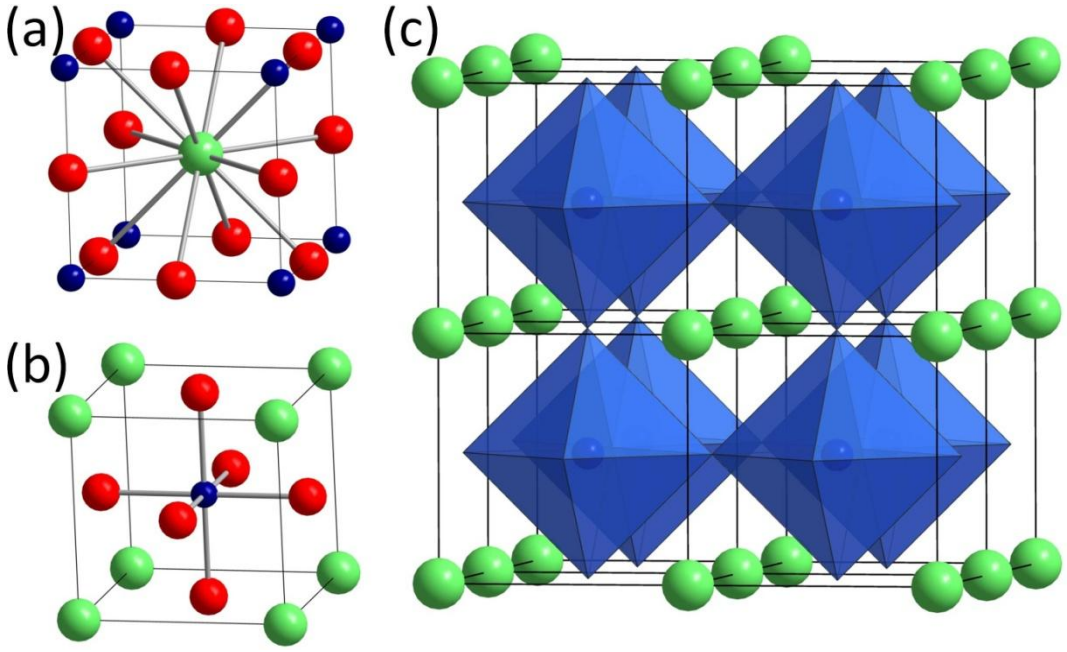

Fig. 1.1 Ideal perovskite structure, space group *Pm*$\bar{3}$*m*, showing the a) cubic A unit cell, b) cubic B unit cell and c) polyhedral view of corner sharing [BX_6] octahedra. The A cations are shown in green, B cations are blue and anions in red

If the anions in the perovskite are halides, the cations will be restricted to only monovalent A-cations and divalent B-cations *e.g.* $KMgF_3$ and $CsSnI_3$. In the case of oxygen containing perovskites, there are many possible A and B cation configurations. The following combinations are possible: $A^{+}B^{5+}O_3$, $A^{2+}B^{4+}O_3$ and $A^{3+}B^{3+}O_3$, as long as the overall positive charge is +6 to balance the negative charge from the oxygen anions. Partial substitution on the A and/or B site is also possible, thus forming more complex perovskites.

In the ideal perovskite where the ions are regarded as rigid spheres, each cation is the perfect size to be in contact with an oxygen anion. The size of the unit cell can be determined from the B-X bond length, as one unit cell is twice this distance, while the face diagonal is twice the A-X bond length. Hence, the ionic radii can be connected via a geometric relationship:

$$r_A + r_X = \sqrt{2}\,(r_B + r_X) \qquad (1.1)$$

where r_A, r_B and r_X are the ionic radii of the A and B site cations and the anion, respectively. However, distortions can occur in the structure so a tolerance factor is added to the equation:

$$t = \frac{r_A + r_X}{\sqrt{2}(r_B + r_X)} \qquad (1.2)$$

where t is the tolerance factor and is ideally equal to one. If there is multiple occupancy on either of the sites, then an average of the ionic radii is used. By using Equation 1.2, the tolerance factor can be calculated and be used as a measure of the degree of distortion of a perovskite from ideal cubic. When t is close to 1, the structure adopts the cubic symmetry. If $t < 1$, the A cation is too small for the cavity formed by the [BX_6] octahedra. Then, the perovskite adopts a distorted structure with a lower symmetry. If the value of t is less than 0.75, the A and B cations are almost the same size and the material will tend to adopt other structures like ilmenite or corundum. Apart from the tolerance factor, there is also a limit on the size of the cations, where $r_A > 0.90$ Å and $r_B > 0.51$ Å.[11]

Although there are examples of perovskites adopting the cubic $Pm\bar{3}m$ structure at room temperature, such as $SrTiO_3$, the majority of perovskites have structures slightly distorted from this ideal cubic structure. The flexibility of the structure allows slight distortions to occur in order to minimise the bond strains when there is a mismatch in the size of the ions. The lowering of the symmetry of a perovskite may arise from one or a combination of the following distortions:

a) Rotation or tilting of the BO_6 octahedra (Fig. 1.2),

b) Distortion of the octahedra,

c) Displacement of the cations from the centre of their coordination polyhedra, or

d) Cation ordering in complex perovskites where multiple cations occupy the same site.

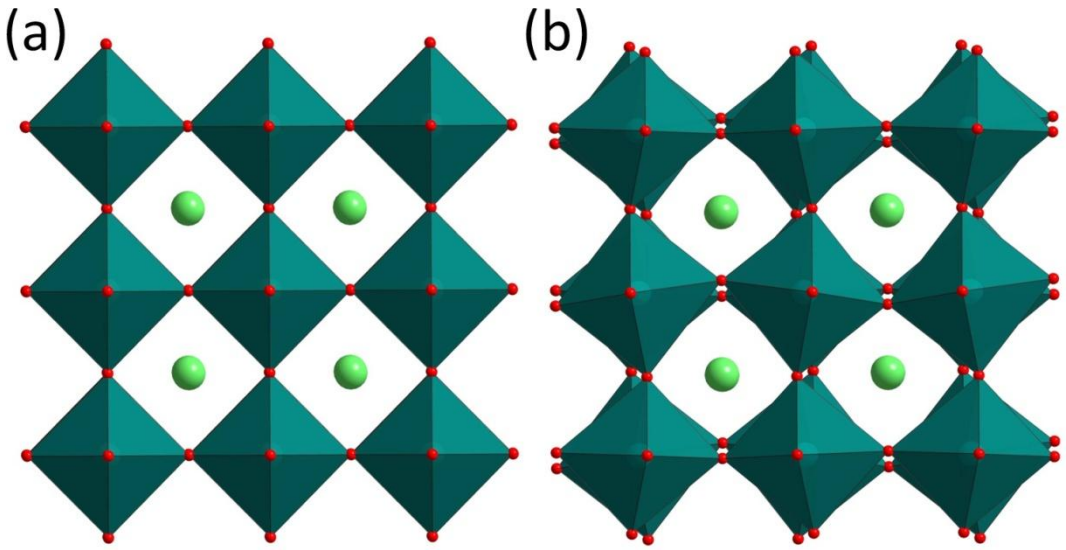

Fig. 1.2 Structure of a) an ideal cubic perovskite, space group *Pm$\bar{3}$m* and b) an orthorhombic perovskite, space group *Pnma*

When these distortions take place, this results in the cubic unit cell being distorted along;

1) the edges of the unit cell (i.e. the [100] direction), to result in a tetragonal cell,

2) the face diagonal (i.e. the [110] direction), to give an orthorhombic cell,

3) the volume diagonal of the cube (i.e. the [111] direction), to give a rhombohedral cell, or

4) any arbitrary [hk0] or [hk1] directions, to give a monoclinic or triclinic cell, respectively.[13]

It is this wide range of possible distortions and the various combinations of elements present that give rise to the numerous perovskites available. These structural distortions give rise to interesting properties such as dielectric, piezoelectric, pyroelectric and ferroelectric properties. These properties are defined as follows; a dielectric material is an electrical insulator that can be polarised with the application of an electric field. A piezoelectric material exhibits an electrical polarisation when mechanically stressed or undergoes mechanical deformation on the application of an electric field. A pyroelectric material is a material that has a polarisation which is temperature dependent but is not necessarily reversible. A ferroelectric material is one that displays a spontaneous polarisation that can be reversed upon the application of an external electric field. One of the characteristics of a ferroelectric material is that it yields a hysteresis loop when the polarisation is measured as a function of applied electric field. The physical properties and applications of some perovskites are listed in Table 1.1 below.

Table 1.1 Examples of perovskites and perovskite-based materials with their properties and applications

Materials	Properties	Applications	References
$BaTiO_3$	dielectric, ferroelectric, piezoelectric, pyroelectric	capacitors, sensors, motor starters, switches, transducers, controllers	[12,14]
$(Ba_{1-x}Sr_x)TiO_3$	pyroelectric	pyrodetector	[14]
$(Ba_{1-x}La_x)TiO_3$	semiconductor	thermistors, capacitors	[15-16]
$CaTiO_3$	dielectric	capacitors, electromagnetic resonators for microwave devices	[17-18]
$SrTiO_3$	paraelectric	memory devices	[19-20]
$PbTiO_3$	pyroelectric, piezoelectric	pyrodetector, acoustic transducer, infrared sensors	[14,21-22]
$Pb(Zr_xTi_{1-x})O_3$,	dielectric, pyroelectric, piezoelectric, electro-optic	non-volatile memory, pyrodetector, surface acoustic wave device substrate, wave guide device, transducers, sensors, actuators	[12,14,22-23]
$(Pb_{1-y}La_y)(Zr_xTi_{1-x})O_3$	pyroelectric, electro-optic	pyrodetector, wave guide device, optical memory, display	[14,24-25]
$SrCeO_3$, $BaCeO_3$	H^+ conductors	electrolytes for electrochemical hydrogen pumps	[26-28]
$BaInO_{2.5}$	O^{2-} conductors	oxygen sensors, oxygen conducting membranes and solid oxide fuel cells	[29-30]
$LiNbO_3$	piezoelectric, pyroelectric	pyrodetector, surface acoustic wave device	[14,31]
$K(Ta_xNb_{1-x})O_3$	pyroelectric, piezoelectric, electro-optic	pyrodetector, wave guide device, frequency doubler	[14,32]
$Pb(Mg_{1/3}Nb_{2/3})O_3$	dielectric	memory devices, capacitor, actuators	[12]
$La_{1-x}Ca_xMnO_{3-\delta}$	colossal magnetoresistance	magnetic recording for read-head technology	[33]
Bi_2WO_6, $Bi_2VO_{5.5}$	dielectric, ion conductive, photocatalytic	solid oxide fuel cells	[34-35]

One of the most widely studied perovskite is $BaTiO_3$. It is well-known for having ferroelectric and piezoelectric properties. $BaTiO_3$ is widely used in applications such as capacitors since it has a very high relative permittivity of 1,000 - 10,000 depending on the temperature. The ferroelectricity in $BaTiO_3$ arises

from a displacement of the titanium ions away from the centrosymmetric position within the oxygen octahedra (Fig. 1.3). The *t* value of $BaTiO_3$ is 1.07 (Ba^{2+} – 1.61 Å, Ti^{4+} – 0.605 Å)[36] and due to the Ti^{4+} ion being too small for the octahedral void, it therefore moves towards five of the oxygens in the octahedron. Neighbouring Ti^{4+} ions will undergo similar displacement and therefore a permanent dipole is formed.

$BaTiO_3$ has a Curie temperature of ~ 120 ^oC; the Curie temperature is the temperature at which the spontaneous polarisation falls to zero and the relative permittivity (or dielectric constant) reaches a maximum. Below the Curie temperature $BaTiO_3$ has a tetragonal structure that is non-centrosymmetric and polar, thus it is ferroelectric and exhibits a very high relative permittivity that varies with applied electric field and temperature. Above the Curie temperature, $BaTiO_3$ undergoes a phase transition to a cubic structure (centrosymmetric and non-polar) so it is no longer ferroelectric and becomes paraelectric. Between 5 and -90 ^oC, the structure is orthorhombic and below -90 ^oC, it is rhombohedral.[37-38]

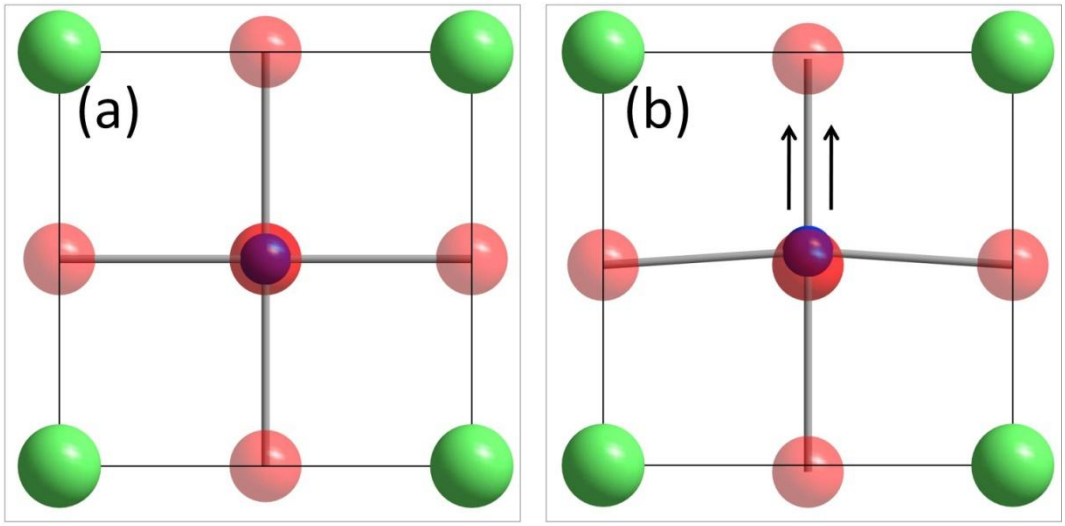

Fig. 1.3 Crystal structure of $BaTiO_3$, a) High temperature cubic phase and b) Room temperature tetragonal phase with cation displacement. The green spheres represents Ba, blue is Ti and red is O

The properties of $BaTiO_3$ can be modified by partial substitution on either the A or B site. For example, $Ba_{1-x}Sr_xTiO_3$ is a solid solution of $BaTiO_3$ and $SrTiO_3$, where the A-site is occupied by either Ba^{2+} or Sr^{2+} ions. At room temperature, $BaTiO_3$ and Ba-rich $Ba_{1-x}Sr_xTiO_3$ materials have tetragonal lattice and are ferroelectric, whereas $SrTiO_3$ and Sr-rich $Ba_{1-x}Sr_xTiO_3$ materials are cubic and not ferroelectric (i.e. they are paraelectric).[39] Substituting Ba for Sr has the effect of decreasing the Curie temperature and increasing the dielectric constant.[40-42] Substituting the Ti^{4+} in $BaTiO_3$ with Zr^{4+} can also lower the Curie temperature.[43-44] A solid solution of $BaTi_{1-x}Zr_xO_3$ can be formed for the whole compositional range. At the other end member, $BaZrO_3$ is paraelectric at all temperatures.

Another important perovskite widely used for its piezoelectric property is $PbZr_{1-x}Ti_xO_3$ (PZT). It is a solid solution of $PbTiO_3$ and $PbZrO_3$, where the B site is occupied by either Zr^{4+} or Ti^{4+} ions. $PbTiO_3$ has a Curie temperature of 490 ^oC, at which it undergoes a phase transition from the paraelectric cubic phase to ferroelectric tetragonal phase. In contrast, $PbZrO_3$ is an antiferroelectric material at room temperature. It has a Curie temperature at 230 ^oC, where a phase transition from paraelectric cubic to antiferroelectric orthorhombic phase occurs.[45-46] The phase diagram of PZT has a morphotropic phase boundary (MPB) at x = 0.48. The term MPB describes the phase boundary where a change in composition results in a change of phase.[13] The MPB of PZT is a region on its phase diagram where an abrupt change from a tetragonal Ti-rich region to a rhombohedral Zr-rich region, is observed over a small compositional range.[47] PZT solid solutions close to the MPB exhibit superior ferroelectric and piezoelectric properties. Structural studies by Noheda *et al.* revealed a narrow region of monoclinic phases with *Cm* and *Cc* symmetries near the MPB.[45,48] It is thought that this monoclinic phase may be

responsible for the remarkably high piezoelectric response of PZT. PZT is the most widely used piezoelectric, despite the fact that it contains lead; no existing material has properties superior to it.

1.4 Hexagonal Perovskites

If the value of the tolerance factor, *t*, is > 1, either due to the A-cation being too large or the B-cation is too small, then the perovskite structure will be distorted to form hexagonal perovskites. The close packed layers are stacked in a hexagonal manner leading to face sharing of the [BO_6] octahedra. Structures containing face-sharing octahedra are less stable than those with corner sharing octahedra[49] so some hexagonal perovskites overcome this restriction by forming metal-metal bonds between the B ions of the BX_6 octahedra, which are strong enough to overcome the metal-metal repulsion.[50] As a consequence of these stability restrictions, hexagonal perovskites are less commonly found compared to cubic perovskites.

One type of hexagonal perovskite adopts the space group $P6_3/mmc$ and can be found in $BaNiO_3$ (Fig. 1.4). A polyhedral representation of the structure in Fig. 1.4b shows the chains of face-sharing BX_6 octahedra orientated along the *c*-axis. Just like the cubic perovskites, hexagonal perovskites can also undergo distortions leading to a variety of structures with lower symmetry.

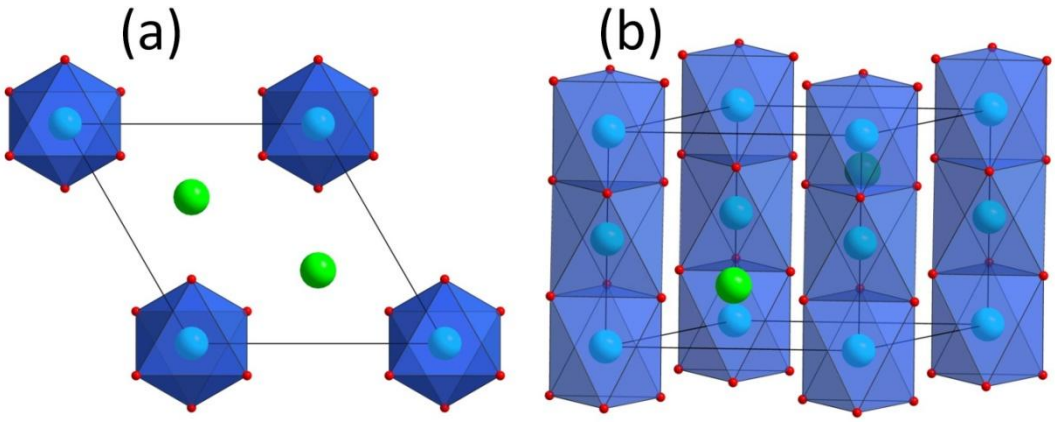

Fig. 1.4 Crystal structure of $BaNiO_3$, space group $P6_3/mmc$, a) along the *c*-axis and b) polyhedral structure

A second type of hexagonal perovskite is found for rare-earth manganites $RMnO_3$ (R=Ho-Lu,Y). They adopt a distorted hexagonal structure with space group $P6_3cm$.[51] The structure of $YMnO_3$ (Fig. 1.5) in particular, consists of MnO_5 polyhedra corner-linked to form triangular lattice layers. The MnO_5 polyhedra are tilted in a way to induce trimerisation of Mn^{3+} ions in each Mn layer, along with the downward displacement of two thirds of the Y ions and the upward displacement of one third of the Y ions.[52] These distortions lead to the absence of centrosymmetry of the crystal and the appearance of ferroelectric polarisation perpendicular to the layers.[53-54]

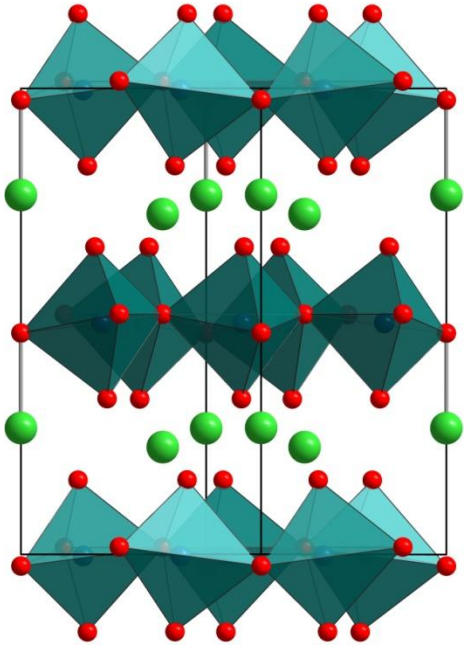

Fig. 1.5 Crystal structure of $YMnO_3$, space group $P6_3cm$

Hexagonal manganites are a class of materials that may be multiferroic, which are materials that simultaneously possess two or more of the so-called 'ferroic' properties: ferroelectricity, ferromagnetism and ferroelasticity.[55] Coupling between ferroelectric and ferromagnetic order parameters would lead to magnetoelectric effects, where the magnetisation can be adjusted by an applied electric field and vice versa. This effect can lead to new forms of sensors, transistors and multi-state memory devices for data storage.[56-58] However, single phase materials that possess both ferroelectricity and ferromagnetism are relatively rare.

1.5 Doped TiO_2

TiO_2 exists in three common crystalline forms: rutile (tetragonal, $P4_2/mnm$), anatase (tetragonal, $I4_1/amd$) and brookite (orthorhombic, $Pbca$).[59] Each of these

polymorphs contains titanium atoms surrounded by a distorted octahedron of six oxygen atoms. The three forms differ in the way the octahedral units are linked by various combinations of edge and corner sharing to give extended network structures. In the rutile structure (Fig. 1.6a), two opposing edges of each octahedron are shared to form linear chains and the TiO_6 chains are linked together via corner connection. Anatase has no corner sharing but has four edges shared per octahedron (Fig. 1.6b). The structure can be described as zigzag chains of the octahedra linked together by edge sharing. In the case of brookite, the octahedra share three edges and also corners (Fig. 1.6c). The octahedra are arranged parallel to the *c*-axis and are cross-linked by edge-sharing.[49]

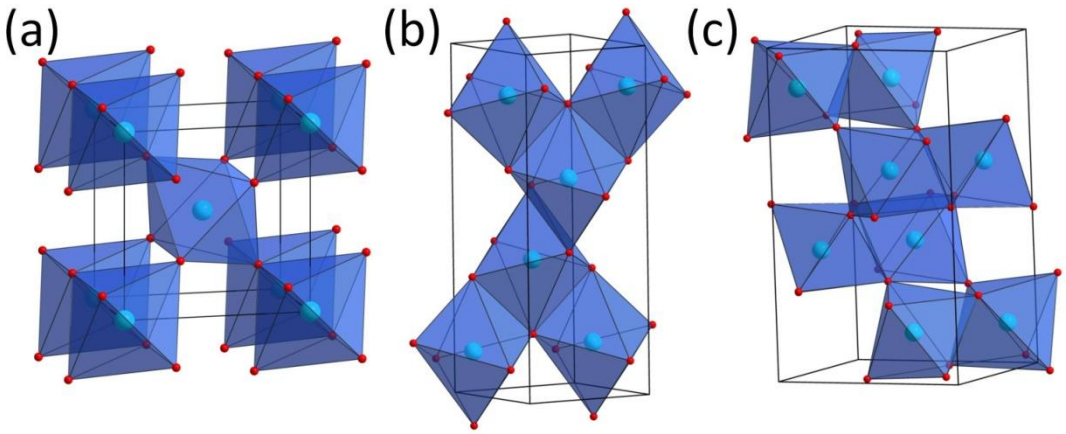

Fig. 1.6 Crystal structure of TiO_2 a) rutile, b) anatase and c) brookite

The anatase phase is stable up to 600-1000^{o}C but at temperatures above that, it converts to the rutile phase.[60-63] However, the exact temperature for this conversion is affected by several factors such as preparation conditions, amount of impurities present and the morphology and size of the particles.[62,64-66] Addition of dopants to TiO_2 can also affect the temperature at which the anatase to rutile phase transition occurs.[67]

The three polymorphs exhibit different physical properties. For example, rutile has the highest density among the three polymorphs and also the highest refractive index. Anatase on the other hand, has the widest band gap, while the properties of brookite fall between those of rutile and anatase. Table 1.2 lists some of the properties of the three TiO_2 polymorphs.

Table 1.2 Different TiO_2 polymorphs and some of their physical properties

Polymorph	Crystal system	Space group	Density (gcm^{-3})	Optical band gap (eV)	Refractive index
Rutile	Tetragonal	$P4_2/mnm$	4.13-4.26	3.0	2.72
Brookite	Orthorhombic	*Pbca*	3.99-4.11	3.11	2.63
Anatase	Tetragonal	$I4_1/amd$	3.79-3.84	3.19	2.52

The most widespread use of TiO_2 is in the area of white pigments. The rutile phase has a high refractive index and therefore scatters light very effectively, offering whiteness and brightness to the products in which it is used. It is widely used in paint, coatings, foods, toothpastes and sunscreen. TiO_2 is also used in gas sensing devices due to its changes in electrical or optical properties on adsorption of specific molecules on the surface of the material.[68] Another interesting property of TiO_2 is its ability to act as a photocatalyst, where the anatase is widely reported to be more active than the rutile phase.[69-72] TiO_2 is a suitable photocatalyst for a variety of applications such as the decomposition of water into oxygen and hydrogen for solar energy conversion and the degradation of organic pollutants for waste-water treatment.[5-6,73-74] These applications are possible due to TiO_2 being a semiconductor with a band gap suitable for the absorption of UV radiation. When UV light is absorbed by TiO_2, some of the electrons in the valence band will be excited to the conduction band. This process results in the formation of electron holes in the valence band and free electrons in the conduction band of TiO_2. These electron and hole pairs can then initiate various reactions on any adsorbed molecules. Generally,

the electrons can reduce adsorbed O_2 to produce superoxide radical ion, $\cdot O_2^-$. At the same time, the holes can react with surface hydroxyl groups or H_2O molecules to produce strongly oxidising ·OH radicals.[5,75-77] This process will then initiate the degradation of a wide range of organic pollutants into carbon dioxide and water.

The titanium in TiO_2 can be replaced by other metals in order to modify its optical properties. Different metals have been doped into TiO_2. For example, Li *et al.* prepared La doped TiO_2 by the sol-gel method and found that the La inhibits the phase transformation of TiO_2, enhances the thermal stability of TiO_2, reduces the crystallite size and results in the presence of Ti^{3+} on the surface of the sample.[78] Nagaveni *et al.* doped TiO_2 with W^{6+}, V^{5+}, Ce^{4+}, Zr^{4+}, Fe^{3+} and Cu^{2+} by a solution combustion method and reported that doping was only successful for a limited range of dopant concentrations.[79] Choi *et al.* found that doping with Fe^{3+}, Mo^{5+}, Ru^{3+}, Os^{3+}, Re^{5+}, V^{4+} and Rh^{3+} at 0.1-0.5 at. % significantly increased the photoreactivity while Co^{3+} and Al^{3+} decreased the photoreactivity.[80] The metal ions which are found to inhibit the anatase to rutile phase transformation are Si^{4+}, W^{6+}, Nb^{5+}, Ta^{5+}, Cr^{3+},[81-82] while the metal ions which are reported to promote the phase transformations are Ni^{2+}, Co^{2+}, Mn^{4+}, Fe^{3+}, Cu^{2+}, and Ag^{+}.[83-84]

1.6 Hydrothermal synthesis

The materials described so far have traditionally been made by conventional solid state synthesis where high temperatures above 1000 ^oC are used for long periods of time to force reaction between individual metal oxides. The high temperatures used usually only give the most thermodynamically stable structure and

offer little control over the particle size of the product. This method also requires repetitive grinding and high temperature firing of oxide precursors, which if incomplete may result in the appearance of impurity products or unreacted starting materials. Volatile metals, such as Na and Bi, may easily be lost at high temperatures. Other synthesis techniques involving sol-gel and co-precipitation, which involve making an amorphous precursor phase, are also not always convenient because of the firing or annealing post-treatment at high temperature. As the properties of these materials depend greatly on their composition and morphology, new synthesis techniques that can control these factors are needed. Hence, other techniques that use milder conditions have been developed such as hydrothermal and solvothermal synthesis.

The term 'hydrothermal' was first used by the British geologist, Sir Roderick Murchison (1792-1871) to describe the action of water at elevated temperature and pressure, resulting in the formation of various rocks and minerals.[85] Hydrothermal synthesis usually refers to chemical reactions in aqueous solvents that are heated in a closed system, above 100 ^{o}C and 1 bar.[86] Although it has also been defined as any reaction carried out in the presence of a solvent above room temperature and pressures greater than 1 atm in a closed system.[87] If non-aqueous solvents are used instead, the process is called solvothermal synthesis.[88] The temperature and pressure conditions first facilitate the dissolution of the chemical reagents and then the products are formed by crystallisation. This technique provides a one-step reaction route to complex materials. In contrast to the conventional solid state synthesis, it offer several advantages such as the use of lower temperatures, greater control on particle size and the production of phase pure and homogeneous materials. The milder conditions also allow the synthesis of metastable phases that are otherwise

difficult to obtain with conventional solid state synthesis. The use of solvents also offers higher diffusivity and dissolving power which increases the mobility of dissolved ions and allows better mixing of the reagents.[85,89-90] This increased mobility allows reactions to proceed at lower temperatures or for shorter periods of time. However, hydrothermal syntheses also have certain disadvantages. Since the reactions are carried out in a closed vessel, it is not possible to observe the growth of the crystals, which limits the amount of useful information available for understanding new materials. The closed hydrothermal system can also be affected by many factors such as pH, temperature, reagent concentrations, pressure and solvent filling levels, meaning that as yet, a full exploration of reaction conditions has not been made. Exploratory hydrothermal synthesis often involves a trial and error approach.

Hydrothermal synthesis is usually performed in a reaction vessel called an autoclave. The autoclaves are made up of a strong alloy such as steel to withstand the pressure developed during the reaction. Generally, highly acidic or basic conditions are used so the autoclave contains a Teflon liner, which protects it from corrosion and provides a chemically inert vessel for reaction. Hydrothermal reactions are usually performed in conventional ovens where temperatures up to a maximum temperature of 250 ^{o}C can be used, at which point the Teflon starts to deform. Recently, autoclaves made wholly of Teflon have allowed for hydrothermal synthesis of crystalline materials using microwaves.[91]

Historically, hydrothermal synthesis has been used for the growth of large quartz crystals and mixed metal fluorides,[85,92-93] and since then it has offered a low temperature route to a number of materials such as zeolites[94-95] and metal-organic

framework (MOF) materials.[96] In the next section, reported hydrothermal syntheses of perovskites and TiO_2 materials are reviewed with a particular focus on how the synthesis conditions can alter the crystal size, shape and product formed.

1.7 Hydrothermal Synthesis of Perovskites

Perovskites can be made using a variety of techniques, such as conventional solid state synthesis, sol-gel, molten-salt, micro-emulsion, hydrothermal and solvothermal synthesis. However, only the hydrothermal route will be considered in this section. Among the various types of perovskites that have been prepared hydrothermally, perovskite titanates are the most commonly reported.[97]

1.7.1 Hydrothermal synthesis of $BaTiO_3$

$BaTiO_3$ is the most extensively studied material among the titanate perovskites. The excellent ferroelectric and piezoelectric properties of $BaTiO_3$ have driven research into new synthetic routes to its synthesis. The direct hydrothermal crystallisation of $BaTiO_3$ was found to occur at temperatures as low as 80 ^oC from basic solutions containing $Ba(OH)_2$ and Ti alkoxides in the 1950s.[98] In comparison, the conventional solid state route to the same material involves repeated ball-milling and solid-state reaction of $BaCO_3$ and TiO_2 powders at temperatures greater than 900 ^oC.[99] The hydrothermal route not only offers a quicker and milder route to pure and crystalline $BaTiO_3$ but the particle size and shape can be controlled. Various Ba

and Ti precursors have been used to prepare $BaTiO_3$ hydrothermally but typically barium salts ($BaCl_2$ or $Ba(OH)_2$) and Ti alkoxides or TiO_2 were used.[100-106]

There are two mechanisms proposed for the formation of $BaTiO_3$ from $Ba(OH)_2$ and TiO_2.[107-108] The first mechanism involves heterogeneous nucleation where $BaTiO_3$ grows on the surface of undissolved TiO_2 particles by reaction with dissolved barium ions to yield core-shell type intermediates before the complete consumption of the remaining solid reagents. The second mechanism involves homogeneous nucleation where the dissolution of both Ba and Ti sources first occurs, then followed by the direct formation of $BaTiO_3$ from solution or at the surface of remaining TiO_2 particles. It is possible that both mechanisms may occur simultaneously, or depending on the reaction conditions, one may be preferred over the other. The growth of the $BaTiO_3$ may eventually lead to larger particles or secondary nucleation of new particles on to already formed crystals.[109]

As mentioned above, $BaTiO_3$ has a different crystal structure depending on the temperature, with the tetragonal phase stable at room temperature. The structure which $BaTiO_3$ adopts is dependent on the hydrothermal reaction conditions. Ciftci *et al.* prepared cubic $BaTiO_3$ by reacting TiO_2 with a strongly alkaline solution of $Ba(OH)_2$ at temperatures below ~150 ^oC for 24 hours.[110] Reactions carried out above 150 ^oC resulted in a mixture of cubic and tetragonal phases, with the content of the tetragonal phase increasing with increasing reaction temperature. Dutta *et al.* synthesised several $BaTiO_3$ powders from reaction of TiO_2 with different Ba precursors at 240 ^oC. The $BaTiO_3$ formed had a mixture of cubic and tetragonal phases, and the tetragonal content varied in the following order:

$I^- \sim Br^- \sim Cl^-$ > acetate > NO_3^- > OH^-.[101]

The particle size can also be controlled. By increasing the reaction temperature from 80 to 240 ^{o}C, the particle size of $BaTiO_3$ obtained increased from ~50 to ~100 nm.[110] Increasing the pH of the reaction solution was also found to increase particle size.[102] Habib *et al.* found that particle size also depends on the initial titania precursor. Reaction with fine grained 70% anatase-30%rutile TiO_2 (particle size 25 nm) formed $BaTiO_3$ faster than a reaction using pure anatase (particle size 110-125 nm), which yielded $BaTiO_3$ particles with a TiO_2 core.[111] The particle size obtained from 70% anatase-30%rutile TiO_2 (30-50 nm) is much smaller than from pure anatase (50-100 nm).

The use of various solvents also appears to provide a certain degree of control over the particle size and shape. Wada *et al.* obtained elliptical spheres with average size of 150 nm for hydrothermal reactions of TiO_2 and $Ba(OH)_2$ at 240 ^{o}C for 18 hours.[112] But when polar solvents such as ethanol and 2-methoxyethanol were used instead, they obtained irregular particles (~10 nm) and nanocubes (~23 nm) respectively. They also performed solvothermal reactions using a 40:60 mixture of 2-methoxyethanol and ethanol, and obtained sharp-edged nanocubes (12-15 nm). Adireddy *et al.* obtained monodispersed $BaTiO_3$ nanocubes (20 nm) via solvothermal reaction using a mixture of water, butanol and oleic acid as solvent.[113]

Niederberger *et al.* excluded both water and air from the reagent mixture and showed that controlled synthesis of monodispersed and non-agglomerated nanocrystallites $BaTiO_3$ (~6 nm) was possible.[114] Du *et al.* reported even smaller $BaTiO_3$ particles (3.7 nm) by using a mixed solvent system.[115] Ba acetate or $Ba(OH)_2$ was dissolved in oleic acid and then titanium *n*-butoxide in hexadecene was added to get the oil phase. A second aqueous phase in the form of NaOH solution

was then added and the reaction mixture was heated at 180 ^{o}C for 12 hours. When the hexadecene was replaced with toluene or heptane, the particle size increased to 4.1 and 6.7 nm, respectively. Xia *et al.* obtained $BaTiO_3$ nanotoruses from a reaction of TiO_2 and $Ba(OH)_2$ in alkaline water-ethanol mixture heated at 180 ^{o}C for 8-48 hours.[116]

Solvothermal reactions carried out under microwave heating can also reduce the reaction time for $BaTiO_3$ synthesis. Bilecka *et al.* reported the synthesis of $BaTiO_3$ from the reaction of Ba and Ti isopropoxide in benzyl alcohol microwave heated to 200 ^{o}C for 1 minute.[117]

1.7.2 Hydrothermal synthesis of doped $BaTiO_3$

Hydrothermal synthesis of doped $BaTiO_3$ is also possible, with metal ions such as Eu^{2+} and Mg^{2+} being used to substitute Ba^{2+} in $BaTiO_3$, but Sr^{2+} seems to be the most commonly described (Table 1.3).

Table 1.3 Examples of hydrothermally prepared doped $BaTiO_3$

Material	Reagents	Conditions	References
Sr doped $BaTiO_3$	$TiCl_4$, $Ba(OH)_2$, $Sr(OH)_2$, NaOH	300 ^{o}C / 5-100 h	[118]
	$Ti(OC_2H_5)_4$, $Ba(OH)_2.H_2O$, $Sr(OH)_2.H_2O$	150 – 300 ^{o}C / 3 h	[119]
	$Ti(iOPr)_4$, Ba, Sr, benzyl alcohol	200 ^{o}C / 48 h	[120]
	$Ti(OH)_4$, $Ba(OH)_2$, $Sr(OH)_2$	200 ^{o}C	[121]
	$TiCl_4$, $BaCl_2$, $SrCl_2$, ethanol, ethyl glycol, NaOH	240 ^{o}C / 24 h	[122]
	$TiCl_4$, $BaCl_2$, $Sr(NO_3)_2$, KOH	240 ^{o}C / 8 h	[123]
	$Ti(OC_4H_9)_4$, $Ba(CH_3COO)_2$, $Sr(NO_3)_2$, ethylene glycol, NH_3, KOH	200 ^{o}C / 12 h	[124]
Eu doped $BaTiO_3$	TiO_2, $Ba(OH)_2$, Eu acetate,	150 ^{o}C / 3 h	[125]
	$Ti(OC_4H_9)_4$, $Ba(CH_3COO)_2$, Eu_2O_3, NaOH	300 ^{o}C	[126]
Mg doped $BaTiO_3$	$TiCl_4$, $BaCl_2$, $MgCl_2$, NaOH	220-260 ^{o}C / 10-16 h	[127]

Roeder *et al.* prepared a solid solution of $Ba_{1-x}Sr_xTiO_3$ at temperatures below 100 ^oC by reacting nanosized TiO_2 powders with $BaCl_2$ and $SrCl_2$ in NaOH solutions.[128] They reported that a large excess of Ba and Sr precursors, relative to Ti, was needed to obtain a single phase solution. They observed that reactions carried out at a Ba/Sr : Ti ratio of 1.1 : 1 results in the formation of Ba-rich and Sr-rich phases. The use of a chelating ligand such as EDTA has also been reported to facilitate formation of phase pure $Ba_{1-x}Sr_xTiO_3$. Gersten *et al.* prepared phase pure $Ba_{0.55}Sr_{0.45}TiO_3$ at 90-120 ^oC by reacting Ba and Sr acetate with TiO_2, in the presence of EDTA.[129] Reactions without EDTA at 70-160 ^oC resulted in Ba-rich and Sr-rich phases. They suggest that EDTA reduces the adsorption affinity of Sr, as Sr reacts more quickly with TiO_2 than Ba, thus preventing preferential incorporation of Sr.

$Ba_{1-x}Sr_xTiO_3$ with different morphologies has been observed. Yang *et al.* prepared single crystal $Ba_{1-x}Sr_xTiO_3$ dendrites hydrothermally by first dissolving $Ti(SO_4)_2$ in dilute HNO_3 and adding KOH solution to make a Ti hydroxide suspension. Then Ba and Sr nitrates were added, and heated to 200 ^oC for 6 hours.[130] They also observed $Ba_{1-x}Sr_xTiO_3$ with spherical and star-like morphology by just varying the concentration of KOH.[131] Solvothermal reactions also alter the shape of $Ba_{1-x}Sr_xTiO_3$. For example, Wei *et al.* reported the formation of spherical and cube-like $Ba_{1-x}Sr_xTiO_3$ nanocrystals by using a mixture of ethylenediamine and ethanolamine as the solvent,[124] while Hou *et al.* obtained nanocubes by reacting $TiCl_4$ with $SrCl_2$ and $BaCl_2$ in a mixed solution of water-ethanol-ethylene glycol monomethyl ether.[122]

There are fewer reports on hydrothermally prepared B-site substituted $BaTiO_3$. Currently, there are reports on doped $BaTiO_3$ where Ti is substituted with Mn, Ce and Fe and Zr. Zr^{4+} readily substitutes Ti^{4+} in the perovskite structure. Vivekanandan *et al.* prepared $BaTi_{1-x}Zr_xO_3$ by reacting TiO_2 with $ZrOCl_2$ heated at 85-130 ^oC for 2-6 hours.[132] They observed dendritic growth of the crystals for $x < 0.5$. Samples with higher Zr content have almost spherical shapes. Lee *et al.* prepared $BaTi_{1-x}Zr_xO_3$ by adding H_2O_2 in a mixed aqueous solution of $BaCl_2$, $ZrOCl_2$ and $TiCl_4$.[133] They found that the dielectric constant increased from 1700 ($x = 0$) to 3500 ($x = 0.2$).

1.8 Hydrothermal Sythesis of TiO_2

There are two ways in which TiO_2 is usually produced commercially. The first method called the "sulfate process" involves dissolving titanium ore in sulfuric acid to produce a suspension of titanium oxyhydroxide, which then undergoes filtration and firing to give TiO_2. In the "chloride process", the titanium ore is reacted with HCl gas at a high temperature to produce $TiCl_4$. A high yield of TiO_2 is then achieved by reacting $TiCl_4$ with oxygen gas at temperatures above 1000 ^oC.[134]

Many groups have prepared TiO_2 hydrothermally where the morphology and phase can be controlled.[135-142] For example, TiO_2 nanoparticles were prepared by adding Ti isopropoxide dropwise to an acidic ethanol-water solution, and reacted at 240 ^oC for 4 hours. The product was mainly anatase with particle size in the range of 7-25 nm.[143]

TiO_2 nanorods have also been synthesised hydrothermally. Cozzoli *et al.* prepared anatase TiO_2 nanorods by hydrolysis of Ti tetraisopropoxide in oleic acid as surfactant at temperatures as low as 80 ^oC.[144] Zhang *et al.* on the other hand, obtained TiO_2 nanorods by heating $TiCl_4$ solution at 60-150 ^oC for 12 hours in the presence of acid or inorganic salts.[145] Xie *et al.* obtained TiO_2 nanorods from solvothermal reactions involving Ti isopropoxide in ethylene glycol and ethylenediamine. By varying the concentration of ethylenediamine, TiO_2 nanorods with different diameters can be made.[142]

Hollow TiO_2 nanospheres were obtained by heating TiF_4 solution at 180 ^oC for 20 hours,[146] while solvothermal reactions carried out with TiF_4 in a water-2-propanol mixture, in the presence of HF, resulted in TiO_2 nanosheets. The nanosheets also exhibit better photoreactivity (more than 5 times) when compared with commercial TiO_2, Degussa P25.[147]

Most hydrothermal synthesis of TiO_2 has been focussed on the preparation of anatase since it forms easily at low temperatures and has a high photoreactivity. The rutile phase is usually prepared using high temperatures as it is the most thermodynamically stable phase. However, annealing reactions tend to give low surface area rutile, which is not suitable for applications such as catalysis. Several studies have developed hydrothermal synthesis routes to selectively prepare the different phases. Cheng *et al.* prepared rutile and anatase TiO_2 hydrothermally by using $TiCl_4$ as a starting material and heating at 220 ^oC for 2 hours.[148] They concluded that high acidity and a high concentration of $TiCl_4$ solutions favour rutile formation, whereas solutions with pH values of 3.4 to 8.2 favour the anatase phase. By increasing the pH to 10, Zheng *et al.* prepared pure brookite TiO_2.[149] Yoon *et al.*

selectively prepared different TiO_2 phases via microwave-solvothermal reactions.[150] Reactions involving $TiCl_4$ in ethanol, propanol and butanol gave anatase TiO_2 while reactions in octanol yielded rutile TiO_2. When $TiCl_3$ was used instead, the brookite phase was obtained in reactions done in butanol. However, a small amount of rutile was also detected.

A study done by Tomita *et al.* utilised a water soluble titanium complex prepared from titanium powder, hydrogen peroxide, NH_3(aq) and a carboxylic acid.[151] This synthesis method involved making a titanium complex first, which was then hydrothermally treated to make TiO_2. By changing the carboxylic acid used, different phases of TiO_2 could be made. They found that using citric acid, tartaric acid or malic acid, results in the anatase phase while glycolic acid gives rutile TiO_2. A mixture of anatase and rutile can also be made by using lactic acid. Kobayashi *et al.* used the same method to make a Ti glycolate complex and varied the amount of NH_3 during hydrothermal treatment. They found that the brookite phase can be obtained with excess amount of NH_3.[138]

A simpler hydrothermal route for rutile TiO_2 was reported by Kandiel *et al.*, where they used a commercially available solution of titanium bisammonium lactato dihydroxide (TiBALD) as the starting material.[152] The TiBALD solution in water was heated at 200 ^oC for 24-96 hours and yielded TiO_2 rutile nanorods. As yet, these reports of hydrothermal synthesis of rutile TiO_2 have not yet been expanded on to form doped versions of the materials.

1.9 Aims of the Project

The aim of this research project was to synthesise new and known mixed metal oxides by hydrothermal synthesis, via a single-step reaction, i.e. without any high temperature annealing to bring about crystallisation. Currently, it is still very difficult to predict the outcome of new hydrothermal reactions, and many of the hydrothermal reactions mentioned earlier in this chapter represent experimental observations rather than being the result of design in synthesis. Accumulation of these observations may allow better predictability in synthesis outcomes and greater understanding of the chemistry involved. This will allow better tuning of the reaction conditions that will give greater control on the crystal size and shape of the materials and explore new phases that are not attainable by other synthesis methods.

The materials chosen for study were important families of oxides that have properties for application in important areas and for which new controlled synthesis methods would be very useful. The materials were also selected to provide more complex structural chemistry than those typically reported in the literature from hydrothermal chemistry, in particular, materials containing mixture of metals, either as dopants or in solid solutions. The aim was to extend the use of hydrothermal synthesis to complex materials and to investigate the extent to which forming homogeneous mixed-metal oxide materials directly from solution is possible. The materials in this work were characterised with various diffraction and spectroscopic techniques to study their structures fully and, where appropriate, an investigation of their properties was carried out.

Chapter 2 details the experimental method used throughout the work, providing background information on the techniques and describes the instruments used.

Chapter 3 describes the hydrothermal synthesis of perovskite titanates with A-site substitution, particularly on $NaCe_{1-x}La_xTi_2O_6$. This study was to investigate the scope for the preparation of complex perovskite solid solutions by hydrothermal synthesis, to prove the degree of element mixing using a variety of structural probes and to investigate the level of defects in the samples.

Chapter 4 describes the synthesis of B-site substituted perovskites and how reaction conditions can dramatically affect the morphology of the materials as in the case of $NaLa(Ti_{1-x}Zr_x)_2O_6$. On the other hand, the study on $NaBi(Ti_{1-x}Zr_x)_2O_6$ investigates the effect of B-site substitution on the piezoelectric and ferroelectric properties.

Chapter 5 describes the synthesis of a rare-earth manganite, $YMnO_3$ and explores the possibility of doping this material with Fe hydrothermally.

Chapter 6 describes the synthesis of phase pure rutile TiO_2 instead of the anatase phase expected by low temperature synthesis and then modifying the synthesis to prepare W and Sn doped TiO_2 in the rutile phase. This chapter also describes the hydrothermal synthesis of Ce doped anatase TiO_2 and the investigation of its catalytic properties.

Chapter 7 gives an overall conclusion to the work in this thesis and any future work that can be carried out.

1.10 References

(1) Izyumskaya, N.; Alivov, Y.; Morkoc, H. *Crit. Rev. Solid State Mater. Sci.* **2009**, *34*, 89.

(2) Skinner, S. J. *Int. J. Inorg. Mater.* **2001**, *3*, 113.

(3) Pena, M. A.; Fierro, J. L. G. *Chem. Rev.* **2001**, *101*, 1981.

(4) Fernandez-Garcia, M.; Martinez-Arias, A.; Hanson, J. C.; Rodriguez, J. A. *Chem. Rev.* **2004**, *104*, 4063.

(5) Hoffmann, M. R.; Martin, S. T.; Choi, W. Y.; Bahnemann, D. W. *Chem. Rev.* **1995**, *95*, 69.

(6) Mills, A.; Davies, R. H.; Worsley, D. *Chem. Soc. Rev.* **1993**, *22*, 417.

(7) Braun, J. H.; Baidins, A.; Marganski, R. E. *Prog. Org. Coat.* **1992**, *20*, 105.

(8) Barker, P. J.; Branch, A. *Prog. Org. Coat.* **2008**, *62*, 313.

(9) Weir, A.; Westerhoff, P.; Fabricius, L.; Hristovski, K.; von Goetz, N. *Environ. Sci. Technol.* **2012**, *46*, 2242.

(10) Navrotsky, A.; Weidner, D. J.; American Geophysical Union: Washington D.C., 1989; Vol. 45

(11) Bhalla, A. S.; Guo, R. Y.; Roy, R. *Mater. Res. Innovations* **2000**, *4*, 3.

(12) Haertling, G. H. *J. Am. Ceram. Soc.* **1999**, *82*, 797.

(13) Rodel, J.; Jo, W.; Seifert, K. T. P.; Anton, E. M.; Granzow, T.; Damjanovic, D. *J. Am. Ceram. Soc.* **2009**, *92*, 1153.

(14) Chandler, C. D.; Roger, C.; Hampdensmith, M. J. *Chem. Rev.* **1993**, *93*, 1205.

(15) Jung, Y. S.; Na, E. S.; Paik, U.; Lee, J.; Kim, J. *Mater. Res. Bull.* **2002**, *37*, 1633.

(16) Brutchey, R. L.; Cheng, G. S.; Gu, Q.; Morse, D. E. *Adv. Mater.* **2008**, *20*, 1029.

(17) Kucheiko, S.; Choi, J. W.; Kim, H. J.; Jung, H. J. *J. Am. Ceram. Soc.* **1996**, *79*, 2739.

(18) Liu, T.; Zhao, X. Z.; Chen, W. *J. Am. Ceram. Soc.* **2006**, *89*, 1153.

(19) Szot, K.; Speier, W.; Bihlmayer, G.; Waser, R. *Nat. Mater.* **2006**, *5*, 312.

(20) Joshi, P. C.; Krupanidhi, S. B. *J. Appl. Phys.* **1993**, *73*, 7627.

(21) Takayama, R.; Tomita, Y.; Iijima, K.; Ueda, I. *Ferroelectrics* **1991**, *118*, 325.

(22) Muralt, P. *J. Micromech. Microeng.* **2000**, *10*, 136.

(23) Damjanovic, D. *Rep. Prog. Phys.* **1998**, *61*, 1267.

(24) Haertling, G. H. *Ferroelectrics* **1987**, *75*, 25.

(25) Okazaki, K.; Nagata, K. *J. Am. Ceram. Soc.* **1973**, *56*, 82.

(26) Matsumoto, H.; Hamajima, S.; Yajima, T.; Iwahara, H. *J. Electrochem. Soc.* **2001**, *148*, D121.

(27) Iwahara, H.; Uchida, H.; Ono, K.; Ogaki, K. *J. Electrochem. Soc.* **1988**, *135*, 529.

(28) Uchida, H.; Kimura, H.; Iwahara, H. *J. Appl. Electrochem.* **1990**, *20*, 390.

(29) Yoshinaga, M.; Yamaguchi, M.; Furuya, T.; Wang, S. R.; Hashimoto, T. *Solid State Ionics* **2004**, *169*, 9.

(30) Rolle, A.; Vannier, R. N.; Giridharan, N. V.; Abraham, F. *Solid State Ionics* **2005**, *176*, 2095.

(31) Bulmer, C. H.; Burns, W. K.; Hiser, S. C. *Appl. Phys. Lett.* **1986**, *48*, 1036.

(32) Wang, H. Q.; Zhang, X. W.; Dai, Y. J. *Mater. Lett.* **2012**, *67*, 145.

(33) Mathur, N. D.; Burnell, G.; Isaac, S. P.; Jackson, T. J.; Teo, B. S.; MacManusDriscoll, J. L.; Cohen, L. F.; Evetts, J. E.; Blamire, M. G. *Nature* **1997**, *387*, 266.

(34) Kendall, K. R.; Navas, C.; Thomas, J. K.; zurLoye, H. C. *Chem. Mater.* **1996**, *8*, 642.

(35) Zhang, C.; Zhu, Y. F. *Chem. Mater.* **2005**, *17*, 3537.

(36) Shannon, R. D. *Acta Crystallogr. Sect. A* **1976**, *32*, 751.

(37) Kwei, G. H.; Lawson, A. C.; Billinge, S. J. L.; Cheong, S. W. *J. Phys. Chem.* **1993**, *97*, 2368.

(38) Wasche, R.; Denner, W.; Schulz, H. *Mater. Res. Bull.* **1981**, *16*, 497.

(39) Baumert, B. A.; Chang, L. H.; Matsuda, A. T.; Tsai, T. L.; Tracy, C. J.; Gregory, R. B.; Fejes, P. L.; Cave, N. G.; Taylor, D. J.; Otsuki, T.; Fujii, E.; Hayashi, S.; Suu, K. *J. Appl. Phys.* **1997**, *82*, 2558.

(40) Lahiry, S.; Mansingh, A. *Thin Solid Films* **2008**, *516*, 1656.

(41) Syamaprasad, U.; Galgali, R. K.; Mohanty, B. C. *Mater. Lett.* **1988**, *7*, 197.

(42) Hilton, A. D.; Ricketts, B. W. *J. Phys. D-Appl. Phys.* **1996**, *29*, 1321.

(43) Nanakorn, N.; Jalupoom, P.; Vaneesorn, N.; Thanaboonsombut, A. *Ceram. Int.* **2008**, *34*, 779.

(44) Dong, L.; Stone, D. S.; Lakes, R. S. *J. Appl. Phys.* **2012**, *111*.

(45) Noheda, B.; Cox, D. E.; Shirane, G.; Gonzalo, J. A.; Cross, L. E.; Park, S. E. *Appl. Phys. Lett.* **1999**, *74*, 2059.

(46) Viehland, D. *Phys. Rev. B* **1995**, *52*, 778.

(47) Woodward, D. I.; Knudsen, J.; Reaney, I. M. *Phys. Rev. B* **2005**, *72*, 8.

(48) Noheda, B.; Cox, D. E.; Shirane, G.; Guo, R.; Jones, B.; Cross, L. E. *Phys. Rev. B* **2001**, *63*, 9.

(49) Wells, A. F. *Structural Inorganic Chemistry*; 5th ed.; Clarendon Press: Oxford, 1984.

(50) Mitchell, R. H. *Perovskites: Modern and Ancient*; Almaz Press, 2002.

(51) Anderson, M. T.; Greenwood, K. B.; Taylor, G. A.; Poeppelmeier, K. R. *Prog. Solid State Chem.* **1993**, *22*, 197.

(52) Choi, T.; Horibe, Y.; Yi, H. T.; Choi, Y. J.; Wu, W. D.; Cheong, S. W. *Nat. Mater.* **2010**, *9*, 253.

(53) Yakel, H. L.; Koehler, W. C. *Acta Cryst.* **1963**, *16*, 957.

(54) Katsufuji, T.; Masaki, M.; Machida, A.; Moritomo, M.; Kato, K.; Nishibori, E.; Takata, M.; Sakata, M.; Ohoyama, K.; Kitazawa, K.; Takagi, H. *Phys. Rev. B* **2002**, *66*, 8.

(55) Schmid, H. *Ferroelectrics* **1994**, *162*, 665.

(56) Fiebig, M.; Lottermoser, T.; Frohlich, D.; Goltsev, A. V.; Pisarev, R. V. *Nature* **2002**, *419*, 818.

(57) Fujimura, N.; Ishida, T.; Yoshimura, T.; Ito, T. *Appl. Phys. Lett.* **1996**, *69*, 1011.

(58) Ito, D.; Fujimura, N.; Yoshimura, T.; Ito, T. *J. Appl. Phys.* **2003**, *93*, 5563.

(59) Diebold, U. *Surf. Sci. Rep.* **2003**, *48*, 53.

(60) Breckenridge, R. G.; Hosler, W. R. *Phys. Rev.* **1953**, *91*, 793.

(61) Balachandran, U.; Eror, N. G. *J. Solid State Chem.* **1982**, *42*, 276.

(62) Kumar, K. N. P.; Keizer, K.; Burggraaf, A. J. *J. Mater. Chem.* **1993**, *3*, 1141.

(63) Gribb, A. A.; Banfield, J. F. *Am. Mineral.* **1997**, *82*, 717.

(64) Izutsu, H.; Nair, P. K.; Mizukami, F. *J. Mater. Chem.* **1997**, *7*, 855.

(65) Zhang, H. Z.; Banfield, J. F. *J. Phys. Chem. B* **2000**, *104*, 3481.

(66) Zhang, H. Z.; Banfield, J. F. *J. Mater. Chem.* **1998**, *8*, 2073.

(67) Mahanty, S.; Roy, S.; Sen, S. *J. Cryst. Growth* **2004**, *261*, 77.

(68) Korotcenkov, G. *Mater. Sci. Eng. B* **2007**, *139*, 1.

(69) Tanaka, K.; Capule, M. F. V.; Hisanaga, T. *Chem. Phys. Lett.* **1991**, *187*, 73.

(70) Linsebigler, A. L.; Lu, G. Q.; Yates, J. T. *Chem. Rev.* **1995**, *95*, 735.

(71) Carp, O.; Huisman, C. L.; Reller, A. *Prog. Solid State Chem.* **2004**, *32*, 33.

(72) Hashimoto, K.; Irie, H.; Fujishima, A. *Jpn. J. Appl. Phys.* **2005**, *44*, 8269.

(73) Fujishima, A.; Zhang, X. T.; Tryk, D. A. *Surf. Sci. Rep.* **2008**, *63*, 515.

(74) Khan, S. U. M.; Al-Shahry, M.; Ingler, W. B. *Science* **2002**, *297*, 2243.

(75) Fox, M. A.; Dulay, M. T. *Chem. Rev.* **1993**, *93*, 341.

(76) Nosaka, Y.; Daimon, T.; Nosaka, A. Y.; Murakami, Y. *Phys. Chem. Chem. Phys.* **2004**, *6*, 2917.

(77) Tachikawa, T.; Fujitsuka, M.; Majima, T. *J. Phys. Chem. C.* **2007**, *111*, 5259.

(78) Li, F. B.; Li, X. Z.; Hou, M. F. *Appl. Catal. B-Environ.* **2004**, *48*, 185.

(79) Nagaveni, K.; Hegde, M. S.; Madras, G. *J. Phys. Chem. B* **2004**, *108*, 20204.

(80) Choi, W. Y.; Termin, A.; Hoffmann, M. R. *J. Phys. Chem.* **1994**, *98*, 13669.

(81) Okada, K.; Yamamoto, N.; Kameshima, Y.; Yasumori, A.; MacKenzie, K. J. D. *J. Am. Ceram. Soc.* **2001**, *84*, 1591.

(82) Ohtsuka, Y.; Fujiki, Y.; Suzuki, Y. *J. Japan. Assoc. Mineral. Petrol. Econ. Geol.* **1982**, *77*, 117.

(83) Iida, Y.; Ozaki, S. *J. Am. Ceram. Soc.* **1961**, *44*, 120.

(84) Chao, H. E.; Yun, Y. U.; Xingfang, H. U.; Larbot, A. *J. Eur. Ceram. Soc.* **2003**, *23*, 1457.

(85) Yoshimura, M.; Byrappa, K. *J. Mater. Sci.* **2008**, *43*, 2085.

(86) Rabenau, A. *Angew. Chem. Int. Ed.* **1985**, *24*, 1026.

(87) Byrappa, K.; Yoshimura, M. *Handbook of hydrothermal technology*; Noyes Publications: NJ, USA, 2001.

(88) Demazeau, G. *J. Mater. Chem.* **1999**, *9*, 15.

(89) Walton, R. I. *Chem. Soc. Rev.* **2002**, *31*, 230.

(90) Somiya, S.; Roy, R. *Bull. Mater. Sci.* **2000**, *23*, 453.

(91) Komarneni, S.; Roy, R.; Li, Q. H. *Mater. Res. Bull.* **1992**, *27*, 1393.

(92) Laudise, R. A. *Chem. Eng. News* **1987**, *65*, 30.

(93) Leblanc, M.; Ferey, G.; Depape, R. *Mater. Res. Bull.* **1984**, *19*, 1581.

(94) Cundy, C. S.; Cox, P. A. *Chem. Rev.* **2003**, *103*, 663.

(95) Cheetham, A. K.; Ferey, G.; Loiseau, T. *Angew. Chem. Int. Ed.* **1999**, *38*, 3268.

(96) Meek, S. T.; Greathouse, J. A.; Allendorf, M. D. *Adv. Mater.* **2011**, *23*, 249.

(97) Modeshia, D. R.; Walton, R. I. *Chem. Soc. Rev.* **2010**, *39*, 4303.

(98) Flaschen, S. S. *J. Am. Chem. Soc.* **1955**, *77*, 6194.

(99) Beauger, A.; Mutin, J. C.; Niepce, J. C. *J. Mater. Sci.* **1983**, *18*, 3543.

(100) Xia, C. T.; Shi, E. W.; Zhong, W. Z.; Guo, J. K. *J. Eur. Ceram. Soc.* **1995**, *15*, 1171.

(101) Dutta, P. K.; Asiaie, R.; Akbar, S. A.; Zhu, W. D. *Chem. Mater.* **1994**, *6*, 1542.

(102) Asiaie, R.; Zhu, W. D.; Akbar, S. A.; Dutta, P. K. *Chem. Mater.* **1996**, *8*, 226.

(103) Dutta, P. K.; Gregg, J. R. *Chem. Mater*. **1992**, *4*, 843.

(104) Clark, I. J.; Takeuchi, T.; Ohtori, N.; Sinclair, D. C. *J. Mater. Chem.* **1999**, *9*, 83.

(105) Li, Y.; Gao, X. P.; Li, G. R.; Pan, G. L.; Yan, T. Y.; Zhu, H. Y. *J. Phys. Chem. C.* **2009**, *113*, 4386.

(106) Zhu, W.; Wang, C. C.; Akbar, S. A.; Asiaie, R. *J. Mater. Sci.* **1997**, *32*, 4303.

(107) Hertl, W. *J. Am. Ceram. Soc.* **1988**, *71*, 879.

(108) Eckert, J. O.; HungHouston, C. C.; Gersten, B. L.; Lencka, M. M.; Riman, R. E. *J. Am. Ceram. Soc.* **1996**, *79*, 2929.

(109) Testino, A.; Buscaglia, M. T.; Buscaglia, V.; Viviani, M.; Bottino, C.; Nanni, P. *Chem. Mater.* **2004**, *16*, 1536.

(110) Ciftci, E.; Rahaman, M. N.; Shumsky, M. *J. Mater. Sci.* **2001**, *36*, 4875.

(111) Habib, A.; Haubner, R.; Stelzer, N. *Mater. Sci. Eng. B* **2008**, *152*, 60.

(112) Wada, S.; Nozawa, A.; Ohno, M.; Kakemoto, H.; Tsurumi, T.; Kameshima, Y.; Ohba, Y. *J. Mater. Sci.* **2009**, *44*, 5161.

(113) Adireddy, S.; Lin, C. K.; Cao, B. B.; Zhou, W. L.; Caruntu, G. *Chem. Mater.* **2010**, *22*, 1946.

(114) Niederberger, M.; Pinna, N.; Polleux, J.; Antonietti, M. *Angew. Chem. Int. Ed.* **2004**, *43*, 2270.

(115) Du, H. C.; Wohlrab, S.; Weiss, M.; Kaskel, S. *J. Mater. Chem.* **2007**, *17*, 4605.

(116) Xia, F.; Liu, J. W.; Gu, D.; Zhao, P. F.; Zhang, J.; Che, R. C. *Nanoscale* **2011**, *3*, 3860.

(117) Bilecka, I.; Djerdj, I.; Niederberger, M. *Chem. Commun.* **2008**, 886.

(118) Leoni, M.; Viviani, M.; Nanni, P.; Buscaglia, V. *J. Mater. Sci. Lett.* **1996**, *15*, 1302.

(119) Um, M. H.; Kumazawa, H. *J. Mater. Sci.* **2000**, *35*, 1295.

(120) Niederberger, M.; Garnweitner, G.; Pinna, N.; Antonietti, M. *J. Am. Chem. Soc.* **2004**, *126*, 9120.

(121) Wei, X. Z.; Padture, N. P. *J. Ceram. Process. Res.* **2004**, *5*, 175.

(122) Hou, B.; Xu, Y.; Wu, D.; Sun, Y. H. *Powder Technol.* **2006**, *170*, 26.

(123) Miao, H. Y.; Zhou, Y. H.; Tan, G. Q.; Dong, M. *J. Electroceram.* **2008**, *21*, 553.

(124) Wei, X.; Xu, G.; Ren, Z. H.; Wang, Y. G.; Shen, G.; Han, G. R. *J. Cryst. Growth* **2008**, *310*, 4132.

(125) Rath, M. K.; Pradhan, G. K.; Pandey, B.; Verma, H. C.; Roul, B. K.; Anand, S. *Mater. Lett.* **2008**, *62*, 2136.

(126) Pazik, R.; Wiglusz, R. J.; Strek, W. *Mater. Res. Bull.* **2009**, *44*, 1328.

(127) Dong, M.; Miao, H. Y.; Tan, G. Q.; Pu, Y. P. *J. Electroceram.* **2008**, *21*, 573.

(128) Roeder, R. K.; Slamovich, E. B. *J. Am. Ceram. Soc.* **1999**, *82*, 1665.

(129) Gersten, B. L.; Lencka, M. M.; Riman, R. E. *J. Am. Ceram. Soc.* **2004**, *87*, 2025.

(130) Yang, L. L.; Wang, Y. G.; Wang, Y. J.; Wang, X. F.; Guo, X. J.; Han, G. R. *J. Alloy. Compd.* **2010**, *500*, L1.

(131) Yang, L. L.; Wang, Y. G.; Wang, Y. J.; Wang, X.; Wang, X. F. *J. Ceram. Soc. Jpn.* **2012**, *120*, 43.

(132) Vivekanandan, R.; Philip, S.; Kutty, T. R. N. *Mater. Res. Bull.* **1987**, *22*, 99.

(133) Lee, B. W.; Cho, S. B. *J. Eur. Ceram. Soc.* **2005**, *25*, 2009.

(134) Walton, R. I. *McGraw-Hill Encyclopedia of Science and Technology*; 10th Edition ed.; McGraw-Hill: New York, 2007.

(135) Yang, J.; Mei, S.; Ferreira, J. M. F. *J. Am. Ceram. Soc.* **2000**, *83*, 1361.

(136) Yang, J.; Mei, S.; Ferreira, J. M. F. *J. Am. Ceram. Soc.* **2001**, *84*, 1696.

(137) Tomita, K.; Kobayashi, M.; Petrykin, V.; Yin, S.; Sato, T.; Yoshimura, M.; Kakihana, M. *J. Mater. Sci.* **2008**, *43*, 2217.

(138) Kobayashi, M.; Tomita, K.; Petrykin, V.; Yoshimura, M.; Kakihana, M. *J. Mater. Sci.* **2008**, *43*, 2158.

(139) Kobayashi, M.; Petrykin, V.; Kakihana, M.; Tomita, K. *J. Am. Ceram. Soc.* **2009**, *92*, S21.

(140) Oh, J. K.; Lee, J. K.; Kim, S. J.; Park, K. W. *J. Ind. Eng. Chem.* **2009**, *15*, 270.

(141) Andersson, M.; Osterlund, L.; Ljungstrom, S.; Palmqvist, A. *J. Phys. Chem. B* **2002**, *106*, 10674.

(142) Xie, R. C.; Shang, J. K. *J. Mater. Sci.* **2007**, *42*, 6583.

(143) Chae, S. Y.; Park, M. K.; Lee, S. K.; Kim, T. Y.; Kim, S. K.; Lee, W. I. *Chem. Mater.* **2003**, *15*, 3326.

(144) Cozzoli, P. D.; Kornowski, A.; Weller, H. *J. Am. Chem. Soc.* **2003**, *125*, 14539.

(145) Zhang, Q. H.; Gao, L. *Langmuir* **2003**, *19*, 967.

(146) Yang, H. G.; Zeng, H. C. *J. Phys. Chem. B* **2004**, *108*, 3492.

(147) Yang, H. G.; Liu, G.; Qiao, S. Z.; Sun, C. H.; Jin, Y. G.; Smith, S. C.; Zou, J.; Cheng, H. M.; Lu, G. Q. *J. Am. Chem. Soc.* **2009**, *131*, 4078.

(148) Cheng, H. M.; Ma, J. M.; Zhao, Z. G.; Qi, L. M. *Chem. Mater.* **1995**, *7*, 663.

(149) Zheng, Y. Q.; Shi, E. W.; Cui, S. X.; Li, W. J.; Hu, X. F. *J. Am. Ceram. Soc.* **2000**, *83*, 2634.

(150) Yoon, S.; Lee, E. S.; Manthiram, A. *Inorg. Chem.* **2012**, *51*, 3505.

(151) Tomita, K.; Petrykin, V.; Kobayashi, M.; Shiro, M.; Yoshimura, M.; Kakihana, M. *Angew. Chem. Int. Ed.* **2006**, *45*, 2378.

(152) Kandiel, T. A.; Dillert, R.; Feldhoff, A.; Bahnemann, D. W. *J. Phys. Chem. C.* **2010**, *114*, 4909.

Chapter 2 – Experimental Techniques

2.1 Hydrothermal Synthesis

The hydrothermal synthesis of the materials in this work was carried out in Teflon-lined stainless steel autoclaves which were purchased from Parr Instrument Company. The equipment used consisted of a stainless steel autoclave, Teflon liner, spring, corrosion disc and bursting disc (Fig. 2.1). The Teflon liners used had capacities ranging from 18-23 mL. However, a larger autoclave with a 100 mL Teflon liner was also occasionally used to scale up reactions. The highest temperature that can be used is 250 ^{o}C, above which the liner will melt.

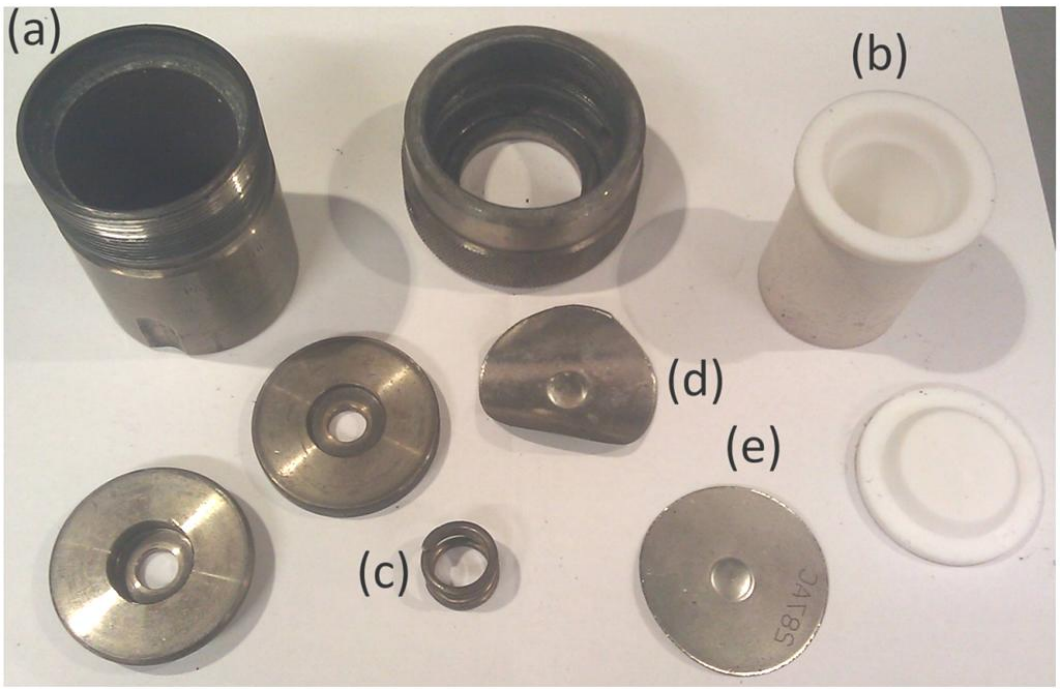

Fig. 2.1 a) Steel autoclave, b) Teflon liner, c) spring, d) corrosion disc and e) bursting disc

Reagents and solvents were added to the liners to a fill level of 70-80% and sealed tightly in the autoclave before heating in the oven. The oven used was a Carbolite PF30 oven with a fan-circulated airflow. The autoclaves were placed in a pre-heated oven, usually 240 ^{o}C, for the chosen reaction time. Then, the autoclaves were taken out and left to cool to room temperature. The solid products were then recovered by suction filtration, washed thoroughly with warm water and dried overnight at 70 ^{o}C in a drying oven. The products were then ground into powder for further characterisation. The above represents the general synthetic processes used. Further details are given in the subsequent chapters.

2.2 Powder X-ray Diffraction

Powder X-ray diffraction (XRD) was used to examine the structure of solids and obtain information on the unit cell such as the size and symmetry. It is also a useful method to check the phase purity of the samples made by comparison to the expected pattern of a reference material. This is possible due to the wavelength of X-rays being comparable to the interplanar spacings in crystals (~10^{-10} m or 1Å). The electron densities of the atoms in the solid scatter the X-rays and constructive and destructive interference results in a diffraction pattern. By examining the peak positions in a diffraction pattern, the size and shape of the unit cell can be determined. The relative intensities of the peaks provide information about the arrangement and types of atoms within the unit cell, while analysis of the peak widths can give the crystallite size of the material studied.

In a crystal, the atoms are ordered in such a way that a pattern is repeated periodically in three dimensions. A unit cell is the simplest building block of a crystal which is chosen to describe the arrangement of atoms. The unit cell has dimensions *a*, *b* and *c* (which run parallel to the *x*, *y* and *z* axes respectively) and angles α, β and γ. The dimensions and angles of a unit cell provide it with unique characteristics that enable classification into groups based upon symmetry. There are seven different types of possible unit cells, known as crystal systems. These are listed in Table 2.1.

All unit cells contain an array of points, called lattice points, which represent equivalent positions in the structure. This produces a limited number of arrangements and the possible lattice types in three dimensions (Fig. 2.2) are:

a) Primitive (P) – lattice points on the cell vertices only
b) Body-centred (I) – one additional lattice point at the centre of the cell
c) Face-centred (F) – one additional lattice point at the centre of each face of the cell
d) Base-centred (A, B or C) – one additional lattice point at the centre of one face

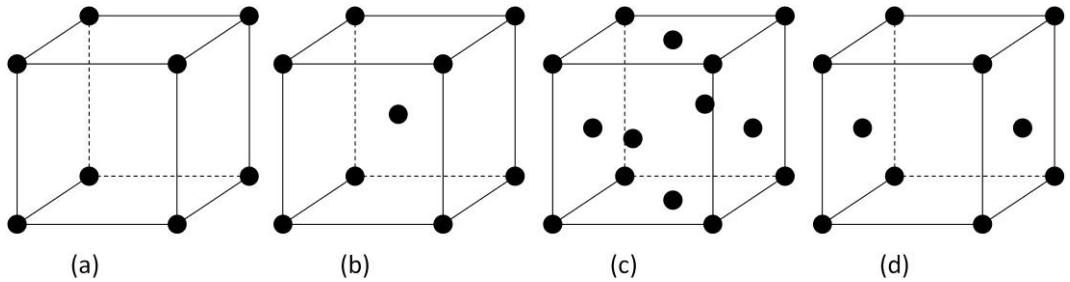

Fig. 2.2 Different lattice types for a cube, (a) primitive, (b) body centred, (c) face centred and (d) side centred

The combination of these lattice types with the seven crystal systems gives rise to the 14 Bravais lattices. There are only 14 Bravais lattices because certain combinations of lattice type and crystal system can be represented by a smaller unit cell. The unit cell contents can possess one of 32 point group symmetries that are consistent with the translational symmetry of the Bravais lattices. The combination of these point groups with the 14 Bravais lattices gives 230 possible space groups.

Table 2.1 The seven crystal systems, Bravais lattices and point groups assigned to the crystal systems

Crystal system	Lattice parameters	Cell volume	Bravais lattice	Point groups
Cubic	$a = b = c$ $\alpha = \beta = \gamma = 90^o$	$V = a^3$	P, I, F	$m\bar{3}m$, $\bar{4}3m$, 432, $m\bar{3}$, 23
Tetragonal	$a = b \neq c$ $\alpha = \beta = \gamma = 90^o$	$V = a^2c$	P, I	4/*mmm*, $\bar{4}2m$, 4*mm*,422, 4/*m*, -4, 4
Orthorhombic	$a \neq b \neq c$ $\alpha = \beta = \gamma = 90^o$	$V = abc$	P, C, I , F	*mmm*, *mm*2, 222
Monoclinic	$a \neq b \neq c$ $\alpha = \beta = 90^o$, $\gamma \neq 90^o$	$V = abcsin\beta$	P, C	2/*m*, *m*, 2
Triclinic	$a \neq b \neq c$ $\alpha \neq \beta \neq \gamma$	$V = abc\sqrt{1 - cos^2\alpha - cos^2\beta - cos^2\gamma + 2cos\alpha cos\beta cos\gamma}$	P	1, $\bar{1}$
Hexagonal	$a = b \neq c$ $\alpha = \beta = 90^o$, $\gamma = 120^o$	$V = \frac{\sqrt{3}a^2c}{2}$	P	6/*mmm*, $\bar{6}m2$, 6*mm*, 622, 6/*m*, $\bar{6}$, 6
Rhombohedral	$a = b = c$ $\alpha = \beta = \gamma \neq 90^o$	$V = a^3\sqrt{1 - 3cos^2\alpha + 2cos^3\alpha}$	R	$\bar{3}m$, 3m, 32, $\bar{3}$, 3

When X-rays hit a crystalline sample, they are scattered in various directions. The Bragg equation (Equation 2.1) describes the scattering as reflections from a set of lattice planes. Interference will occur when two reflected beams meet and it

occurs constructively if the path difference ($x + x$), which is given by $2d\sin\theta$, is a whole number of wavelength (Fig. 2.3):

$$n\lambda = 2d\ sin\theta \qquad (2.1)$$

where n is an integer, λ is the wavelength of X-rays, d is the spacing between the atomic planes and θ is the angle between the incident ray and the scattering planes.

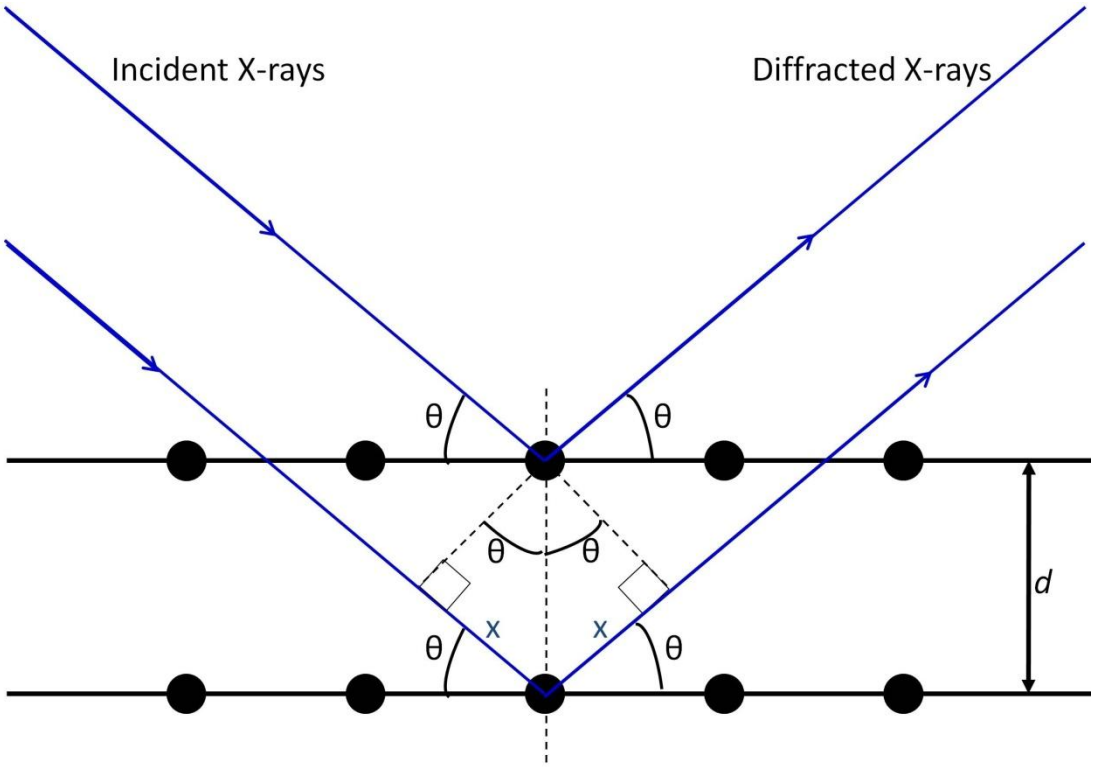

Fig. 2.3 Diffraction of parallel beams of X-rays by from lattice planes separated by a distance, *d*

In order to observe constructive interference from a specific set of planes, the planes must be correctly oriented relative to the incident X-ray beam. For a crystalline powder sample, a large number of crystallites are present in random orientations so it can be assumed that for any given lattice planes, there will be some

crystals oriented with appropriate Bragg angle for constructive interference to occur. Thus, all "Bragg peaks" are measured from the sample as a function of angle θ.

The lattice planes within a set are equally spaced and parallel to each other. This regular distance is called the *d*-spacing. These planes are described by a set of integers, (*hkl*), called Miller indices. The Miller indices refer to the reciprocal of the points at which the *a*, *b*, and *c* axes of the lattice planes are intersected by the plane, denoted *h*, *k* and *l* from a defined origin. If a plane is parallel to an axis, then the intercept is infinity which gives a Miller index of zero. This parent plane is one of a set of equidistant parallel planes that includes one running through the origin.

The 2θ peak positions in the X-ray diffraction pattern can be indexed in terms of Miller indices (*hkl*). The Miller indices relate the peak positions or *d*-spacings to the lattice parameters by an equation specific to the crystal system. Table 2.2 shows the relationship between the *d*-spacing and Miller indices for the different crystal systems.[1]

Table 2.2 Relationship between *d*-spacing and Miller indices for each crystal system

Crystal system	Relationship between *d*-spacing and Miller indices
Cubic	$\frac{1}{d^2} = \frac{h^2 + k^2 + l^2}{a^2}$
Tetragonal	$\frac{1}{d^2} = \frac{h^2 + k^2}{a^2} + \frac{l^2}{c^2}$
Orthorhombic	$\frac{1}{d^2} = \frac{h^2}{a^2} + \frac{k^2}{b^2} + \frac{l^2}{c^2}$
Hexagonal	$\frac{1}{d^2} = \frac{4}{3}\left(\frac{h^2 + hk + k^2}{a^2}\right) + \frac{l^2}{c^2}$
Monoclinic	$\frac{1}{d^2} = \frac{1}{sin^2\beta}\left(\frac{h^2}{a^2} + \frac{k^2 sin^2\beta}{b^2} + \frac{l^2}{c^2} - \frac{2hl\, cos\beta}{ac}\right)$
Rhombohedral	$\frac{1}{d^2} = \frac{(h^2 + k^2 + l^2)sin^2\alpha + 2(hk + kl + hl)(cos^2\alpha - cos\alpha)}{a^2\,(1 - 3cos^2\alpha + 2cos^3\alpha)}$
Triclinic	$\frac{1}{d^2} = \frac{1}{V^2}(S_{11}h^2 + S_{22}k^2 + S_{33}l^2 + 2S_{12}hk + 2S_{23}kl + 2S_{13}hl)$ where $S_{11} = b^2c^2sin^2\alpha$, $S_{22} = a^2c^2sin^2\beta$, $S_{33} = a^2b^2sin^2\gamma$ $S_{12} = abc^2(cos\alpha\, cos\beta - cos\gamma)$, $S_{23} = a^2bc(cos\beta\, cos\gamma - cos\alpha)$, $S_{13} = ab^2c(cos\gamma\, cos\alpha - cos\beta)$

Assigning Miller indices to each peak in a diffraction pattern is simple for cubic symmetry but for lower symmetry systems, the number of peaks increases and indexing becomes more difficult. In the case of a cubic system, the pattern can be indexed by rearranging Bragg's equation (Equation 2.1) and substituting into the first equation in Table 2.2. This gives:

$$sin^2\theta = A(h^2 + k^2 + l^2),\ where\ A = \left(\frac{\lambda}{2a}\right)^2 \qquad (2.2)$$

In the case of tetragonal crystals, by combining Bragg's equation (Equation 2.1) and the second equation in Table 2.2, an equation for indexing tetragonal crystals is obtained:

$$sin^2\theta = A(h^2 + k^2) + Cl^2,\ where\ A = \left(\frac{\lambda}{2a}\right)^2, C = \left(\frac{\lambda}{2c}\right)^2 \qquad (2.3)$$

Lower symmetry patterns are usually indexed using a computer software. When all the peaks in the powder diffraction pattern have been assigned with the correct Miller indices, the Bravais lattice type and cell parameters can then be determined. For primitive cubic lattices, all possible reflections will appear in the diffraction pattern. However, some reflections are not observed in body centred and face centred lattices. These are called systematic absences, which arise from destructive interference between similar lattice planes. The conditions for systematic absences in terms of Miller indices are listed in Table 2.3 below for some simple situations.[1]

Table 2.3 Conditions for systematic absence in different lattice types

Centering	Condition for systematic absences
Body-centred, I	$h + k + l$ = odd number
Face-centred, F	h, k, l not all even or not all odd numbers
A-centred, A	$k + l$ = odd number
B-centred, B	$h + l$ = odd number
C-centred, C	$h + k$ = odd number
Rhombohedral, R	$-h + k + l$ = not multiples of 3

The size of the crystals can affect the width of the peaks in a diffraction pattern if the crystals themselves or ordered domains within a large particle are small. Small crystals can therefore cause broadening and this allows powder XRD to be used for estimating crystallite sizes. The relationship between crystallite size and the peak width is determined by the Scherrer equation:

$$\beta = \frac{K\lambda}{Lcos\theta} \tag{2.4}$$

where β is the full width at half maximum (FWHM) of a peak in radians, K is a constant (0.9), θ is the peak position and L is the mean crystallite size. The peak width also depends on instrumental broadening. This effect can be corrected by subtracting the FWHM of a standard reference sample with negligible size broadening, β_I, from the measured sample, β_S.

$$\beta^2 = \beta_S^2 - \beta_I^2 \tag{2.5}$$

where β_S is FWHM for sample measured, β_I is FWHM due to instrumental resolution.

2.2.1 Instruments used

All XRD measurements in this work were performed on the samples in their powder state. There were three different diffractometers used in this work. Routine XRD measurements of the as-prepared materials were carried out on a Bruker D5000 powder X-ray diffractometer. It operated with non-monochromated Cu K_α radiation with wavelengths of λ_1 = 1.5405 Å and λ_2 = 1.5443 Å. The sample was placed into a shallow well in an Al sample holder and packed down with a glass slide to ensure an even surface. Typical scans were measured between a 2θ angle of 10^o and 50^o. The time per step was set at 1.7 seconds with step size of 0.02^o making the overall scan time about 1 hour.

Once the scans were completed, the XRD pattern was analysed using the program EVA. The program allows for the comparison of the measured pattern with a database of known structures. The reference database used was the 2008-release of the JCPDS Powder Diffraction File database.[2]

In situ heating XRD were carried out on a Bruker D8 Advance diffractometer. It also operated with non-monochromated Cu K_α radiation. The samples were packed into a Macor ceramic sample holder and inserted into the chamber of an Anton Paar XRK900 heating stage. Typical scans were measured between a 2θ angle of 10^o and 60^o. The time per step was set at 1.2 seconds with step size of 0.016^o, so each scan took 70 minutes. The scans were measured in air from a starting temperature of 30 ^{o}C, at 25 ^{o}C intervals up to a maximum of 900 ^{o}C.

High resolution powder XRD measurements were carried out on a Philips X'pert Pro powder diffractometer with a curved Johansson monochromator, giving

high-resolution diffraction using the Cu $K_{\alpha 1}$ single wavelength. Typical scans were measured between a 2θ angle of 10^{o} and 100^{o}. The time per step was set at 9.4 seconds, step size of 0.013^{o}, with total scan time about 18 hours.

2.3 Neutron Diffraction

An alternative to using X-rays as a source of scattering radiation is to use neutrons. Neutron and X-ray diffraction are complementary techniques in analysing the crystal structure of a material. The fundamental difference between the two is that neutrons are scattered by the atomic nuclei while X-rays are scattered by the electron clouds. Hence, neutron scattering factors vary comparatively little with atomic number, and irregularly with atomic number, unlike X-ray scattering factors, which increase with atomic number (as the electron density increases). So the neutron scattering by light elements, like Na and O, is similar to heavier elements, like Bi and La, whereas X-rays are scattered much more by the heavier elements. This scattering property of neutrons is very useful for structural determination for oxide materials like perovskites, where an accurate determination of the oxygen positions gives important information on the octahedral tilting. The oxygen positions can be difficult to obtain from X-ray diffraction if a much heavier element is present.

Another advantage of using neutrons for diffraction is that there is no angular dependence of the intensity of the diffracted beam, whereas the intensity of the peaks in X-ray diffraction decreases with increasing incident angle. Therefore, for a given λ and 2θ range more Bragg peaks can be measured accurately. However, one drawback is that some isotopes will absorb neutrons, making detection of these

isotopes more difficult and producing radioactive samples. In most cases the radioactive species produced are short-lived and requiring only a short amount of time before they return to normal levels. Another disadvantage of neutrons is that they are scattered more weakly than X-rays so in general larger sample quantities are needed.

2.3.1 Instruments used

Neutron diffraction was carried out at station D2B, which is a high-resolution two-axis diffractometer, at the Institut Laue-Langevin (ILL), in Grenoble, France. The research facility houses a high-flux nuclear reactor, which operates at a thermal power of 58.4 MW using a single fuel-element of ^{235}U. The fuel-element sits in the centre of a heavy water filled moderating tank of diameter 2.5 m.

Approximately 1 g of sample was placed into thin walled vanadium canisters. Vanadium was used due to its very low neutron scattering length. The canister position was adjusted so that the stainless steel top was clear of the beam and only the lower region lay in the beam path. A wavelength of 1.594 Å was selected with a Ge crystal monochromator. A complete scan at room temperature between $0 < 2\theta < 160^{o}$ typically takes 6 hours**.**

2.3.2 The Rietveld method

The Rietveld method, which was developed in the late 1960s, is widely used to refine crystal structures from X-ray or neutron diffraction patterns.[3-4] For most powder diffraction patterns, overlap occurs between Bragg reflections, especially for lower-symmetry materials due to the polycrystalline nature of a powder sample. The Rietveld method overcomes this difficulty due to peak overlaps by calculating the expected intensity for each individual step in the diffraction pattern. So instead of analysing each individual reflection, this method performs a curve fitting procedure by fitting the observed intensity, $Y_{i(obs)}$, of each equally spaced steps *i* over the entire pattern, with the calculated background intensity ($Y_{i(bkg)}$) and the sum of the contribution of reflections close to the *i* powder pattern step ($Y_{i(Bragg)}$):

$$Y_{i(obs)} = Y_{i(bkg)} + \sum Y_{i(Bragg)} \qquad (2.6)$$

The Rietveld method uses a least-squares technique to minimise the residual S_y between the observed intensity $Y_{i(obs)}$ and the calculated intensity $Y_{i(calc)}$ for all the steps *i.e.* until an optimum fit is obtained between the whole observed powder diffraction pattern and the entire calculated one:

$$S_y = \sum_i \frac{(Y_{i(obs)} - Y_{i(calc)})^2}{Y_{i(obs)}} = \sum_i w_i (Y_{i(obs)} - Y_{i(calc)})^2 \qquad (2.7)$$

where w_i is the statistical weight that equals $1/Y_{i(obs)}$, and $Y_{i(calc)}$ is the intensity of each step which can be calculated by a mathematical expression that includes the factors related to both the structure and the diffractometer used. So certain information is needed beforehand to calculate $Y_{i(calc)}$ such as the space group, unit cell lattice parameters, atomic positions and instrumental details. This is obtained by

building a model appropriate for the likely crystal chemistry of the material to be studied.

The indicators of the quality of the least-squares refinement between the calculated and observed patterns is estimated in the residual *R*-factors as defined by the following (Table 2.4):

Table 2.4 The numerical criteria of fit for the Rietveld method[5]

Parameter	Expression
R-pattern	$R_p = \frac{\sum \lvert Y_{i(obs)} - Y_{i(calc)} \rvert}{Y_{i(obs)}}$
R-weighted pattern	$R_{wp} = \sqrt{\frac{\sum w_i (Y_{i(obs)} - Y_{i(calc)})^2}{\sum w_i Y_{i(obs)}^2}}$
R-expected	$R_{exp} = \sqrt{\frac{\sum (M - P)}{\sum w_i Y_{i(obs)}^2}}$
R-Bragg	$R_B = \frac{\sum \lvert I_{k(obs)} - I_{k(calc)} \rvert}{\sum I_{k(obs)}}$
Goodness-of-fit	$GOF = \chi^2 = \frac{R_{wp}}{R_{exp}} = \sqrt{\frac{\sum w_i \left(Y_{i(obs)} - Y_{i(calc)}\right)^2}{(M - P)}}$

where M is the number of steps in the diffraction pattern, P is the number of refined parameters, and $I_{k(obs)}$ and $I_{k(calc)}$ are the observed and calculated intensities of the k^{th} Bragg reflection.

R-pattern and *R*-weighted pattern are measures of how well the calculated pattern fits the data, based on the residual at each step. *R*-expected is the value for the theoretically best fit that can be produced from the model and data, determined by the number of steps in the data and number of parameters refined. Goodness-of-fit is the ratio of the *R*-weighted pattern and *R*-expected and gives a measure of how well the data have been fitted. *R*-Bragg relates only to the goodness-of-fit of the

Bragg reflections in the structure being modelled, meaning any second phases present will be disregarded.

A good fit with the refined structure model will be shown by a low residual value. The *R*-weighted pattern, R_{wp} is the one most commonly considered as it constains S_y which is the quantity to be minimised by the least-square refinements. The goodness-of-fit, χ^2, which is directly proportional to S_y is also typically regarded and ideally is 1.

Refinements of the powder XRD and neutron diffraction data were performed using the TOPAS Academic software.[6] A text editor software, jEdit, was also used to create and modify the input files needed to start a refinement in TOPAS. Detector zero error and sample height corrections were allowed to refine, and the Lorentz-Polarisation factor and axial divergence corrections were applied but constrained to theoretical values. The peak shape function used in all refinements was the modified Thompson-Cox-Hastings pseudo-Voight (TCHZ). In some cases, instead of a full Rietveld refinement, a Pawley peak intensity fit was used to refine lattice parameters accurately.

2.4 Scanning Electron Microscopy & Energy Dispersive X-ray Analysis

Scanning Electron Microscopy (SEM) is a technique used to study the size and morphology of materials. In SEM analysis, a high energy beam of electrons is used to scan over the surface of a sample. The electron beam, which typically has an energy ranging from 0.2 to 40 keV, is focused by one or two condenser lenses to a spot about 0.4 to 5 nm in diameter. The beam then passes through pairs of scanning coils or pairs of deflector plates in the electron column, which deflect the beam in the *x* and *y* axes so that it scans in a raster fashion over a rectangular area of the sample surface. The electron from the beam interacts with the sample resulting in deflection of secondary electrons to a detector, which subsequently converts the signal to voltage, amplifies it and an image is then projected onto a screen.

SEM can produce very high-resolution images of a sample surface, revealing details that are ~1 nm in size. It also has a large depth of field giving a characteristic three-dimensional appearance which is useful in understanding the surface structure of a sample. This technique requires a high level of vacuum and preferably the studied sample must be conducting. Non-conducting samples tend to charge when scanned by the electron beam which reduces the quality of the images obtained. Hence, any non-conducting samples are first sputter coated with a thin layer of conducting material such as gold, platinum or graphite.

Energy dispersive X-ray analysis (EDXA) is a method used for the identification of elements within a sample in an SEM. In its ground state a sample contains unexcited electrons within their respective elemental electron shells. When

a high energy electron beam is targeted at the sample, these electrons may interact with electrons from an inner shell of the sample and excite them so that they are ejected from the electron shell. This results in electron holes being formed so electrons from an outer electron shell will then start to occupy these holes. In doing so, energy in the form of X-rays is emitted. The energy of the X-rays arises from the difference in energy between the shells and varies with atomic number. By collecting and measuring the energy of these X-rays, the elemental composition of the sample can be determined.

2.4.1 Instruments used

SEM images were obtained using a ZEISS SUPRA 55-VP scanning electron microscope with an EDAX Genesis system with a thin window detector and electron backscattering detection system (EBSD). Samples were sputter coated with Au using an electron beam evaporator.

EDXA analysis was performed on uncoated samples in the SEM by zooming in and measuring data on several regions of the sample. Genesis software was used to analyse the data, where peaks were identified and quantified. The EDXA results shown in this work correspond to the calculated atomic average percentage of the elements identified in the EDXA spectrum, by integration of peak areas and use of the internal calibration of the software.

2.5 Raman Spectroscopy

Raman spectroscopy is a technique used to observe vibrational, rotational and other low frequency modes in a system. It was used to investigate the short-range structural features in contrast to the average range structural features examined with X-ray and neutron diffraction techniques. Raman spectroscopy relies on inelastic scattering or Raman scattering of monochromatic light which results from the excitation of the vibrations in molecular or crystalline materials. The monochromatic light used is usually from a laser in the visible, near infrared or near ultraviolet region. The laser light interacts with molecular vibrations, phonons or other excitations in the system.

Typically, when a sample is illuminated with a laser beam, the light will be scattered in different directions. Most of scattered light maintains the same frequency as the incident light, ν_0, as a consequence of elastic scattering, also called Rayleigh scattering (Fig. 2.4). However, a very small portion of the incident light (1 in 10^6 photons) is scattered at frequencies different from the frequency of the incident light. This inelastic scattering is defined as Raman scattering. Inelastic collisions with photons of energy, ν_0, may cause molecules to undergo a transition to a higher virtual energy level which means the photon loses energy and it is emitted at a lower frequency (these shifts are referred as Stokes lines). However, if the molecule is already in a higher energy state, the interaction with the photon can provoke a transition to a lower level, therefore the photon will acquire the excess of energy and will be emitted at a higher frequency (anti-Stoke lines). The scattered light is then collected with a lens and sent through a monochromator. Scattered light that is close

to the frequency of the laser (Rayleigh scattering) is filtered out, while the rest of the collected light is dispersed onto a detector.

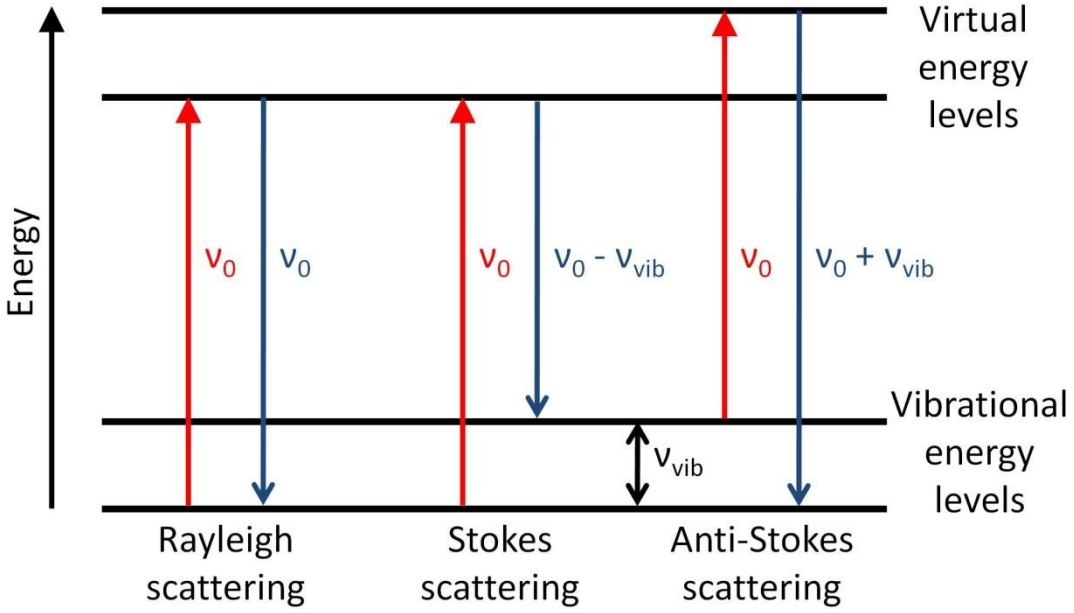

Fig. 2.4 Energy level diagram showing the states involved in Raman signal, with elastic scattering (Rayleigh) and inelastic scattering (Stokes and anti-Stokes)

Raman spectroscopy is a technique for material identification and can be successfully applied to solids, liquids and gases. For liquids and gases, it is correct to refer to vibrational energy levels of the individual molecules in gases while in solids, especially crystals, it is the crystal lattice, which undergoes vibration. These macroscopic vibrational modes are called phonons. It is possible to distinguish between different phases of the same material, as their crystal lattices present different vibrational modes.

2.5.1 Instruments used

Raman spectroscopy was performed at room temperature using a Renishaw InVia Raman microscope equipped with an 1800 line mm^{-1} grating and an argon ion laser operating at 514.5 nm. The Ar laser was first set at 10 mW but the intensity was varied depending on the sample analysed. The program used for recording the Raman spectra was WiRE 3.3. Before any measurements were done, the instrument was first calibrated with the silicon band set at 520.8 cm^{-1}. Measurements were then carried out on powder samples pressed on to a glass slide.

2.6 Fourier Transform Infra-red Spectroscopy

Infrared (IR) spectroscopy uses the infrared region of the electromagnetic spectrum to identify covalent bonding present within materials. IR radiation is passed through the sample and absorbed by covalently bonded molecules at their resonant frequency of vibration. A molecule has many vibrational modes that are only considered "IR active" if they result in an associated change in permanent dipole. In FTIR, the IR radiation is collected by an interferometer, which measures all IR frequencies. A mathematical process called Fourier transformation is then needed to convert the raw data into an actual spectrum, where the absorbance or transmittance is plotted against wavenumber.

2.6.1 Instruments used

In this work, IR has been used to detect water molecules and hydroxide ions in samples as these groups have a characteristic broad feature ~3600-3200 cm^{-1}. The infra-red spectroscopy of materials in this work was performed in the Department of Chemistry undergraduate teaching laboratories, University of Warwick, UK, using a Perkin Elmer Paragon 1000 FT-IR Spectrometer. The data were recorded and analysed using the OPUS software.

2.7 X-ray Absorption Near Edge Structure

X-ray absorption near edge structure (XANES) is a type of absorption spectroscopy that can be used to determine the oxidation state, coordination environment and subtle geometric distortions in materials.[7]

X-rays are absorbed by atoms by various processes. At certain energies, this can involve an electron being ejected from a quantum core level (such as the 1s or 2p level). In this absorption process, the energy of the incident X-ray must be greater than the binding energy of the core level. If this is not the case, the electron excitation will not absorb the X-ray. When the X-ray is absorbed, any excess energy is given to an electron that is ejected from the absorbing atom.

In X-ray absorption, the absorption coefficient μ, gives the probability of X-rays absorption and is calculated according to Beer's Law:

$$I_t = I_o e^{-\mu d} \qquad (2.8)$$

where I_o is the incident X-ray intensity, I_t is the intensity transmitted through the sample and d is the thickness of the material. As the energy increases, the linear absorption coefficient decreases up to when the absorption edge is reached. This means that when the energy of the incident X-ray reaches the binding energy of an inner shell, a sudden increase in absorption will be observed. This gives rise to a so-called absorption edge in the spectrum due to its vertical appearance. This jump is referred to as the absorption edge step, while the maximum intensity of the absorption edge is known as the "white line". The name of the absorption edges are given according to the principle quantum number, n, of the excited electrons (Table 2.5).

Table 2.5 Name of the absorption edges

K edge	1s			
L edge	2s	2p		
M edge	3s	3p	3d	
N edge	4s	4p	4d	4f

X-ray absorption spectroscopy is divided into 3 regions, the pre-edge region, the XANES region and the extended X-ray absorption fine structure region, EXAFS (Fig. 2.5). In this work, XANES is the region that is studied to obtain the oxidation state of the materials.

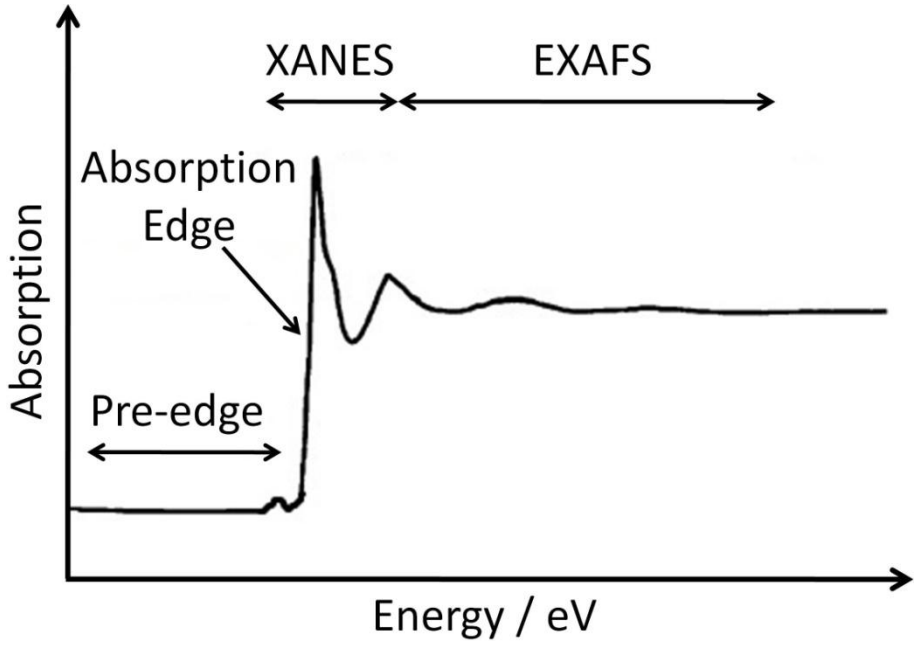

Fig. 2.5 Schematic illustration of an X-ray absorption edge

The pre-edge is particularly sensitive to local structure around the element and oxidation state. The edge energy position is a specific characteristic of the absorbing atom but is dependent on the oxidation state. As the oxidation state increases, the absorption edge position shifts to higher energies.

2.7.1 Instruments used

Ce L_{III}, Fe K and Mn K-edge X-ray absorption fine structure (XANES) experiments were performed using beamline B18 of the Diamond Light Source, UK.[8] This beamline provides X-ray energies in the range 2.05 - 35 keV using a fixed-exit, double-crystal Si (111) monochromator, which provides an energy resolution ($\Delta E/E$) of 2×10^{4}. The optics of the beamline includes a collimating mirror and a toroidal focussing mirror before and after the monochromator, respectively. The measurements were carried out using the Cr coating of these two optical

elements and a pair of harmonic rejection mirrors with a Ni stripe was also used. Under this configuration, the typical flux on the sample is of the order of 5×10^{11} photons and the size of the beam at that position is approximately 200 μm (vertical) by 150 μm (horizontal). The samples were ground finely with polyethylene powder (~ 80% by mass as diluent) under acetone to achieve uniform dispersion and pressed into 13 mm diameter pellets of ~1 mm thickness under a pressure of 5 tonnes. The reference materials for the Ce containing samples were CeO_2 (used as provided by Sigma Aldrich) and $CeAlO_3$ (prepared by solid-state reaction between Al_2O_3 and CeO_2 at 1450 °C under a flow of 5 % H_2 in N_2 for 10 hours) provided examples of cerium with well-defined oxidation states and coordination environments. The reference materials used for Fe containing samples were $FeCl_2$, Fe_2O_3 and Fe_3O_4, while the reference for Mn containing samples were $MnCl_2$, MnO_2, Mn_2O_3 and Mn_3O_4. XANES data were collected in transmission mode with ion chambers before and behind the sample filled with appropriate mixtures of inert gases to optimise sensitivity. The spectra were measured with a step size equivalent to less than 0.5 eV. Data were normalised using the program Athena with a linear pre-edge and polynomial post-edge background subtracted from the raw $\ln(I_t/I_o)$ data.

2.8 Brunauer-Emmett-Teller

Brunauer-Emmett-Teller (BET) is a standard tool for determining the surface area of a material. The BET theory describes the physical adsorption of gas molecules on a solid surface. The method is based on a model of multilayer adsorption that satisfies the following conditions: (1) Adsorption occurs on adsorbing sites and also above the adsorbed molecules, (2) The number of adsorbing sites per layer is constant, (3) The energy of the first layer adsorbing sites is uniform and (4) The molecules in all layers above the first behave as if in a bulk liquid. Given these conditions, the resulting BET equation is expressed as[9]:

$$\frac{P/P^o}{n(1-P/P^o)} = \frac{1}{n_m c} + \frac{c-1}{n_m c}\left(\frac{P}{P^o}\right) \qquad (2.9)$$

where P/P^o is the relative pressure, n is the amount adsorbed per unit mass of adsorbent, n_m is the BET monolayer capacity and c is usually related to the net heat of adsorption by $c = exp(q^{st} - q_L)/RT$, where q^{st} is the isosteric heat of adsorption in the monolayer and q_L is the heat of condensation.

Adsorption is reversible due to the weak bonds involved between gas molecules and the surface. Gas physisorption is considered to be non-selective, hence the surface is filled step by step depending on the available solid surface and the relative pressure. Filling the first layer enables the measurement of the surface area of the material, because the amount of gas adsorbed when the mono-layer is saturated is proportional to the entire surface area of the sample. The complete adsorption/desorption analysis is called an adsorption isotherm. The surface area of a solid is the total surface of the sample that is in contact with the external environment. It is expressed as $m^2\ g^{-1}$ of dry sample.

2.8.1 Instruments used

The specific surface area of the samples was determined from the adsorption/desorption isotherms of nitrogen using a Micromeritics ASAP 2020 analyser. Prior to analysis, the samples were degassed at 200 °C for 10 hours under vacuum to remove surface contamination and adsorbed species. Then known amounts of nitrogen gas are introduced at cryogenic temperatures up to saturation pressure. A vacuum is then applied and the gas removed, which may result in hysteretic behaviour. The relative pressure and quantity of gas adsorbed are measured to give an adsorption isotherm. The specific surface area of the samples was calculated by the BET method based on the N_2 adsorption isotherm data.

2.9 X-ray Photoelectron Spectroscopy

X-ray photoelectron spectroscopy (XPS) was used to study the electronic structure and the chemical composition at the surface of the sample. It is a technique that uses X-rays to eject electrons from inner-shell orbitals. The kinetic energy, E_K, of these photoelectrons is determined by the energy of the X-ray radiation, $h\nu$, and the electron binding energy, E_B, as shown below:

$$E_K = h\nu - E_B \tag{2.10}$$

where h is Planck's constant and ν is frequency. The photons from the X-ray will be absorbed by atoms on the sample causing the ionisation of electrons. By measuring the kinetic energy of the electrons and the known energy of the photons, the electron binding energy can be calculated. However, the electrons are released within the

solid instead of a vacuum, so the work function, φ, is introduced into the equation. The work function is defined as the minimum energy needed to remove the electron from the solid into a vacuum. The equation becomes:

$$E_K = h\nu - E_B - \varphi \qquad (2.11)$$

By using photons with much higher energy than the work function, the kinetic energy spectrum will give an energy distribution similar to that of occupied levels within the solid. Although the X-rays can penetrate into the solid, any photoelectrons excited in the solid can only travel a short distance before undergoing inelastic collisions with the lattice. Hence, this technique is highly surface specific. An approximation is usually applied to the photoelectron spectra called the Koopmans' Theorem, which states that the ionisation energy is equal to the negative of the orbital energy. It assumes that the emission of the photoelectron is faster relative to the relaxation of the other electrons in the atom. However, in reality, several relaxation processes occur at a time scale comparable to that of the photoemission. As the other electrons relax to lower energy states, they partially screen the newly created hole and make more energy available to the outgoing photoelectron.

Core level XPS spectra usually consist of sharp lines similar to a spectrum for a free atom. This is because the core orbitals tend to be highly contracted and hence do not interact much with their environment and are not involved in bonding. Since the core levels of atoms have specific binding energies for each element, it makes XPS an important technique for identifying the atoms present in the sample.

The atom-like nature of core levels means that atomic coupling schemes can be used on them. Core levels with angular momentum quantum number, $l > 0$, are

split by spin-orbit interaction. This is because the ionisation process leaves behind an unpaired electron, with $s = 1/2$, which couples with the orbital angular momentum, l, to give states $j = l \pm 1/2$. The relative intensities of the doublet peaks correspond to the ratio of their degeneracies:

$$Ratio\ of\ intensities = \frac{2j_+ + 1}{2j_- + 1} \qquad (2.12)$$

where $j_+ = l + s$ and $j_- = l - s$. Spin-orbital splitting is larger the more tightly bound the orbital and the deeper the level, the larger the lifetime broadening effect.

The binding energy of an electron also depends on other factors such as the formal oxidation state of the atom and the chemical environment. Any change to these factors causes the binding energy to change and this is called chemical shift.

2.9.1 Instruments used

XPS results reported in this thesis were obtained at two different facilities. The XPS results reported in Section 6.2 of Chapter 6 were obtained at Wolfson Science Laboratory in Cardiff University. The XPS spectra were collected using a Kratos Axis Ultra-DLD XPS with a monochromatic X-ray source. The samples were sent to Cardiff in powder form in glass vials. The samples were then pressed onto adhesive carbon tape and stuck onto the sample holders.

The XPS results reported in Section 6.4 of Chapter 6 were obtained at the National EPSRC XPS User's Service (NEXUS) at Newcastle University, an EPSRC Mid-Range Facility. The samples were stuck on to carbon tape and placed on Al foil. These were then placed inside plastic containers and sent to Newcastle University.

In both cases, a survey scan was first carried out for each sample and then a more detailed scan was performed on selected main peaks depending on the elemental composition of each sample. The carbon peak was also taken for all the samples as it was needed for calibration purposes. The XPS data were analysed using CasaXPS software. All the data were calibrated to the C 1s signal which was assigned a value of 284.8 eV. Curve fits were performed using a Shirley background and a Gaussian peak shape with 30% Lorentzian character.

2.10 Other techniques

2.10.1 Solid state NMR

Solid state NMR was used to probe the local structure of specific nuclei to determine the local structure of a material. It gives information on a number of nearest neighbours, level of disorder and may show the presence of defects in the local structure.

Solid state NMR was performed at the University of St. Andrews by Martin Peel and Professor Sharon Ashbrook. NMR spectra were acquired using a Bruker 600 Avance III spectrometer, equipped with a wide-bore 14.1 T magnet, giving Larmor frequencies of 158.7 MHz for ^{23}Na (I = 3/2) and 92.1 MHz for ^{2}H (I = 1). Powdered samples were packed into conventional 4-mm ZrO_2 rotors, and a magic-angle spinning (MAS) rate of 12.5 kHz was employed. ^{23}Na chemical shifts were referenced to 1 M NaCl(aq) using a secondary reference NaCl(s) (δ_{iso} = 7.8 ppm), and ^{2}H chemical shifts were referenced to deuterated tetramethylsilane, using the OD resonance of fully deuterated malonic acid (δ_{iso} = 13.0 ppm) as a secondary

reference. Conventional ^{23}Na and ^{2}H MAS NMR spectra were obtained using single-pulse experiments at 14.1 T, with typical pulse lengths of 1.5 and 4 μs, respectively. Recycle intervals of 5 and 3 s were used for ^{23}Na and ^{2}H, respectively, with a radiofrequency nutation rate of ~100 kHz and ~50 kHz, respectively.

2.10.2 Transmission Electron Microscopy

Transmission Electron Microscopy (TEM) is a microscopy technique whereby a beam of highly energetic electrons is transmitted through a thin sample, interacting with the specimen as it passes through, to examine samples at a very high magnification. TEM images were obtained by Dr Reza Kashtiban, Department of Physics, University of Warwick, on a JEOL 2100 LaB_6 instrument, operating at 200 kV. The sample was dispersed ultrasonically in ethanol and then deposited dropwise onto 3 mm lacey of carbon grids supplied by Agar.

2.10.3 Thermogravimetric analysis

Thermogravimetric analysis (TGA) is an analytical technique used to determine a material's thermal stability by monitoring the mass change that occurs when the sample is heated. This technique was used to determine the exact amount of water present in the starting materials and as-prepared materials.

TGA measurements were carried out by Luke Daniels, Department of Chemistry, University of Warwick, using a Mettler Toledo systems TGA/DSC 1-600

instrument**.** Typical measurements were performed in air with a heating rate of 10 ^{o}C/min from room temperature up to1000 ^{o}C,

2.10.4 Inductively coupled plasma optical emission spectroscopy

Inductively coupled plasma optical emission spectroscopy (ICP-OES) is an analytical technique used to determine the atomic composition of materials. It is a type of emission spectroscopy that uses inductively coupled plasma to produce excited atoms and ions that emit radiation at wavelengths characteristic of a particular element. Measurements were performed by MEDAC Ltd.

2.10.5 Photocatalysis and Photoluminescence

Photocatalysis measurements were performed by measuring the H_2 and O_2 evolved from the breakdown of methanol when visible light and UV light (420 nm filter used) was exposed to the sample. Photocatalytic measurements were also carried out on the decomposition of methylene blue. The measurements were made by David Martin and Dr. Junwang Tang at University College London.

2.10.6 Dielectric measurements

Samples that were investigated for their dielectric properties were first pressed into a pellet of diameter 13 mm using a load of 2 tonnes. Approximately 1 g of powder was used to make each pellet. The pellets were placed on Pt foil and

heated to 1100 ^{o}C, at a heating rate of 5 ^{o}C/min, for 2 hours. After being left to cool to room temperature, another heating run at 1150 ^{o}C for 4 hours was carried out. The mass, thickness and diameter of the pellets were then measured to determine their density. Silver paint was then applied on both faces of the pellet for dielectric and piezoelectric measurements.

Piezoelectricity

First, the pellets were poled by placing them in silicone oil and applying a fixed voltage for 1 minute. The longitudinal piezoelectric coefficient, d_{33}, was then measured at 5 different points on each sides of the pellet using a YE2730A d_{33} meter. An average and standard deviation of these values was then calculated.

Dielectric hysteresis

The hysteresis measurement was performed on pellets immersed in silicone oil using a triangular waveform at a frequency of 50 mHz. The peak voltage was increased until a current peak associated with the coercive field was observed. Data were collected using Labview software.

Dielectric permittivity

The dielectric permittivity and loss of the pellets were measured at frequencies of 1 kHz, 10 kHz, 100 kHz and 1 MHz using a HP 4192 A LF Impedance Analyser at a heating rate of 60 ^{o}C h^{-1}. The pellets were heated from 30 to 600 ^{o}C.

2.11 References

(1) Weller, M. T. *Inorganic Materials Chemistry*; Oxford University Press Inc.: New York, 2008.

(2) JCPDS; International Center for Diffraction Data: PA, U.S.A, 2008

(3) Rietveld, H. M. *Acta. Cryst.* **1967**, *22*, 151.

(4) Rietveld, H. M. *J. Appl. Cryst.* **1969**, *2*, 65.

(5) Topas Academic technical reference

(6) Coelho, A. A.; Evans, J. S. O.; Evans, I. R.; Kern, A.; Parsons, S. *Powder Diffr.* **2011**, *26*, S22.

(7) Fernandez-Garcia, M. *Cat. Rev. - Sci. Eng.* **2002**, *44*, 59.

(8) Dent, A. J.; Cibin, G.; Ramos, S.; Smith, A. D.; Scott, S. M.; Varandas, L.; Pearson, M. R.; Krumpa, N. A.; Jones, C. P.; Robbins, P. E. 14th International Conference on X-Ray Absorption Fine Structure (XAFS14), Camerino, ITALY, 2009.

(9) Sing, K. S. W.; Everett, D. H.; Haul, R. A. W.; Moscou, L.; Pierotti, R. A.; Rouquerol, J.; Siemieniewska, T. *Pure Appl. Chem.* **1985**, *57*, 603.

Chapter 3 – Hydrothermal Synthesis and Characterisation of A-site Substituted Titanate Perovskites

3.1 Background

Perovskites display a large array of possible distortions which lead to a wide range of interesting and useful properties. Although perovskites have an empirical formula ABX_3, any pair of ions can be included in the structure as long as they have the appropriate ionic radii at each site and the total positive charge is equal to the negative charge from the anions. The structure can also be made more complex when multiple ions substitute the A or/and B ions. This chapter will focus on A-site substituted perovskites

Most perovskites that have interesting properties are usually complex, with different combinations of metal ions present. For example, the most extensively used perovskite material in electronic devices is $PbZr_xTi_{1-x}O_3$ (PZT), as it has impressive piezoelectric properties. However, the success of PZT releases more lead, mainly in the form of lead oxide, into the environment. Lead oxide is toxic and is volatile at the high temperatures used during calcinations and sintering processes. This environmental concern over the toxicity of lead has increased the need to develop alternative lead-free materials with properties approaching that of PZT. Alternative materials such as $NaBiTi_2O_6$ and $KNbO_3$ have been developed. However, the piezoelectric properties of these materials are still inferior to PZT, hence, a number

of studies have aimed to improve their properties by making complex combinations such as (K,Na)$BiTi_2O_6$ and (K,Na)NbO_3-$LiTaO_3$-$LiSbO_3$.[1-6]

The hydrothermal synthesis of $NaBiTi_2O_6$ was reported by Lencka *et al*., where they developed a thermodynamic model of a heterogeneous aqueous electrolyte system enabling them to predict the required conditions for the hydrothermal synthesis of $NaBiTi_2O_6$.[7] They performed the synthesis by reacting $Bi(NO_3)_3{\cdot}5H_2O$ and TiO_2 in NaOH solutions at 200 ^oC. On the other hand, Jing *et al*. obtained $NaBiTi_2O_6$ from $Bi(NO_3)_3{\cdot}5H_2O$ and Ti tetrabutoxide in NaOH solutions at 160-220 ^oC.[8] They showed how the morphology was changed from spherical agglomerates to uniform cubic particles depending on the NaOH concentration. Setinc *et al.* prepared $NaBiTi_2O_6$ hydrothermally from $Bi(NO_3)_3{\cdot}5H_2O$ and TiO_2 and investigated the effect of temperature, reaction time and concentration of NaOH.[9] Liu *et al*. showed that $NaBiTi_2O_6$ nanowhiskers with diameters of 20 nm can be obtained by using a combination of sol-gel and hydrothermal techniques.[10] Wang *et al.* obtained $NaBiTi_2O_6$ microcubes, by increasing the NaOH concentration from 4 M to 10 M. Sardar and Walton studied the hydrothermal synthesis of a variety of bismuth titanate materials that crystallise from $NaBiO_3$ and TiO_2.[11] By altering the reagent ratios, pH and reaction time, different products were obtained and they successfully prepared $NaBiTi_2O_6$ in a one-step reaction when the Bi:Ti ratio was 1:2 and 10 M NaOH were used.

The structure of $NaBiTi_2O_6$ at room temperature has been widely reported as rhombohedral *R*3*c*.[12-13] However, recent studies on both single crystals and sintered ceramics have reported a monoclinic *Cc* symmetry instead.[14-15] $NaBiTi_2O_6$ also

undergo phase transitions upon heating to tetragonal symmetry (270-300 ^{o}C) and then cubic above 500 ^{o}C.[16-20]

$NaLaTi_2O_6$ is an analogue of $NaBiTi_2O_6$. It is usually prepared by the ceramic method from the reaction of Na_2CO_3, La_2O_3 and TiO_2 at 1200 ^{o}C.[21-22] Its hydrothermal synthesis has not been investigated as much as $NaBiTi_2O_6$. Shi *et al*. prepared $NaLaTi_2O_6$ hydrothermally using TiN and $La(NO_3)_3{\cdot}6H_2O$ in sodium hydroxide solution.[23] The structure of $NaLaTi_2O_6$ has not been generally agreed in the literature. It has been reported to be cubic $Pm\bar{3}m$[24], tetragonal $I4/mcm$[25], rhombohedral $R\bar{3}c$[22,26] and orthorhombic *Pnma*[21,27-28]. Garg *et al*. performed Rietveld refinement on both high resolution X-ray and neutron powder diffraction data of $NaLaTi_2O_6$.[26] They reported a significantly better goodness-of-fit for the rhombohedral structural model compared to the tetragonal and orthorhombic structure.

Another related perovskite is $NaCeTi_2O_6$. Wright *et al*. synthesised this material by hydrothermally using TiF_3 and $CeCl_3{\cdot}7H_2O$ in sodium hydroxide solutions.[29] They showed that substitution on the A-site (Ce^{3+} with Nd^{3+}) or B-site (Ti^{4+} with V^{4+}) was easily achieved under hydrothermal conditions. They reported the structure of $NaCeTi_2O_6$ to be orthorhombic, *Pnma*, the same as "synthetic loparite" which was made by ceramic method.[30] The "synthetic loparite" is $NaCeTi_2O_6$ made from Na_2CO_3, CeO_2 and TiO_2 in reducing conditions and at high temperatures. However, this method results in minor CeO_2 and rutile TiO_2 being present as impurities.

The aim of the work described in this chapter was to investigate a reproducible hydrothermal route to complex perovskite solid solutions and examine

the degree of element mixing using a variety of structural probes. The materials discussed in this chapter are a solid solution of $NaCe_{1-x}La_xTi_2O_6$ and A-site substituted $NaBiTi_2O_6$. The structure of these materials was determined from X-ray and neutron diffraction techniques with the aim of understanding the differences reported in the literature between different studies. XANES at the Ce L_{III}-edge was used to confirm the oxidation state of Ce while ^{23}Na NMR provided an insight on how the paramagnetic effect of Ce and the A-site disorder affects the Na environment. The level of defects present in the hydrothermally prepared samples was also investigated using IR and ^{2}H NMR. Attempts on controlling the particle size and morphology of these materials were also performed by varying the solvents used.

3.2 Hydrothermal Synthesis of $NaCe_{1-x}La_xTi_2O_6$

Hydrothermal syntheses of the samples were performed using ~20 mL Teflon-lined stainless steel autoclaves. Stoichiometric amounts of $CeCl_3 \cdot 7H_2O$ (Sigma Aldrich, 99.9%), $LaCl_3 \cdot 7H_2O$ (Alfa, 99%) and TiF_3 (Alfa, 98%) were weighed according to the values shown in Table 3.1. The exact amount of water in the salts was determined by thermogravimetric analysis to allow accurate measurement of Ce and La. The reagents were then mixed in 5 mL deionised water for 5 min in a Teflon liner. Then, 5 mL of NaOH solution (8 M) was added and stirred so that the final NaOH concentration was 4 M. The reaction mixture was then stirred for 1 hour before it was sealed in a steel autoclave and placed in an oven pre-heated at 240 ^{o}C. After heating for 24 hours, the autoclaves were left to cool to room temperature. The solid products were recovered by suction filtration, washed

thoroughly with warm water and dried overnight at 70 ^{o}C in a drying oven. The products were then ground into powder for further characterisation.

Deuterated samples of $NaCeTi_2O_6$ and $NaLaTi_2O_6$ were prepared using the same procedure as above but using D_2O and NaOD. The deuterated samples were prepared for solid-state NMR to investigate the level of defects in the samples, thus samples once crystallised were washed with copious amounts of deionised H_2O to ensure that any surface D_2O or $[OD]^-$ was removed and that any remaining deuterium was present only within the crystal structure.

Solvothermal reactions were also carried out, where ethylene glycol was used to replace water as the solvent. $CeCl_3{\cdot}7H_2O$ / $LaCl_3{\cdot}7H_2O$ and TiF_3 were mixed with stirring in 5 mL ethylene glycol for 15 min, then 1.6 g NaOH was added and the mixture stirred for 1 hour. The reaction vessel was then sealed and heated at 240 ^{o}C for 24 hours. Reactions with a 1:1 mixture of H_2O and ethylene glycol were prepared by mixing the reagents in 2 mL deionised water, then 3 mL NaOH (4 M) was added and the mixture stirred for 15 min. Then 5 mL ethylene glycol was added and stirred for 1 hour before being sealed and heated at 240 ^{o}C for 24 hours.

Table 3.1 Amounts measured for $NaCe_{1-x}La_xTi_2O_6$ synthesis

La conc., x	$CeCl_3{\cdot}7H_2O$/g	$LaCl_3{\cdot}7H_2O$/g	TiF_3/g	NaOH (aq)/mL	H_2O/mL
0	0.3726	-	0.2622	5	5
0.1	0.3353	0.0371			
0.2	0.2981	0.0743			
0.3	0.2608	0.1114			
0.4	0.2235	0.1485			
0.5	0.1863	0.1857			
0.6	0.1490	0.2228			
0.7	0.1118	0.2599			
0.8	0.0745	0.2971			
0.9	0.0373	0.3342			
1	-	0.3714			

3.3 Characterisation of $NaCe_{1-x}La_xTi_2O_6$

3.3.1 Powder XRD

The reaction gave a brown product for $NaCeTi_2O_6$ and the colour of the solids becomes paler with increasing La concentration until $NaLaTi_2O_6$, which is white. Powder XRD studies were carried out to confirm that the hydrothermal synthesis of the complete series of $NaCe_{1-x}La_xTi_2O_6$, for the range $0 \leq x \leq 1$ was successful. $NaCeTi_2O_6$ has been reported to have an orthorhombic *Pnma* structure[29-30] while several different structures have been reported for $NaLaTi_2O_6$ at room temperature including cubic ($Pm\bar{3}m$)[24], rhombohedral ($R\bar{3}c$)[22,26], tetragonal ($I4/mcm$)[25] and orthorhombic (*Pnma*)[21,27-28] unit cells. Ranjan *et al.* attributed the contradicting reports for $NaLaTi_2O_6$ in the literature to the fact that the distortion of the perovskite structure is weak and that other authors had used only X-ray diffraction data for structure analysis.[22] They collected powder neutron diffraction data and by using Rietveld refinement showed that $NaLaTi_2O_6$ prepared by solid-state synthesis has a structure best described with the rhombohedral, $R\bar{3}c$ space group.

The powder XRD data collected for the $NaCe_{1-x}La_xTi_2O_6$ series (Fig. 3.1) agree with the structure reported for $NaLaTi_2O_6$ with $R\bar{3}c$ space group. However, the weak peaks caused by slight distortions in the perovskite structure could not be clearly resolved by XRD. Although the end member $NaCeTi_2O_6$ has been reported in the literature with the space group *Pnma,*[29-30] there were fewer peaks observed in the XRD pattern than were expected for this model. The XRD data also showed that the products obtained were pure as no impurity peaks were observed. The crystallite

sizes of the materials, obtained by Scherrer analysis, were estimated to be between 40-50 nm (Table 3.2).

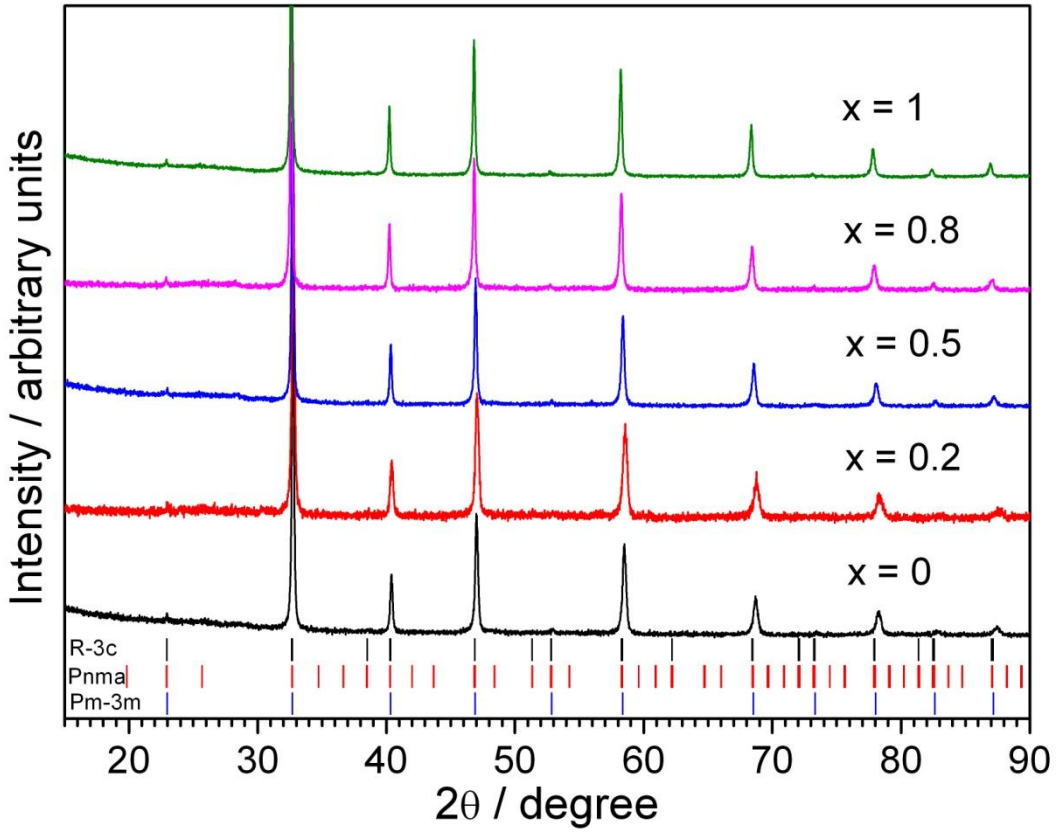

Fig. 3.1 Powder XRD of $NaCe_{1-x}La_xTi_2O_6$ samples, where the tick marks show the peak positions for perovskites with rhombohedral *R*$\bar{3}$*c*, orthorhombic, *Pnma* and cubic *Pm*$\bar{3}$*m* unit cells

Table 3.2 Crystallite size of $NaCe_{1-x}La_xTi_2O_6$ obtained from Scherrer analysis of XRD

La conc., x	0	0.2	0.5	0.8	1
Crystallite size / nm	51.7	40.8	50.0	45.2	43.3

3.3.2 Neutron diffraction

The weak peaks expected for rhombohedral $R\bar{3}c$ were observed in the neutron diffraction data, which are more sensitive to oxygen positions than X-rays in these metal oxides. Owing to the limited time available to collect the neutron diffraction data, only the diffraction pattern of the two end members and x = 0.5 sample ($NaCeTi_2O_6$, $NaCe_{0.5}La_{0.5}Ti_2O_6$, $NaLaTi_2O_6$) were measured. Rietveld refinement of the neutron diffraction data, shown in Fig. 3.2, allows a space group to be assigned, which is $R\bar{3}c$, for all three samples. The refined structural parameters and refinement summary are given in Table 3.3.

Other structural models reported in the literature were also considered specifically cubic $Pm\bar{3}m$, orthorhombic *Pnma* and tetragonal *I*4/*mcm* (Fig. 3.3 and Fig. 3.4). Two peaks at 40^o and 75^o was not expected in the cubic model thus the cubic $Pm\bar{3}m$ was ruled out. Like the XRD data, fewer peaks were observed in the neutron diffraction pattern than was expected for the orthorhombic model. The tetragonal model (*I*4/*mcm*) was also tested for $NaLaTi_2O_6$ but it gave a slightly poor fit (R_{wp} = 4.044) than the $R\bar{3}c$ model (R_{wp} = 3.207). Ranjan *et al.* also obtained a better fit using the rhombohedral $R\bar{3}c$ model than the tetragonal *I*4/*mcm*.[22] A similar result was obtained for $NaCeTi_2O_6$ where the fit was better for $R\bar{3}c$ (R_{wp} = 4.046) than *I*4/*mcm* (R_{wp} = 4.588).

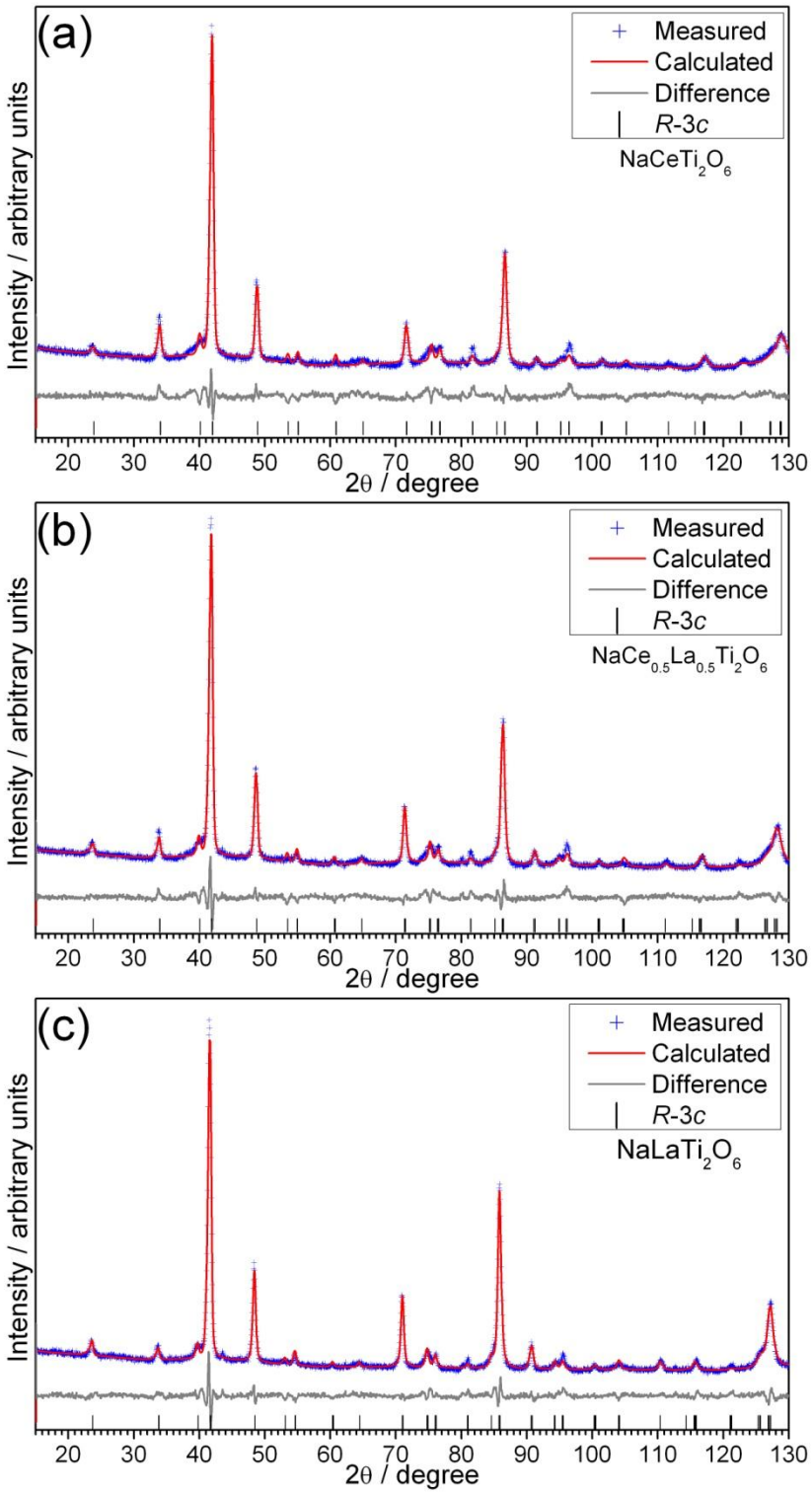

Fig. 3.2 Rietveld refinement of neutron diffraction of $NaCe_{1-x}La_xTi_2O_6$, a) x = 0, b) x = 0.5 and c) x = 1, with the points showing the measured neutron diffraction pattern, red line the calculated, grey the difference and the tick marks the peak positions for $R\bar{3}c$ space group

Table 3.3 Refined structural parameters and *R*-factors of $NaCe_{1-x}La_xTi_2O_6$ for x = 0, 0.5 and 1 from neutron diffraction data

Sample	**x = 0**	**x = 0.5**	**x = 1**
Space group	$R\bar{3}c$	$R\bar{3}c$	$R\bar{3}c$
***a* = *b* (Å)**	5.4427(15)	5.4565(9)	5.4853(8)
***c* (Å)**	13.3356(65)	13.3857(38)	13.4378(34)
Cell volume (Å^3)	342.111(257)	345.138(152)	350.147(136)
Na/Ce/La (*x*, *y*, *z*)	(0,0,0.25)	(0,0,0.25)	(0,0,0.25)
Ti (*x*, *y*, *z*)	(0,0,0)	(0,0,0)	(0,0,0)
O (*x*, *y*, *z*)	(0.5360(5),0,0.25)	(0.5332(5),0,0.25)	(0.5291(3),0,0.25)
Occupancy			
Na	0.5	0.5	0.5
Ce	0.5	0.25	-
La	-	0.25	0.5
Ti	1	1	1
O	1	1	1
R_{wp}	4.046	3.168	3.207
R_p	3.009	2.435	2.482
Gof	0.606	0.500	0.497
Temperature factors			
Na	1.4071(882)	1.1045(658)	1.1107(491)
Ce	1.4071(882)	1.1045(658)	-
La	-	1.1045(658)	1.1107(491)
Ti	0.0465(727)	0.2900(675)	0.4655(532)
O	2.8056(529)	2.3623(416)	1.3654(262)

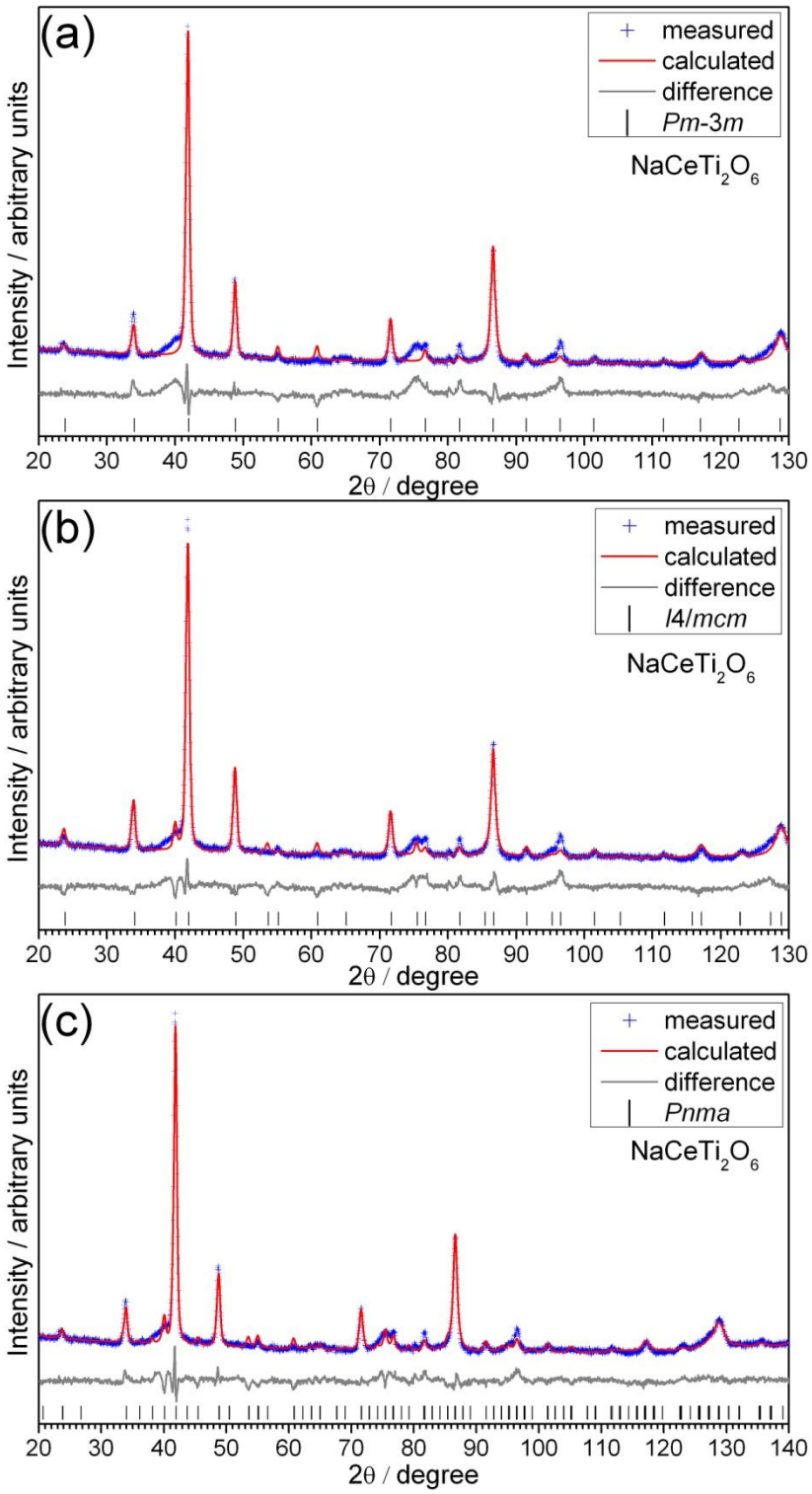

Fig. 3.3 Rietveld refinement of neutron diffraction of $NaCeTi_2O_6$ with the points showing the measured neutron diffraction pattern, red line the calculated, grey the difference and the tick marks the peak positions for a) cubic *Pm*$\bar{3}$m, b) tetragonal *I*4/*mcm* and c) orthorhombic *Pnma* space group

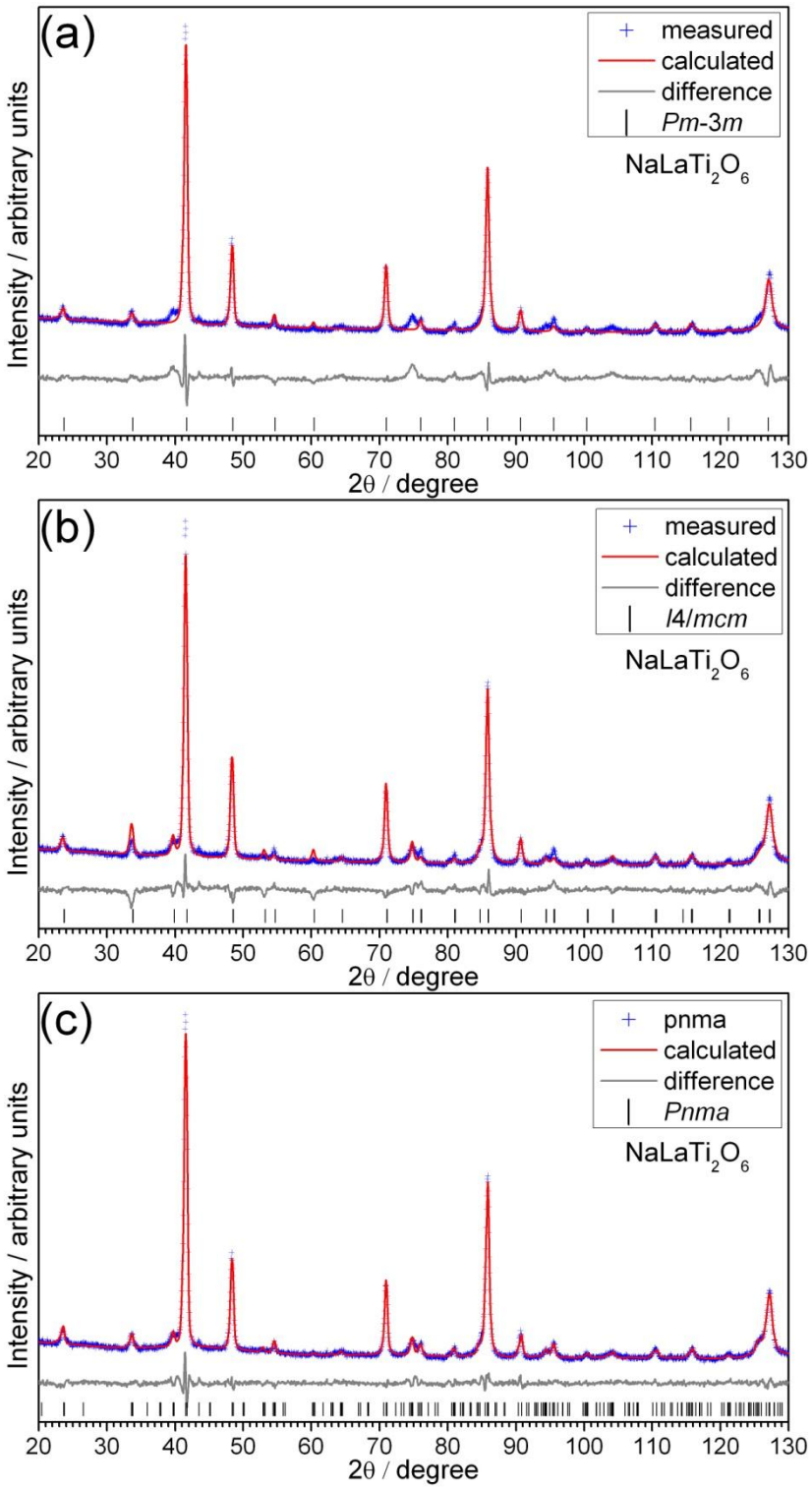

Fig. 3.4 Rietveld refinement of neutron diffraction of $NaLaTi_2O_6$ with the points showing the measured neutron diffraction pattern, red line the calculated, grey the difference and the tick marks the peak positions for a) cubic *Pm*$\bar{3}$m, b) tetragonal *I*4/*mcm* and c) orthorhombic *Pnma* space group

The cell parameters were obtained from Rietveld refinement of XRD data and a combined Rietveld refinement of the neutron and XRD powder data, where applicable (Table 3.4and Table 3.5). The formation of a solid solution was confirmed by changes in the cell parameters, shown in Fig. 3.5. Both the *a* and *c* lattice parameter increased as the La concentration is increased. This is due to La^{3+} ions (1.36 Å, 12 coordination) having a larger ionic radius than Ce^{3+} (1.34 Å, 12 coordination).[31]

Table 3.4 Refined structural parameters and *R*-factors of $NaCe_{1-x}La_xTi_2O_6$ for x = 0, 0.5 and 1 from combined refinement of neutron diffraction and XRD data

Sample	**x = 0**	**x = 0.5**	**x = 1**
Space group	$R\bar{3}c$	$R\bar{3}c$	$R\bar{3}c$
***a* = *b* (Å)**	5.4476(13)	5.4579(4)	5.4864(13)
***c* (Å)**	13.3339(66)	13.3907(17)	13.4392(64)
Cell volume (Å^3)	342.690(240)	345.461(62)	350.328(235)
Na/Ce/La (*x*, *y*, *z*)	(0, 0, 0.25)	(0, 0, 0.25)	(0, 0, 0.25)
Ti (*x*, *y*, *z*)	(0, 0, 0)	(0, 0, 0)	(0, 0, 0)
O (*x*, *y*, *z*)	(0.5358(9), 0, 0.25)	(0.5156(34), 0, 0.25)	(0.5224(14), 0, 0.25)
Occupancy			
Na	0.5	0.5	0.5
Ce	0.5	0.25	-
La	-	0.25	0.5
Ti	1	1	1
O	1	1	1
R_{wp}	7.839	8.285	5.538
R_p	5.870	5.964	4.338
Gof	1.173	1.171	1.131
Temperature factors			
Na	1.6909(630)	1.2941(503)	0.8246(239)
Ce	1.6909(630)	1.2941(503)	-
La	-	1.2941(503)	0.8246(239)
Ti	0.2524(345)	0.2565(612)	0.2169(308)
O	2.8217(1026)	2.1876(797)	1.3758(602)

Table 3.5 Refined structural parameters and *R*-factors of $NaCe_{1-x}La_xTi_2O_6$ for x = 0.2 and 0.8 from refinement of XRD data

Sample	**x = 0.2**	**x = 0.8**
Space group	$R\bar{3}c$	$R\bar{3}c$
***a* = *b* (Å)**	5.4539(11)	5.4766(6)
***c* (Å)**	13.3786(53)	13.4252(28)
Cell volume (Å^3)	344.633(193)	348.712(103)
Na/Ce/La (*x*, *y*, *z*)	(0, 0, 0.25)	(0, 0, 0.25)
Ti (*x*, *y*, *z*)	(0, 0, 0)	(0, 0, 0)
O (*x*, *y*, *z*)	(0.5100(108), 0, 0.25)	(0.5167(33), 0, 0.25)
Occupancy		
Na	0.5	0.5
Ce	0.4	0.1
La	0.1	0.4
Ti	1	1
O	1	1
R_{wp}	14.177	9.655
R_p	11.114	7.634
Gof	1.101	1.177
Temperature factors		
Na	1.1505(837)	1.0067(494)
Ce	1.1505(837)	1.0067(494)
La	1.1505(837)	1.0067(494)
Ti	0.4082(1058)	0.3821(651)
O	2.9659(2588)	1.6456(1428)

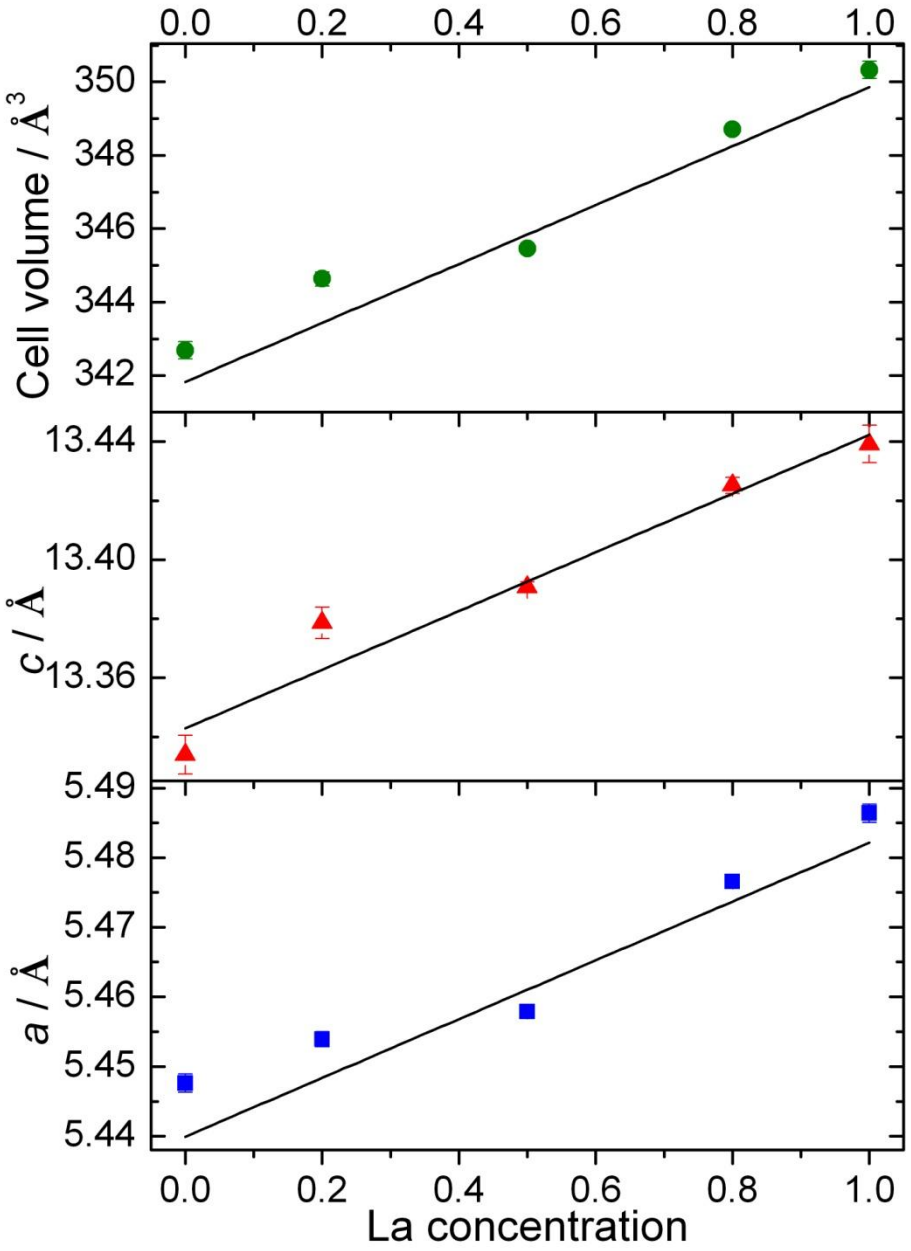

Fig. 3.5 Plot of the lattice parameters and cell volume of $NaCe_{1-x}La_xTi_2O_6$ series calculated by combined analysis of the neutron and XRD powder data

The A–O and Ti–O bond lengths were also calculated from the combined Rietveld refinements (Table 3.6). The Ti–O bond lengths are slightly lower than values reported for other titanate pervovskites such as $SrTiO_3$ (1.951 Å)[32], tetragonal $BaTiO_3$ (2.009 Å)[33] and orthorhombic $CaTiO_3$ (1.949 Å).[34] The tolerance factors calculated for x = 0, 0.5 and 1 all gave values very close to 1 which suggests that

these materials only exhibit very slight distortion in the perovskite structures, thus this is consistent with the rhombohedral unit cell.

Table 3.6 Bond length (in Å) and tolerance factor of $NaCe_{1-x}La_xTi_2O_6$ obtained from combined Rietveld refinement of neutron diffraction and XRD data

Sample	x = 0	x = 0.5	x = 1
A–O × 3 A–O × 6 A–O × 3	2.5289 (48) 2.7294 (4) 2.9188 (48)	2.645 (19) 2.7332 (92) 2.813 (19)	2.5828 (36) 2.7479 (3) 2.9036 (36)
Ti–O × 6	1.9354 (60)	1.9325 (13)	1.9464 (38)
Tolerance factor	0.996	0.999	0.997

3.3.3 Raman spectroscopy

Raman spectroscopy was also used to determine any phase transition with increasing La concentration. In the literature, there are no reports found on the Raman spectrum of $NaCeTi_2O_6$ but there have been several reports for $NaLaTi_2O_6$.[23,35-36] The Raman spectra for the $NaCe_{1-x}La_xTi_2O_6$ series, shown in Fig. 3.6, confirm that the structures of the samples all have distortions from the ideal cubic perovskite as no first order Raman bands are expected for cubic symmetry. The spectra show broad bands consistent with other reports for $NaLaTi_2O_6$ and of related perovskites like $NaBi_2TiO_6$ (*R*3*c*).[25,35,37] This broadening may be due to the disorder on the A-site and the overlapping of multiple Raman modes. The main bands for all the samples are at close to 150, 260, 450, 550 and 830 cm^{-1}. The band at 150 cm^{-1}, assigned to A_1 symmetry, has been attributed to Na-O vibrations.[38-39]. The band at around 260 cm^{-1} is also assigned to A_1 symmetry[38-39] This band is observed in the Raman spectra of $BaTiO_3$ and $PbTiO_3$ at almost the same position, indicating that this band is dominated by Ti-O vibrations.[38] The band at around 450 cm^{-1}, which is most prominent in $NaLaTi_2O_6$, increases in intensity when $NaLaTi_2O_6$ is annealed

at 900 ^{o}C/4 hours (Fig. 3.7). This band has been correlated to the particle size of $NaLaTi_2O_6$; Zhang *et al.* observed an increase in intensity of this band with increasing particle size of $NaLaTi_2O_6$ from 14 to 50 nm.[36] However, the intensity of this band is not as high in $NaCeTi_2O_6$ despite the crystallite size of $NaCeTi_2O_6$, obtained from Scherrer analysis of the XRD, being slightly bigger than $NaLaTi_2O_6$.

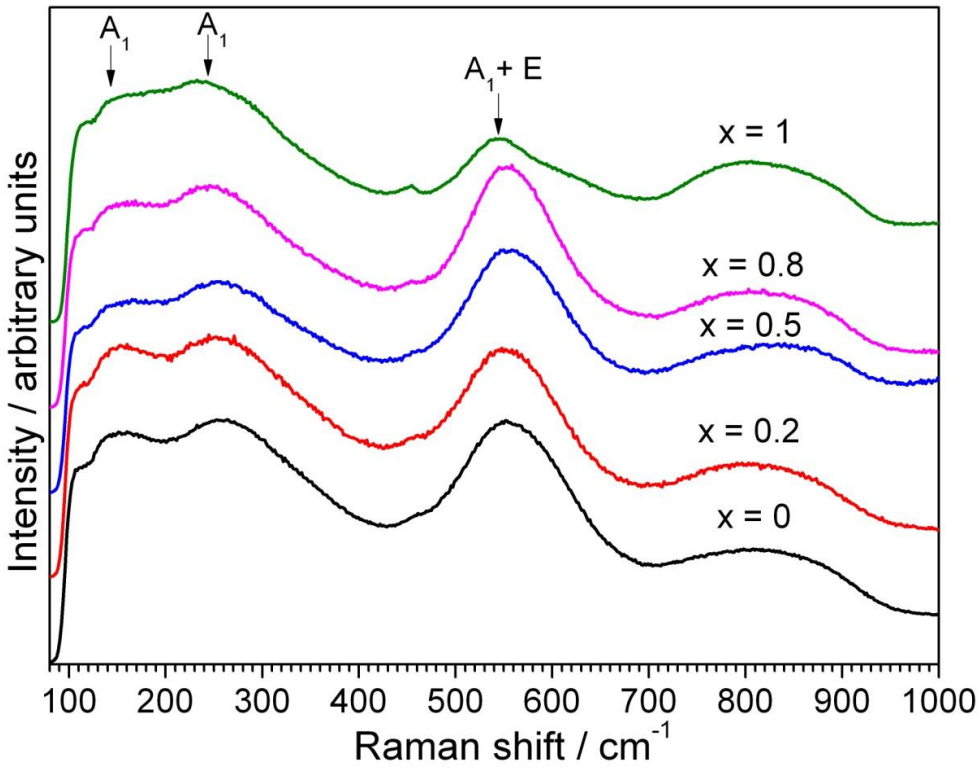

Fig. 3.6 Raman spectra of $NaCe_{1-x}La_xTi_2O_6$ series

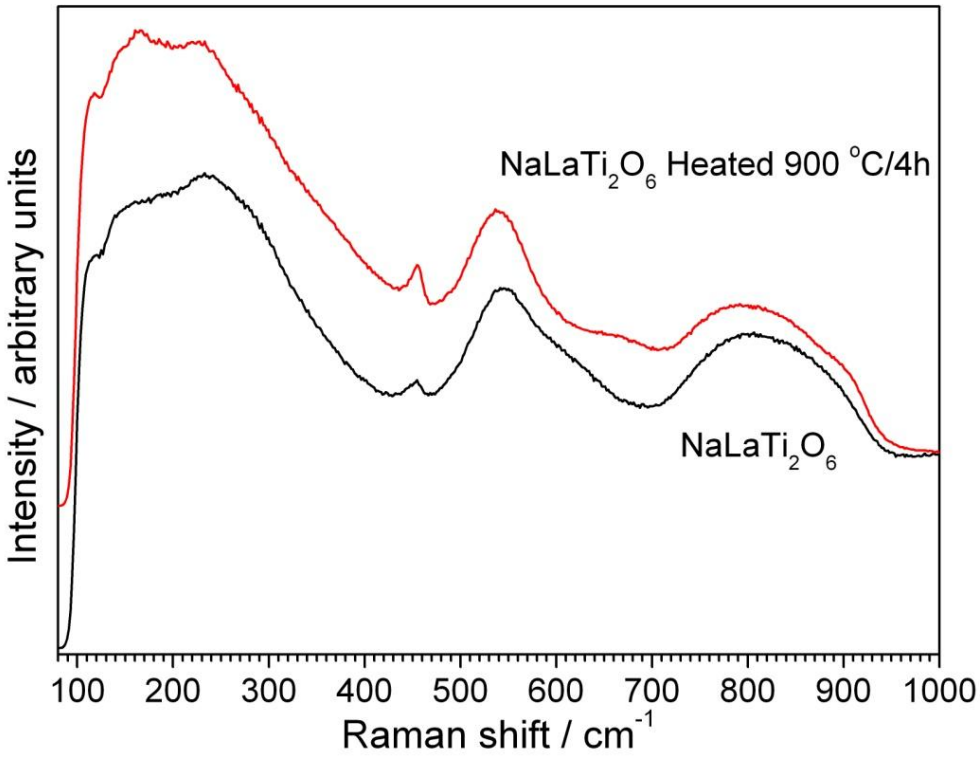

Fig. 3.7 Raman spectra of as-prepared and calcined $NaLaTi_2O_6$

High frequency Raman bands in oxides are usually dominated by vibrations involving oxygen displacements so the band at around 550 cm^{-1} has been reported to be due to Ti-O_6 octahedral vibrations and assigned to a mixture of A_1 and E modes.[25,38-39] For $NaBiTi_2O_6$, with space group *R*3*c*, there are 13 Raman active modes and they are all observed below 700 cm^{-1}, while the high temperature $LaGaO_3$, which has the same space group ($R\bar{3}c$) as $NaLaTi_2O_6$, is expected to have 5 Raman active modes (52, 160, 252 and 444 cm^{-1}) that are also observed below 700cm^{-1}. [40-41] Most published Raman studies for $NaLaTi_2O_6$ and $NaBiTi_2O_6$ only provide Raman data below 700 cm^{-1} so the last broad band at around 830 cm^{-1} is not usually reported. Selvamani *et al.* have reported an increase in the intensity of this band at 830 cm^{-1} as more $BiCrO_3$ is doped into $NaBiTi_2O_6$ and have attributed this band to the presence of oxygen vacancies.[42] In the case of tetragonal $BaTiO_3$,

Raman bands above 700 cm^{-1} have been reported where the band at 720 cm^{-1} is assigned to a mixture of E and A_1 mode while the band at 810 cm^{-1} may arise from the deformation of lattice OH groups as it was not present after annealing at 700 ^oC.[43-44] However, $NaLaTi_2O_6$ still exhibits the broad band at around 830 cm^{-1} even after annealing.

3.3.4 XANES – Oxidation state of Ce

The Ce L_{III}-edge XANES spectra of $NaCeTi_2O_6$ prepared using different reaction times or concentrations of NaOH are shown in Fig. 3.8, along with those for $CeAlO_3$ and CeO_2, where the Ce is known to have oxidation state of +3 and +4, respectively. For the $CeAlO_3$, a single white line is seen that corresponds to the electronic transition $2p_{3/2} \rightarrow (4f^1)5d$, whereas the spectrum of CeO_2 shows a typical double feature comprising of $2p_{3/2} \rightarrow (4f\underline{L})5d$ and $2p_{3/2} \rightarrow (4f^0)5d$ transitions, with an absorption edge shift of ~ 5 eV to higher energy.[45-47] The material $CeAlO_3$ is a tetragonal (*I*4/*mcm*) perovskite[48] which contains Ce (III) in a similar environment to that expected in $NaCeTi_2O_6$. The XANES spectra of various $NaCeTi_2O_6$ samples (prepared with different reaction times) and x = 0.5 sample, all showed distinct differences from the $CeAlO_3$ reference, with some evidence for the presence of Ce^{4+} in addition to the predominant Ce^{3+}: this is clear by the observation of a weak higher energy $2p_{3/2} \rightarrow (4f^0)5d$ feature and a shift of the absorption edge to higher energy. The sample of $NaCeTi_2O_6$ prepared at the shortest reaction time (5 hours) with 4M NaOH appears to show less evidence for presence of Ce^{4+}. The previously published XANES spectrum of hydrothermal $NaCeTi_2O_6$ was compared only with cerium (III) chloride[29] but the current comparison with $CeAlO_3$ provides clear evidence for the

partial oxidation of Ce^{3+} in apparently stoichiometric $NaCeTi_2O_6$. Since the intensity of the white line depends on the coordination number and local geometry about Ce, the position of the absorption edge (simply defined as the energy of 50 % of the edge step) provides the most convenient means of quantifying the oxidation state of Ce. Assuming a linear correlation between edge position and oxidation state[29], as shown in Fig. 3.9, the Ce in $NaCeTi_2O_6$ was estimated to have a mean oxidation state of +3.2 in the material prepared in 4 M NaOH for short reaction time (*i.e.*, 20 % of the cerium is present as Ce^{4+}) to 3.4 in the material prepared in 12 M NaOH. Since the high-resolution powder diffraction experiments showed no evidence for crystalline CeO_2 impurities in the samples, three possible explanations for the presence of Ce^{4+} may be put forward: (1) amorphous CeO_2 is present, (2) the surface of the fine powders contains oxidised cerium or (3) cerium is oxidised within the perovskite structure to accommodate structural defects.

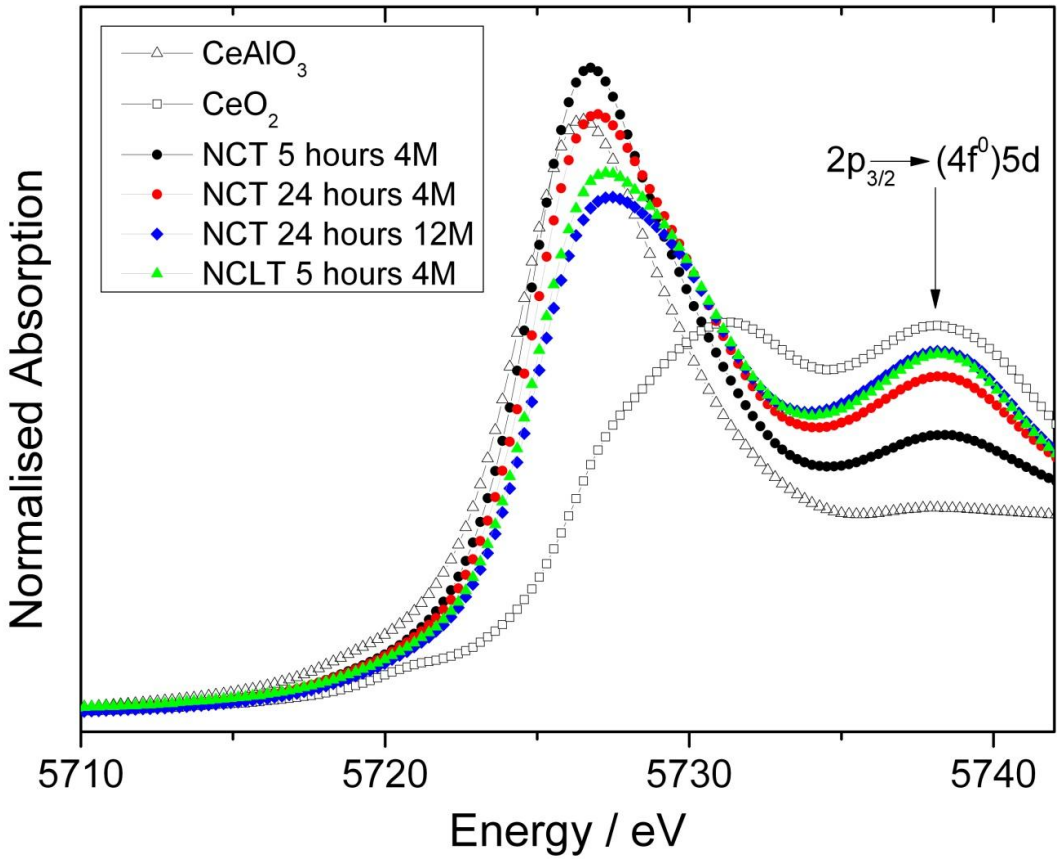

Fig. 3.8 Ce L_{III}-edge XANES spectra of $NaCeTi_2O_6$ and Ce reference materials with known oxidation state. NCT = $NaCeTi_2O_6$ and NCLT = $NaCe_{0.5}La_{0.5}Ti_2O_6$

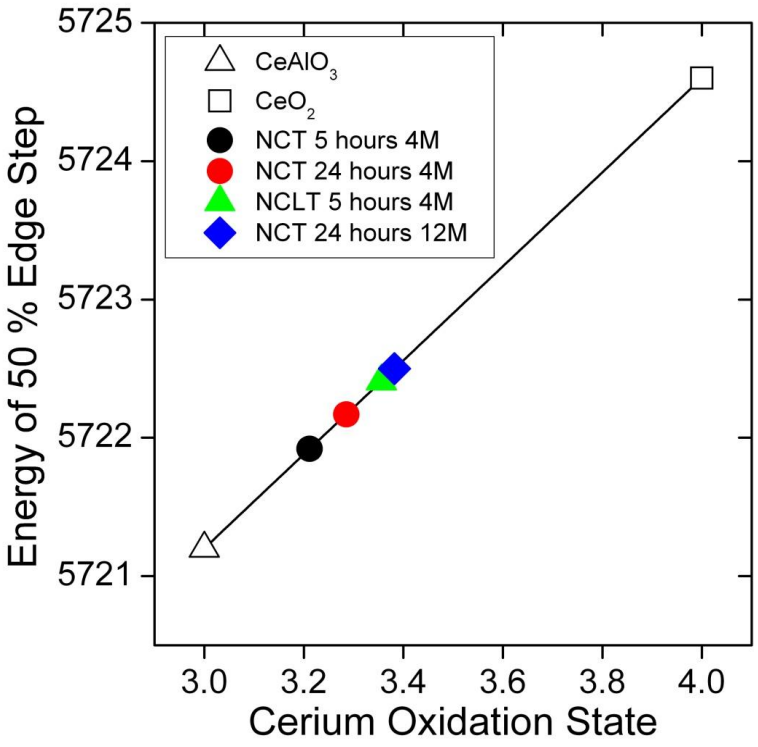

Fig. 3.9 The correlation between oxidation state and edge position, with deduced average oxidation states of the NCT and NCLT materials

3.3.5 Solid state ^{23}Na NMR

The samples were studied by ^{23}Na NMR (I = 3/2) to examine the level of A-site ordering. The chemical shift of ^{23}Na in a site with high coordination number should be close to 0 ppm,[49-51] which is the case for all the samples studied. The chemical shift and linewidth varies across the series (Fig. 3.10). When the chemical shift and linewidth is plotted against the La concentration, the trend in both cases is identical. There are two effects to consider in this case. One is due to the paramagnetic nature of the Ce^{3+} (resulting in paramagnetic contributions to both linewidth and shift) and the other is the disorder due to the three different metals occupying the A-site (again with potential contributions to linewidth – through a distribution of local environments – and to the shift as neighbouring cations vary). It is therefore expected that $NaLaTi_2O_6$ should have the narrowest linewidth since there is no Ce present, hence there is no paramagnetic ion present and there is less local disorder, with only two A-site metals present. As the La concentration is lowered with Ce added to the material, the potential for disorder increases with three A-site metal cations present, and a broadening of the resonance is expected. If the A-site disorder is the only effect on the linewidth, then the x = 0.5 sample should have the broadest peak (i.e. maximum disorder if no clustering or ordering is present). However, the peaks continue to broaden across the series until the x = 0.1 composition is reached. This can be understood in terms of the additional contribution to the linewidth of paramagnetic broadening from Ce. The linewidth then drops slightly at $NaCeTi_2O_6$ as there are only two A-site metals and hence, less A-site disorder.

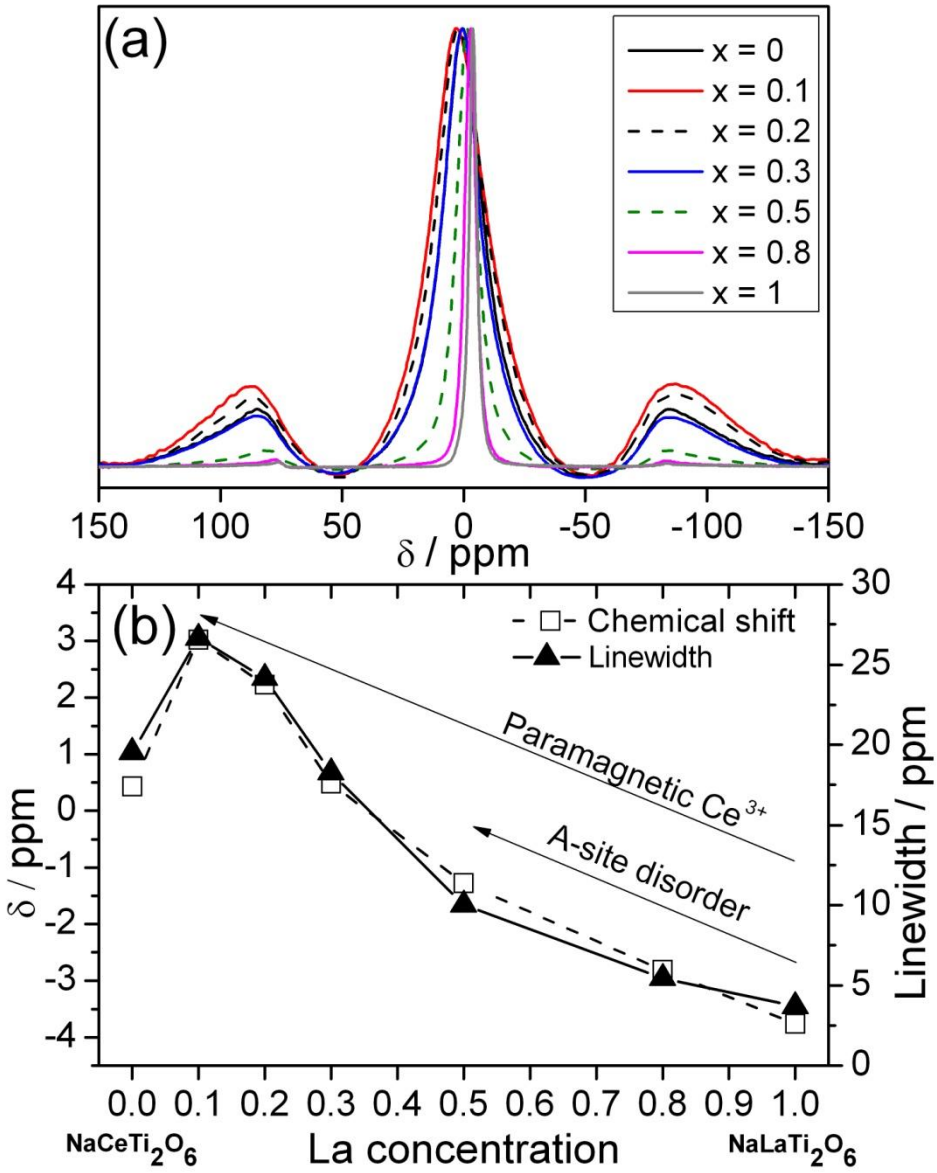

Fig. 3.10 a) ^{23}Na NMR of $NaCe_{1-x}La_xTi_2O_6$ series, b) Trend of the ^{23}Na NMR chemical shift and linewidth

As a comparison, ^{23}Na NMR spectra of physical mixtures of $NaCeTi_2O_6$-$NaLaTi_2O_6$ were also obtained. The physical mixture were prepared by grinding together appropriate amounts of $NaCeTi_2O_6$ and $NaLaTi_2O_6$ with a pestle and mortar until a uniform mixture is obtained. The physical mixture of 20% La (1 $NaCeTi_2O_6$: 4 $NaLaTi_2O_6$) and 50% La (1 $NaCeTi_2O_6$: 1 $NaLaTi_2O_6$) containing sample showed less peak broadening compared to the samples made hydrothermally (Fig. 3.11). This

indicates that when the Ce is not in the same structure as La, no paramagnetic effects are observed. This is consistent with the conclusion that the samples made hydrothermally are a genuine solid solution instead of just a physical mixture of the oxides.

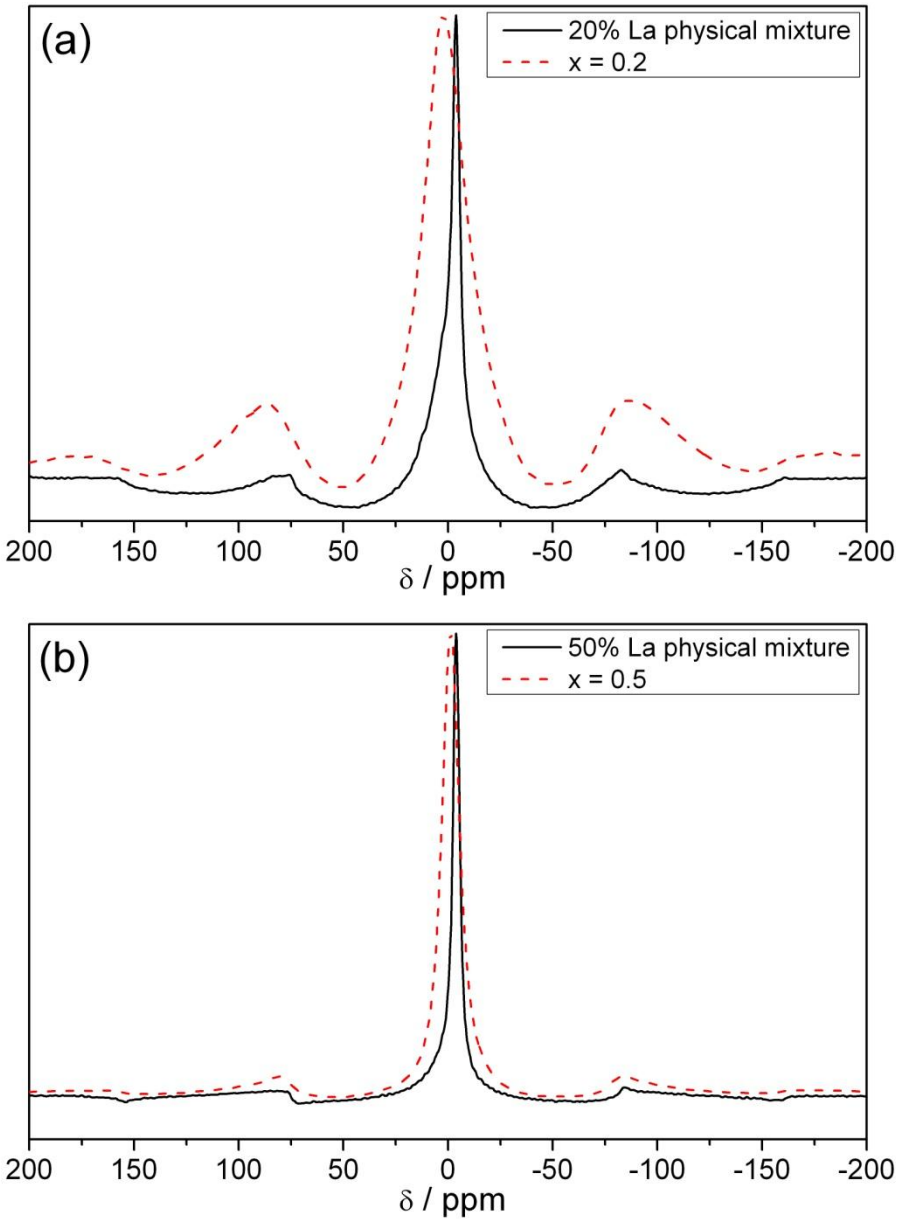

Fig. 3.11 ^{23}Na (14.1 T) MAS NMR of $NaCe_{1-x}La_xTi_2O_6$ and physical mixtures of $NaCeTi_2O_6$-$NaLaTi_2O_6$, (a) x = 0.2 and 20% La and (b) x = 0.5 and 50% La

3.4 Control of morphology and particle size

The images collected by scanning electron microscopy shows that the hydrothermally prepared perovskites have irregular shapes with particle size of around 100 nm, shown in Fig. 3.12. There is little change in morphology between $NaCeTi_2O_6$ and $NaLaTi_2O_6$. The atomic composition of $NaCe_{1-x}La_xTi_2O_6$, obtained from EDXA (Table 3.7), agrees well with the expected values except for the x = 0.8 sample where the La concentration is slightly less than expected.

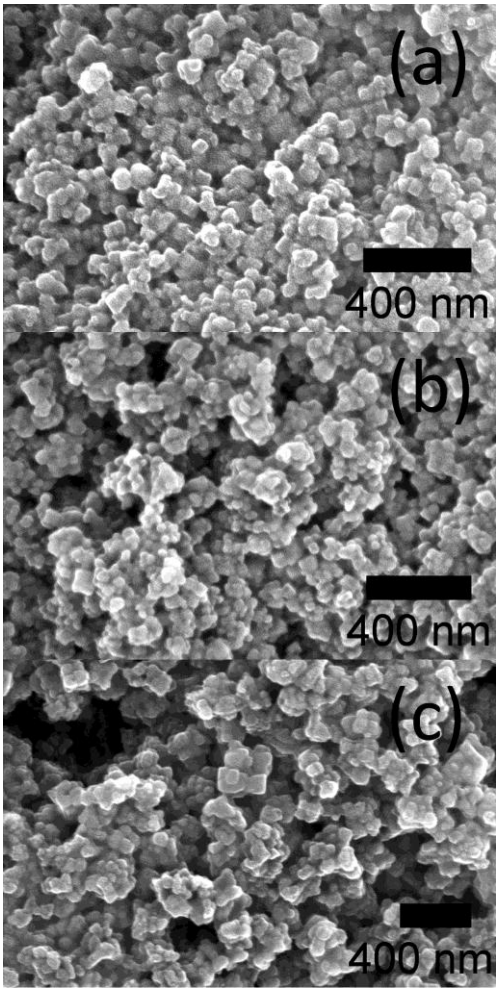

Fig. 3.12 SEM images of $NaCe_{1-x}La_xTi_2O_6$ a) x = 0, b) x = 0.5 and c) x = 1 synthesised in 4 M NaOH solution under hydrothermal conditions

Table 3.7 Atomic composition of $NaCe_{1-x}La_xTi_2O_6$ obtained from EDXA. Expected values from synthesis are in brackets. *Note: La concentration = La/(La+Ce)

La conc., x (Expected value)	Na / %	Ce / %	La / %	Ti / %	La conc.* / %
0	12.7 (10)	11.4 (10)	-	23.4 (20)	0
0.2	12.3 (10)	8.3 (8)	2.6 (2)	23.0 (20)	0.24
0.5	13.1 (10)	4.9 (5)	5.2 (5)	21.2 (20)	0.51
0.8	11.1 (10)	2.5 (2)	6.6 (8)	21.6 (20)	0.73
1	11.2 (10)	-	12.2 (10)	26.4 (20)	1

A certain degree of control on the particle size could be achieved by altering the solvent or by changing the NaOH concentration. From the XRD data (Fig. 3.13), a reduction in the peak width was observed when the NaOH concentration was increased from 4 M to 12 M, suggesting that the particle size has increased. When the reaction was performed in ethylene glycol, the peak broadens, suggesting that smaller particles are obtained. The crystallite size calculated from the Scherrer analysis of the XRD data is shown in Table 3.8.

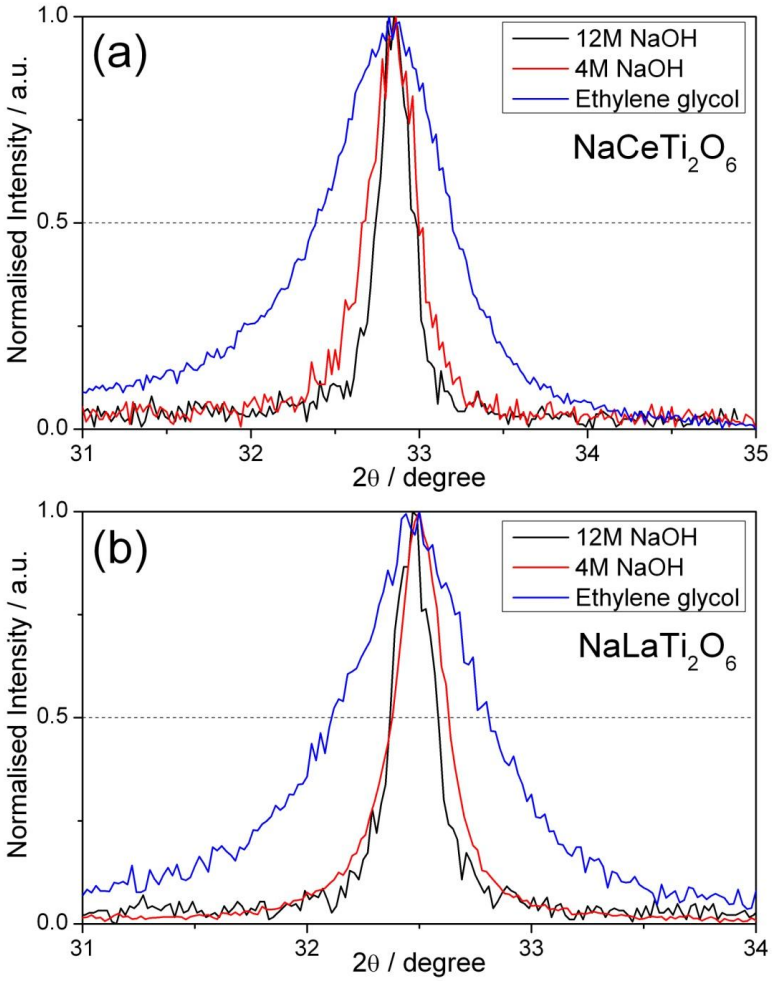

Fig. 3.13 Peak narrowing and broadening of the powder XRD data for (a) $NaCeTi_2O_6$ and (b) $NaLaTi_2O_6$, when the NaOH concentration is increased and when ethylene glycol is used as the solvent respectively

Table 3.8 Crystallite size obtained from Scherrer analysis of XRD data

	Crystallite size / nm	
Conditions	**$NaCeTi_2O_6$**	**$NaLaTi_2O_6$**
Ethylene Glycol	11.9	15.9
4 M NaOH	24.7	30.9
12 M NaOH	47.1	41.7

The XRD results are confirmed by the SEM images shown in Fig. 3.14(a)-(d), where smaller particles were obtained from a solvothermal reaction in ethylene glycol, while bigger particles were obtained with increased NaOH solution.

However, the particles observed in the SEM images were much bigger than those estimated from Scherrer analysis of the XRD data. The morphology of $NaCeTi_2O_6$ and $NaLaTi_2O_6$ particles became more spherical when a 1:1 mixture of H_2O and ethylene glycol was used as shown in Fig. 3.14(e)-(f).

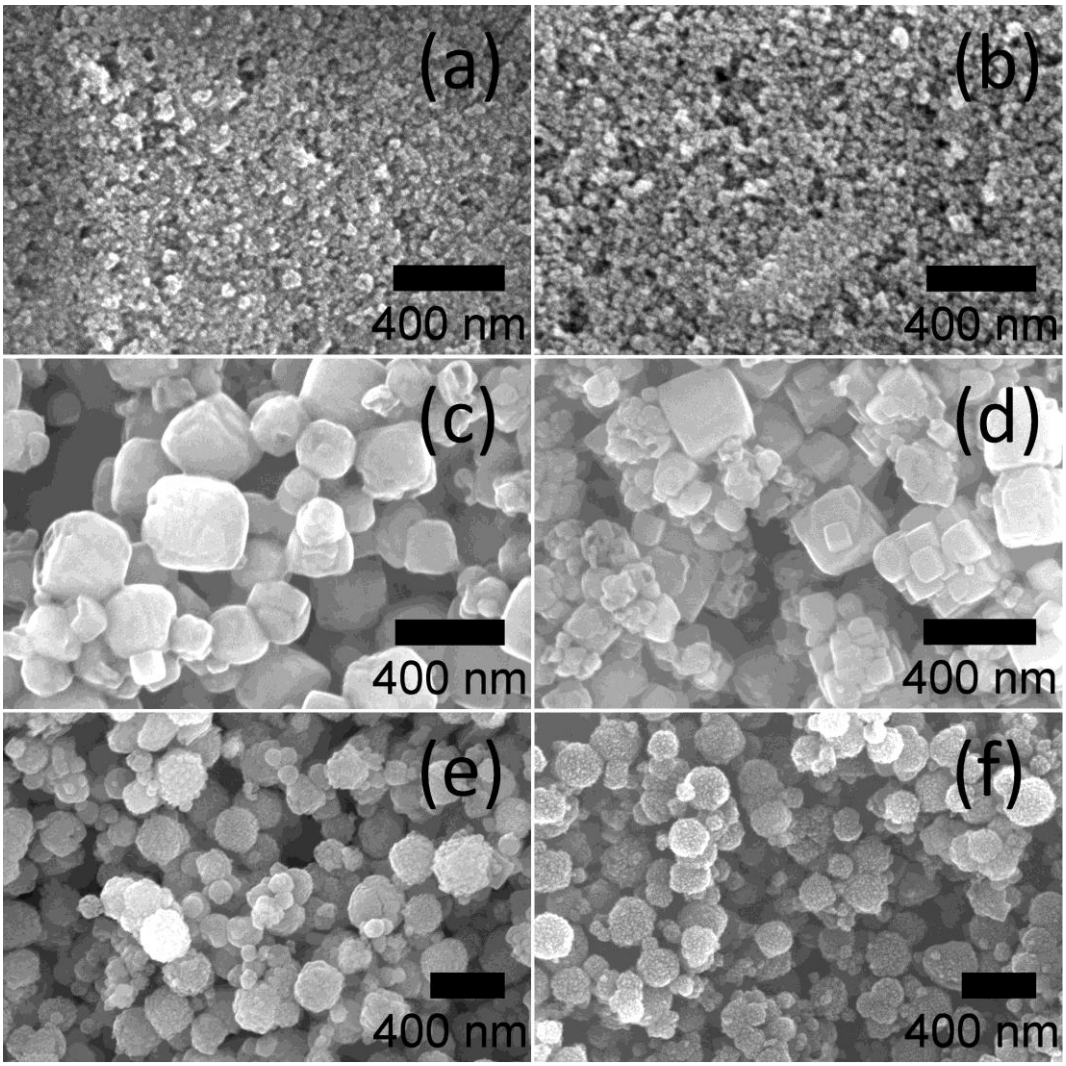

Fig. 3.14 SEM images of $NaCeTi_2O_6$ and $NaLaTi_2O_6$ powders prepared in (a)-(b) ethylene glycol, (c)-(d) 12 M NaOH and (e)-(f) ethylene glycol and water mixture respectively

3.4.1 Solvothermal synthesis of $NaCeTi_2O_6$ and $NaLaTi_2O_6$

Solvothermal reactions with ethylene glycol were carried out as follows: $CeCl_3.7H_2O$ / $LaCl_3.7H_2O$ and TiF_3 were mixed in 5 mL ethylene glycol for 15 min, then 1.6 g NaOH was added and the mixture stirred for 1 hour. The reaction vessel was then sealed and heated at 240 ^oC for 24 hours. Reactions with a 1:1 mixture of H_2O and ethylene glycol were prepared by mixing the reagents in 2 mL deionised water, then 3 mL NaOH (4 M) was added and the mixture stirred for 15 min. Then 5 mL ethylene glycol was added and stirred for 1 hour before being sealed and heated at 240 ^oC for 24 hours.

Solvothermal reactions in ethylene glycol at different temperatures were also investigated. The XRD pattern in Fig. 3.15 and Fig. 3.16 shows that $NaCeTi_2O_6$ and $NaLaTi_2O_6$ starts to form at 170 ^oC respectively, while reactions at lower temperatures yield a broad peak between 25-35^o.

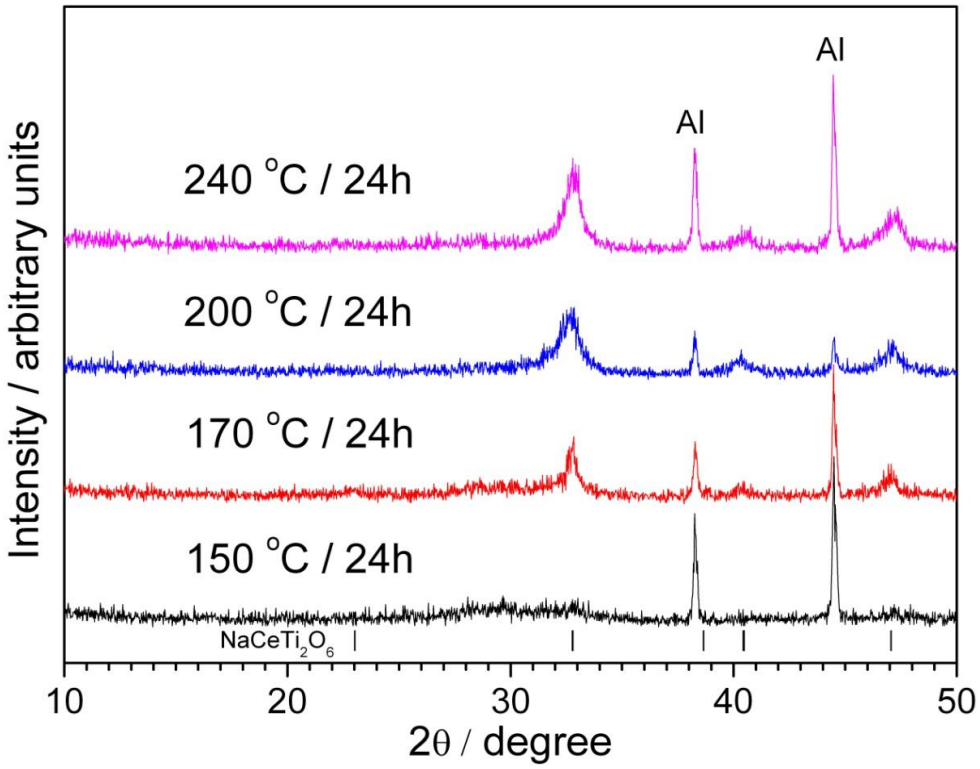

Fig. 3.15 XRD pattern of $NaCeTi_2O_6$ reactions made in ethylene glycol at different temperatures

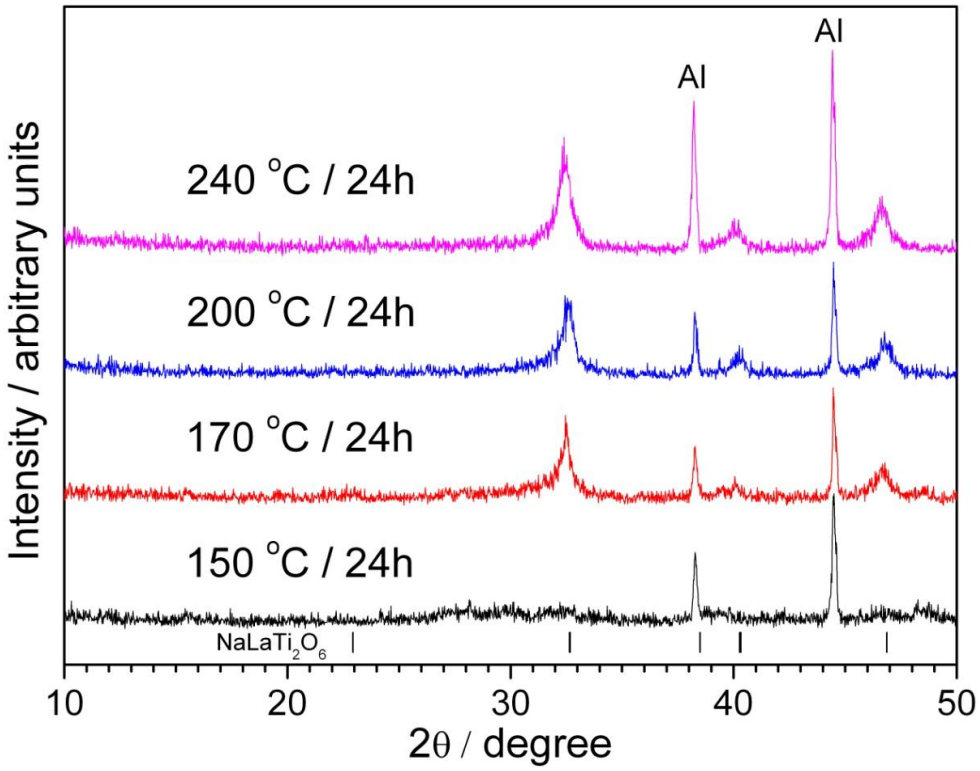

Fig. 3.16 XRD pattern of $NaLaTi_2O_6$ reactions made in ethylene glycol at different temperatures

Following the successful solvothermal synthesis with ethylene glycol, other solvents were also tested. The solvents used were Jeffamine D-4000 Polyetheramine, Ethanolamine and Polyethylene glycol. In all three cases, $NaCeTi_2O_6$ was made but $Ce(OH)_3$ was also observed in the XRD pattern as shown in Fig. 3.17.

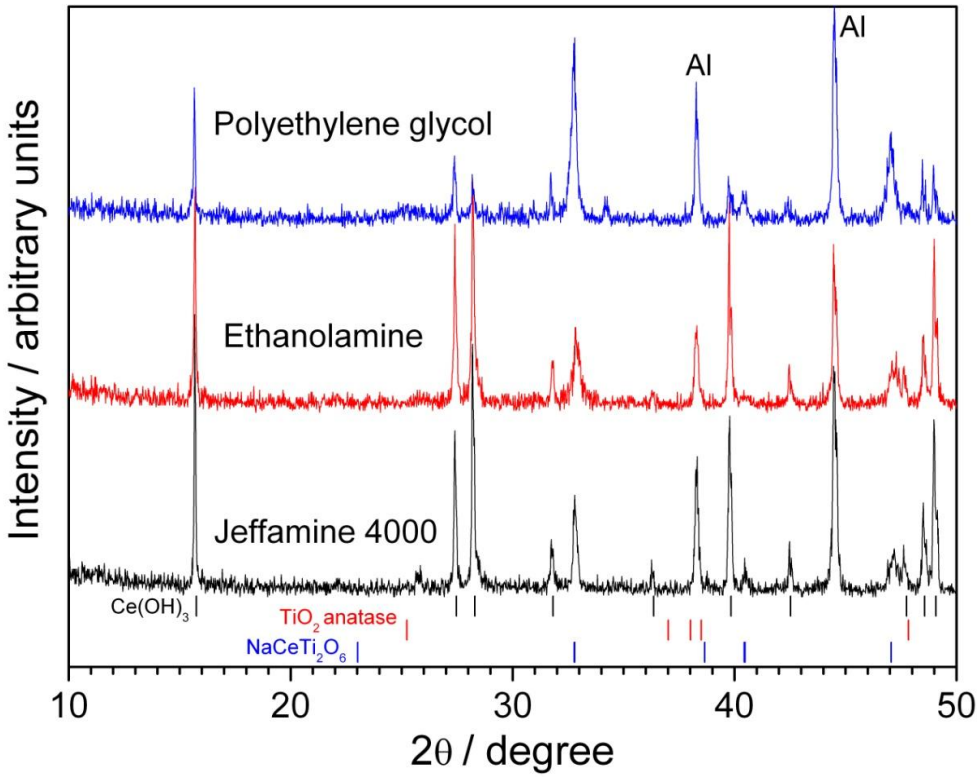

Fig. 3.17 XRD patterns of $NaCeTi_2O_6$ reactions made in different solvents

3.4.2 $NaCeTi_2O_6$ reactions at room temperature

$NaCeTi_2O_6$ reactions where the starting materials were left to stir at room temperature were also carried out. Wright *et al*. reported the preparation of $NaCeTi_2O_6$ at 25 ^oC[29], however, attempts at repeating this result was not achieved in this work. Room temperature reactions only gave an amorphous product, which was most likely to be CeO_2 (Fig. 3.18).

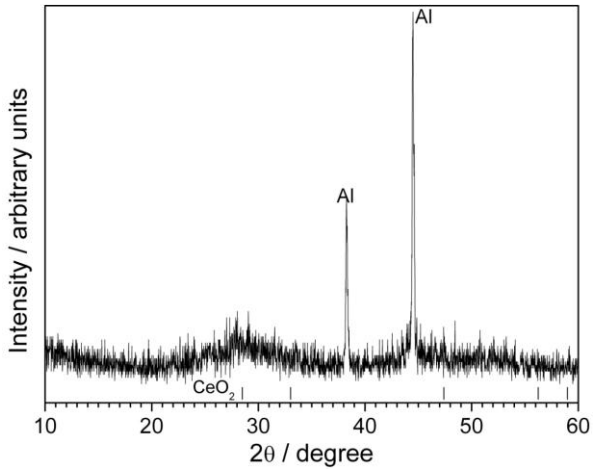

Fig. 3.18 XRD pattern of product obtained from room temperature reactions

3.5 Presence of defects in hydrothermal $NaCe_{1-x}La_xTi_2O_6$

3.5.1 Solid state ^2H NMR of deuterated $NaCeTi_2O_6$ and $NaLaTi_2O_6$

The possibility of water or hydroxide being incorporated in the perovskite structure was investigated by ^2H MAS NMR. Deuterated samples of $NaCeTi_2O_6$ and $NaLaTi_2O_6$ were made with the same procedure as described in Section 3.2 but using D_2O and NaOD. The sample were then washed with copious amounts of deionised H_2O to ensure that any surface D_2O or OD^- was removed and that any remaining deuterium was present only within the crystal lattice. In Fig. 3.19, the ^2H NMR spectra of both of the deuterated perovskites made in D_2O / NaOD gave a small but significant NMR signal. In order to ensure that the low intensity signal observed did not result from natural-abundance levels of ^2H in the probe / rotor, experiments were also conducted for empty rotors. No signal was observed, confirming that the ^2H signal seen in Fig. 3.19 does indeed result from ^2H trapped within the perovskite structure. Once the deuterated $NaLaTi_2O_6$ was heated above 900 ^oC, the signal was not observed indicating that the deuterium-containing species, although contained

within the crystals, is removed on heating. The presence of water in hydrothermally prepared oxides has been reported by other authors. Goh *et al.* observed two separate signals in the ^{1}H NMR of $KNbO_3$ prepared hydrothermally.[52] They attributed one signal to the presence of surface water or hydroxyl and the other signal to hydroxyl ions incorporated in the perovskite lattice. Chien *et al.* performed ^{2}H NMR on deuterated $BaTiO_3$ to verify the presence of OD groups within the $BaTiO_3$ lattice showing a single narrow peak with a broad, overlapping component.[53] They attributed the narrow peak to D_2O trapped between the $BaTiO_3$ crystallites, or close to the surface of the crystals, while the broad component is due to D_2O or OD^- trapped within the $BaTiO_3$ lattice. The ^{2}H NMR peak for $NaCeTi_2O_6$ is slightly shifted compared to $NaLaTi_2O_6$. This is undoubtedly because of the effect of paramagnetic Ce, similar to the shift found in the ^{23}Na NMR spectra. It suggests that the deuterated species is within the perovskite structure since they are influenced by the paramagnetic effect of Ce^{3+}.

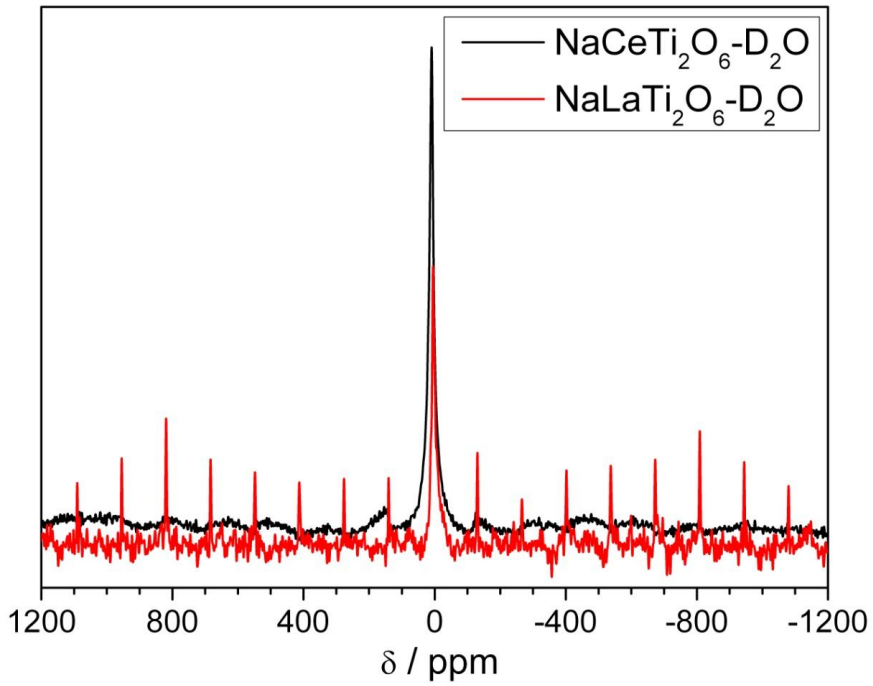

Fig. 3.19 ^{2}H (14.1 T) NMR of deuterated $NaCeTi_2O_6$ and $NaLaTi_2O_6$ prepared in D_2O and NaOD. Spectra were recorded under conditions that enabled quantitative analysis, by comparisons to (natural-abundance) ^{2}H NMR spectra of H_2O

The amount of deuterium within the samples can be quantified using NMR spectroscopy, by comparing the ^2H signal from the sample to that obtained from a natural-abundance sample of a known amount of water. Thus, the concentration (mmol / g) and then a percentage by weight of ^2H in each sample can be determined. For $NaLaTi_2O_6$, the amount of ^2H was calculated to be 1.7 mmol g^{-1} for the centre band signal and 1.4 mmol g^{-1} in the sidebands, resulting in 0.6 % ^2H by weight. For $NaCeTi_2O_6$, the sidebands are broad and too low in intensity to integrate but by integrating the sharp centre band, the amount of ^2H was calculated to be 13.88 mmol g^{-1} in the centre band, which by weight gave 2.78% ^2H. Although assumptions have been made in these calculations, it can be deduced that a significantly larger amount of deuterium is incorporated in the crystal structure of $NaCeTi_2O_6$ compared to $NaLaTi_2O_6$. To rationalise this observation, the presence of Ce^{4+}, seen by XANES, can be used: the extra charge of the Ce^{4+} may be balanced by removal of Na^+ from the A-site, which is then replaced by D_2O molecules.

Based on ICP results to determine the atomic composition (Table 3.9), the nominal $NaCeTi_2O_6$ material is best formulated as $(Na_{0.7}Ce_{0.9}(H_2O)_{0.4})Ti_2O_6$. The calculated atomic composition based on the formula is compared with observed atomic composition from ICP results in Table 3.10. This formulation results in an average Ce oxidation state of +3.6, which is slightly higher but not inconsistent with the XANES analysis described above. On the other hand, the nominal $NaLaTi_2O_6$ material is best formulated with the formula $(Na_{0.7}La_{1.1}(H_2O)_{0.2})Ti_2O_6$, where the La oxidation state is maintained at +3 as expected. Thus, the cerium-containing phase is able to accommodate more A-site water than the lanthanum containing material since it is not possible to oxidise La above the +3 oxidation state.

Table 3.9 Composition of $NaCe_{1-x}La_xTi_2O_6$ in weight percentage obtained from ICP analysis. Expected values calculated from the nominal formula are included in brackets

Sample	Na / wt.%	Ce / wt.%	La / wt.%	Ti / wt.%
$NaCeTi_2O_6$	4.77% (6.48)	35.71% (39.49)	-	27.36% (26.98)
$NaCe_{0.5}La_{0.5}Ti_2O_6$	4.86% (6.49)	20.05% (19.78)	19.71% (19.61)	27.39% (27.03)
$NaLaTi_2O_6$	4.46% (6.50)	-	40.26% (39.28)	27.72% (27.07)

Table 3.10 Calculated atomic composition for suggested formula of $NaCeTi_2O_6$ and $NaLaTi_2O_6$ with H_2O on the A-site.

Suggested Formula	Na / wt.%	Ce / wt.%	La / wt.%	Ti / wt.%
$(Na_{0.7}Ce_{0.9}(H_2O)_{0.4})Ti_2O_6$	4.71	36.96	-	28.07
$(Na_{0.7}La_{1.1}(H_2O)_{0.2})Ti_2O_6$	4.41	-	41.95	26.29

As a final verification of this suggestion, the occupancy of the A-site was investigated in the Rietveld refinement against the powder XRD data. This shows that inclusion of oxygen as a third A-site component (representing a water molecule) and refinement of the occupancy of each species gives a composition consistent with the presence of water at the expense of sodium. This also gave a smaller improvement in the overall fit and, importantly resulted in physically meaningful temperature factors for all sites, which was not the case for the simple model without inclusion of water. We note also that the refinement predicts most water present in the $NaCeTi_2O_6$ end member, entirely consistent with the spectroscopic results presented above. The presence of water molecules on the A-site of a perovskite is not unprecedented; for example, it has been reported for a barium potassium bismuthate perovskite, also prepared by hydrothermal synthesis.[54]

3.5.2 Fourier Transform Infra-Red spectroscopy

The FTIR spectra of $NaLaTi_2O_6$ and $NaCeTi_2O_6$ in Fig. 3.20 showed a sharp band at 550 cm^{-1}, three bands at 1360, 1540 and 1640 cm^{-1} and a broad band between 3000-3600 cm^{-1}. The band at 550 cm^{-1} is the stretching vibration of Ti-O,[10,55-56] while the broad band at 3000-3600 cm^{-1} and the band at 1640 cm^{-1} is due to O-H stretching and H-O-H bending mode, respectively.[43,53,56-60] Upon heating to 900 ^oC, these bands are still present but their intensity were reduced. This could be because all the lattice and surface hydroxyl groups, either as hydroxide or water, were removed upon heating to 900 ^oC but as the sample was left to cool to room temperature, hydroxyl groups from the atmosphere were adsorbed again on to the surface. Chien *et al.* also observed a reduction of in the intensity of these bands, however even after heating to 800 ^oC, these bands are not completely removed.[53]

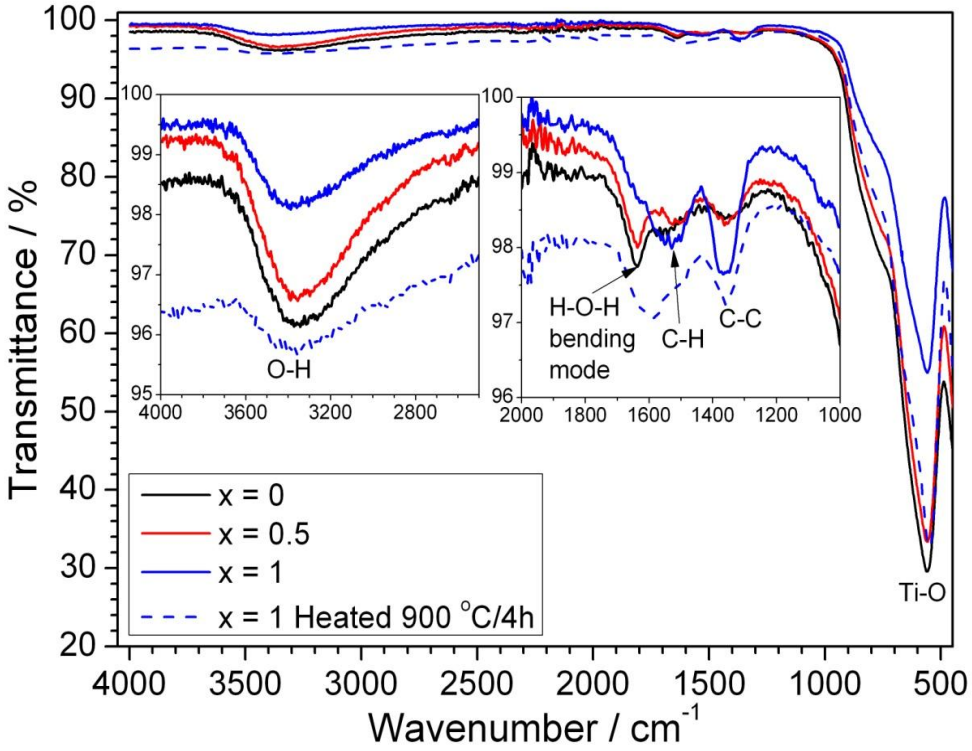

Fig. 3.20 FT-IR spectra of $NaCeTi_2O_6$, $NaLaTi_2O_6$ and $NaLaTi_2O_6$ calcined at 900 ^oC/4 hours in air. The inset shows the zoomed-in view of the IR spectra for the O-H and H-O-H region

The IR spectra of deuterated $NaCeTi_2O_6$ and $NaLaTi_2O_6$ are shown in Fig. 3.21, where the OD and OH stretching are observed. The O-D band[61] reported to be between 2450-2650 cm^{-1} was observed in $NaCeTi_2O_6$ but not in $NaLaTi_2O_6$. This agrees with the ^2H NMR data where the amount of ^2H was only 0.6 wt.% in $NaLaTi_2O_6$ compared to 2.78 wt.% in $NaCeTi_2O_6$. Similar bands due to O-H stretching and H-O-H bending modes were also observed.

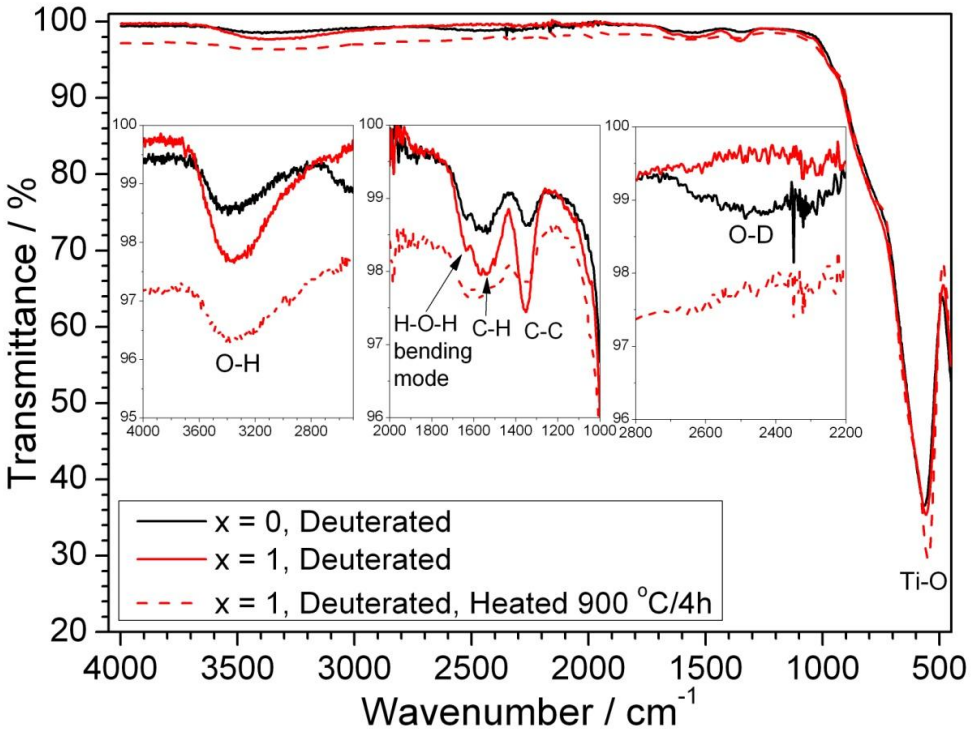

Fig. 3.21 FTIR spectra of deuterated samples of $NaCeTi_2O_6$, $NaLaTi_2O_6$ and $NaLaTi_2O_6$ calcined at 900 °C/4hours. The inset shows the zoomed-in view of the IR spectra for the O-H, H-O-H and O-D region

3.6 Thermal stability

The thermal stability of these materials was studied by in-situ XRD where the sample was heated from 30 to 900 ^{o}C in air and the XRD pattern was collected at intervals of 50 ^{o}C. The contour plot in Fig. 3.22 below shows the in-situ XRD of $NaCeTi_2O_6$. The perovskite remained stable up to 600 ^{o}C. Above this temperature, it started to decompose and CeO_2 was formed, with its most intense peak visible at 28.5^{o}. However, the intensity of this peak starts to decrease at 850 ^{o}C and completely disappears at 900 ^{o}C. Upon heating, the peaks in the XRD pattern became slightly sharper as the crystallite starts to fuse with each other resulting in a larger particle size. The weak superstructure peaks expected for $R\bar{3}c$ was not observed in the XRD pattern and only the peaks expected for a cubic perovskite was observed. When the same measurement was repeated with flowing 5% H_2-N_2 gas, the perovskite remains stable up to 900 ^{o}C (Fig. 3.23). The reducing environment was able to prevent the oxidation of Ce^{3+} to Ce^{4+} from occurring.

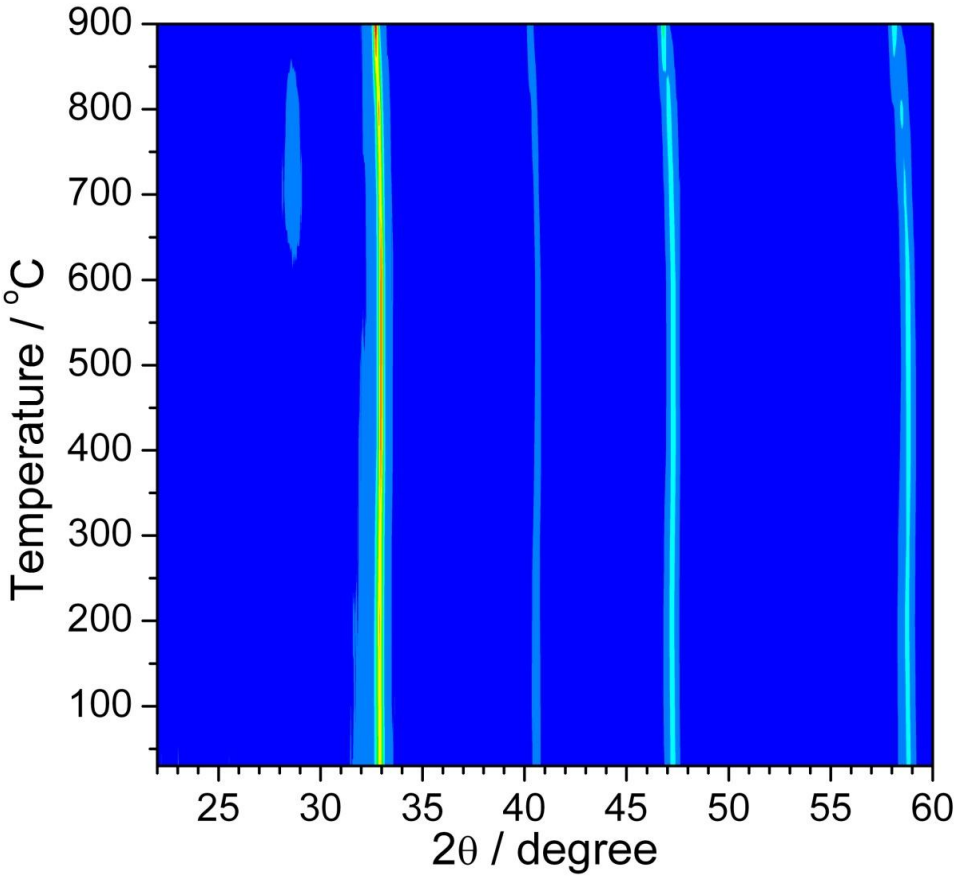

Fig. 3.22 *In-situ* XRD of $NaCeTi_2O_6$ heated from 30 °C to 900 °C in air

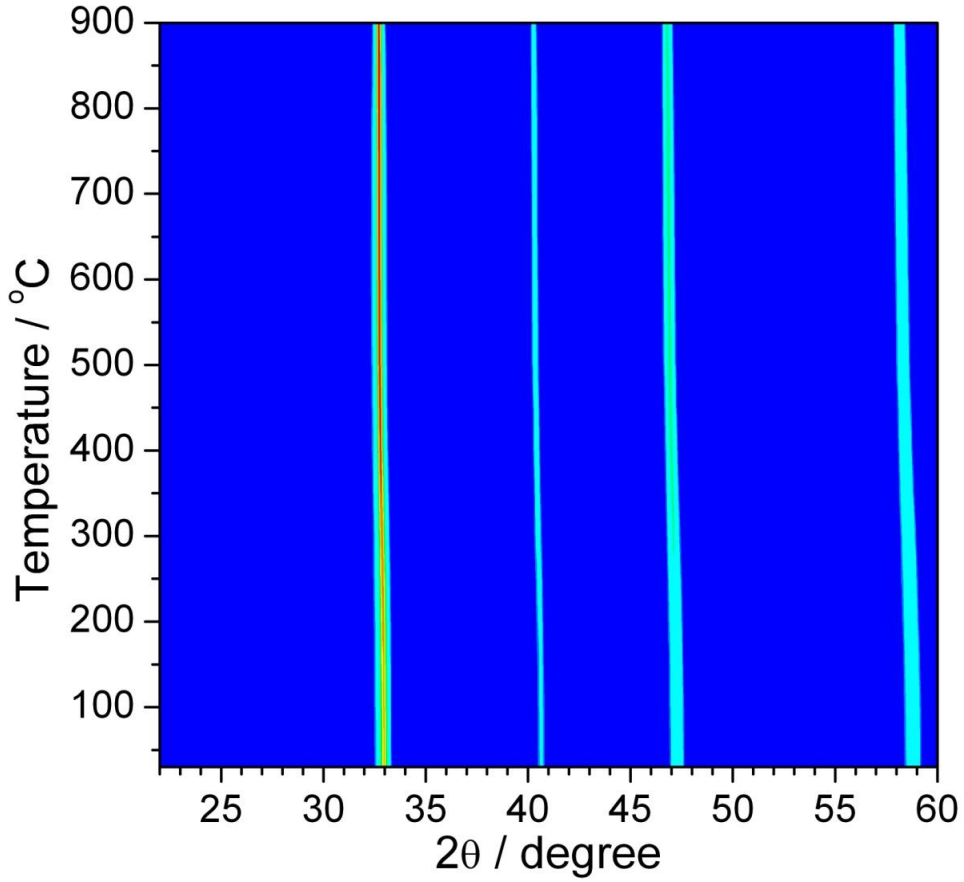

Fig. 3.23 *In-situ* XRD of $NaCeTi_2O_6$ heated from 30 °C to 900 °C in 5% H_2-N_2 gas

In contrast, $NaLaTi_2O_6$ remains stable even after heating to 900 ^oC in air (Fig. 3.24). The oxidation state of La cannot be increased beyond +3 so no further oxidation can occur unlike in Ce. The peaks did not sharpen as much as $NaCeTi_2O_6$ upon heating and no weak superstructure peaks expected for $R\bar{3}c$ were observed.

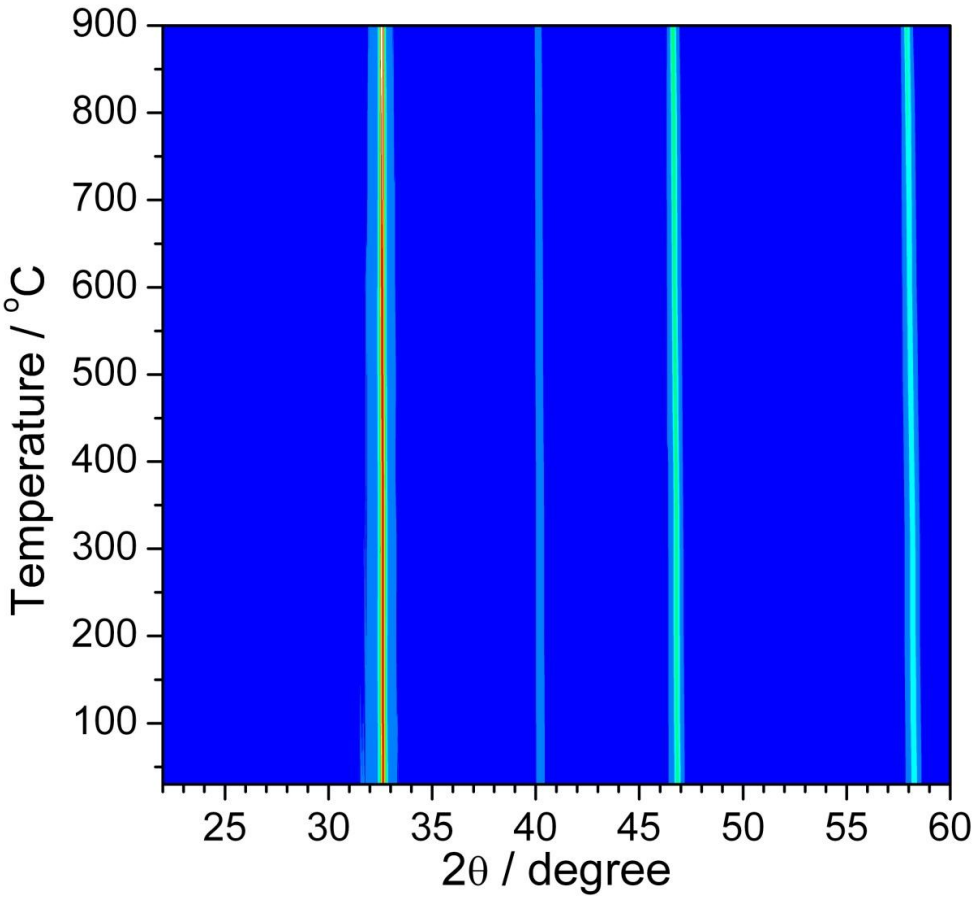

Fig. 3.24 *In-situ* XRD of $NaLaTi_2O_6$ heated from 30 ^oC to 900 ^oC in air

Thermogravimetric analysis (TGA) of these perovskites was also carried out (Fig. 3.25). The first step of mass loss occurs below 200-300 ^oC which can be attributed to the loss of surface adsorbed water or hydroxyl groups. The second step occurs below 400-600 ^oC which could be the loss of water or hydroxyl groups incorporated in the lattice structure. The overall mass loss for the $NaCe_{1-x}La_xTi_2O_6$

samples after heating to 600 ^{o}C is between 2% and 3% with $NaLaTi_2O_6$ showing the most mass loss. This seems to be contrary to the expected trend where $NaCeTi_2O_6$ should have more water incorporated into the lattice, as shown by the ^{2}H NMR, so it should show a greater mass loss than $NaLaTi_2O_6$. However, the TGA includes both surface and lattice water but the NMR only shows the amount of D_2O found in the lattice. Also, from the *in-situ* XRD, the main CeO_2 peak started appearing at 600 ^{o}C and increases in intensity up to 750 ^{o}C, after which it starts to decrease and disappears at 900 ^{o}C. It could be that the sample takes up O_2 to form CeO_2, thus offsetting the mass loss from the water.

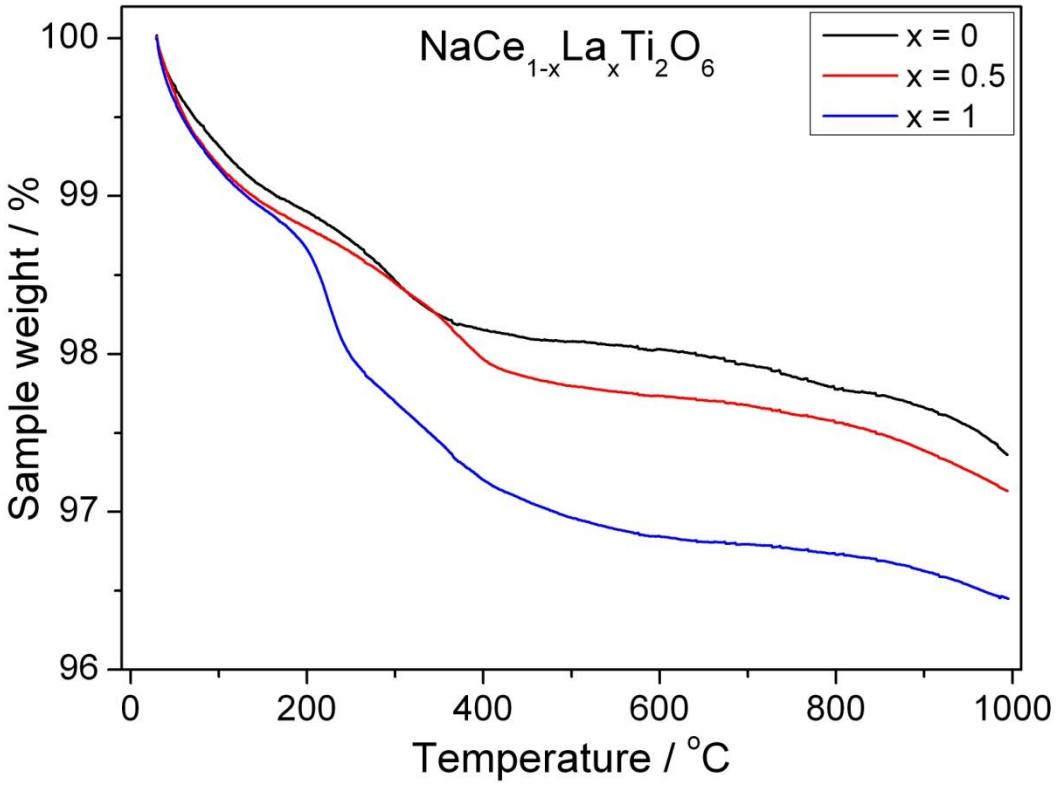

Fig. 3.25 TGA of $NaCe_{1-x}La_xTi_2O_6$ heated from 30 to 1000 ^{o}C in air

3.7 Hydrothermal synthesis of $NaBi_xCe_{1-x}Ti_2O_6$ and $NaBi_xLa_{1-x}Ti_2O_6$

3.7.1 $NaBi_xCe_{1-x}Ti_2O_6$

The synthesis procedure for $NaBi_xCe_{1-x}Ti_2O_6$ is as follows: Appropriate amounts, as shown in Table 3.11, of Bismuth citrate (Sigma Aldrich, 99.99%), $Bi(NO_3)_3{\cdot}5H_2O$ (Sigma Aldrich, 98%), $CeCl_3{\cdot}7H_2O$ (Sigma Aldrich, 99.9%) and Titanium bisammonium lactato dihydroxide (TiBALD) (Sigma Aldrich, 50 wt. % in H_2O) was stirred in a Teflon liner with 3.8 mL deionised water. After 10 min, 5 mL NaOH solution is added so that the final NaOH concentration was 4 M. The mixture was then stirred for a further hour. The liner was then sealed in a steel autoclave and placed in an oven pre-heated to 240 ^oC. After heating for 24 hours, the autoclaves were left to cool to room temperature. The solid products were recovered by suction filtration, washed thoroughly with warm water and dried overnight at 70 ^oC in a drying oven. The products were then ground into powder for further characterisation.

Table 3.11 Amounts measured for $NaBi_xCe_{1-x}Ti_2O_6$ synthesis

Bi conc., x	Bi citrate / g	$CeCl_3{\cdot}7H_2O$/g	TiBALD/mL	NaOH(aq)/mL	H_2O/mL
0	-	0.3726	1.2	5	3.8
0.2	0.0796	0.2981			
0.5	0.1991	0.1863			
0.8	0.3185	0.0745			
1	**$Bi(NO_3)_3{\cdot}5H_2O$/g**	-			
	0.4851				

Initially, the starting materials used to prepare $NaBi_xCe_{1-x}Ti_2O_6$ hydrothermally was $Bi(NO_3)_3{\cdot}5H_2O$ (Sigma Aldrich, 98%), $CeCl_3{\cdot}7H_2O$ (Sigma Aldrich, 99.9%) and TiF_3 (Alfa, 98%). Although the end members can be made

using these precursor, a pure product was not obtained for $NaBi_xCe_{1-x}Ti_2O_6$, particularly x = 0.5 and 0.8 (Fig. 3.26). Although the XRD pattern showed a gradual peak shift with increasing Bi concentration, $Bi_2Ti_2O_7$ were also formed as a side product. $Bi_2Ti_2O_7$ was also observed by Ma *et al*. and Cho *et al.* when they used $Bi(NO_3)_3{\cdot}5H_2O$, Ti isopropoxide and Ti tetra-n-butoxide as the starting materials.[62-63] Hence, other Bi and Ti precursors were tested and the combination of Bi citrate with TiBALD appeared to give pure $NaBi_xCe_{1-x}Ti_2O_6$ samples. However, this combination did not produce pure $NaBiTi_2O_6$, with $Bi_2Ti_2O_7$ observed in the XRD, so $Bi(NO_3)_3{\cdot}5H_2O$ was used instead.

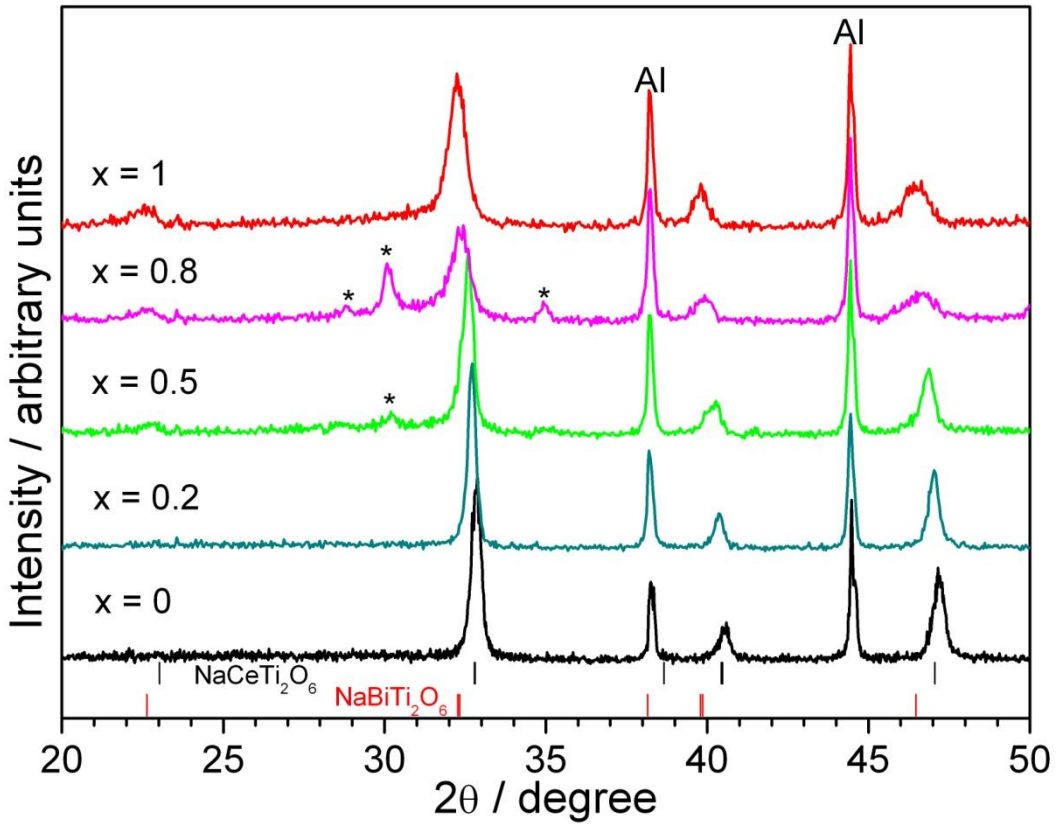

Fig. 3.26 Powder XRD of $NaBi_xCe_{1-x}Ti_2O_6$ samples, using $Bi(NO_3)_3.5H_2O$, $CeCl_3{\cdot}7H_2O$ and TiF_3 in NaOH solution, with tick marks showing the peak positions for $NaCeTi_2O_6$ and $NaBiTi_2O_6$ and * showing the peak position of an impurity phase, $Bi_2Ti_2O_7$

Powder XRD of $NaBi_xCe_{1-x}Ti_2O_6$ (Fig. 3.27) prepared using precursor described in Table 3.11, showed that the samples have the perovskite structure with no impurities observed. The peaks in the XRD pattern shifted to lower 2θ values as more Bi was added to replace Ce. This indicated that the cell volume increased in size. However, there is a sudden shift between x = 0.2 and x = 0.5. The intensity of the peak at 23° also increased from x = 0.5 onwards and the pattern of x = 0.5 and 0.8 are very similar to $NaBiTi_2O_6$. Pawley refinement of the XRD data was carried out using the $R\bar{3}c$ space group for $NaCeTi_2O_6$ and x = 0.2, but samples with higher Bi content and $NaBiTi_2O_6$ were refined using $R3c$ instead.

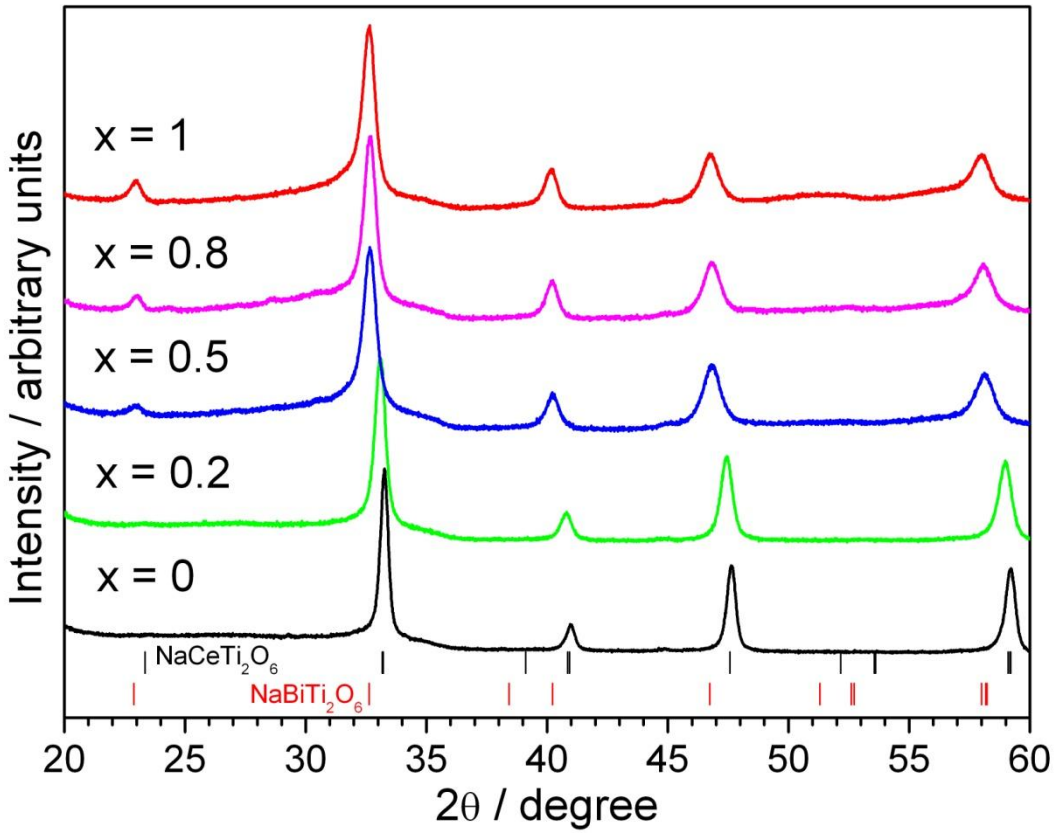

Fig. 3.27 Powder XRD of $NaBi_xCe_{1-x}Ti_2O_6$ samples, using precursors mentioned in Table 3.11. The tick marks shows the peak positions of $NaCeTi_2O_6$ and $NaBiTi_2O_6$

The trend in lattice parameters obtained from the Pawley refinement (Fig. 3.28) showed an increase with increasing Bi concentration, but the increase is not gradual as there is a steep increase from x = 0.2 to x = 0.5. The ionic radius of Ce^{3+} in a 12 coordination environment is 1.34 Å, while the ionic radius of Bi^{3+} in a 12 coordination environment is not available, but it is 1.17 Å in an 8 coordination environment.[31] Assuming that the ionic radius of Bi^{3+} on the A-site is bigger than Ce, it could be that x = 0.5 and 0.8 sample has a higher Bi content than expected causing the steep increase in the lattice parameter.

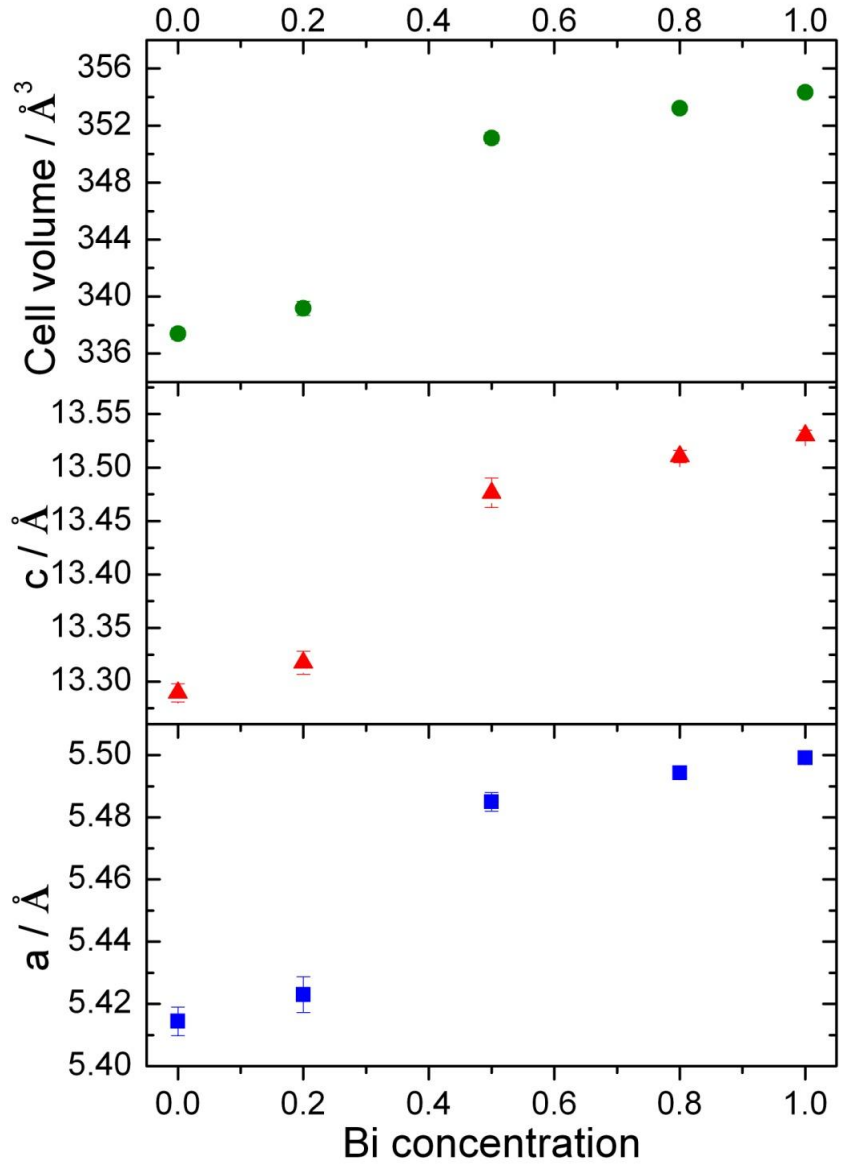

Fig. 3.28 Trend of the lattice parameters and cell volume of $NaBi_xCe_{1-x}Ti_2O_6$

The Raman spectra of the $NaBi_xCe_{1-x}Ti_2O_6$ series (Fig. 3.29) are similar to that of $NaCe_xLa_{1-x}Ti_2O_6$ with broad bands observed at around 150, 250, 550 and 850 cm^{-1}. The $NaCeTi_2O_6$ made from TiBALD also has a band at 450 cm^{-1}, which was less obvious compared to the $NaCeTi_2O_6$ made from TiF_3, shown in Fig. 3.6. However, this band disappeared upon Bi substitution at x = 0.2. At x = 0.5 and 0.8, the band at 250 cm^{-1} became sharper while the band at 550 cm^{-1} start to decrease in intensity and gradually shifts to lower values. These two bands are associated with Ti-O vibrations and Ti-O_6 octahedral vibrations which may result in a change from $R\bar{3}c$ to $R3c$. $NaBiTi_2O_6$ also had three extra bands (180, 450 and 680 cm^{-1}) which was not observed in $NaBiTi_2O_6$ reported in the literature. These extra bands might originate from impurities present in the sample which was not detected by XRD. Raman spectroscopy collects data from a localised area compared to XRD so the impurities may not observed in the XRD, but was detected in the Raman spectra.

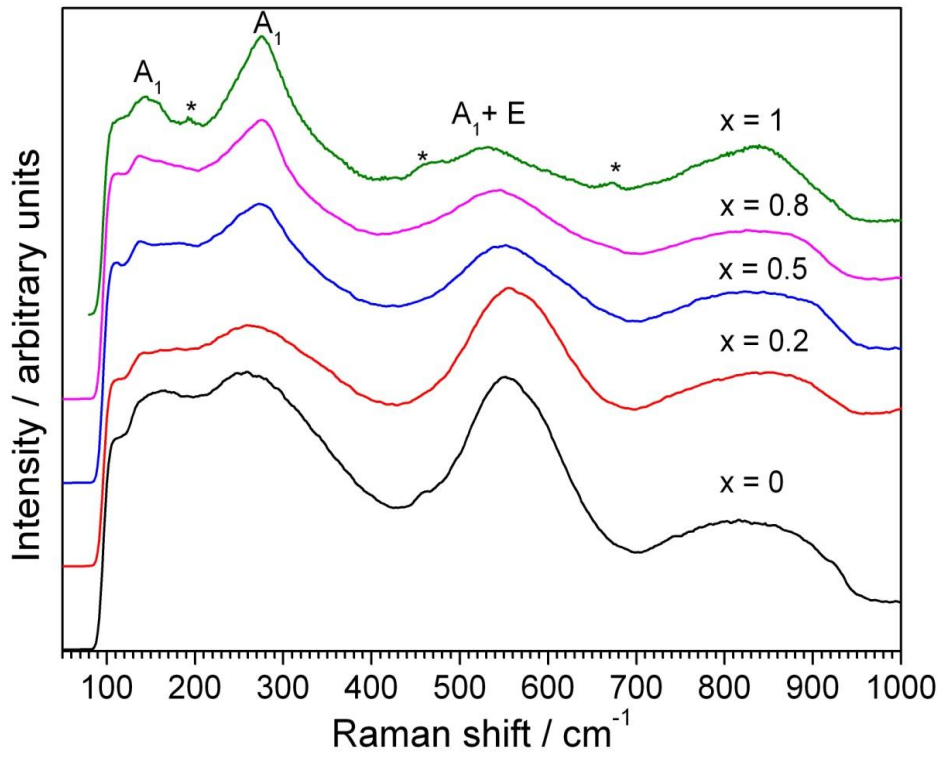

Fig. 3.29 Raman spectra of $NaBi_xCe_{1-x}Ti_2O_6$. The Raman spectra of $NaBiTi_2O_6$ made using TiBALD had extra peaks labelled with *, that are not observed for $NaBiTi_2O_6$ reported in the literature

The SEM images of $NaBi_xCe_{1-x}Ti_2O_6$ made from TiBALD (Fig. 3.30) shows that the particles are irregular shaped with particle size less than 100 nm. $NaBiTi_2O_6$ also show rod-like particles which was not observed in the other material in the series. It is quite likely that the extra bands in the Raman spectrum of $NaBiTi_2O_6$ may come from these impurities.

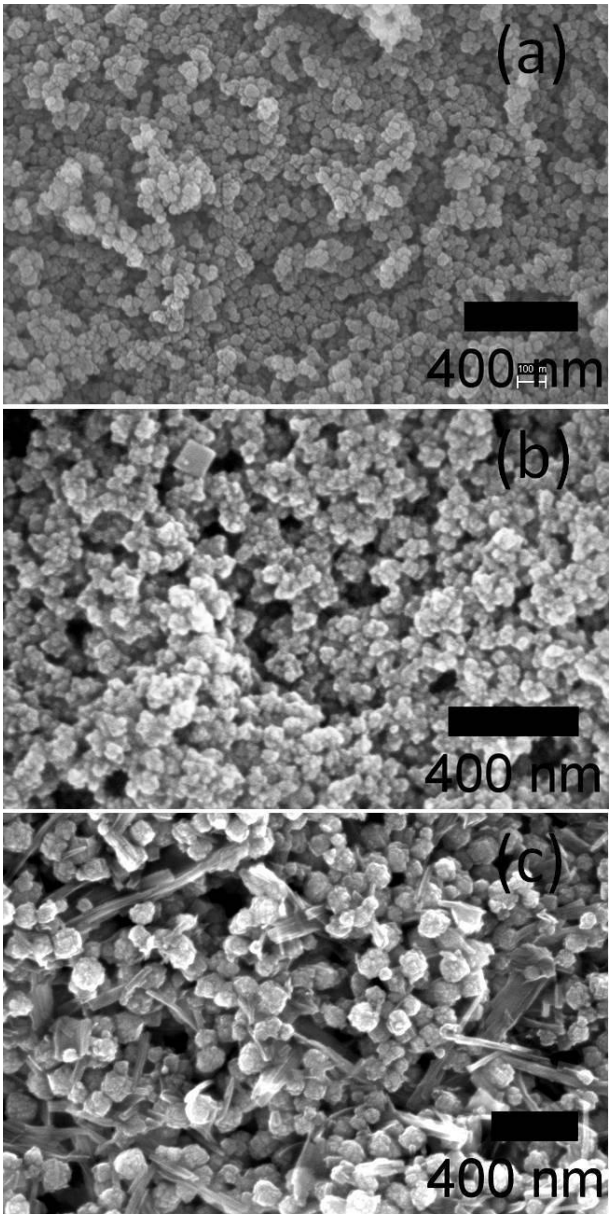

Fig. 3.30 SEM images of $NaBi_xCe_{1-x}Ti_2O_6$ a) x = 0, b) x = 0.5 and c) x = 1

3.7.2 $NaBi_xLa_{1-x}Ti_2O_6$

The synthesis procedure for $NaBi_xLa_{1-x}Ti_2O_6$ is as follows: Appropriate amounts, as shown in Table 3.12, of $Bi(NO_3)_3{\cdot}5H_2O$ (Sigma Aldrich, 98%), $LaCl_3{\cdot}7H_2O$ (Sigma Aldrich, 99%) and TiF_3 (Alfa, 98%) was stirred in a Teflon liner with 5 mL deionised water. After 10 min, 5 mL NaOH solution is added so that the final NaOH concentration is 4 M. The mixture was then stirred for a further hour. The liner was then sealed in a steel autoclave and placed in an oven pre-heated at 240 ^oC. After heating for 24 hours, the autoclaves were left to cool to room temperature. The solid products were recovered by suction filtration, washed thoroughly with warm water and dried overnight at 70 ^oC in a drying oven. The products were then ground into powder for further characterisation.

Table 3.12 Amounts measured for $NaBi_xLa_{1-x}Ti_2O_6$ synthesis

Bi conc., x	$Bi(NO_3)_3{\cdot}5H_2O$/g	$LaCl_3{\cdot}7H_2O$/g	TiF_3/g	NaOH(aq)/mL	H_2O/mL
0	-	0.3714	0.2622	5	5
0.2	0.0970	0.2971			
0.5	0.2426	0.1857			
0.8	0.3881	0.0743			
1	0.4851	-			

Powder XRD of $NaBi_xLa_{1-x}Ti_2O_6$ (Fig. 3.31) showed that the samples have perovskite structure, with no impurity phase observed. The peaks in the XRD pattern shifted to lower 2θ values with increasing Bi concentration indicating an increase in the cell volume. The intensity of the peak at 23^o also increased from x = 0.5 onwards similar to the XRD pattern for $NaBi_xCe_{1-x}Ti_2O_6$. Pawley refinement of the XRD data was carried out using the $R\bar{3}c$ space group for $NaLaTi_2O_6$ and x = 0.2, but samples with higher Bi content and $NaBiTi_2O_6$ were refined using $R3c$ instead.

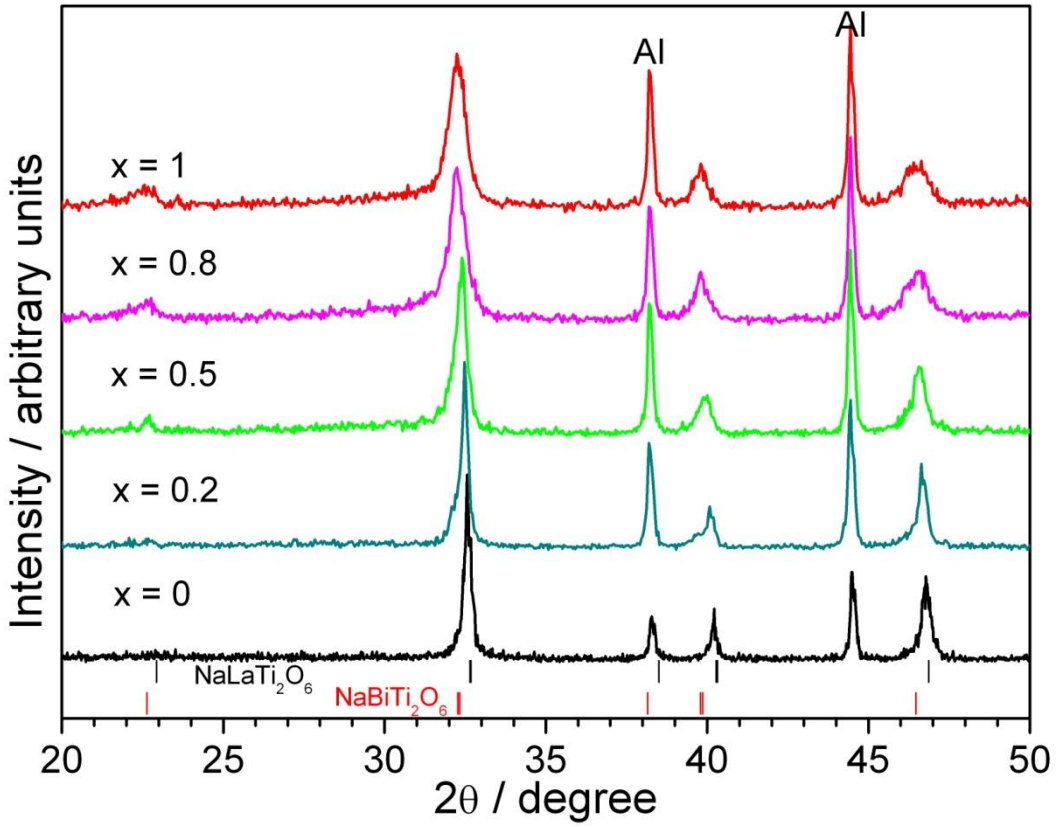

Fig. 3.31 Powder XRD of $NaBi_xLa_{1-x}Ti_2O_6$ samples. The tick marks shows the peak positions of $NaLaTi_2O_6$ and $NaBiTi_2O_6$

The trend in lattice parameters obtained from the Pawley refinement (Fig. 3.32) showed a linear increase in the cell volume with increasing Bi concentration. The *a* lattice parameter also increased linearly but the *c* lattice parameter decreased as more Bi is added. The variation in the lattice parameter showed that Bi was successfully incorporated into the structure.

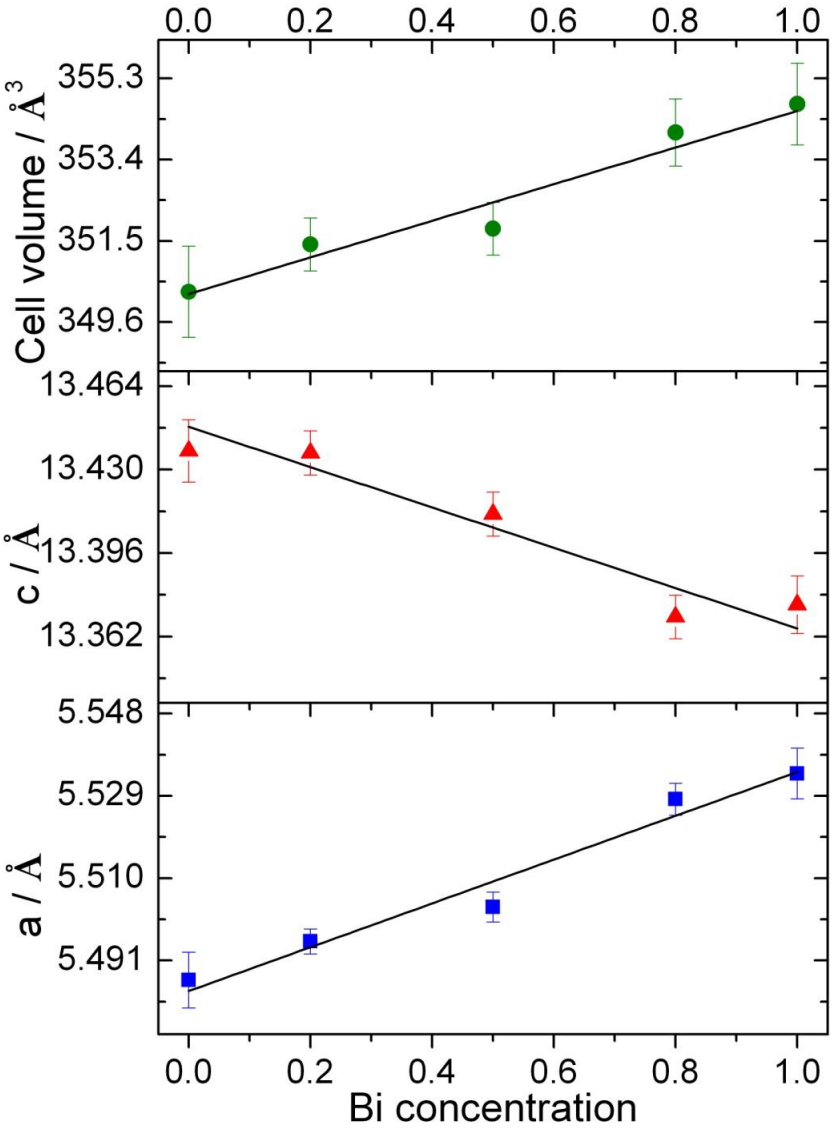

Fig. 3.32 Trend of the lattice parameters and cell volume of $NaBi_xLa_{1-x}Ti_2O_6$ series

The Raman spectra of the $NaBi_xLa_{1-x}Ti_2O_6$ series (Fig. 3.33) are also similar to that of $NaCe_xLa_{1-x}Ti_2O_6$ with broad bands observed at around 150, 250, 550 and 850 cm^{-1}. The band at 450 cm^{-1}, remained up to x = 0.2 and disappeared at higher Bi concentration. The band at 250 cm^{-1} became sharper and shifted to higher values. A similar trend was observed for $NaBi_xCe_{1-x}Ti_2O_6$ so it is quite likely that this band is related to a change in space group from $R\bar{3}c$ to $R3c$. The Raman spectrum of

$NaBiTi_2O_6$ agrees well with the spectrum reported in the literature[38-39] and was much better than the one in Fig. 3.29, as no impurity peaks was observed.

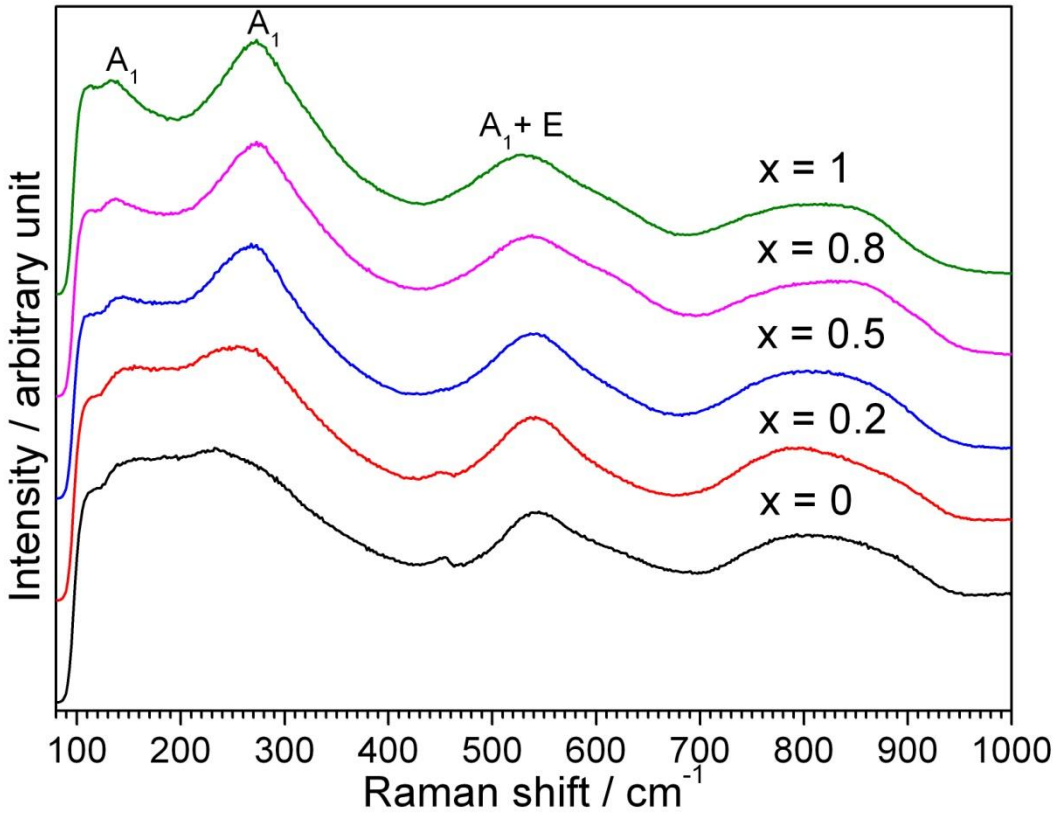

Fig. 3.33 Raman of $NaBi_xLa_{1-x}Ti_2O_6$, where the Raman spectra of $NaLaTi_2O_6$ and $NaBiTi_2O_6$ agrees well with the spectra reported in the literature

The SEM images of the as-prepared $NaBi_xLa_{1-x}Ti_2O_6$ are shown in Fig. 3.34. The particles also have irregular shaped particles and the morphology does not change very much with Bi concentration. No rod-like particles observed for $NaBiTi_2O_6$ confirming the purity of the material.

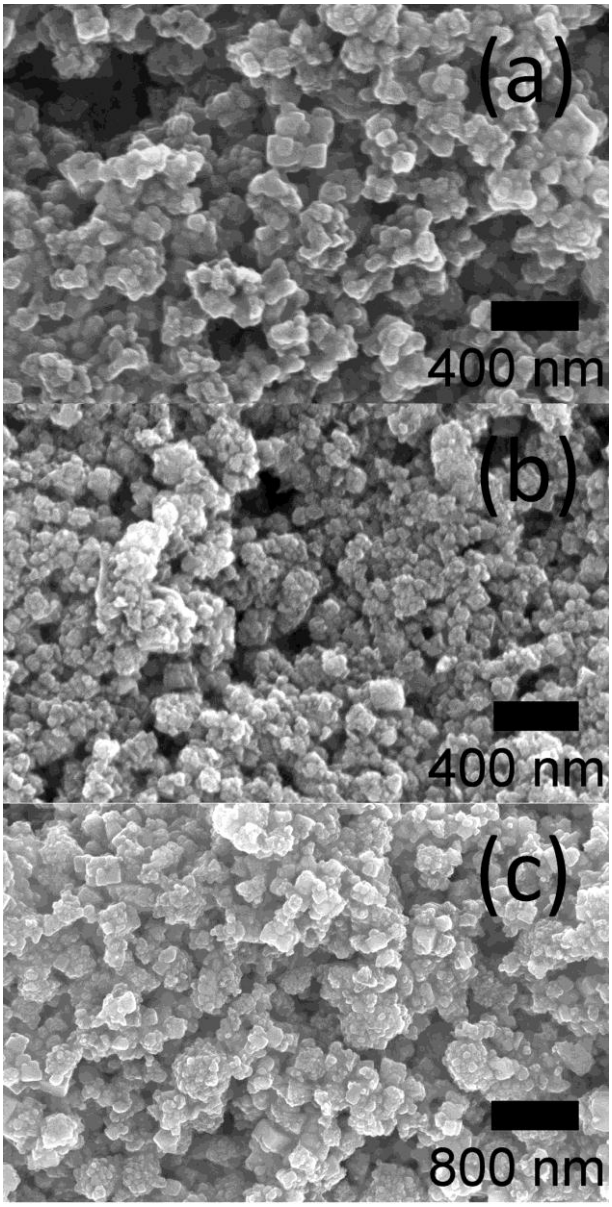

Fig. 3.34 SEM images of $NaBi_xLa_{1-x}Ti_2O_6$ a) x = 0, b) x = 0.5 and c) x = 1

3.8 Hydrothermal reactions of other A-site substituted perovskites

Other reactions were also carried out to attempt to synthesise perovskites hydrothermally. Table 3.13 below lists the reactions performed. Reactions where the NaOH was replaced with KOH and LiOH also did not give any perovskite products. However, perovskite $NaHoTi_2O_6$ was successfully prepared hydrothermally based on the $NaCeTi_2O_6$ reactions, where the $CeCl_3.7H_2O$ was replaced with $Ho(NO_3)_3{\cdot}5H_2O$. The reaction yielded a pink powder which changed to yellow depending on the lighting conditions.

Table 3.13 Hydrothermal reactions undertaken for other A-site substituted perovskites

Target material	Starting reagents	Conditions	XRD Results
$K(Bi_{0.5}Ce_{0.5})Ti_2O_6$	$Bi(NO_3)_3.5H_2O$ + $CeCl_3.7H_2O$ + TiBALD + KOH (aq)	240 ^oC / 24 hours	Broad peak at 28-34^o
$Li(Bi_{0.5}Ce_{0.5})Ti_2O_6$	$Bi(NO_3)_3.5H_2O$ + $CeCl_3.7H_2O$ + TiBALD + LiOH (aq)		CeO_2 + unknown peaks at 27.2^o and 31.8^o
$NaHoTi_2O_6$	$Ho(NO_3)_3.5H_2O$ + TiF_3 + NaOH (aq)		$NaHoTi_2O_6$

3.9 Conclusion

This chapter has shown that a reproducible synthesis route to complex perovskites with up to three different A-site cations can be achieved hydrothermally. From XRD and neutron diffraction data, the $NaCe_{1-x}La_xTi_2O_6$ series are assigned the $R\bar{3}c$ space group and the lattice parameter show a linear increase with increasing La concentration. The particle size and morphology was reduced by using ethylene glycol and increased when the NaOH concentration was increased. ^{23}Na NMR gives a novel way of confirming that the materials produced are a genuine solid solution

by studying the effect of paramagnetic Ce^{3+} and A-site disorder on the chemical shift and linewidth. While ^{2}H NMR showed that D_2O or OD^{-} is present in the perovskite lattice and $NaCeTi_2O_6$ contains a significantly greater amount of these defects than $NaLaTi_2O_6$. XANES showed that some of the Ce^{3+} in all the materials was oxidised to Ce^{4+} and this may provide a possible means of balancing the charge of A-site defects.

3.10 References

(1) Saito, Y.; Takao, H.; Tani, T.; Nonoyama, T.; Takatori, K.; Homma, T.; Nagaya, T.; Nakamura, M. *Nature* **2004**, *432*, 84.

(2) Takenaka, T.; Maruyama, K.; Sakata, K. *Jpn. J. Appl. Phys. Part 1* **1991**, *30*, 2236.

(3) Chu, B. J.; Chen, D. R.; Li, G. R.; Yin, Q. R. *J. Eur. Ceram. Soc.* **2002**, *22*, 2115.

(4) Wang, X. X.; Tang, X. G.; Chan, H. L. W. *Appl. Phys. Lett.* **2004**, *85*, 91.

(5) Elkechai, O.; Manier, M.; Mercurio, J. P. *Phys. Status Solidi A* **1996**, *157*, 499.

(6) Said, S.; Mercurio, J. P. *J. Eur. Ceram. Soc.* **2001**, *21*, 1333.

(7) Lencka, M. M.; Oledzka, M.; Riman, R. E. *Chem. Mater.* **2000**, *12*, 1323.

(8) Jing, X. Z.; Li, Y. X.; Yin, Q. G. *Mater. Sci. Eng. B* **2003**, *99*, 506.

(9) Setinc, T.; Spreitzer, M.; Logar, M.; Suvorov, D. *J. Am. Ceram. Soc.* **2011**, *94*, 3793.

(10) Liu, J. B.; Wang, H.; Hou, Y. D.; Zhu, M. K.; Yan, H.; Yoshimura, M. *Nanotechnology* **2004**, *15*, 777.

(11) Sardar, K.; Walton, R. I. *J. Solid State Chem.* **2012**, *189*, 32.

(12) Jones, G. O.; Thomas, P. A. *Acta Crystallogr. Sect. B-Struct. Commun.* **2002**, *58*, 168.

(13) Ranjan, R.; Dviwedi, A. *Solid State Commun.* **2005**, *135*, 394.

(14) Gorfman, S.; Thomas, P. A. *J. Appl. Crystallogr.* **2010**, *43*, 1409.

(15) Aksel, E.; Forrester, J. S.; Jones, J. L.; Thomas, P. A.; Page, K.; Suchomel, M. R. *Appl. Phys. Lett.* **2011**, *98*, 3.

(16) Siny, I. G.; Tu, C. S.; Schmidt, V. H. *Phys. Rev. B* **1995**, *51*, 5659.

(17) Zvirgzds, J. A.; Kapostins, P. P.; Zvirgzde, J. V.; Kruzina, T. V. *Ferroelectrics* **1982**, *40*, 75.

(18) Dorcet, V.; Trolliard, G.; Boullay, P. *Chem. Mater.* **2008**, *20*, 5061.

(19) Jones, G. O.; Thomas, P. A. *Acta Crystallogr. Sect. B-Struct. Commun.* **2000**, *56*, 426.

(20) Vakhrushev, S. B.; Isupov, V. A.; Kvyatkovsky, B. E.; Okuneva, N. M.; Pronin, I. P.; Smolensky, G. A.; Syrnikov, P. P. *Ferroelectrics* **1985**, *63*, 153.

(21) Mitchell, R. H.; Chakhmouradian, A. R. *J. Solid State Chem.* **1998**, *138*, 307.

(22) Ranjan, R.; Senyshyn, A.; Boysen, H.; Baehtz, C.; Frey, F. *J. Solid State Chem.* **2007**, *180*, 995.

(23) Shi, J. W.; Ye, J. H.; Zhou, Z. H.; Li, M. T.; Guo, L. J. *Chem. Eur. J.* **2011**, *17*, 7858.

(24) Inaguma, Y.; Sohn, J. H.; Kim, I. S.; Itoh, M.; Nakamura, T. *J. Phys. Soc. Jpn.* **1992**, *61*, 3831.

(25) Li, Y.; Qin, S.; Seifert, F. *J. Solid State Chem.* **2007**, *180*, 824.

(26) Garg, R.; Senyshyn, A.; Boysen, H.; Ranjan, R. *J. Phys.-Condes. Matter* **2008**, *20*, 6.

(27) Sun, P. H.; Nakamura, T.; Shan, Y. J.; Inaguma, Y.; Itoh, M. *Ferroelectrics* **1997**, *200*, 93.

(28) Knapp, M. C.; Woodward, P. M. *J. Solid State Chem.* **2006**, *179*, 1076.

(29) Wright, C. S.; Walton, R. I.; Thompsett, D.; Fisher, J. *Inorg. Chem.* **2004**, *43*, 2189.

(30) Chakhmouradian, A. R.; Mitchell, R. H.; Pankov, A. V.; Chukanov, N. V. *Mineral. Mag.* **1999**, *63*, 519.

(31) Shannon, R. D. *Acta Crystallogr. Sect. A* **1976**, *32*, 751.

(32) Abramov, Y. A.; Tsirelson, V. G.; Zavodnik, V. E.; Ivanov, S. A.; Brown, I. D. *Acta Crystallogr. Sect. B-Struct. Commun.* **1995**, *51*, 942.

(33) Buttner, R. H.; Maslen, E. N. *Acta Crystallogr. Sect. B-Struct. Commun.* **1992**, *48*, 764.

(34) Shahzad, K.; Khan, M. N.; Bashir, J. *Ferroelectrics* **2011**, *414*, 162.

(35) Sanjuan, M. L.; Laguna, M. A.; Belous, A. G.; V'Yunov, O. I. *Chem. Mater.* **2005**, *17*, 5862.

(36) Zhang, W. F.; Zhang, X. T.; Guo, H.; Fang, J. L.; Zhang, M. S. *Chem. J. Chin. U.* **1999**, *20*, 515.

(37) Trujillo, S.; Kreisel, J.; Jiang, Q.; Smith, J. H.; Thomas, P. A.; Bouvier, P.; Weiss, F. *J. Phys.-Condes. Matter* **2005**, *17*, 6587.

(38) Kreisel, J.; Glazer, A. M.; Jones, G.; Thomas, P. A.; Abello, L.; Lucazeau, G. *J. Phys.-Condes. Matter* **2000**, *12*, 3267.

(39) Kreisel, J.; Glazer, A. M.; Bouvier, P.; Lucazeau, G. *Phys. Rev. B* **2001**, *63*.

(40) Sanjuan, M. L.; Orera, V. M.; Merino, R. I.; Blasco, J. *J. Phys.-Condes. Matter* **1998**, *10*, 11687.

(41) Inagaki, T.; Miura, K.; Yoshida, H.; Fujita, J.; Nishimura, M. *Solid State Ionics* **1999**, *118*, 265.

(42) Selvamani, R.; Singh, G.; Sathe, V.; Tiwari, V. S.; Gupta, P. K. *J. Phys.-Condes. Matter* **2011**, *23*.

(43) Noma, T.; Wada, S.; Yano, M.; Suzuki, T. *J. Appl. Phys.* **1996**, *80*, 5223.

(44) Shiratori, Y.; Pithan, C.; Dornseiffer, J.; Waser, R. *J. Raman Spectrosc.* **2007**, *38*, 1288.

(45) Dunne, P. W.; Carnerup, A. M.; Wegrzyn, A.; Witkowski, S.; Walton, R. I. *J. Phys. Chem. C.* **2012**, *116*, 13435.

(46) Takahashi, Y.; Sakami, H.; Nomura, M. *Anal. Chim. Acta* **2002**, *468*, 345.

(47) Skanthakumar, S.; Soderholm, L. *Phys. Rev. B* **1996**, *53*, 920.

(48) Feteira, A.; Sinclair, D. C.; Lanagan, M. T. *J. Appl. Phys.* **2007**, *101*, 7.

(49) Ashbrook, S. E.; Le Polles, L.; Gautier, R.; Pickard, C. J.; Walton, R. I. *Phys. Chem. Chem. Phys.* **2006**, *8*, 3423.

(50) Aleksandrova, I. P.; Sukhovsky, A. A.; Ivanov, Y. N.; Yablonskaya, Y. E.; Vakhrushev, S. B. *Ferroelectrics* **2009**, *378*, 16.

(51) Kotecha, M.; Chaudhuri, S.; Grey, C. P.; Frydman, L. *J. Am. Chem. Soc.* **2005**, *127*, 16701.

(52) Goh, G. K. L.; Lange, F. F.; Haile, S. M.; Levi, C. G. *J. Mater. Res.* **2003**, *18*, 338.

(53) Chien, A. T.; Xu, X.; Kim, J. H.; Sachleben, J.; Speck, J. S.; Lange, F. F. *J. Mater. Res.* **1999**, *14*, 3330.

(54) Jiang, H.; Kumada, N.; Yonesaki, Y.; Takei, T.; Kinomura, N.; Yashima, M.; Azuma, M.; Oka, K.; Shimakawa, Y. *Jpn. J. Appl. Phys.* **2009**, *48*.

(55) Busca, G.; Buscaglia, V.; Leoni, M.; Nanni, P. *Chem. Mater.* **1994**, *6*, 955.

(56) Hwang, U. Y.; Park, H. S.; Koo, K. K. *J. Am. Ceram. Soc.* **2004**, *87*, 2168.

(57) Goh, G. K. L.; Haile, S. M.; Levi, C. G.; Lange, F. F. *J. Mater. Res.* **2002**, *17*, 3168.

(58) Shi, E. W.; Xia, C. T.; Zhong, W. Z.; Wang, B. G.; Feng, C. D. *J. Am. Ceram. Soc.* **1997**, *80*, 1567.

(59) Simoes, A. Z.; Moura, F.; Onofre, T. B.; Ramirez, M. A.; Varela, J. A.; Longo, E. *J. Alloy. Compd.* **2010**, *508*, 620.

(60) Kim, C. Y.; Sekino, T.; Niihara, K. *J. Am. Ceram. Soc.* **2003**, *86*, 1464.

(61) Patil, S.; Shah, N.; Blum, F. D.; Rahaman, M. N. *Ceram. Trans.* **2003**, *150*, 79.

(62) Ma, Y. J.; Cho, J. H.; Lee, Y. H.; Kim, B. I. *Mater. Chem. Phys.* **2006**, *98*, 5.

(63) Cho, J. H.; Ma, Y. J.; Lee, Y. H.; Chun, M. P.; Kim, B. I. *J. Ceram. Process. Res.* **2006**, *7*, 91.

Chapter 4 – Hydrothermal Synthesis and Characterisation of B-site Substituted Perovskites

4.1 Background

B-site substitution is possible for perovskite titanates where the Ti can be replaced by other metal cations such as Zr^{4+}, [1-10] Cr^{3+} [11-13] and V^{4+}.[14] The incorporation of these metal cations can induce a phase transition, for example, in $PbZr_{1-x}Ti_xO_3$ (PZT), a tetragonal to rhombohedral phase transition is observed upon incorporation of Zr into $PbTiO_3$. PZT is commonly used close to the morphotropic phase boundary (x = 0.48). At the morphotropic phase boundary, the properties of PZT such as piezoelectric coefficients, dielectric permittivity and remnant polarisation are maximised.[15-16] Studies on doping Zr into $NaBiTi_2O_6$ have also been reported. Rachakom *et al.* prepared $NaBi(Ti_{1-x}Zr_x)_2O_6$, in the compositional range of $0.2 \leq x \leq 0.8$, where they observed a phase transition from rhombohedral to orthorhombic on addition of Zr.[17] Barick *et al.* prepared $NaBi(Ti_{1-x}Zr_x)_2O_6$ for $0 \leq x \leq 0.3$ and observed a reduction in the dielectric constant upon Zr incorporation. Rao *et al.* synthesised $NaBiTi_2O_6$ doped with Ba on the A-site and Zr on the B-site.[18] All of these studies used conventional solid-state synthesis to prepare their samples, which requires heating the samples at high temperature. Currently, there are no reports on the hydrothermal synthesis of $NaBi(Ti_{1-x}Zr_x)_2O_6$. There are also no reports on the synthesis of $NaLa(Ti_{1-x}Zr_x)_2O_6$ although there are reports on synthesis of the end members, $NaLaTi_2O_6$ and $NaLaZr_2O_6$. In both materials, the synthesis of the Ti

end member, $NaLaTi_2O_6$ and $NaBiTi_2O_6$, via hydrothermal methods have been described in the previous chapter but the synthesis of the Zr end member, $NaLaZr_2O_6$ and $NaBiZr_2O_6$ has only been done at high temperatures.[19-21]

In this chapter, the hydrothermal synthesis of perovskites with B-site substitution is described, specifically $NaLa(Ti_{1-x}Zr_x)_2O_6$ and $NaBi(Ti_{1-x}Zr_x)_2O_6$, where the Ti is substituted by Zr. The objective was to determine the feasibility of substituting Ti with Zr via hydrothermal synthesis and explore the possibility of increasing structural distortion to induce a phase transition that could change their electronic properties. Since $NaBiTi_2O_6$ is known for its ferroelectric properties, the effect of Zr on these properties was investigated. $NaLaTi_2O_6$ is not reported to have any ferroelectric properties so it was interesting to investigate whether the addition of Zr could give rise to those properties by increasing structural distortion.

4.2 Hydrothermal synthesis of $NaLa(Ti_{1-x}Zr_x)_2O_6$

Hydrothermal syntheses of the samples were performed using ~20 mL Teflon-lined stainless steel autoclaves. Stoichiometric amounts of $LaCl_3 \cdot 7H_2O$ (Alfa, 99%), TiF_3 (Alfa, 98%) and $ZrOCl_2 \cdot 8H_2O$ (Sigma Aldrich, 99.5%) were weighed according to the values shown in Table 4.1. The reagents were then mixed in 5 mL deionised water for 5 min in a Teflon liner. Then, 5 mL of NaOH solution was added and stirred so that the final NaOH concentration was 4 M. The reaction mixture was then stirred for 1 hour before it was sealed in a steel autoclave and placed in an oven pre-heated to 240 ^oC. After heating for 24 hours, the autoclaves were left to cool to room temperature. The solid products were recovered by suction filtration, washed

thoroughly with warm water and dried overnight at 70 ^{o}C in a drying oven. The products were then ground into powders for further characterisation.

Table 4.1 Amounts measured for $NaLa(Ti_{1-x}Zr_x)_2O_6$ synthesis

Zr conc., x	$LaCl_3 \cdot 7H_2O$/g	$ZrOCl_2 \cdot 8H_2O$/g	TiF_3/g	NaOH(aq)/mL	H_2O/mL
0	0.3714	-	0.2622	5	5
0.1		0.0644	0.1888		
0.2		0.1289	0.1678		
0.3		0.1934	0.1468		
0.4		0.2578	0.1259		
0.5		0.3222	0.1049		

All the reactions gave a white powder for the Zr concentration range $0 \leq x \leq 0.5$. Powder XRD of $NaLa(Ti_{1-x}Zr_x)_2O_6$ shown in Fig. 4.1, indicated that all the samples have the perovskite structure. The peaks in the XRD pattern gradually shift to lower 2θ values upon increasing Zr concentration. This indicates that Zr was incorporated into the structure and increases the cell volume, since the ionic radius of Zr^{4+} (0.72 Å, 6 coordination) is bigger than Ti^{4+} (0.605 Å, 6 coordination).[22] However, the samples with Zr content between $0.2 \leq x \leq 0.4$ show peak splitting, with $x = 0.3$ being the most noticeable. On the other hand, the peak splitting seems to disappear in $x = 0.5$ although the peaks remain asymmetric, with a tailing at the side with higher 2θ for each peak. Peak splitting may indicate a phase transition to lower symmetry but it is also possible that a second phase with a similar unit cell may be present. This second phase may have slightly different lattice parameters from the $NaLa(Ti_{1-x}Zr_x)_2O_6$ phase hence the peak positions are close to each other. For example, the two phases may be perovskites containing different amounts of Zr and Ti, where one may be Zr-rich and the other is Ti-rich, instead of forming a homogeneous single phase.

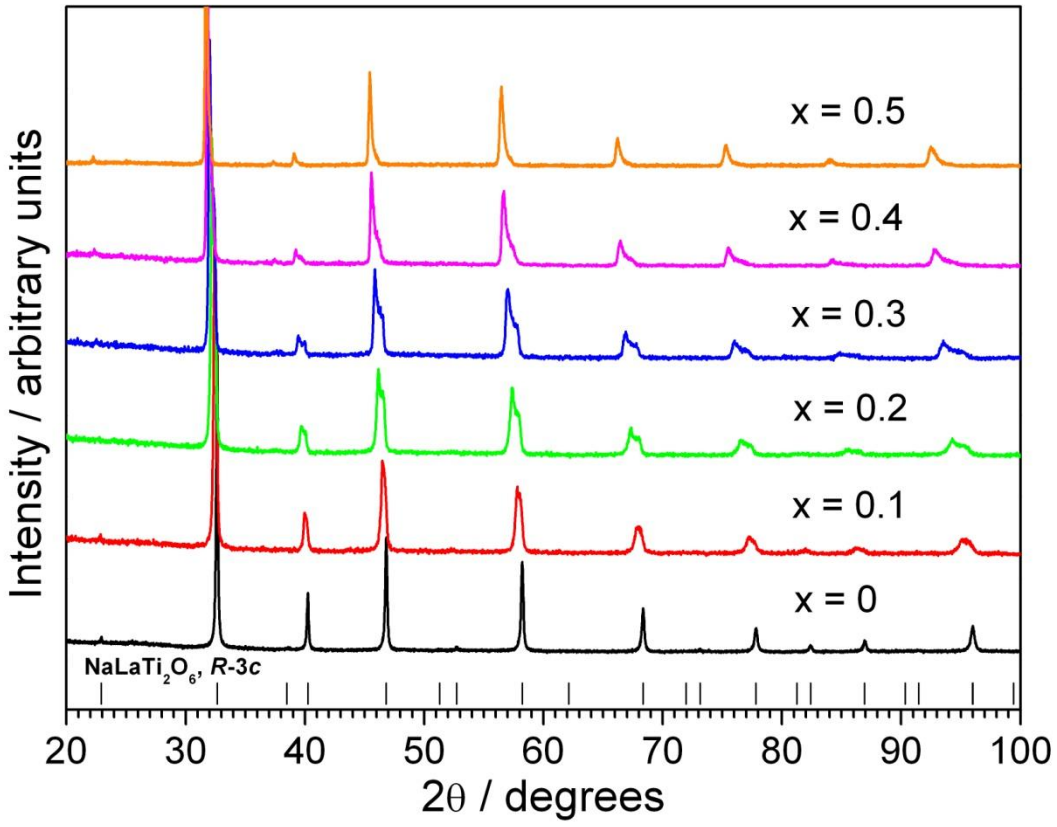

Fig. 4.1 Powder XRD of $NaLa(Ti_{1-x}Zr_x)_2O_6$, where the tick marks correspond to $NaLaTi_2O_6$ with space group $R\bar{3}c$

Pawley refinement was carried out on the XRD patterns of x = 0 and 0.1 with the $R\bar{3}c$ model (Fig. 4.2) and the fit agrees well with the observed pattern. However, when the XRD patterns of the x = 0.3 (Fig. 4.3) and x = 0.5 (Fig. 4.4) sample were refined with the $R\bar{3}c$ or *Pnma* models, the peak splitting or peak asymmetry were not fitted properly. The Pawley fit for both patterns were significantly improved when two $R\bar{3}c$ unit cells were used instead. This provides more evidence that two phases may be present. The summary of the refinements are shown in Table 4.2.

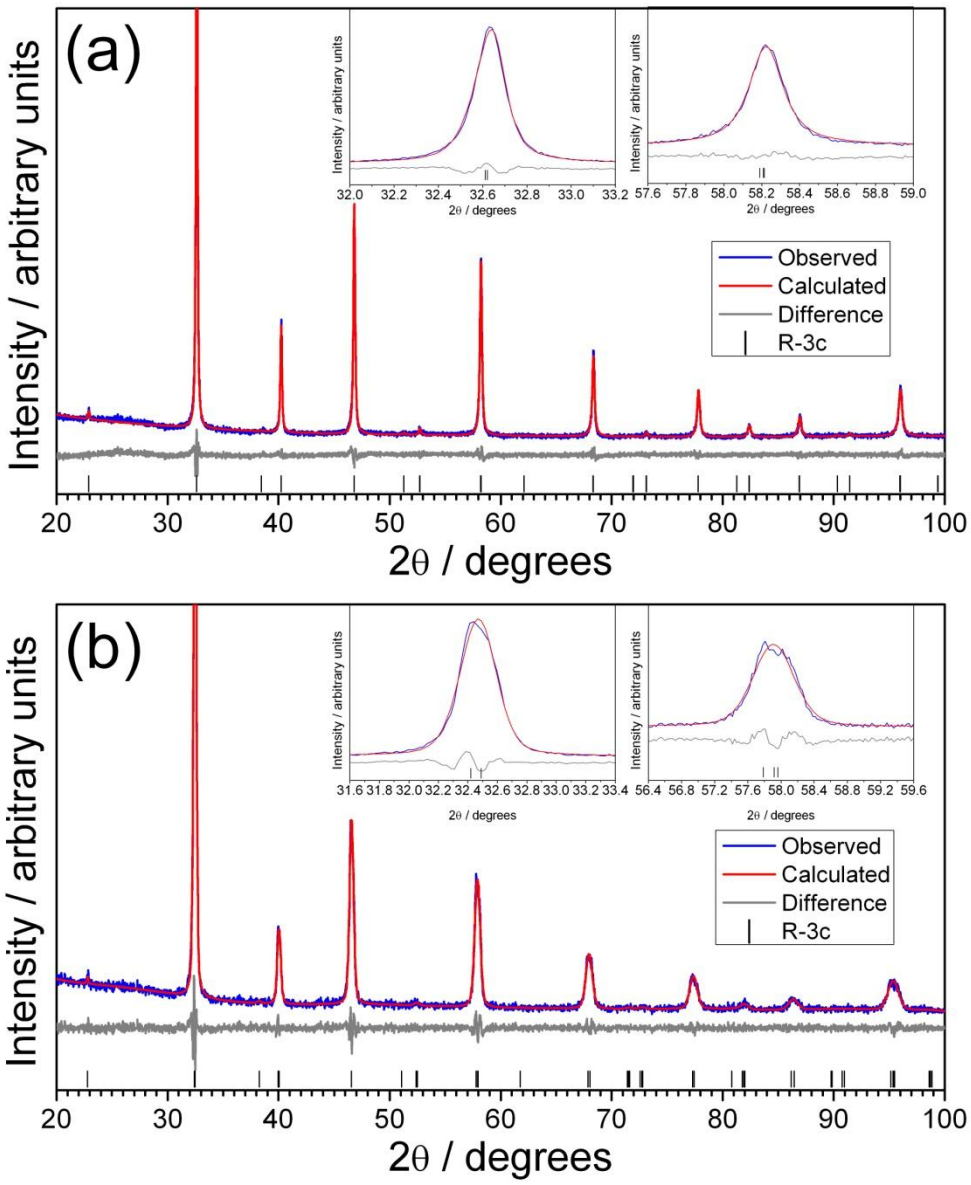

Fig. 4.2 XRD of $NaLa(Ti_{1-x}Zr_x)_2O_6$, a) x = 0 and b) x = 0.1 refined with $R\bar{3}c$. The two insets show the fits for the peaks at 32.6° and 58.2°.

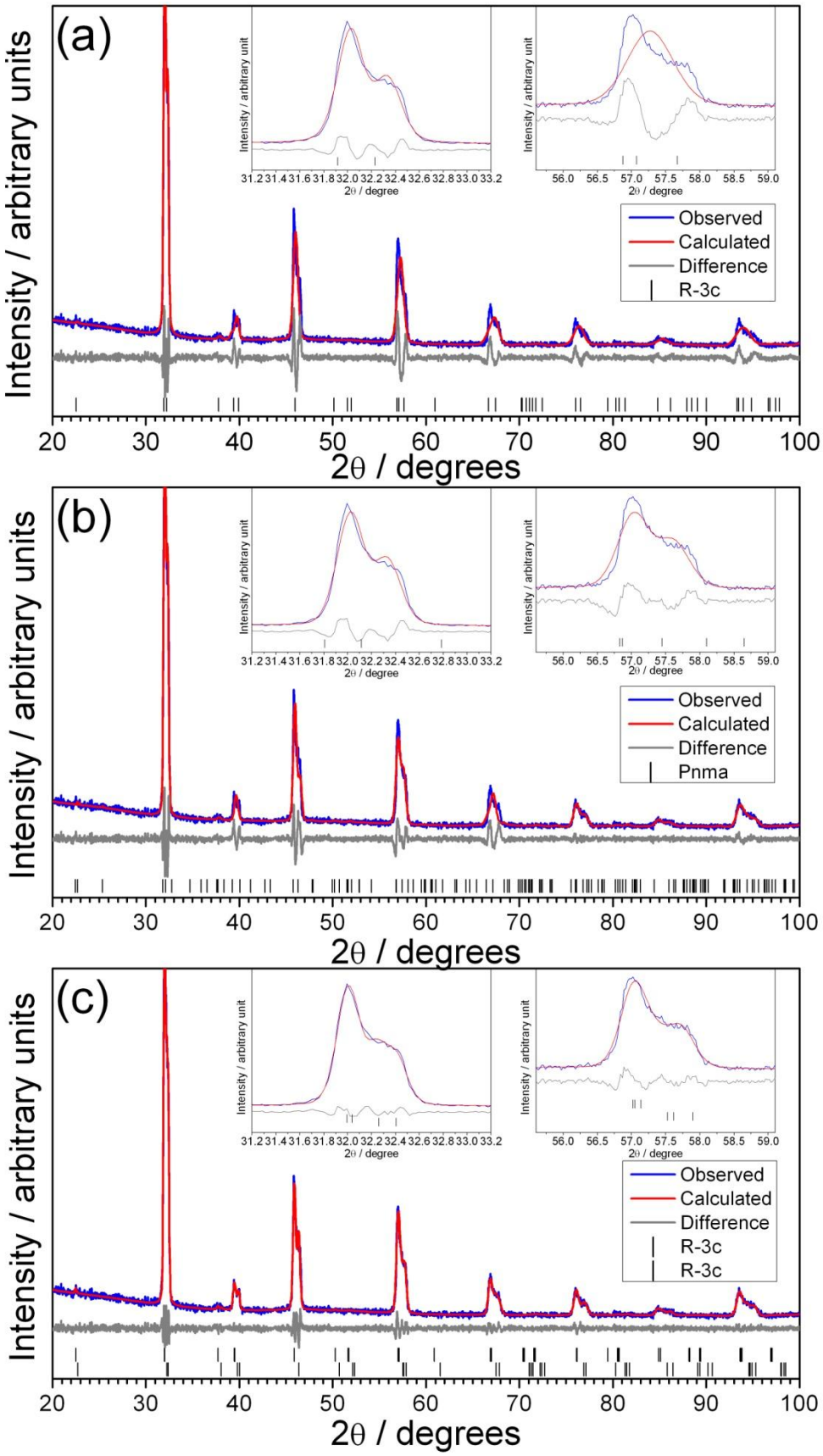

Fig. 4.3 XRD of the x = 0.3 sample, refined with a) $R\bar{3}c$, b) *Pnma* and c) two $R\bar{3}c$ model. The two insets show the fits for the peaks at 32° and 57°.

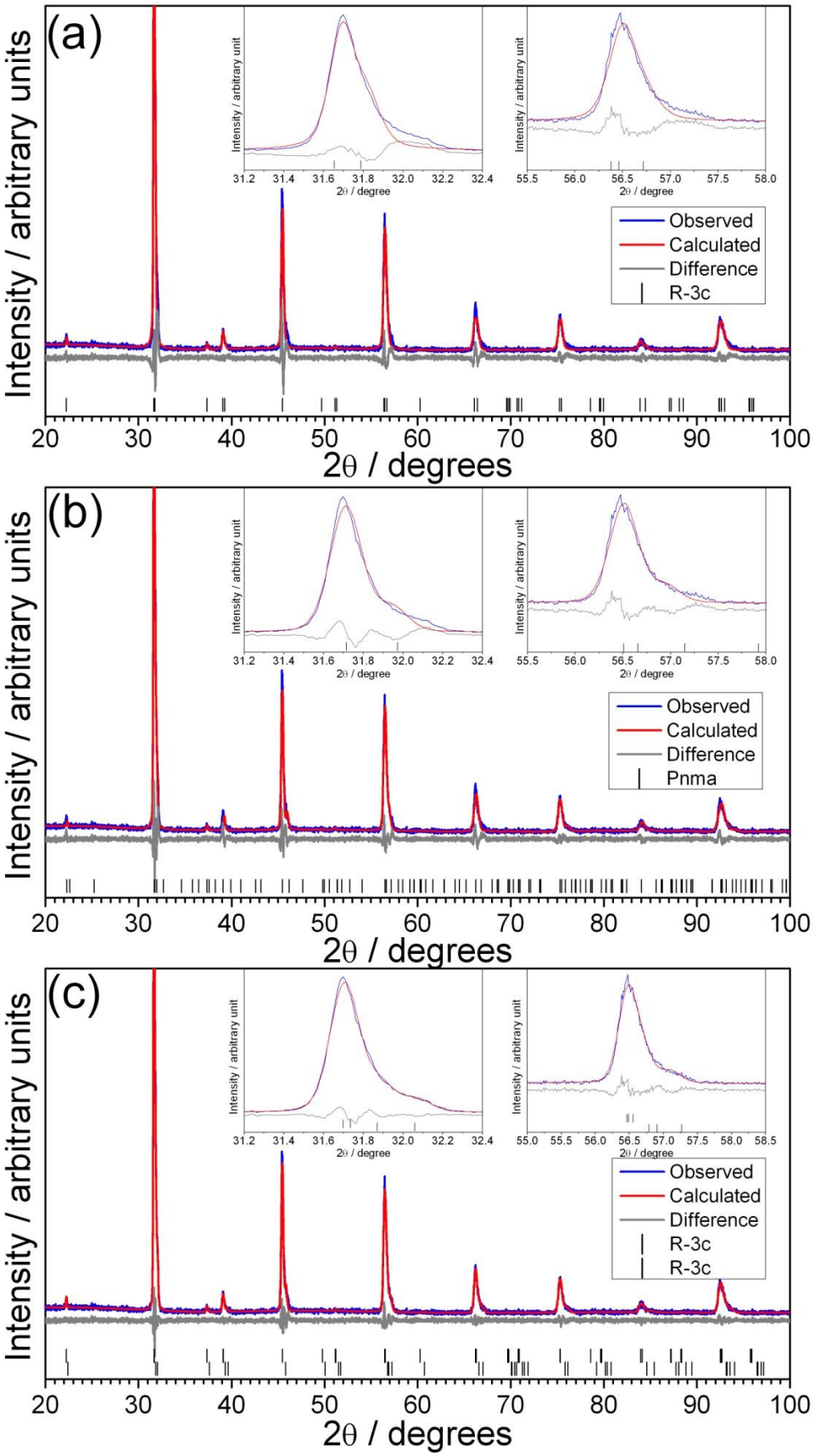

Fig. 4.4 XRD of the x = 0.5 sample, refined with a) $R\bar{3}c$, b) *Pnma* and c) two $R\bar{3}c$ model. The two insets show the fits for the peaks at 31.7° and 56.5°.

Table 4.2 Summary of Pawley refinement for $NaLa(Ti_{1-x}Zr_x)_2O_6$ refined using different space groups

(1) Sample	**x = 0**
Space group	$R\bar{3}c$
***a* (Å)**	**5.4856 (6)**
***b* (Å)**	**5.4856 (6)**
***c* (Å)**	**13.4419 (25)**
Cell volume (Å^3)	**350.295 (104)**
R_{wp}	**5.197**
R_p	**4.088**
Gof	**1.194**

(2) Sample	**x = 0.1**
Space group	$R\bar{3}c$
***a* (Å)**	**5.5075 (39)**
***b* (Å)**	**5.5075 (39)**
***c* (Å)**	**13.5321 (86)**
Cell volume (Å^3)	**355.472 (548)**
R_{wp}	**7.118**
R_p	**5.601**
Gof	**1.150**

(3) Sample	**x = 0.2**			
Space group	*Pnma*	$R\bar{3}c$	**TWO $R\bar{3}c$**	
***a* (Å)**	5.5599 (12)	5.5296 (89)	**5.5140 (40)**	**5.5603 (52)**
***b* (Å)**	7.7764 (37)	5.5296 (89)	**5.5140 (40)**	**5.5603 (52)**
***c* (Å)**	5.5144 (39)	13.6324 (221)	**13.5474 (99)**	**13.6328 (169)**
Cell volume (Å^3)	238.420 (211)	360.981 (1299)	**356.713 (578)**	**365.018 (817)**
R_{wp}	8.287	8.883	**6.117**	
R_p	6.257	6.750	**4.706**	
Gof	1.484	1.569	**1.088**	

(4) Sample	**x = 0.3**			
Space group	*Pnma*	$R\bar{3}c$	**TWO $R\bar{3}c$**	
***a* (Å)**	5.4598 (25)	5.6035 (54)	**5.5453 (19)**	**5.5902 (28)**
***b* (Å)**	7.9214 (38)	5.6035 (54)	**5.5453 (19)**	**5.5902 (28)**
***c* (Å)**	5.6223 (25)	13.5316 (132)	**13.4947 (51)**	**13.6650 (95)**
Cell volume (Å^3)	243.162 (194)	367.959 (793)	**359.378 (279)**	**369.829 (447)**
R_{wp}	10.626	11.560	**7.659**	
R_p	7.567	8.108	**5.952**	
Gof	1.656	1.777	**1.185**	

(5) Sample	**x = 0.4**			
Space group	*Pnma*	$R\bar{3}c$	**TWO $R\bar{3}c$**	
***a* (Å)**	5.4587 (11)	5.6190 (9)	**5.5856 (17)**	**5.6255 (21)**
***b* (Å)**	7.9447 (10)	5.6190 (9)	**5.5856 (17)**	**5.6255 (21)**
***c* (Å)**	5.6260 (6)	13.6019 (34)	**13.5557 (39)**	**13.7530 (89)**
Cell volume (Å^3)	243.988 (64)	371.919 (160)	**366.256 (246)**	**376.921 (379)**
R_{wp}	16.865	22.464	**13.270**	
R_p	12.206	16.089	**9.836**	
Gof	1.644	2.160	**1.285**	

(6) Sample	**x = 0.5**			
Space group	*Pnma*	$R\bar{3}c$	**TWO $R\bar{3}c$**	
***a* (Å)**	5.4707 (9)	5.6487 (6)	**5.6116 (9)**	**5.6409 (9)**
***b* (Å)**	7.9709 (14)	5.6487 (6)	**5.6116 (9)**	**5.6409 (9)**
***c* (Å)**	5.6383 (9)	13.7516 (15)	**13.6269 (22)**	**13.7949 (38)**
Cell volume (Å^3)	245.867 (72)	380.003 (88)	**371.624 (141)**	**380.142 (167)**
R_{wp}	12.198	14.663	**10.256**	
R_p	9.478	10.708	**7.945**	
Gof	1.296	1.545	**1.085**	

The trend of the lattice parameters for $NaLa(Ti_{1-x}Zr_x)_2O_6$ is shown in Fig. 4.5. The cell volume and lattice parameter *a* increased upon increasing Zr substitution. For the lattice parameter *c*, the values increased up to x = 0.2. At x = 0.3, the lattice parameter *c* for the first $R\bar{3}c$ drops while the second $R\bar{3}c$ increases. Beyond that, both values continue to increase.

Upon addition of Zr, the cell volume showed a general increase, even for the two phase samples ($0.2 \leq x \leq 0.5$). As mentioned earlier, the two phases may be perovskites containing different amounts of Zr and Ti, where one may be Zr-rich and the other is Ti-rich. However, it is also possible that there is variation on the A-site. So along with the 1:1 ratio of Na and La expected in these materials, another perovskite that is Na deficient such as $La_{2/3}TiO_3$ [23] may have been made. Other Na:La ratios are possible e.g. $Na_{0.2}La_{0.6}TiO_3$. So for example, when the x = 0.2 sample was prepared, instead of only the $NaLaTi_{0.8}Zr_{0.2}O_6$ being formed, a Na

deficient phase may have been made as well. In this model, the Zr:Ti ratio is as expected in both phases. This would explain why the cell volumes of both phases exhibit an almost linear increase with increasing Zr concentration.

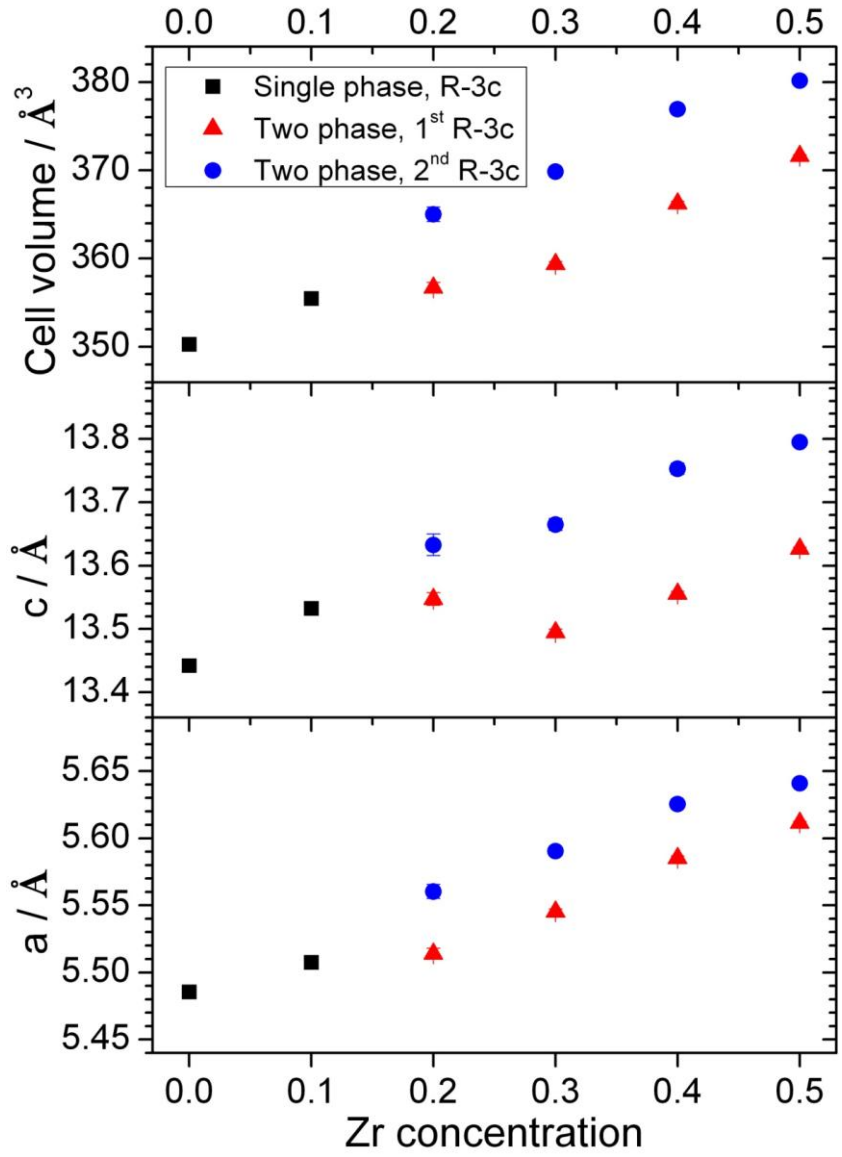

Fig. 4.5 Trend of the lattice parameters and cell volume of $NaLa(Ti_{1-x}Zr_x)_2O_6$ series

Reactions carried out for Zr concentration at x = 0.6 and above yields the perovskite structure (Fig. 4.6). However, other impurities were also present, in

particular, ZrO_2 and $La(OH)_3$. The end member $NaLaZr_2O_6$ was not obtained hydrothermally although its synthesis by ceramic method has been reported.[19]

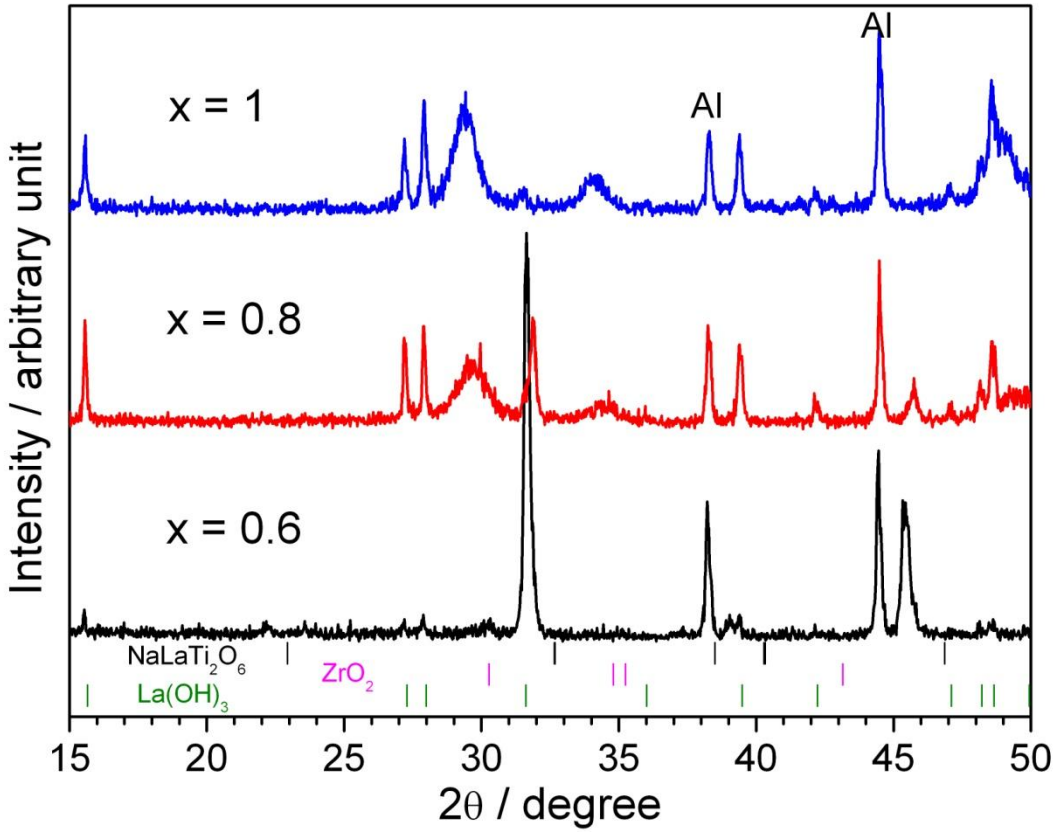

Fig. 4.6 XRD of $NaLa(Ti_{1-x}Zr_x)_2O_6$ for x = 0.6, 0.8 and 1, where the tick marks correspond to $NaLaTi_2O_6$, tetragonal ZrO_2 and $La(OH)_3$

The Raman spectra of $NaLa(Ti_{1-x}Zr_x)_2O_6$ (Fig. 4.7) are similar to those obtained for the $NaCe_{1-x}La_xTi_2O_6$ series in Chapter 3. The spectra showed four broad bands between 100 and 900 cm^{-1} with an extra band at around 450 cm^{-1}. This broadening may be due to the disorder on both the A-site and B-site and the overlapping of multiple Raman modes. The most prominent feature in the spectra is the change in the intensity of the 450 cm^{-1} band. As mentioned in the previous chapter, the intensity of this band has been correlated to the particle size of $NaLaTi_2O_6$ and the same effect may be observed for $NaLa(Ti_{1-x}Zr_x)_2O_6$ as well.

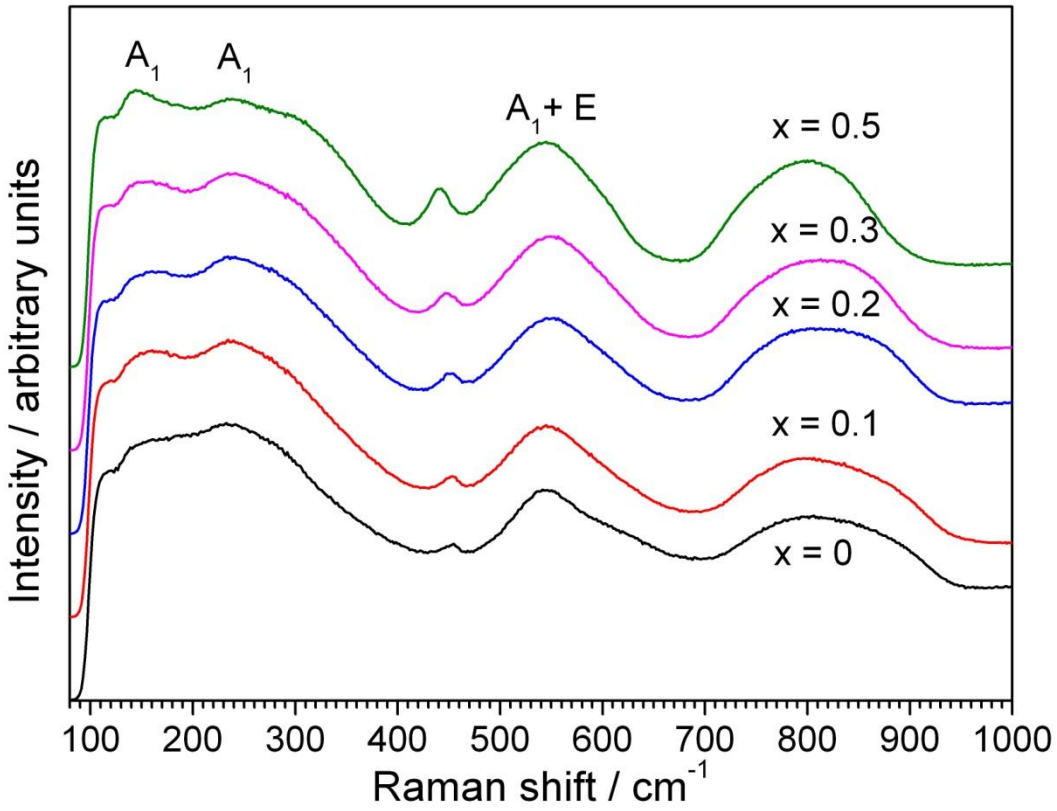

Fig. 4.7 Raman spectra of $NaLa(Ti_{1-x}Zr_x)_2O_6$ series

4.3 Control of Morphology

The $NaLa(Ti_{1-x}Zr_x)_2O_6$ series showed a drastic change in morphology with chemical composition as shown by the SEM images in Fig. 4.8. Undoped $NaLaTi_2O_6$ has irregularly shaped particles and the addition of Zr at x = 0.1 did not appear to affect the particle shape very much. But upon increasing the Zr content to x = 0.3, the particles became bigger and more cubic and at even higher Zr concentration, flower-shaped particles are formed. At x = 0.6, ZrO_2 impurities were observed in the XRD pattern and the "petals" of the flower-like particles became narrower. The SEM images show that the particle size increases with increasing Zr content which agrees with the Raman spectra in Fig. 4.7. The atomic composition of the materials

was also confirmed by EDXA and the values obtained match the expected values as shown in Table 4.3.

The flower-shaped morphology have also been observed by Chai *et al*. when they hydrothermally prepared $La_{0.5}Ba_{0.5}MnO_3$.[24] They proposed that the flower-like structure was formed via a nucleation-aggregation-crystallisation growth mechanism, where $La_{0.5}Ba_{0.5}MnO_3$ nanoparticles were first formed, which was then followed by a slow agglomeration and subsequent crystallisation.

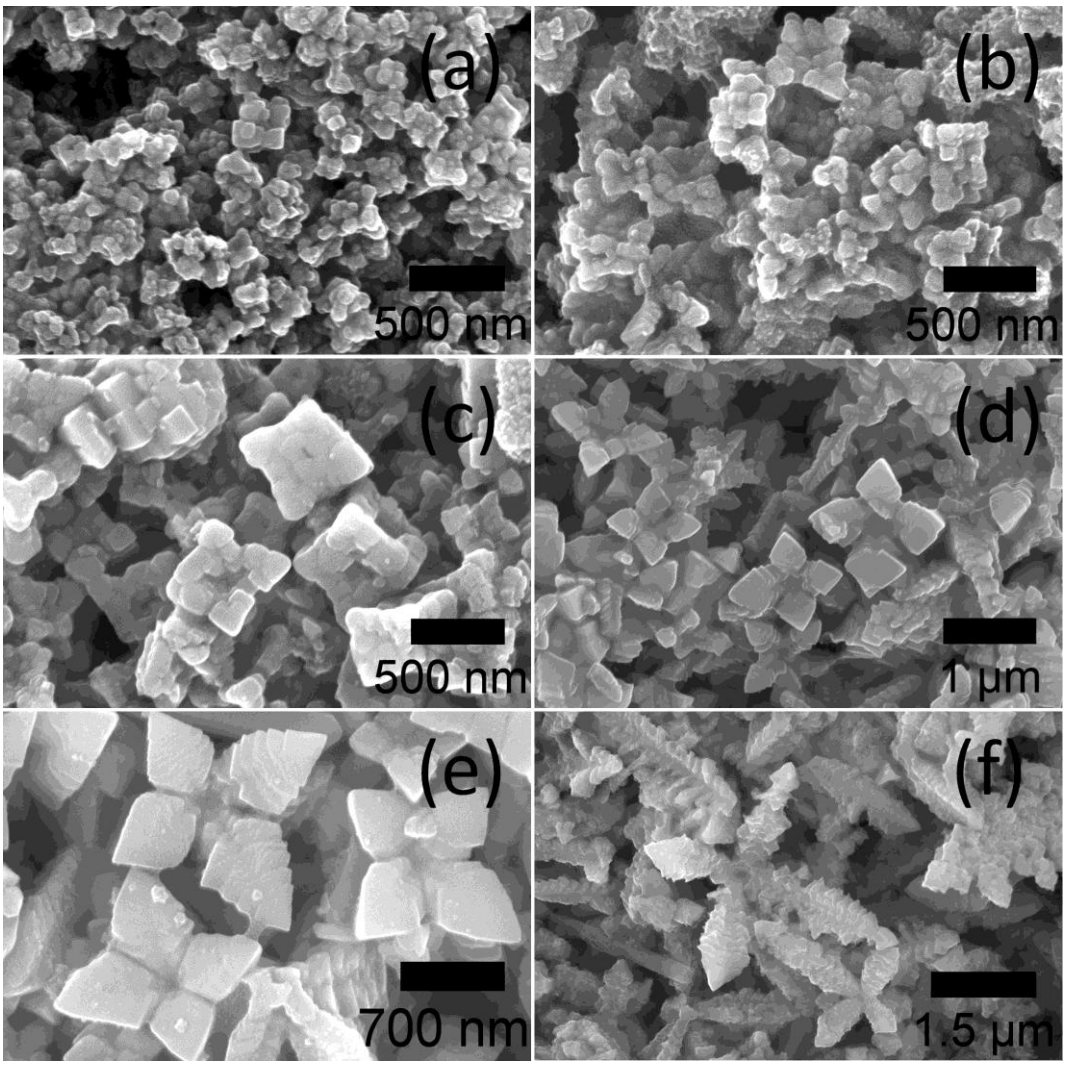

Fig. 4.8 SEM images of $NaLa(Ti_{1-x}Zr_x)_2O_6$ for a) x = 0, b) x = 0.1, c) x = 0.3, d) x = 0.4, e) x = 0.50 and f) x = 0.60

Table 4.3 Atomic composition of $NaLa(Ti_{1-x}Zr_x)_2O_6$ obtained from EDXA. Expected values from synthesis are in brackets. *Note: Zr concentration = [Zr / (Zr + Ti)]

Zr conc., x (Nominal value)	Na / %	La / %	Zr / %	Ti / %	Zr conc.*
0	11.2 (10)	12.2 (10)	-	26.4 (20)	0
0.1	12.3 (10)	10.2 (10)	1.8 (2)	17.1 (18)	0.10
0.2	12.0 (10)	9.1 (10)	4.4 (4)	14.8 (16)	0.23
0.3	12.1 (10)	9.4 (10)	6.2 (6)	12.5 (14)	0.33
0.4	11.4 (10)	11.2 (10)	8.8 (8)	12.9 (12)	0.41
0.5	13.1 (10)	10.7 (10)	10.2 (10)	10.1 (10)	0.50

The morphology of x = 0.5 sample can also be changed by increasing the NaOH concentration and by changing the solvent. By increasing the NaOH concentration from 4 M to 8 M, cubic particles were obtained (Fig. 4.9a). On the other hand, by using a mixture of H_2O and ethylene glycol as the solvent and 4 M NaOH, the particles became spherical (Fig. 4.9b).

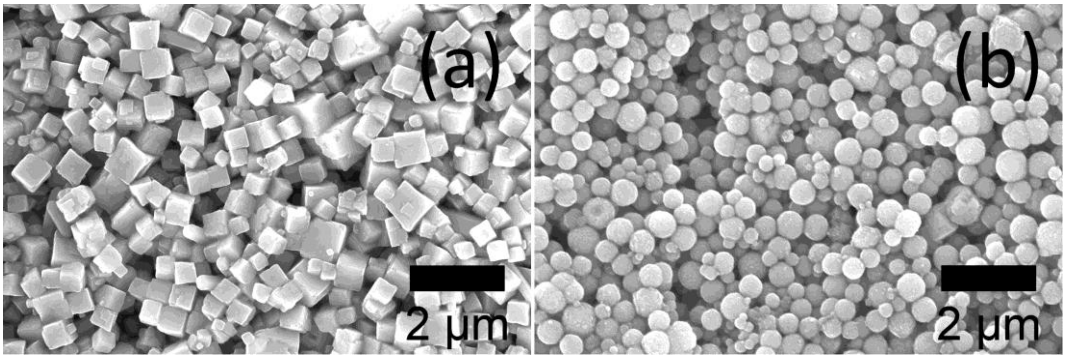

Fig. 4.9 SEM images of $NaLa(Ti_{0.5}Zr_{0.5})_2O_6$ in a) 8 M NaOH and b) mixture of H_2O and ethylene glycol

4.3.1 Effect of synthesis time

The x = 0.5 sample was also made at different heating periods to study the effect of synthesis time on the crystal morphology. Even after only 1 hour at 240 ^{o}C, the flower-shaped particles can already be observed although some regions were poorly formed (Fig. 4.10a-b). After 6 hours, the flower shape is properly formed. There is a variation in the sizes of the particles ranging from 500 nm to 2 μm (Fig. 4.10c-d). Longer reactions up to 7 days did not produce any significant change to the particle size or the size variation (Fig. 4.10e-f).

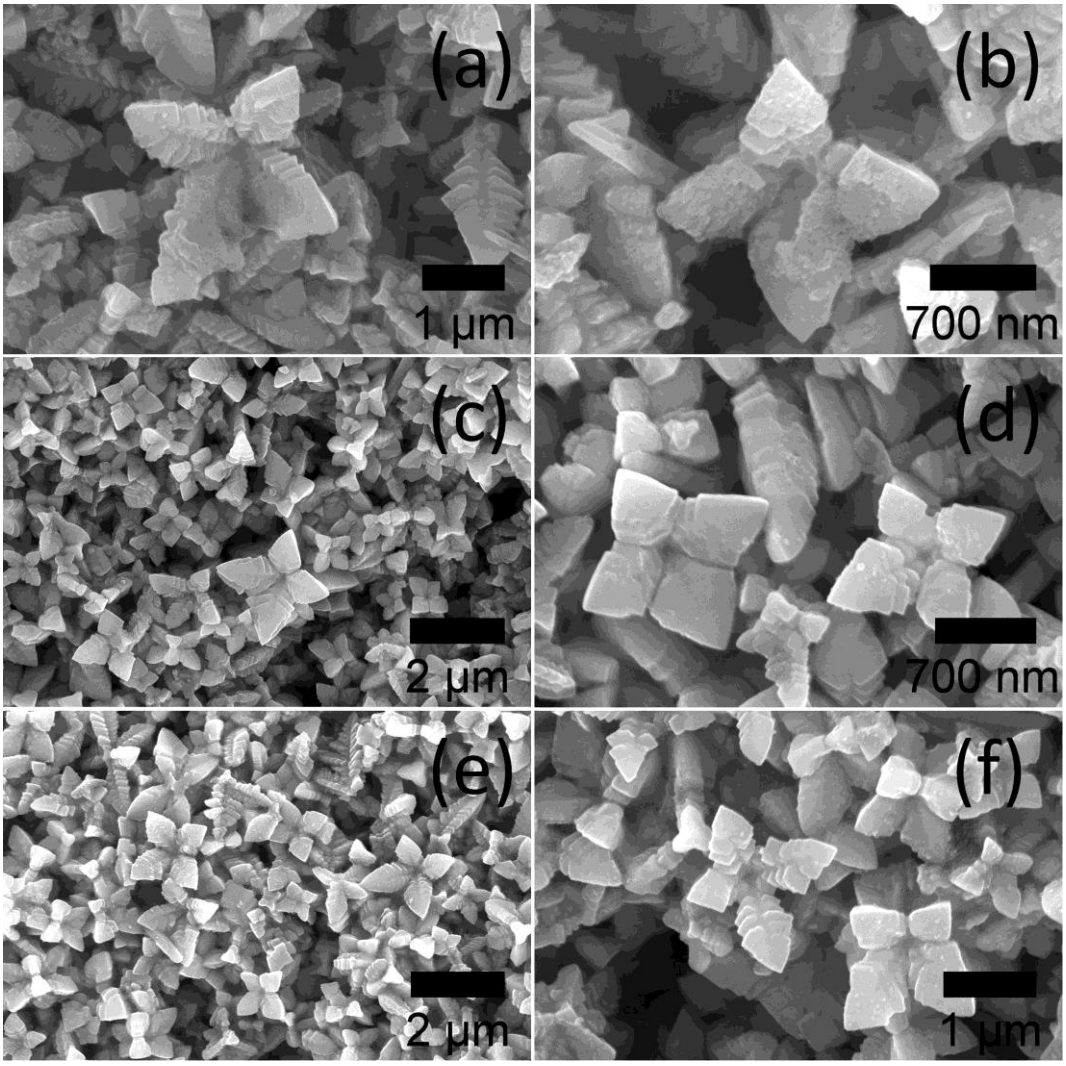

Fig. 4.10 SEM images of $NaLa(Ti_{0.5}Zr_{0.5})_2O_6$ prepared at 240 ^{o}C with different reaction times, (a)-(b) 1 hour, (c)-(d) 6 hours and (e)-(f) 7 days

4.3.2 Solvothermal reactions of $NaLa(Ti_{0.5}Zr_{0.5})_2O_6$

Solvothermal reactions with different solvents mixed with water were also carried out for x = 0.5 since it exhibits interesting morphology. When a 1:1 mixture of propanol-H_2O was used, the flower-shaped particles were not completely formed. Some particles are cube-shaped while others have four pointed corners which look like the early stages of the "petal" formation (Fig. 4.11a). While reactions carried out in 1:1 ethanolamine-H_2O mixture yielded irregular shaped particles with a small number of flowers formed (Fig. 4.11b). Reactions in 1:1 ethylene glycol-H_2O mixture with 8 M NaOH (Fig. 4.11c) gave spherical particles similar to Fig. 4.9b, although the particles obtained were smaller. This effect is in contrast to the hydrothermal reactions, where increasing the NaOH concentration resulted in bigger particles. When a 1:1 polyethylene glycol-H_2O mixture was used, cubic particles were formed instead (Fig. 4.11d). However, when a 3:7 polyethylene glycol-H_2O mixture was used, the higher H_2O content allowed the flower-shaped particles to form although there are still some cubic particles present in the sample as well (Fig. 4.11e). When the reactions were carried out in pure solvents, without the presence of H_2O, the perovskite phase was not obtained. This shows that the amount of H_2O is crucial in the formation of the flower-shaped particles.

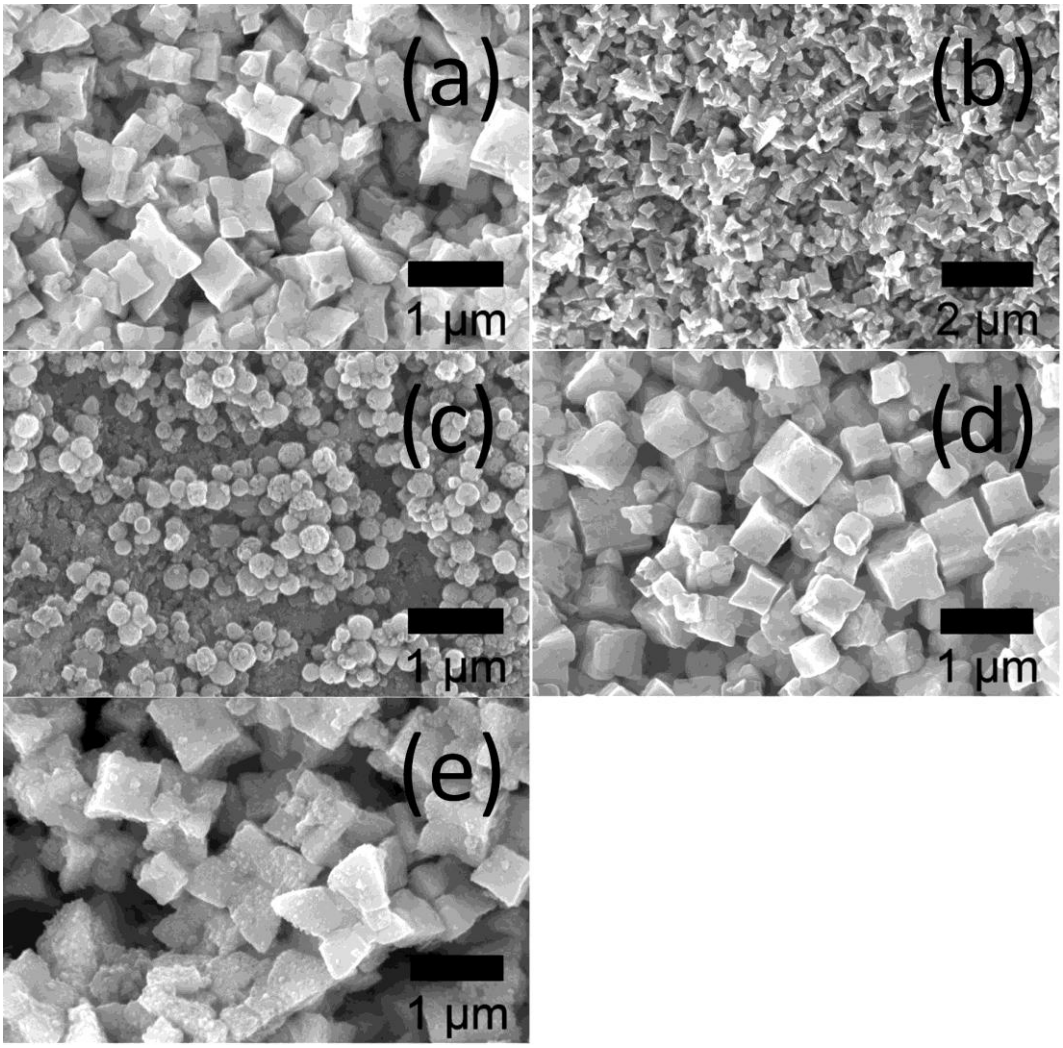

Fig. 4.11 SEM images of $NaLa(Ti_{0.5}Zr_{0.5})_2O_6$ in (a) 1:1 propanol-H_2O mixture, b) 1:1 ethanolamine-H_2O, c) 1:1 ethylene glycol-H_2O with 8 M NaOH, d) 1:1 polyethylene glycol-H_2O and e) 3:7 polyethylene glycol-H_2O mixture

4.4 Hydrothermal synthesis of $NaBi(Ti_{1-x}Zr_x)_2O_6$

Hydrothermal syntheses of the samples were performed using ~20 mL Teflon-lined stainless steel autoclaves. Stoichiometric amounts of $NaBiO_3 \cdot 2H_2O$ (Acros, 85%), TiF_3 (Alfa, 98%) and $ZrOCl_2 \cdot 8H_2O$ (Sigma Aldrich, 99.5%) were weighed according to the values shown in Table 4.4. The reagents were then mixed in 2 mL deionised water for 5 min in a Teflon liner. Then, 18 mL of NaOH solution

was added and stirred so that the final NaOH concentration was 10 M. The reaction mixture was then stirred for 1 hour before it was sealed in a steel autoclave and placed in an oven pre-heated at 240 ^{o}C. After heating for 4 days, the autoclaves were left to cool to room temperature. The solid products were recovered by suction filtration, washed thoroughly with warm water and dried overnight at 70 ^{o}C in a drying oven. The products were then ground into powder for further characterisation.

Table 4.4 Amounts measured for $NaBi(Ti_{1-x}Zr_x)_2O_6$ synthesis

Zr conc., x (Nominal value)	$NaBiO_3$ / g	TiF_3 / g	$ZrOCl_2.8H_2O$ / g	NaOH (aq) / mL	H_2O / mL
0	0.6320	0.4195	-	18	2
0.01		0.4153	0.0129		
0.05		0.3985	0.0645		
0.1		0.3776	0.1289		

The reactions yielded pale yellow powders and their powder XRD patterns (Fig. 4.12) showed that the undoped and doped samples have the perovskite structure with no impurity peaks observed.

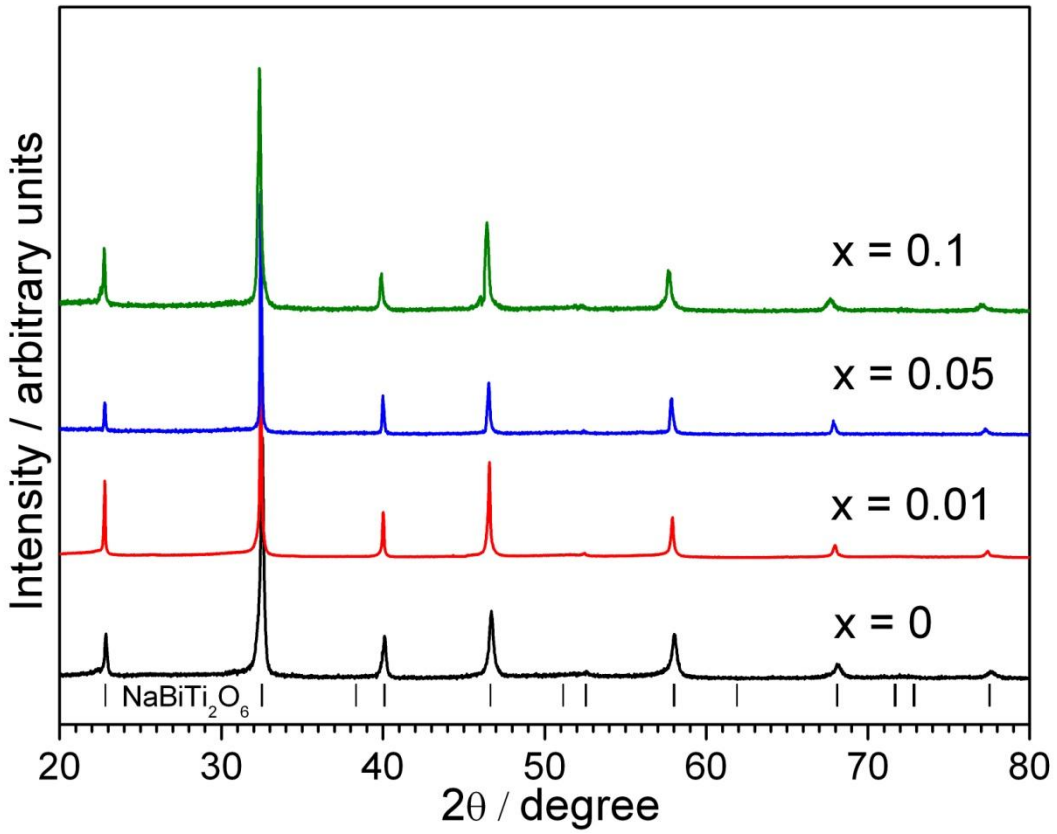

Fig. 4.12 XRD of $NaBi(Ti_{1-x}Zr_x)_2O_6$ samples, where the tick marks correspond to $NaBiTi_2O_6$ with space group *R*3*c*

The peaks for the Zr doped samples are slightly shifted to lower 2θ values with increasing Zr concentration indicating an expansion of the cell volume. The structure of $NaBiTi_2O_6$ is generally agreed to be rhombohedral, *R*3*c*[25-28], although recent studies have suggested monoclinic *Cc* symmetry.[29-30] The observed XRD patterns match the simulated pattern for $NaBiTi_2O_6$ *R*3*c*, hence the XRD pattern for all the samples were refined with the space group *R*3*c* (Fig. 4.13) and the refinement summary is shown below in Table 4.5. The occupancy was fixed to the expected amount during the refinement. Both the *a* and *c* lattice parameters increased linearly (Fig. 4.14) as expected since the Zr^{4+} ions (0.72 Å) have a bigger ionic radius than Ti^{4+} (0.605 Å).[22] This confirms that Zr has been successfully incorporated into the structure.

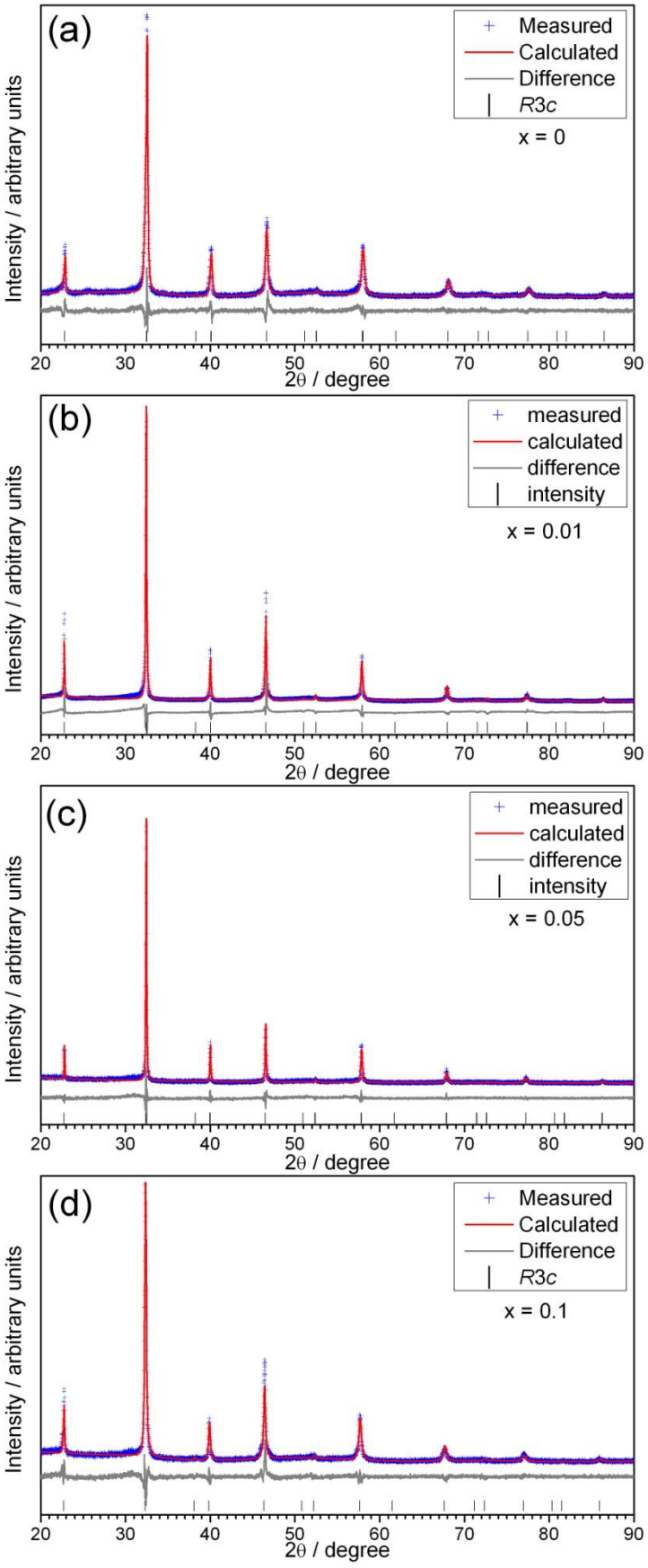

Fig. 4.13 XRD of a) x = 0, b) x = 0.01, c) x = 0.05 and d) x = 0.1 refined with space group *R*3*c*

Table 4.5 Refined structural parameters and *R*-factors of $NaBi(Ti_{1-x}Zr_x)_2O_6$ from XRD

Sample	**x = 0**	**x = 0.01**	**x = 0.05**	**x = 0.1**
Space group	*R*3*c*	*R*3*c*	*R*3*c*	*R*3*c*
***a* = *b* (Å)**	5.5015(13)	5.5050(10)	5.5162(6)	5.5341(17)
***c* (Å)**	13.4876(58)	13.4950(30)	13.5235(26)	13.5482(75)
Cell volume ($Å^3$)	353.531(367)	354.183(136)	356.369(76)	359.341(352)
Na/Bi (*x*,*y*,*z*)	(0,0,0.264(2))	(0,0,0.266(2))	(0,0,0.261(2))	(0,0,0.275(2))
Ti/Zr (*x*,*y z*)	(0,0,0.018(2))	(0,0,0.020(2))	(0,0,0.016(3))	(0,0,0.016(3))
O (*x*,*y*,*z*)	(0.163(4),0.387(6), 0.0833)	(0.160(4),0.380(6), 0.0833)	(0.153(6),0.369(9), 0.0833)	(0.153(3),0.369(5), 0.0833)
Occupancy				
Na	0.5	0.5	0.5	0.5
Bi	0.5	0.5	0.5	0.5
Ti	1	0.99	0.95	0.9
Zr	-	0.01	0.05	0.1
O	1	1	1	1
R_{wp}	15.231	16.255	14.913	15.223
R_p	12.052	12.683	11.524	11.836
Gof	1.310	1.696	1.263	1.289
Temperature factors				
Na	5.916(160)	7.693(222)	6.764 (24)	7.031(182)
Bi	5.916(160)	7.693(222)	6.764(24)	7.031(182)
Ti	0.802(117)	0.192(139)	0.694(153)	0.120(92)
Zr	-	0.192(139)	0.694(153)	0.120(92)
O	0.314(366)	0.870(303)	0.239(441)	0.372(270)

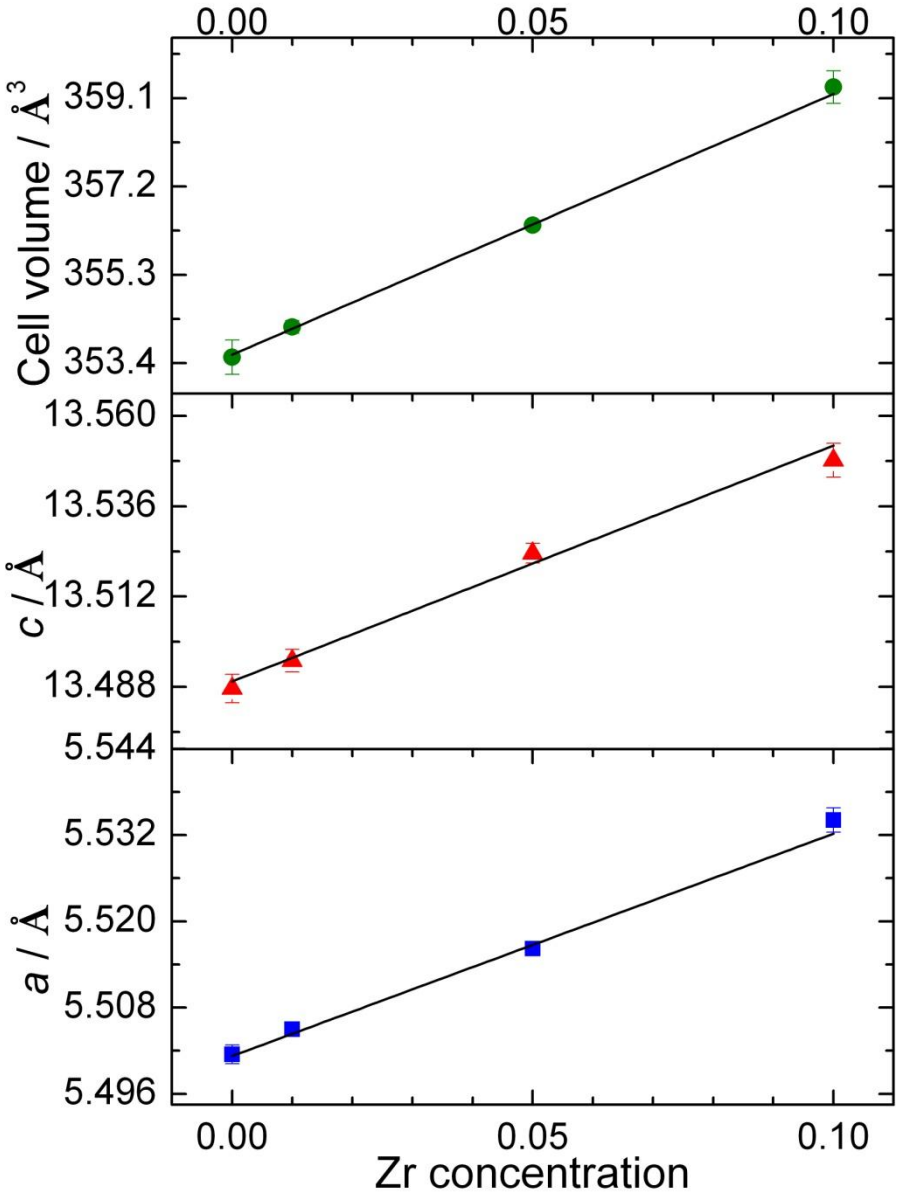

Fig. 4.14 Trend of the lattice parameters and cell volume of $NaBi(Ti_{1-x}Zr_x)_2O_6$ series

Attempts at synthesising higher Zr substitution of x = 0.2 and 0.5 hydrothermally resulted in tetragonal ZrO_2 observed in the XRD pattern (Fig. 4.15). The end member, $NaBiZr_2O_6$, was also not produced as the hydrothermal reaction mainly produced ZrO_2 instead.

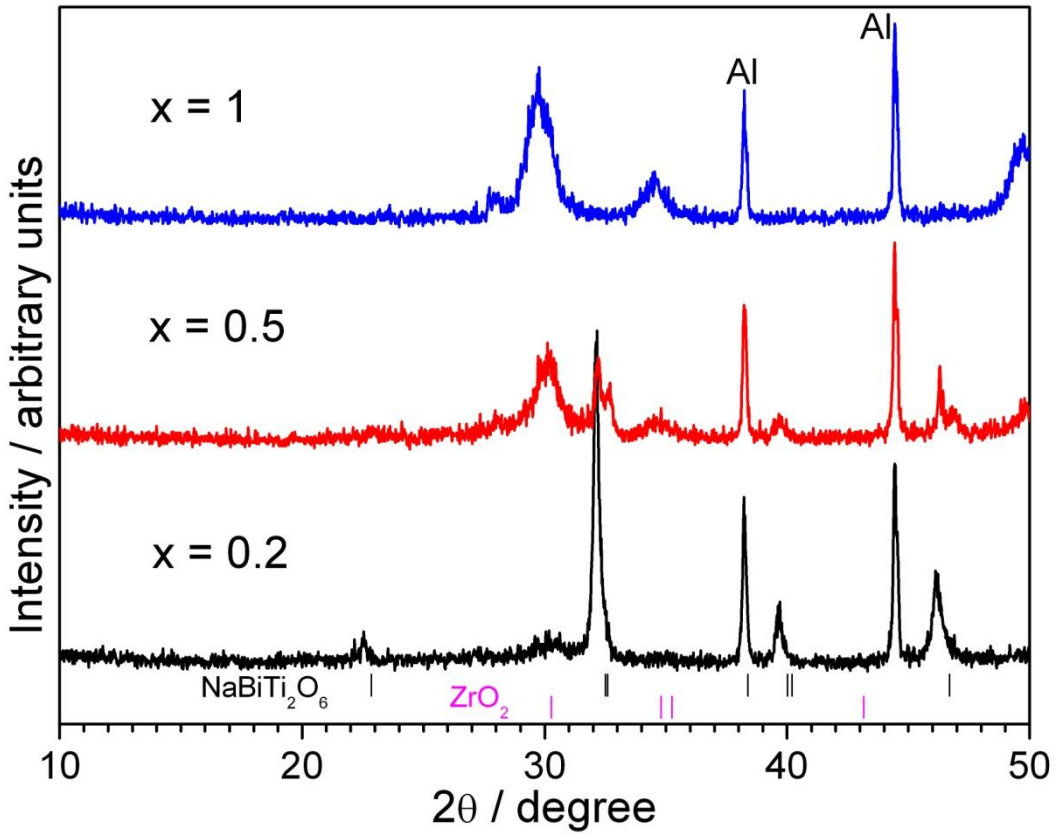

Fig. 4.15 XRD of $NaBi(Ti_{1-x}Zr_x)_2O_6$ reactions for x = 0.2, 0.5 and 1, where the tick marks correspond to $NaBiTi_2O_6$ and tetragonal ZrO_2

The Raman spectra of $NaBi(Ti_{1-x}Zr_x)_2O_6$ shown in Fig. 4.16 agree well with previous Raman studies of $NaBiTi_2O_6$. From group theory, $NaBiTi_2O_6$ is expected to have 13 Raman active modes i.e. $7A_1 + 6E$.[25] However, the spectra observed for all three samples show only five broad bands. This reduction in the number of observed modes may be due to the overlapping of multiple Raman modes and the broadening of the peaks due to the disorder on both the A-site and B-site. The position of the bands is roughly at 135, 270, 530, 590 and 820 cm^{-1}. The addition of Zr had very little effect on the Raman spectra of $NaBiTi_2O_6$.

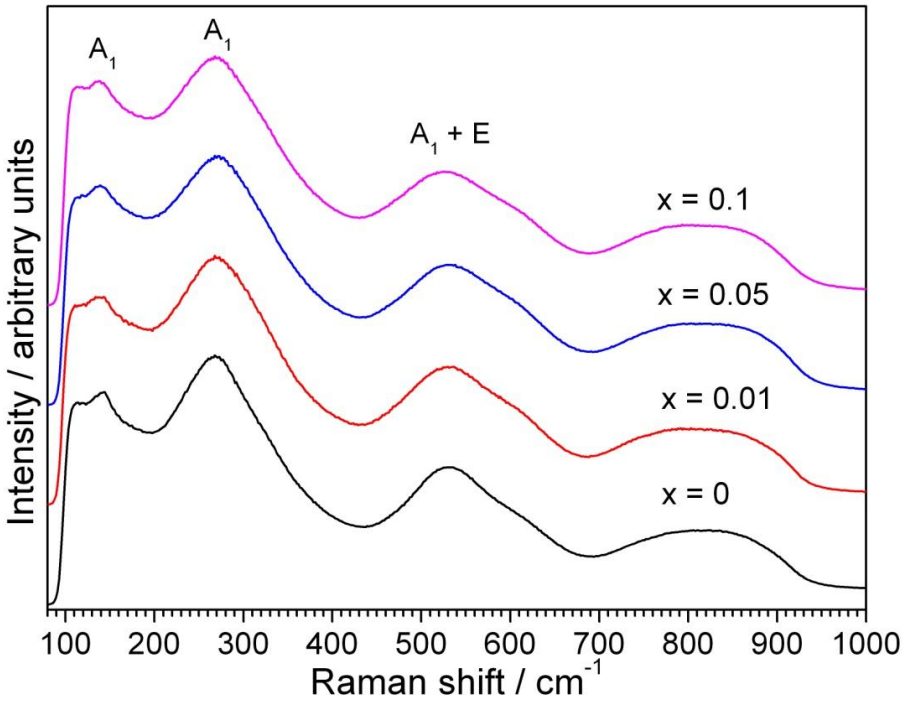

Fig. 4.16 Raman spectra of $NaBi(Ti_{1-x}Zr_x)_2O_6$ with increasing Zr concentration

The hydrothermal synthesis of $NaBi(Ti_{1-x}Zr_x)_2O_6$ gave cubic particles which are 2-4 μm in size as shown in Fig. 4.17. The atomic composition was determined by EDXA and the presence of Zr was confirmed in the doped samples, with the calculated Zr content similar to the expected values (Table 4.6).

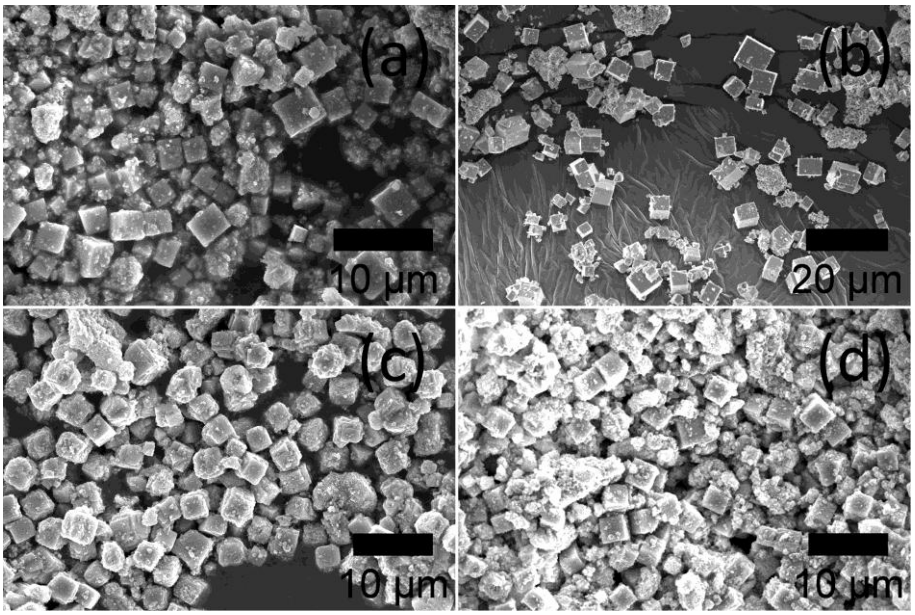

Fig. 4.17 SEM images of $NaBi(Ti_{1-x}Zr_x)_2O_6$ a) x = 0, b) x = 0.01, c) x = 0.05 and d) x = 0.1 made from hydrothermal synthesis

Table 4.6 Atomic composition of $NaBi(Ti_{1-x}Zr_x)_2O_6$ obtained from EDXA. Expected values are in brackets. *Note: Zr concentration = [Zr / (Zr + Ti)]

Zr conc., x (Nominal value)	Na / %	Bi / %	Zr / %	Ti / %	Zr conc.*
0	10.9 (10)	10.9 (10)	-	21.8 (20)	0
0.05	10.6 (10)	8.6 (10)	0.6 (1)	16.3 (19)	0.04
0.1	9.7 (10)	9.3 (10)	1.8 (2)	15.0 (18)	0.11

^{23}Na NMR of the $NaBi(Ti_{1-x}Zr_x)_2O_6$ series (Fig. 4.18) showed a single peak at close to -4 ppm. The undoped $NaBiTi_2O_6$ and x = 0.05 have the same chemical shift while x = 0.1 is slightly shifted to negative values. The linewidth of the x = 0.1 is also broader than the undoped $NaBiTi_2O_6$ and x = 0.05 sample. This suggests that there is additional disorder present in x = 0.1 which affects the environment around the Na^+ ion.

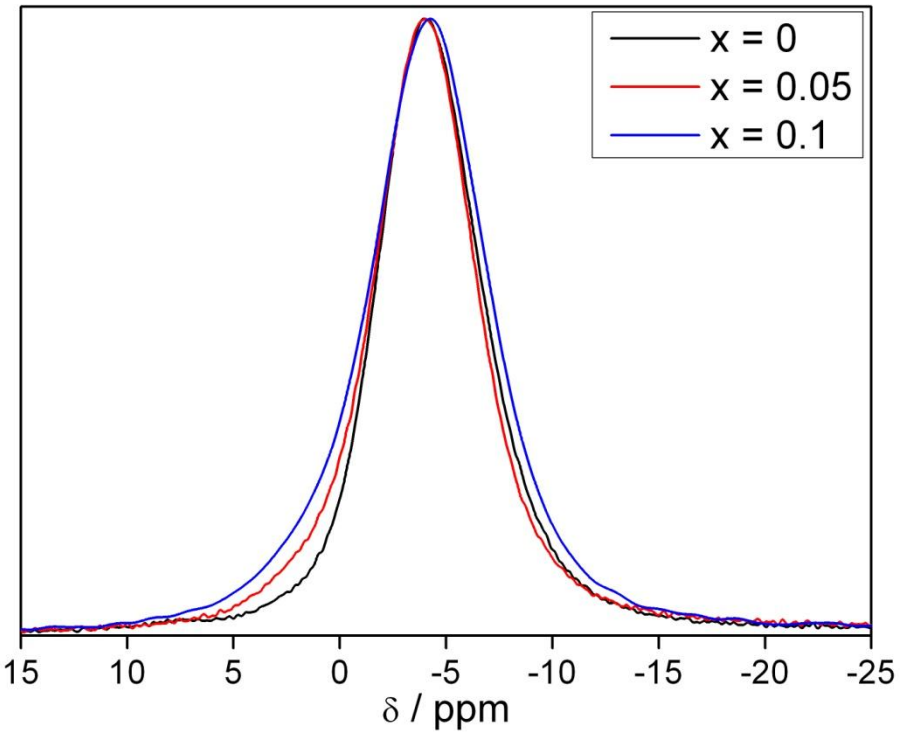

Fig. 4.18 ^{23}Na NMR of $NaBi(Ti_{1-x}Zr_x)_2O_6$ for x = 0, 0.05 and 0.1

The ^{19}F NMR spectrum of $NaBi(Ti_{1-x}Zr_x)_2O_6$ for both x = 0 and x = 0.01 showed a peak at -225 ppm which corresponds to ^{19}F in the samples (Fig. 4.19). The highest intensity peak at -125 ppm is from the Teflon present in the rotor of the equipment, with its sidebands at -34, -78, 167 and -211 ppm respectively. The peak at -225 ppm is relatively weak compared to the Teflon but it does confirm that a small amount of F is present in the as-prepared samples.

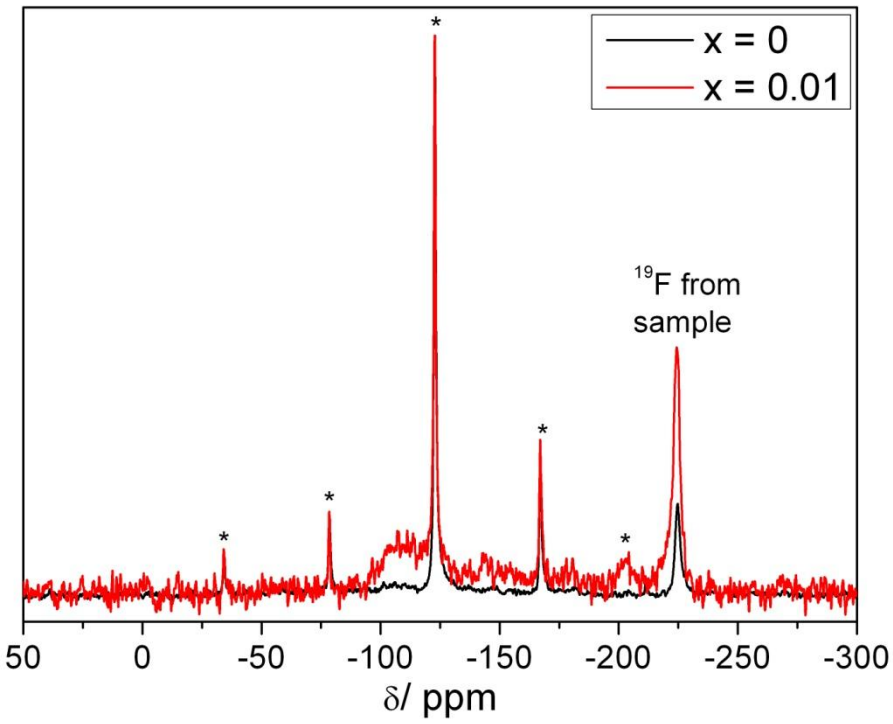

Fig. 4.19 ^{19}F NMR of $NaBiTi_2O_6$ for x = 0 and 0.01, with the ^{19}F peak arising from the sample observed at -225 ppm and peaks labelled with * are due to the Teflon present in the rotor of the equipment

4.5 Ferroelectricity and Piezoelectricity

Ferroelectrics are materials that have a spontaneous electric polarisation that can be reversed by the application of an electric field. A ferroelectric material exhibits a hysteresis loop in a plot of polarisation against electric field. When an

electric field is applied to a ferroelectric material, the saturated polarisation will be reached. This may be due to an atomic displacement (as in the case of titanate perovskites) occurring in the material which results in a dipole moment being generated. When the applied electric field is removed, the displacement remains and shows a residual polarisation in the absence of applied electric field. In order to reverse the direction of the polarisation, a coercive electric field is needed.

The dielectric hysteresis of the $NaBi(Ti_{1-x}Zr_x)_2O_6$ series were investigated to determine the effect of doping Zr into $NaBiTi_2O_6$. The samples were pressed into pellets and heated to 1150 ^oC for 4 hours. Silver paint was then coated on both sides of the pellet to form an electrode.

A hysteresis loop was observed for $NaBiTi_2O_6$ and $x = 0.01$ but this hysteresis loop was lost upon the addition of Zr from $x = 0.05$ onwards, as shown in Fig. 4.20. The loop becomes more elliptical and the remnant polarisation (polarisation at zero field) was reduced with increasing Zr substitution. This trend is similar to the results obtained by Rachakom *et al.* where they observed elliptical loops for $NaBi(Ti_{1-x}Zr_x)_2O_6$ with Zr concentration between $0.2 \leq x \leq 0.8$.[17] This result showed that the $NaBiTi_2O_6$ and the $x = 0.01$ is a ferroelectric.

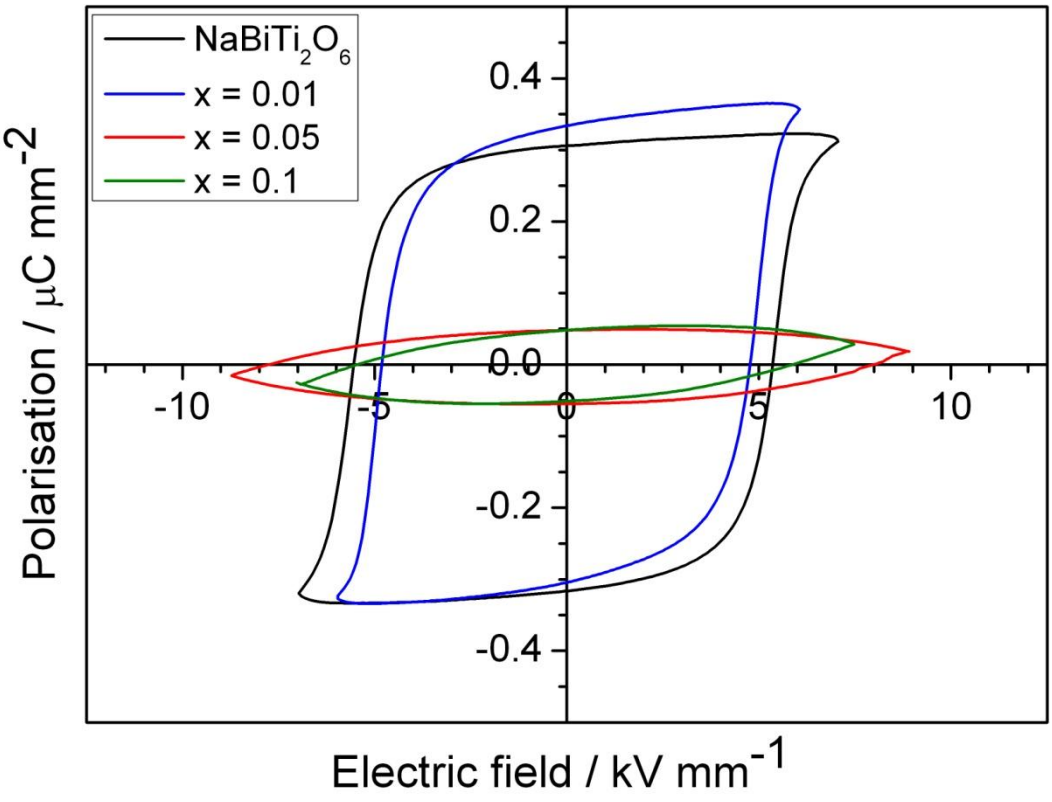

Fig. 4.20 Polarisation hysteresis for $NaBi(Ti_{1-x}Zr_x)_2O_6$

The piezoelectric coefficient, d_{33}, of the $NaBi(Ti_{1-x}Zr_x)_2O_6$ samples are plotted against the electric field applied on the $NaBi(Ti_{1-x}Zr_x)_2O_6$ pellet (poling field) as shown in Fig. 4.21. Undoped $NaBiTi_2O_6$, x = 0.01 and 0.05 showed a hysteresis loop as the poling field was varied. This is not the case for x = 0.1, as no hysteresis loop was obtained due to the sample breaking down electrically during poling.

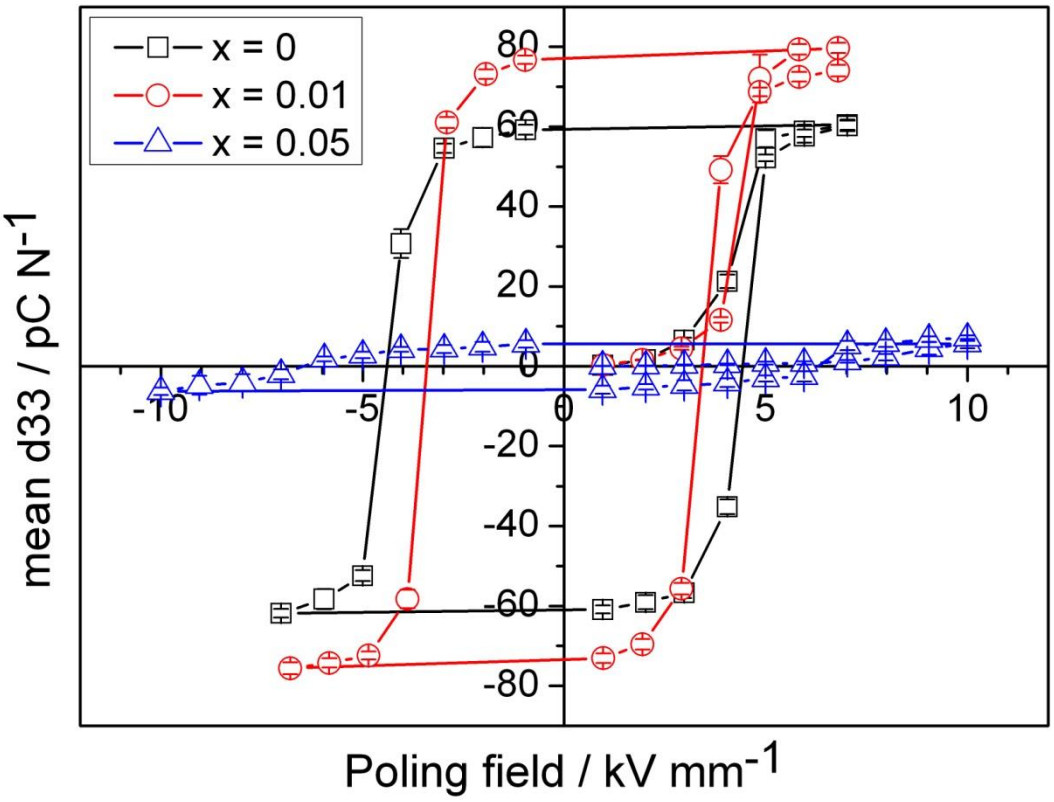

Fig. 4.21 Piezoelectric coefficient, d_{33} of $NaBi(Ti_{1-x}Zr_x)_2O_6$

The maximum mean piezoelectric coefficient, d_{33} value, for the $NaBi(Ti_{1-x}Zr_x)_2O_6$ series are shown in Table 4.7. The d_{33} value for the undoped $NaBiTi_2O_6$ is higher compared to another hydrothermal $NaBiTi_2O_6$ reported in the literature (53 pC N^{-1}).[31] The addition of Zr to x = 0.01 improves the piezoelectric property, where an increase in d_{33} value to 79 pC N^{-1} was observed. However, further addition of Zr to x = 0.05 and higher results in the reduction of the d_{33} value. All four samples were pelletize and heated with the same conditions, however the relative density of the pellets varied. As shown in Table 4.7, the x = 0 and x = 0.01 pellet had similar densities but the x = 0.05 and x = 0.1 pellets had lower densities. The lower densities of the higher Zr samples would explain their poorer polarisation and piezoelectric responses.

Both the x = 0 and x = 0.01 pellet had similar densities and both also had F in their structure, so the higher piezoelectric response of the x = 0.01 is most likely due to the presence of Zr.

Table 4.7 Piezoelectric coefficient, d_{33}, and relative density of $NaBi(Ti_{1-x}Zr_x)_2O_6$. Note: Relative density was calculated from observed density/theoretical density

Zr conc., x	Maximum mean d_{33} / pC N^{-1}	Relative density* / %
0	61.9 ± 1.1	95.0
0.01	79.7 ± 1.3	95.2
0.05	7.1 ± 0.7	79.9
0.1	0.5 ± 0.2	77.8

The permittivity and dielectric loss of hydrothermal $NaBiTi_2O_6$, shown in Fig. 4.22, are similar to that reported in previous studies for $NaBiTi_2O_6$ made by conventional solid state synthesis. The maximum permittivity is observed at ~350 ^oC and a slight shoulder was observed at ~200 ^oC. However, the values of the permittivity (648) is much lower than solid-state $NaBiTi_2O_6$ (~3400)[32] or hydrothermal $NaBiTi_2O_6$ in the literature (~2800)[31].

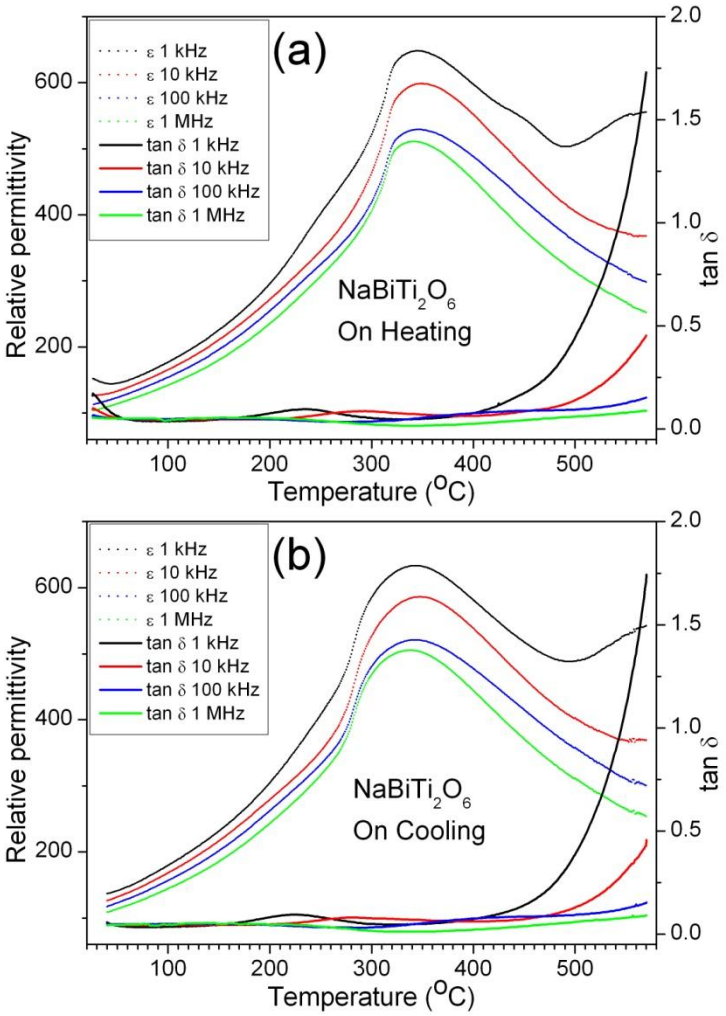

Fig. 4.22 Permittivity and dielectric loss of $NaBiTi_2O_6$ at frequencies 1 kHz, 10 kHz, 100 kHz and 1 MHz upon a) heating from 25-570 °C and b) cooling from 570-40 °C

The maximum permittivity for the x = 0.1 sample was observed at ~360 °C with a value of 2450 (Fig. 4.23), which is closer to the value reported for hydrothermal $NaBiTi_2O_6$.

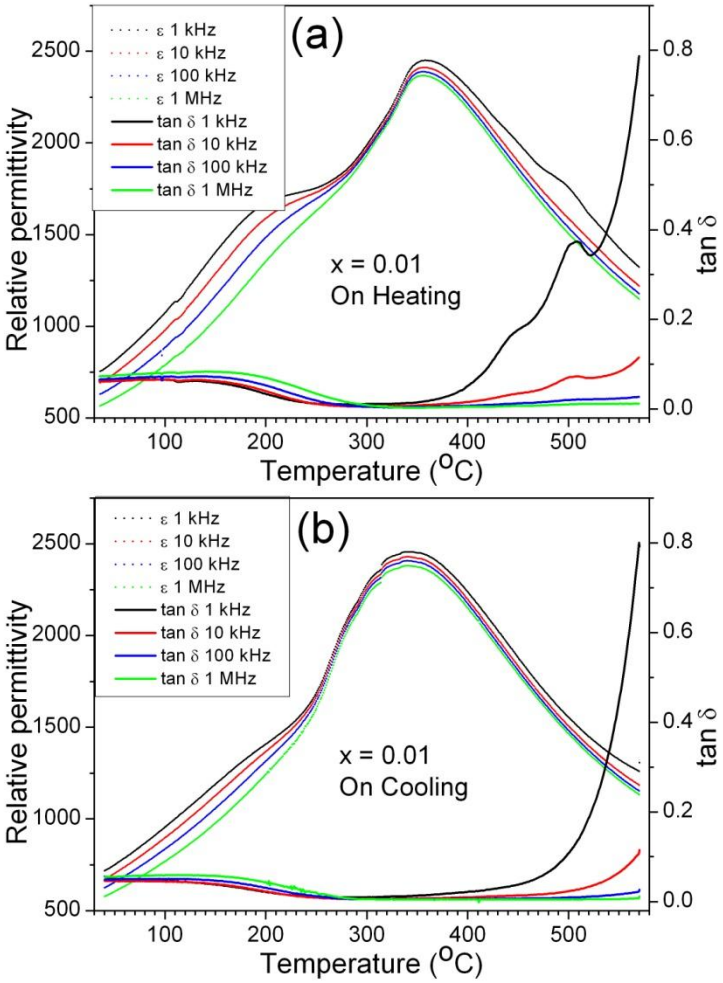

Fig. 4.23 Permittivity and dielectric loss of x = 0.01 at frequencies 1 kHz, 10 kHz, 100 kHz and 1 MHz upon a) heating from 25-570 °C and b) cooling from 570-40 °C

4.6 Hydrothermal synthesis of other B-site substituted perovskites

Other hydrothermal synthesis of B-site substituted perovskites are listed in Table 4.8 below. The synthesis of the end members $NaAZr_2O_6$ for A = Ce, La and Bi was not achieved hydrothermally. The main product formed in these reactions was ZrO_2 instead. Hydrothermal reactions aimed at substituting Ti^{4+} with Ge^{4+} resulted in the formation of $Bi_{12}GeO_{20}$ as an impurity phase.

Table 4.8 Hydrothermal reactions undertaken for other B-site substituted perovskites

Target material	Starting reagents	Results
$NaCe(Ti_{0.9}Zr_{0.1})_2O_6$ (10% Zr)	$CeCl_3.7H_2O$ + TiF_3 + $Zr(NO_3)_4$ + NaOH (aq)	$NaCeTi_2O_6$ + $Zr_xCe_{1-x}O_2$
$NaCe(Ti_{0.8}Zr_{0.2})_2O_6$ (20% Zr)	$CeCl_3.7H_2O$ + TiF_3 + $ZrOCl_2.8H_2O$ + NaOH (aq)	$NaCeTi_2O_6$ + ZrO_2 (tetragonal)
$NaCeZr_2O_6$	$CeCl_3.7H_2O$ + $ZrOCl_2.8H_2O$ + NaOH (aq)	CeO_2 + ZrO_2 (tetragonal)
	$CeCl_3.7H_2O$ + $Zr(NO_3)_4$ + NaOH (aq)	ZrO_2 (tetragonal)
	$CeCl_3.7H_2O$ + Zr ethoxide + NaOH (aq)	CeO_2 + ZrO_2 (tetragonal)
$NaLa(Ti_{0.9}Zr_{0.1})_2O_6$ (10% Zr)	$LaCl_3.7H_2O$ + TiF_3 + Zr ethoxide + NaOH (aq)	$NaLa(Ti_{1-x}Zr_x)_2O_6$
$NaLa(Ti_{0.5}Zr_{0.5})_2O_6$ (50% Zr)	$LaCl_3.7H_2O$ + TiF_3 + Zr ethoxide + NaOH (aq)	$NaLa(Ti_{1-x}Zr_x)_2O_6$ + ZrO_2 (tetragonal)
$NaLa(Ti_{0.9}Zr_{0.1})_2O_6$ (10% Zr)	$LaCl_3.7H_2O$ + TiF_3 + $Zr(NO_3)_4$ + NaOH (aq)	$NaLa(Ti_{1-x}Zr_x)_2O_6$
$NaLa(Ti_{0.8}Zr_{0.2})_2O_6$ (20% Zr)	$LaCl_3.7H_2O$ + TiF_3 + $Zr(NO_3)_4$ + NaOH (aq)	$NaLa(Ti_{1-x}Zr_x)_2O_6$
$NaLaZr_2O_6$	$LaCl_3.7H_2O$ + $ZrOCl_2.8H_2O$ + NaOH (aq)	$La(OH)_3$ + ZrO_2 (tetragonal)
	$LaCl_3.7H_2O$ + Zr ethoxide + NaOH (aq)	$La(OH)_3$ + ZrO_2 (tetragonal)
$NaBiZr_2O_6$	$Bi(NO_3)_3.5H_2O$ + $ZrOCl_2.8H_2O$ + NaOH (aq)	ZrO_2 (tetragonal)
	$Bi(NO_3)_3.5H_2O$ + $Zr(NO_3)_4$ + NaOH (aq)	Bi_2O_3 + ZrO_2 (tetragonal)
	$Bi(NO_3)_3.5H_2O$ + Zr ethoxide + NaOH (aq)	Bi + ZrO_2 (monoclinic)
	$NaBiO_3$ + $ZrOCl_2.8H_2O$ + NaOH (aq)	ZrO_2 (tetragonal)
$NaBi(Ti_{0.9}Ge_{0.1})_2O_6$	$NaBiO_3$ + TiF_3 + GeO_2 + NaOH (aq)	$NaBiTi_2O_6$ + $Bi_{12}GeO_{20}$

4.7 Conclusion

B-site substituted perovskites, in particular, $NaLa(Ti_{1-x}Zr_x)_2O_6$ (for $0 \leq x \leq 0.5$) and $NaBi(Ti_{1-x}Zr_x)_2O_6$ (for $0 \leq x \leq 0.1$) have been synthesised hydrothermally. The $NaLa(Ti_{1-x}Zr_x)_2O_6$ and $NaBi(Ti_{1-x}Zr_x)_2O_6$ series were assigned the space group $R\bar{3}c$ and $R3c$ respectively. $NaLa(Ti_{1-x}Zr_x)_2O_6$, showed splitting in the XRD peaks which was most obvious in the x = 0.2-0.4 samples. This splitting may result from the presence of two separate phases instead of a single homogeneous phase. $NaLa(Ti_{0.5}Zr_{0.5})_2O_6$ gave flower-shaped particles and their morphology can be changed to either cubes upon increased NaOH concentration or spheres by using an ethylene glycol / water mixture as the solvent. The effect of the reaction time and the use of different solvent/water mixture on the morphology were also investigated.

The lattice parameter of $NaBi(Ti_{1-x}Zr_x)_2O_6$, obtained from refinement of XRD patterns, increased with increasing Zr concentration confirming that the Zr has been incorporated into the perovskite structure. The addition of Zr has little effect on the Raman spectra of $NaBiTi_2O_6$. SEM images showed that cubic particles were obtained. The addition of Zr at x = 0.01 resulted in improvement in the piezoelectricity but higher Zr doping degrades the polarisation hysteresis and piezoelectric properties. The work showed the potential for making complex solid solutions of ferroelectric perovskites for real applications.

4.8 References

(1) Weber, U.; Greuel, G.; Boettger, U.; Weber, S.; Hennings, D.; Waser, R. *J. Am. Ceram. Soc.* **2001**, *84*, 759.

(2) Yu, Z.; Guo, R. Y.; Bhalla, A. S. *Appl. Phys. Lett.* **2000**, *77*, 1535.

(3) Pontes, F. M.; Escote, M. T.; Escudeiro, C. C.; Leite, E. R.; Longo, E.; Chiquito, A. J.; Pizani, P. S.; Varela, J. A. *J. Appl. Phys.* **2004**, *96*, 4386.

(4) Outzourhit, A.; Raghni, M. A. E.; Hafid, M. L.; Bensamka, F. *J. Alloy. Compd.* **2002**, *340*, 214.

(5) Ostos, C.; Mestres, L.; Matinez-Sarrion, M. L.; Garcia, J. E.; Albareda, A.; Perez, R. *Solid State Sci* **2009**, *11*, 1016.

(6) Fukushima, J.; Kodaira, K.; Matsushita, T. *J. Mater. Sci.* **1984**, *19*, 595.

(7) Noheda, B.; Cox, D. E.; Shirane, G.; Gonzalo, J. A.; Cross, L. E.; Park, S. E. *Appl. Phys. Lett.* **1999**, *74*, 2059.

(8) Guo, R.; Cross, L. E.; Park, S. E.; Noheda, B.; Cox, D. E.; Shirane, G. *Phys. Rev. Lett.* **2000**, *84*, 5423.

(9) Noheda, B.; Gonzalo, J. A.; Cross, L. E.; Guo, R.; Park, S. E.; Cox, D. E.; Shirane, G. *Phys. Rev. B* **2000**, *61*, 8687.

(10) Noheda, B.; Cox, D. E.; Shirane, G.; Guo, R.; Jones, B.; Cross, L. E. *Phys. Rev. B* **2001**, *63*, 9.

(11) Mitchell, R. H.; Chakhmouradian, A. R. *J. Solid State Chem.* **1999**, *144*, 81.

(12) Wang, D. F.; Ye, J. H.; Kako, T.; Kimura, T. *J. Phys. Chem. B* **2006**, *110*, 15824.

(13) Kim, K. T.; Kim, C. I. *Thin Solid Films* **2005**, *472*, 26.

(14) Wright, C. S.; Walton, R. I.; Thompsett, D.; Fisher, J. *Inorg. Chem.* **2004**, *43*, 2189.

(15) Damjanovic, D. *Rep. Prog. Phys.* **1998**, *61*, 1267.

(16) Rodel, J.; Jo, W.; Seifert, K. T. P.; Anton, E. M.; Granzow, T.; Damjanovic, D. *J. Am. Ceram. Soc.* **2009**, *92*, 1153.

(17) Rachakom, A.; Jaiban, P.; Jiansirisomboon, S.; Watcharapasorn, A. *Nanoscale Res Lett* **2012**, *7*, 5.

(18) Rao, K. S.; Tilak, B.; Rajulu, K. C. V.; Swathi, A.; Workineh, H.; Ieee International Conference on Solid Dielectrics ICSD, Potsdam, GERMANY, 2010.

(19) Knapp, M. C.; Woodward, P. M. *J. Solid State Chem.* **2006**, *179*, 1076.

(20) Lily; Kumari, K.; Prasad, K.; Yadav, K. L. *J. Mater. Sci.* **2007**, *42*, 6252.

(21) Prasad, K.; Lily; Kumari, K.; Yadav, K. L. *J. Phys. Chem. Solids* **2007**, *68*, 1508.

(22) Shannon, R. D. *Acta Crystallogr. Sect. A* **1976**, *32*, 751.

(23) Kim, I. S.; Nakamura, T.; Inaguma, Y.; Itoh, M. *J. Solid State Chem.* **1994**, *113*, 281.

(24) Chai, P.; Liu, X. J.; Wang, Z. L.; Lu, M. F.; Cao, X. Q.; Meng, J. *Cryst. Growth Des.* **2007**, *7*, 2568.

(25) Kreisel, J.; Glazer, A. M.; Jones, G.; Thomas, P. A.; Abello, L.; Lucazeau, G. *J. Phys.-Condes. Matter* **2000**, *12*, 3267.

(26) Rout, D.; Moon, K. S.; Kang, S. J. L.; Kim, I. W. *J. Appl. Phys.* **2010**, *108*, 7.

(27) Sardar, K.; Walton, R. I. *J. Solid State Chem.* **2012**, *189*, 32.

(28) Elkechai, O.; Manier, M.; Mercurio, J. P. *Phys. Status Solidi A* **1996**, *157*, 499.

(29) Gorfman, S.; Thomas, P. A. *J. Appl. Crystallogr.* **2010**, *43*, 1409.

(30) Aksel, E.; Forrester, J. S.; Jones, J. L.; Thomas, P. A.; Page, K.; Suchomel, M. R. *Appl. Phys. Lett.* **2011**, *98*, 3.

(31) O'Brien, A.; Woodward, D. I.; Sardar, K.; Walton, R. I.; Thomas, P. A. *Appl. Phys. Lett.* **2012**, *101*.

(32) Said, S.; Mercurio, J. P. *J. Eur. Ceram. Soc.* **2001**, *21*, 1333.

Chapter 5 – Hydrothermal Synthesis of $YMnO_3$ and Investigation of Doping with Fe

5.1 Background

Rare-earth manganites have been studied due to their ferroelectric and ferromagnetic properties. Recent studies on $YMnO_3$ have reported coupling between ferroelectric and antiferromagnetic ordering.[1-3] Such multiferroic materials have potential application in next-generation devices such as spin-based transistors and advanced magnetic memory storage.[4-6]

$YMnO_3$ can exist as one of two polymorphs, hexagonal $P6_3cm$ (structure shown in Section 1.4, Fig. 1.5) and orthorhombic *Pnma*. The hexagonal phase is stable at room temperature. The hexagonal phase of $YMnO_3$ may be transformed at high temperature (1270 K) and pressure (35-40 kbar) to the orthorhombic phase.[3] It is the hexagonal phase which is of interest since it has both ferroelectric and antiferromagnetic properties. The ferroelectric properties of $YMnO_3$ result from a cooperative tilting of the MnO_5 bipyramids below the Curie temperature, which results in a displacement of the rare-earth ions along the *c* axis. At the same time, the magnetism arises from Mn^{3+} spins, which order antiferromagnetically in the *a-b* plane at low temperatures (~ 70 K).[7-9] The coupling between the ferroelectric and magnetic property can lead to the so-called magnetoelectric effect, which refers to the electric response of the material upon the application of a magnetic field or vice-versa.[10-11]

Traditionally, rare-earth manganites have been prepared by conventional solid state reactions between the rare-earth oxides and manganese oxide. Such reactions require high annealing temperature of ~1400 ^{o}C to eliminate Mn_3O_4 phase that may also be formed.[12] However, hydrothermal routes to these rare-earth manganites, particularly $YMnO_3$, which is the material studied in this chapter, have been reported. Stampler *et al.* prepared hexagonal $YMnO_3$ hydrothermally from Y_2O_3 and Mn_2O_3 in basic NaOH solution.[12] A high reaction temperature of 350 ^{o}C for 48 hours was required so the conventional Teflon lined autoclaves could not be used. Instead, they performed the reaction in a stainless steel Parr pressure vessel which can withstand higher temperature and pressures. Zheng *et al*. reported the synthesis of hexagonal $YMnO_3$ at a lower temperature, 230 ^{o}C for 48 hours.[13] They first prepared solutions of $Y(NO_3)_3$, $KMnO_4$ and $MnCl_2$ with known concentrations, and then mixing the solutions before hydrothermal treatment.

There are several studies on the A- and B-site substituted $YMnO_3$ reported in the literature,[14-18] with several of them investigating the effect of substituting Mn with Fe on the structure and properties.[19-23] Fe doping is interesting because the end members $YMnO_3$ and $YFeO_3$ have different structures at room temperature despite having the same ionic radius for Fe^{3+} and Mn^{3+} cations. Both $YMnO_3$ and $YFeO_3$ also exhibit antiferromagnetic ordering. However, this ordering occurs at a low temperature for $YMnO_3$ (~70 K) but it occurs at 650 K in the case of $YFeO_3$.[24-25] $YMn_{1-x}Fe_xO_3$ has also been reported to show enhanced room temperature ferromagnetic properties and exhibits a ferroelectric hysteresis loop.[26] $YFeO_3$ crystallises in the orthorhombic phase *Pnma* so there is a limit to doping Fe into $YMnO_3$. Veres *et al*. reported the formation of the hexagonal phase of $YMn_{1-x}Fe_xO_3$

by conventional solid-state synthesis, but only up to x = 0.1.[20] However, Samal *et al*. extended this limit to x = 0.3 by using gel-pyrolysis technique.[21]

There are currently no reports on the hydrothermal synthesis of $YMn_{1-x}Fe_xO_3$. However, the hydrothermal synthesis of other manganites has been reported such as $HoMnO_3$[27] and $La_{0.5}Ba_{0.5}MnO$.[28] In this chapter, an investigation on the hydrothermal synthesis of phase pure hexagonal $YMnO_3$ and the substitution of Mn by Fe will be described.

5.2 Hydrothermal synthesis of $YMn_{1-x}Fe_xO_3$

Hydrothermal syntheses of the samples were performed using ~20 mL Teflon-lined stainless steel autoclaves. Solutions of the starting materials were made to ensure better mixing of the reagents. The following solutions were made: Y^{3+} (0.4 M) from $Y(NO_3)_3{\cdot}6H_2O$, Mn^{7+} (0.12 M) from $KMnO_4$, Mn^{2+} from $MnCl_2{\cdot}4H_2O$ and Fe^{2+} (0.48 M) from $FeCl_2{\cdot}4H_2O$. The amounts used in a typical reaction are shown in Table 5.1. The water content of the starting materials was determined by thermogravimetric analysis. $Y(NO_3)_3{\cdot}6H_2O$ (aq) was first mixed with $KMnO_4$ (aq) for 1 minute, before excess KOH was added. Then $MnCl_2{\cdot}4H_2O$ (aq) was added last and the mixture was left to stir for 1 hour. Different order of mixing was tested and it was found that mixing $KMnO_4$ and $MnCl_2$ results in a precipitate to be formed. Hence, addition of $MnCl_2$ was done at the last step to allow thorough mixing of the Y^{3+} before any precipitate was formed. In the case of Fe-doped samples, $FeCl_2{\cdot}4H_2O$ and $MnCl_2{\cdot}4H_2O$ were first mixed together before being added into the reaction mixture. The Teflon liner was then sealed in a steel autoclave and placed in an oven

pre-heated at 240 ^{o}C. After heating for 24 hours, the autoclaves were left to cool to room temperature. The solid products were recovered by suction filtration, washed thoroughly with warm water and dried overnight at 70 ^{o}C in a drying oven. The products were then ground into powder for further characterisation.

The reaction was performed according to the following equation:

$$\mathbf{5}\ \mathrm{Y(III)} + \mathbf{1}\ \mathrm{Mn(VII)} + \mathrm{KOH} + \mathbf{(4\text{-}x)}\ \mathrm{Mn(II)} + \mathbf{x}\ \mathrm{Fe(II)} \longrightarrow \mathbf{5}\ \mathrm{Y(Mn(III)_{1-x},Fe(III)_x)_3}$$

The ratios of reagents were chosen so that a comproportionation reaction between Mn(VII) and Mn(II)/Fe(II) would lead to Mn(III)/Fe(III). This method has previously been found to be successful for $A_{1-x}B_xMnO_3$ orthorhombic perovskites.[29]

Table 5.1 Amounts measured for $YMn_{1-x}Fe_xO_3$ synthesis

Fe conc., x	**$Y(NO_3)_3{\cdot}6H_2O$/ mL**	**$KMnO_4$/ mL**	**KOH/g**	**$MnCl_2{\cdot}4H_2O$/ mL**	**$FeCl_2{\cdot}4H_2O$/ mL**
0	3	2	9.4	2	-
0.1				1.75	0.25
0.2				1.5	0.5
0.4				1	1
0.6				0.5	1.5
0.7				0.25	1.75
0.8				-	2
1		-		-	2.5

The reaction gave a dark blue/black powder for $YMnO_3$ and $YMn_{1-x}Fe_xO_3$, while $YFeO_3$ had a dark red colour. The synthesis method used in this work was similar to Zheng *et al.* described in the previous section,[13] however, KOH was also added to the reaction. When the reactions were carried out without any KOH, only a small amount of solid was obtained which mainly consisted of MnO_2 and no $YMnO_3$ was produced.

The XRD of the as-prepared samples, shown in Fig. 5.1, showed that the two end members have different structures. $YMnO_3$ was formed purely as the hexagonal polymorph but the peak intensity ratio in the powder XRD is different when compared to the average pattern expected for $YMnO_3$ (Fig. 5.2), suggesting preferred orientation in the sample. Upon addition of Fe at low levels (x = 0.1 and 0.2), the hexagonal structure was retained. However, a small peak at 33.3^o due to $YFeO_3$ is also present and other impurity peaks were observed. From the JCPDS database, these impurity peaks matched with the XRD of birnessite ($K_{0.5}Mn_2O_{4.3}$) and YMn_2O_5. At x = 0.4 and 0.6, a mixture of $YMnO_3$ and $YFeO_3$ phases were clearly observed. At higher Fe content, only the $YFeO_3$ peaks were observed and the $YMnO_3$ peaks disappeared. However, a small amount of birnessite ($K_{0.5}Mn_2O_{4.3}$) was still present. At 100% Fe, pure orthorhombic $YFeO_3$ was obtained. This observation agrees well with the literature from solid-state synthesis, where the hexagonal structure is reported to be stable up to x = 0.1-0.3 and above x = 0.5, the orthorhombic structure is more stable. Between x = 0.3 and 0.5, a mixture of hexagonal and orthorhombic phase was reported to be present.[20-21]

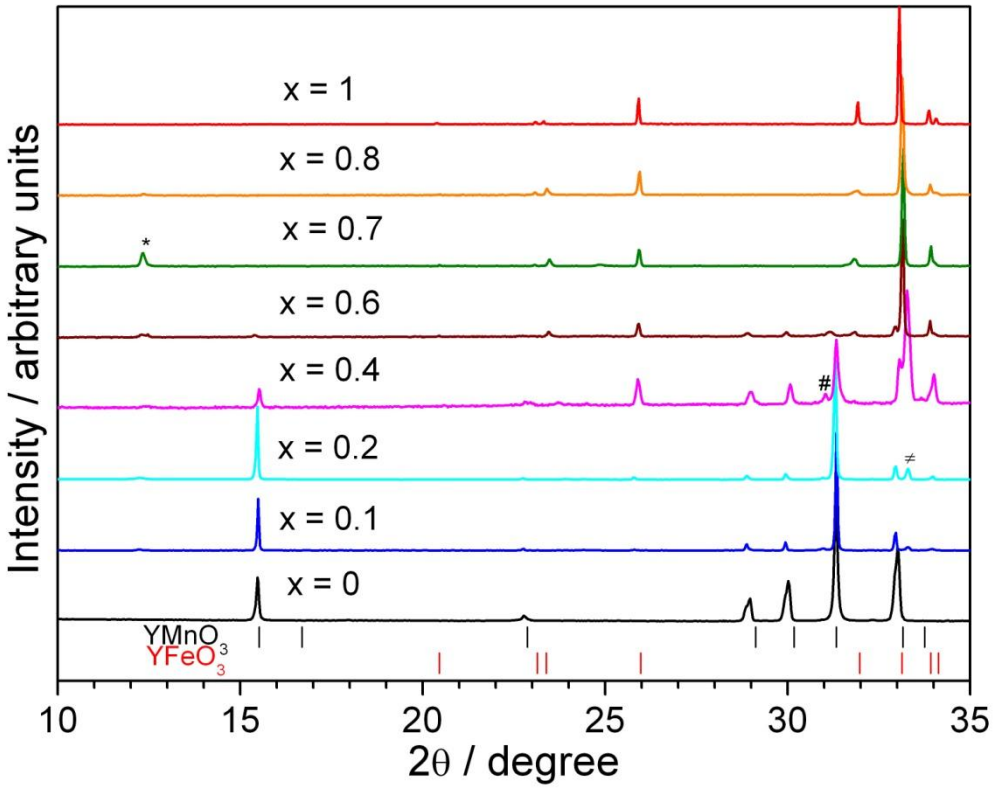

Fig. 5.1 Powder XRD of $YMn_{1-x}Fe_xO_3$. Peaks that are labelled with *, ≠ and # are due to birnessite ($K_{0.5}Mn_2O_{4.3}$), $YFeO_3$ and YMn_2O_5 respectively

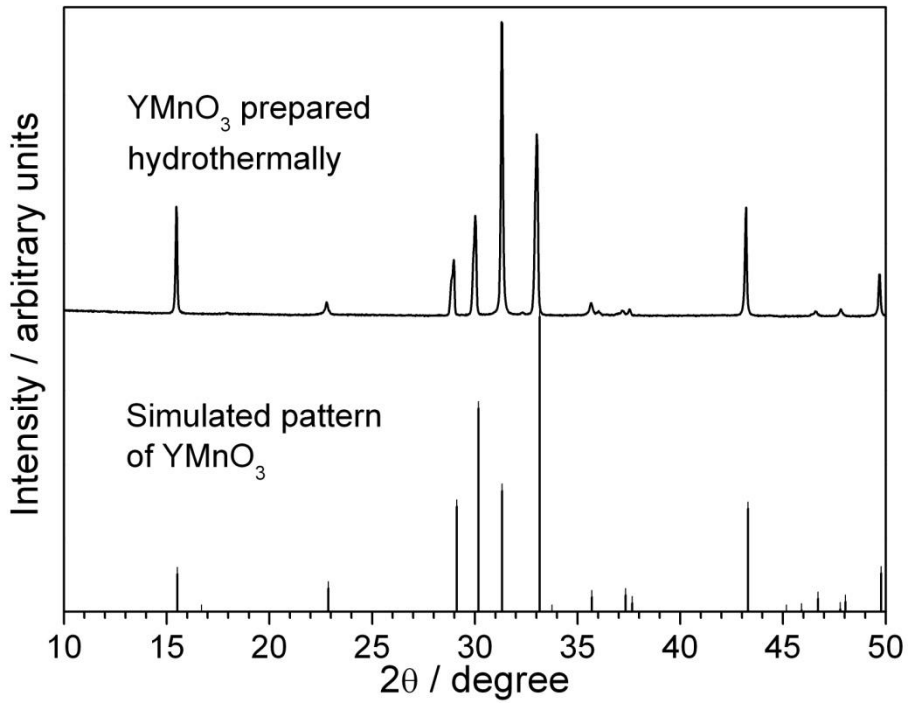

Fig. 5.2 XRD of $YMnO_3$ prepared hydrothermally compared with expected pattern of $YMnO_3$

The XRD of $YMnO_3$ and low Fe doped samples (x = 0.1 and 0.2) were refined with the hexagonal unit cell, space group $P6_3cm$. $YFeO_3$ and high Fe doped samples (x = 0.7 and 0.8) were refined with the orthorhombic unit cell, space group *Pnma*. The x = 0.4 and 0.6 samples were refined as a two-phase mixture. The Pawley refinement for $YMn_{1-x}Fe_xO_3$ samples are shown in Fig. 5.3 and Fig. 5.4. The summary of all the refinements performed and the lattice parameters obtained are shown in Table 5.2. Note that due to the high level of preferred orientation, a full Rietveld analysis of the samples was not undertaken.

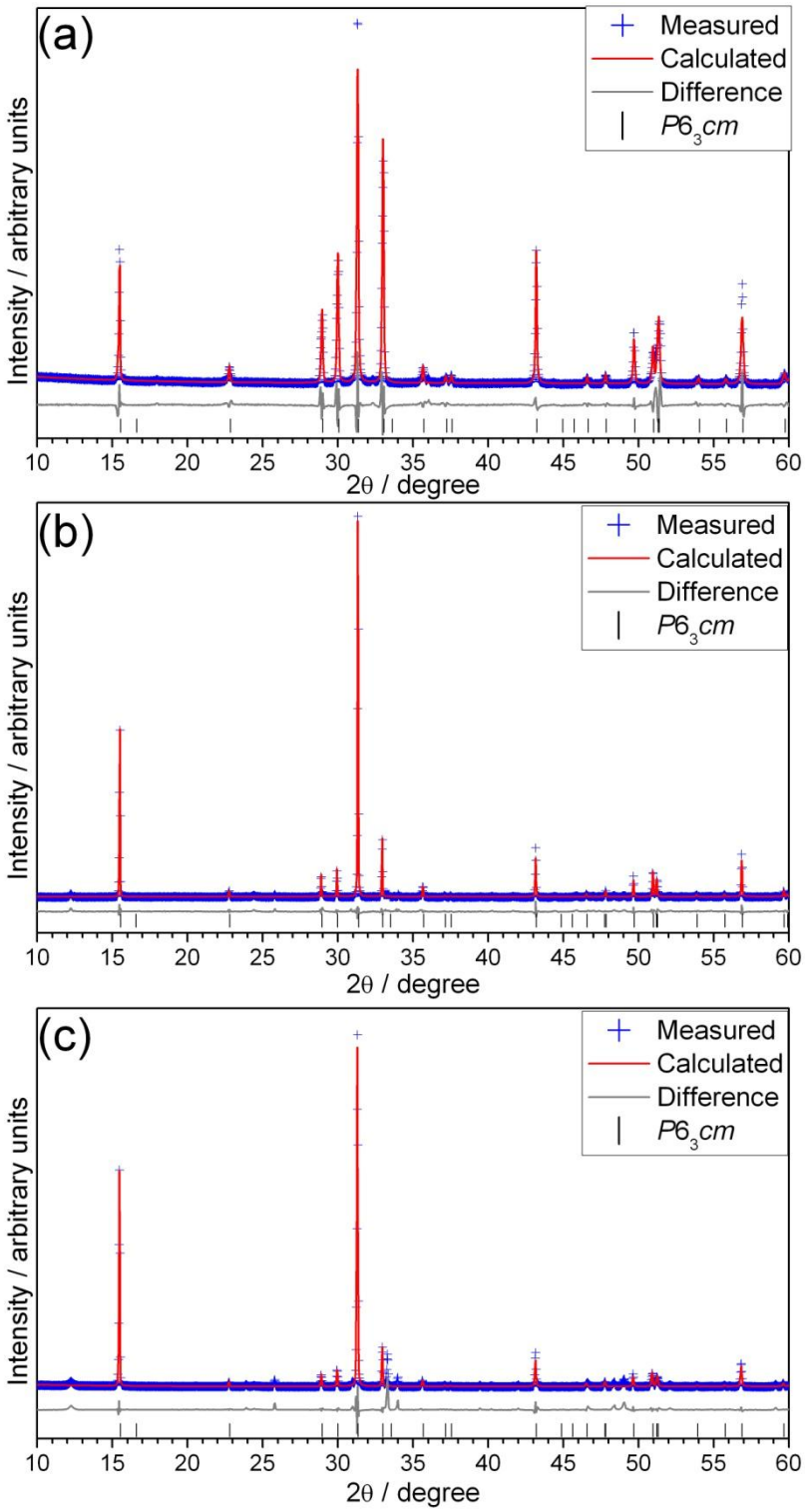

Fig. 5.3 Pawley refinement of $YMn_{1-x}Fe_xO_3$ for a) x = 0, b) x = 0.1, and c) x = 0.2 refined with hexagonal unit cell with space group *P6₃cm*

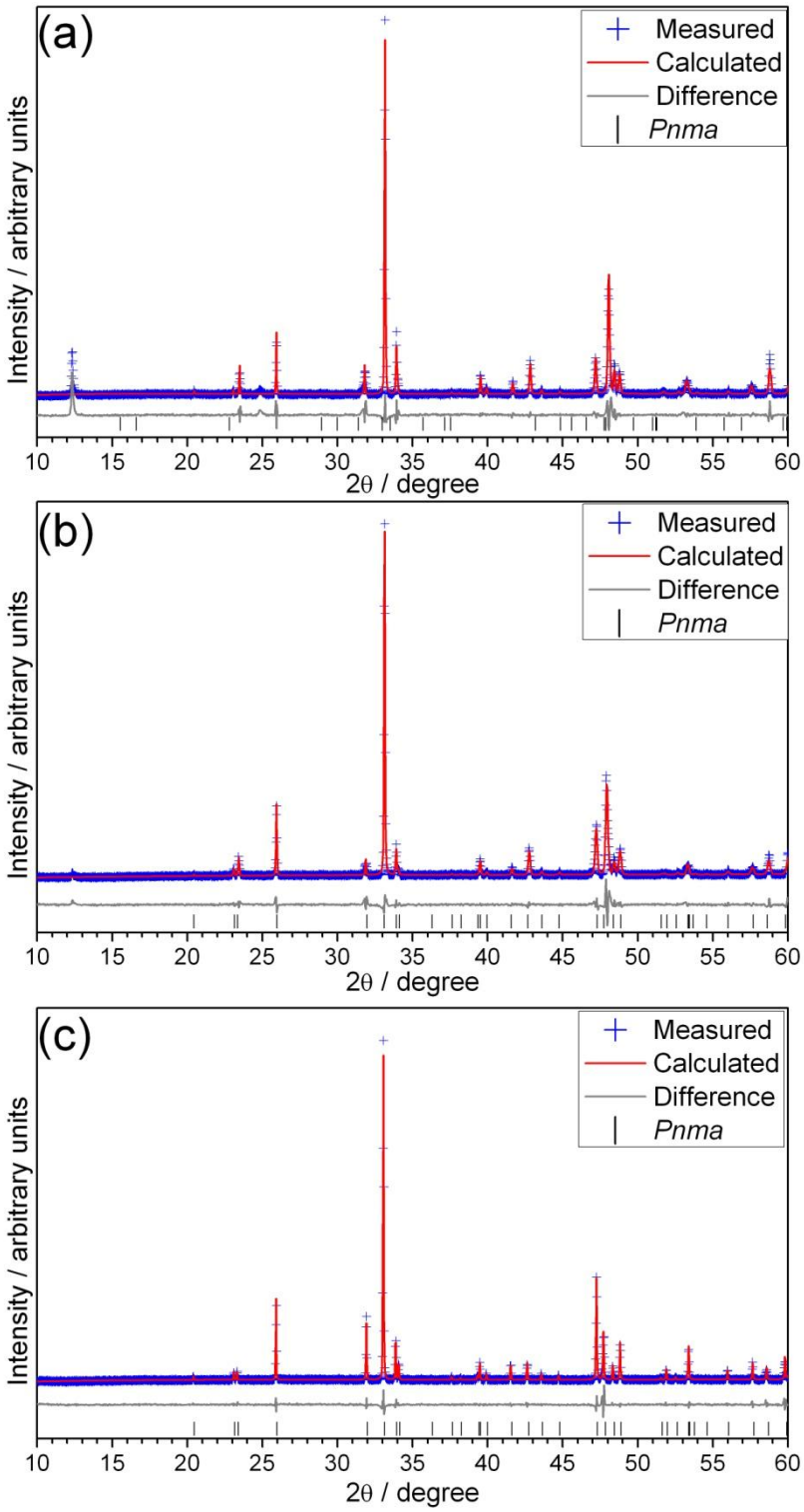

Fig. 5.4 Pawley refinement of $YMn_{1-x}Fe_xO_3$ for a) x = 0.7, b) x = 0.8, and c) x = 1 refined with orthorhombic unit cell with space group *Pnma*

Table 5.2 Summary of Pawley refinement for $YMn_{1-x}Fe_xO_3$ series

Fe conc.,x	Space group	*a* / Å	*b* / Å	*c* / Å	Cell volume / Å^3	R_{wp}	R_p	gof
0	$P6_3cm$	6.1539(2)	6.1539(2)	11.3958(4)	373.745(28)	7.306	4.259	5.897
0.1	$P6_3cm$	6.1697(1)	6.1697(1)	11.3947(1)	375.637(12)	7.811	4.807	3.205
0.2	$P6_3cm$	6.1646(2)	6.1646(2)	11.4046(3)	375.333(27)	10.464	5.392	9.201
0.4	$P6_3cm$	6.1539(5)	6.1539(5)	11.4176(9)	374.469(72)	6.506	4.672	2.410
	Pnma	5.6329(6)	7.5022(8)	5.3191(8)	224.782(47)			
0.6	$P6_3cm$	6.1539(8)	6.1539(8)	11.4438(16)	375.320(113)	6.392	3.975	2.741
	Pnma	5.6246(4)	7.5578(4)	5.2614(6)	223.662(33)			
0.7	*Pnma*	5.6164(4)	7.5625(3)	5.2768(3)	224.134(21)	7.556	3.939	3.464
0.8	*Pnma*	5.6070(3)	7.5835(3)	5.2807(3)	224.539(20)	5.493	3.528	2.380
1	*Pnma*	5.5959(1)	7.6142(1)	5.2838(7)	225.136(6)	4.494	2.909	1.896

The trend in the lattice parameters of the $YMn_{1-x}Fe_xO_3$ samples are shown in Fig. 5.5 and Fig. 5.6. Initial doping of x = 0.1 resulted in an increase in the cell volume but further doping reduces the cell volume up to x = 0.4. The ionic radius of Fe^{3+} and Mn^{3+} are the same in an octahedral environment (0.645 Å)[30] so no dramatic changes in the lattice parameter are expected. The *a* lattice parameter increased at x = 0.1 and decreased slightly upon further Fe doping, while the *c* lattice parameter showed the opposite trend where it dropped at x = 0.1 and increased up to x = 0.4. Samal *et al*. reported a similar trend where the *a* lattice parameter increased and the *c* lattice parameter decreased up to x = 0.2.[21] Since any changes in the lattice parameter is not expected to be from the difference in the size of the ions, the variation in lattice parameter was attributed to the reduced tilting of the MnO_5 bipyramids upon Fe substitution.[31] Hence, the XRD results provide evidence for Fe doping up to x = 0.1 into $YMnO_3$ in the as-prepared samples, but at x = 0.2 and above, $YFeO_3$ begins to appear as a significant extra phase.

Upon further addition of Fe, the orthorhombic structure becomes more prevalent. The variation in lattice parameter for Fe-rich samples starting from x = 0.6 showed a gradual increase in the cell volume. The *a* lattice parameter increased

linearly while the *c* lattice parameter decreased. A similar trend was also observed by other authors.[32-33]

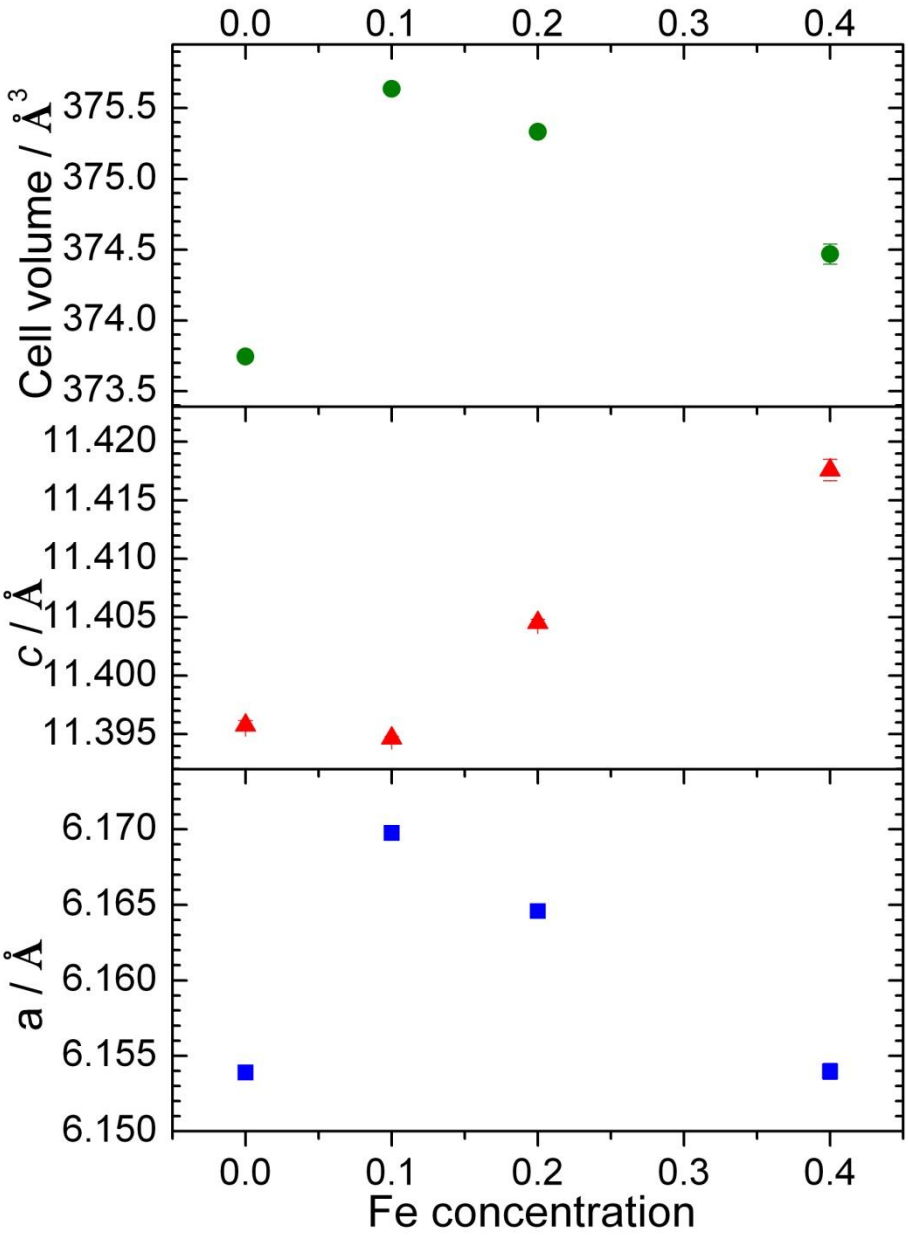

Fig. 5.5 Trends of hexagonal lattice parameters and cell volume of $YMn_{1-x}Fe_xO_3$ for $0 \leq x \leq 0.4$

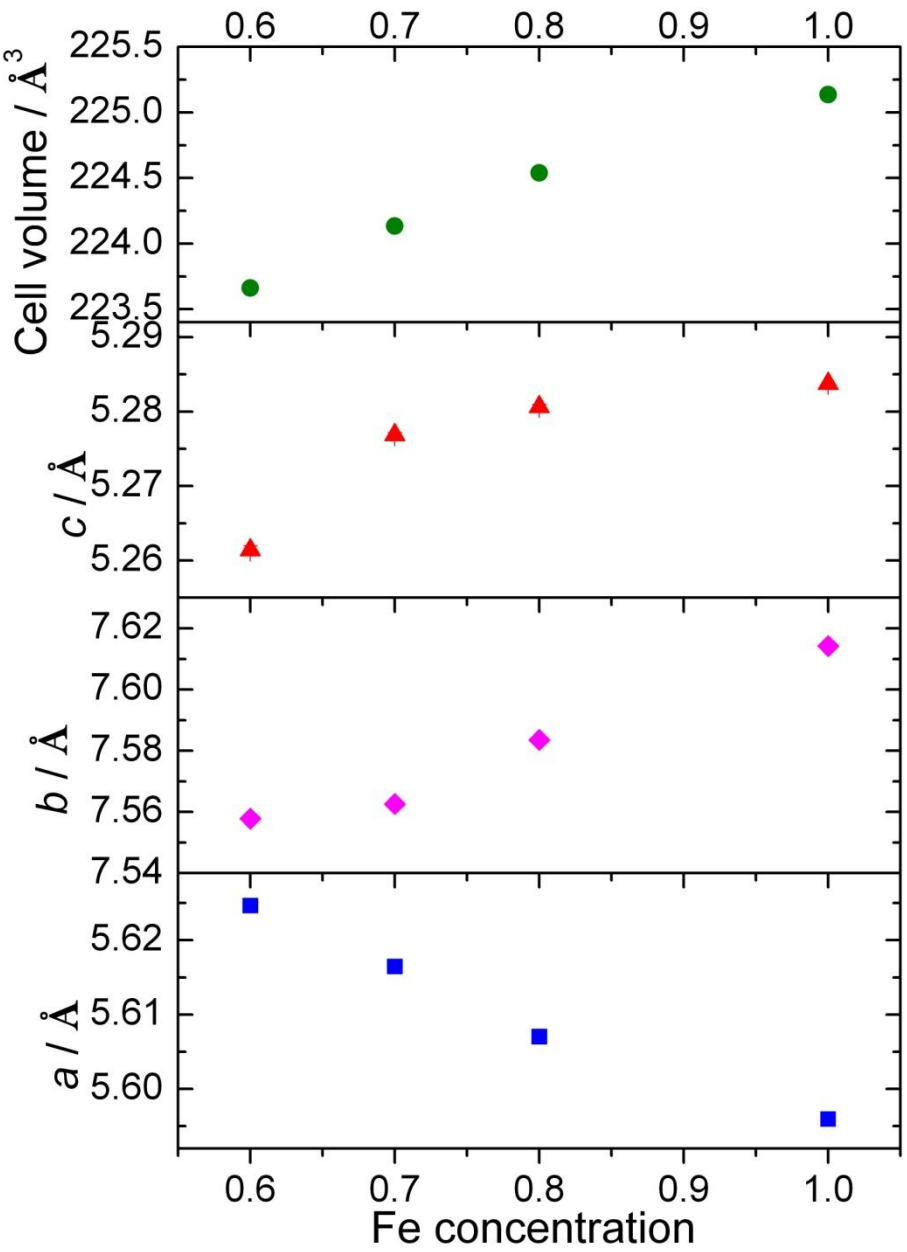

Fig. 5.6 Trend of orthorhombic lattice parameters and cell volume of $YMn_{1-x}Fe_xO_3$ for $0.6 \leq x \leq 1$

Raman spectroscopy was also used to determine the phase present with increasing Fe concentration (Fig. 5.7). The Raman spectrum of $YMnO_3$ is very different to $YFeO_3$ as expected due to the difference in structure. Iliev *et al.* studied Raman scattering of a single crystal hexagonal $YMnO_3$ at room temperature and assigned their atomic vibrations according to lattice-dynamical calculations.[34]

Fukumura *et al.* studied the Raman spectra of $YMnO_3$ for a wide temperature range of 15-1200 K.[35] $YMnO_3$ has a hexagonal structure with space group $P6_3cm$ and theoretically 38 Raman active modes are expected (9 A_1 + 14 E_1 + 15 E_2).[34] However, the Raman spectrum of $YMnO_3$ showed fewer peaks than expected where a main peak is located at 684 cm^{-1}, which has a shoulder at lower values, and a broad peak at 100-160 cm^{-1}. The measured spectrum is similar to those reported in the literature for polycrystalline $YMnO_3$.[35-38] The peak at 684 cm^{-1} can be assigned to E_1 symmetry, while the broad peak at 100-160 cm^{-1} may be due to an overlap of two modes, E_2 and A_1. The shoulder peak at ~640 cm^{-1} was not observed by other authors and is currently unassigned. One possible explanation for this shoulder peak is from orthorhombic $YMnO_3$ although it is unlikely since the main Raman peak for orthorhombic $YMnO_3$ is at 616 cm^{-1} and it was not detected by XRD.[39-40] Upon addition of up to x = 0.2, similar Raman spectra were obtained with the peak at 684 cm^{-1} slightly shifted to lower values. This shift may be due to differences in particle size of the samples.[41]

$YMn_{1-x}Fe_xO_3$ samples between x = 0.4 and 0.8 showed peaks due to orthorhombic $YFeO_3$ between 100 and 500 cm^{-1}. However, these samples also show a strong peak at 635 cm^{-1} which is similar to the unassigned shoulder peak found in lower Fe doped samples. The intensity of the peak is very high that it is unlikely to be from birnessite impurity or orthorhombic $YMnO_3$. From the XRD, the x = 0.4 sample was a mixture of $YMnO_3$ and $YFeO_3$ but in the Raman spectrum, the main $YMnO_3$ peak was not observed at 684 cm^{-1}. The Raman spectrum of $YFeO_3$ matches well with those reported in the literature.[42-43] The peaks are assigned according to assignment made on analogous orthorhombic materials.[39]

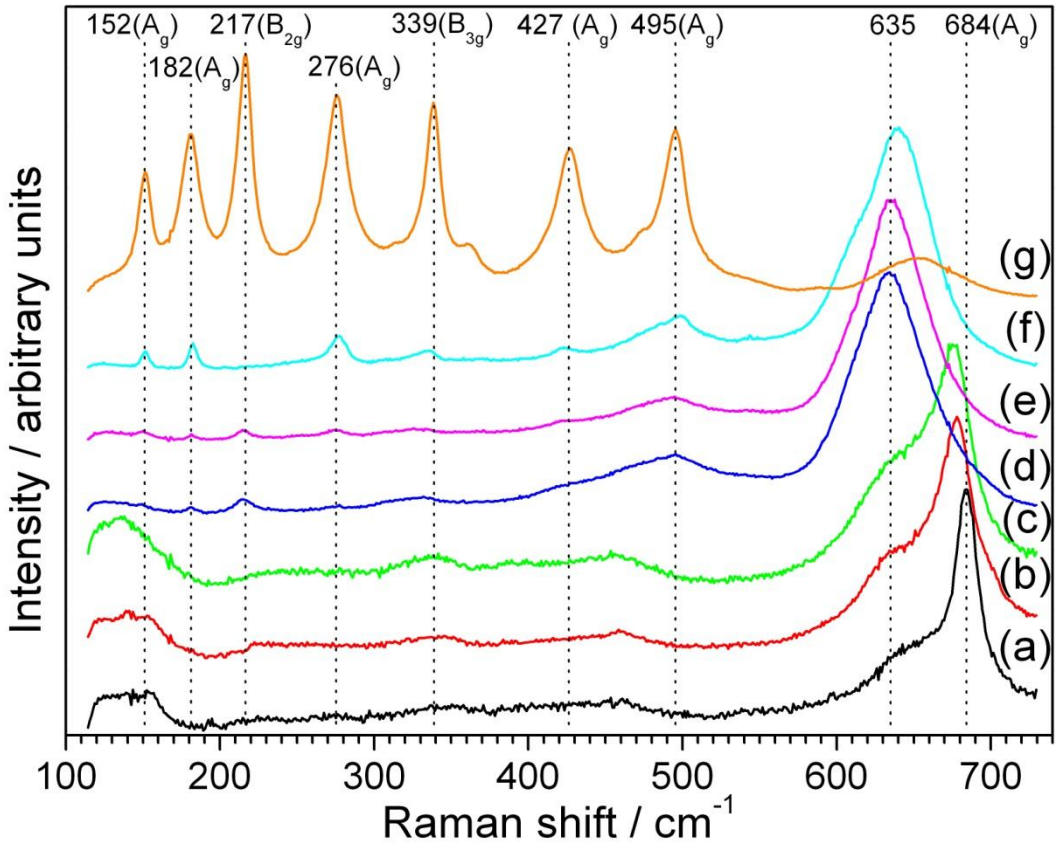

Fig. 5.7 Raman spectra of $YMn_{1-x}Fe_xO_3$ for a) x = 0, b) x = 0.1, c) x = 0.2, d) x = 0.4, e) x = 0.7, f) x = 0.8 and g) x = 1

SEM and EDXA were carried out by collaborators in the Institute of Physics, Chinese Academy of Sciences, Beijing. The SEM images $YMnO_3$ (Fig. 5.8) consisted of sheet-like particles ranging in size from 1-20 μm with thickness of 100-200 nm. The sheet shape crystals explain the preferred orientation in the XRD. The x = 0.1 sample is also sheet-like with some of the particles having a hexagonal shape. As the Fe content was increased to x = 0.2, the thickness increased and the sheet-like particles disappear. The Fe-rich samples tend to form rectangular boxes up to $YFeO_3$ (Fig. 5.9), where the particles are of uniform size with relatively smooth surfaces.

The atomic composition of the samples was determined by EDXA (Table 5.3). The composition of the x = 0.1 and x = 0.8 samples was close to the expected values. However, the Fe concentration for the x = 0.2 and x = 0.7 samples was lower than expected which could be due to higher amount of impurities formed in these samples compared to the x = 0.1 and x = 0.8.

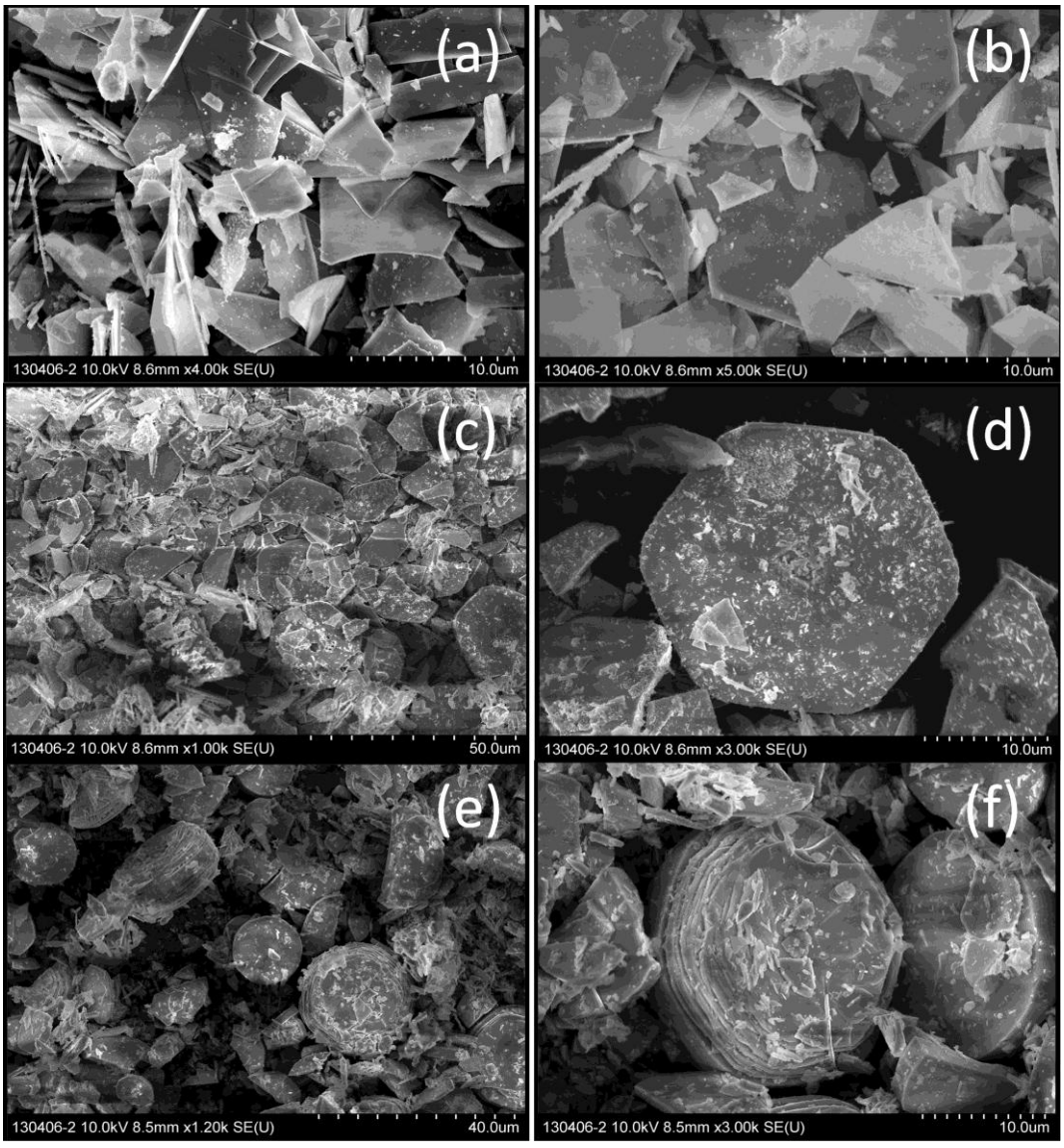

Fig. 5.8 SEM images of $YMn_{1-x}Fe_xO_3$ for a-b) x = 0, c-d)) x = 0.1, and e-f) x = 0.2

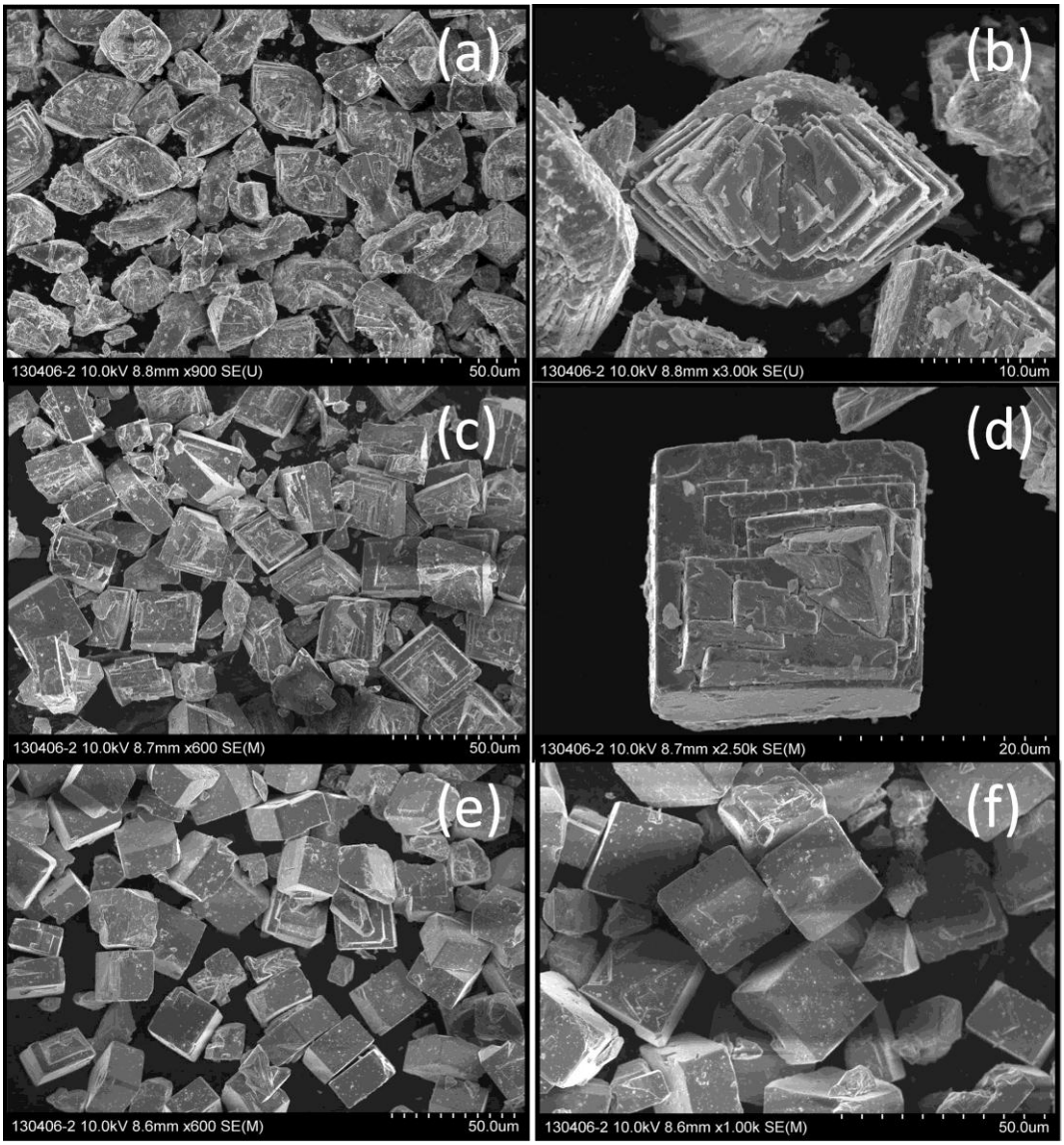

Fig. 5.9 SEM images of $YMn_{1-x}Fe_xO_3$ for a-b) x = 0.7, c-d)) x = 0.8, and e-f) x = 1

Table 5.3 Atomic compositions of $YMn_{1-x}Fe_xO_3$ obtained from EDXA. Expected values from synthesis are in brackets. Note: Fe concentration = [Fe / (Fe + Mn)]

Fe conc, x (Nominal value)	Y / %	Mn / %	Fe / %	Fe conc. / x
0	15.8 (20)	16.1 (20)	-	0
0.1	26.3 (20)	23.7 (18)	2.5 (2)	0.09
0.2	23.4 (20)	18.6 (16)	2.9 (4)	0.13
0.7	19.0 (20)	6.2 (6)	8.5 (14)	0.58
0.8	17.3 (20)	4.6 (4)	17.6 (16)	0.79
1	22.59 (20)	-	20.2 (20)	1

The oxidation state of Mn and Fe were determined using XANES. The XANES data were normalised to the edge step using the post-edge background in the EXAFS region. The edge was then defined as the energy corresponding to 50% of the edge step. This method provides an estimation of oxidation state but does not take into account the fact that the metals in the reference compounds may be in different local environments. In this case, the reference used for Mn(III) and Mn(IV) was Mn_2O_3 and MnO_2, which both contain manganese in an octahedral environment. However, this is not the case in the $YMn_{1-x}Fe_xO_3$ samples, so only an estimation of the oxidation state of Mn can be obtained.

Fig. 5.10 shows the Mn K-edge XANES for $YMn_{1-x}Fe_xO_3$. All the $YMn_{1-x}Fe_xO_3$ samples studied has similar edge positions and is very close to Mn_2O_3 so it can be concluded that the oxidation state of Mn is close to 3+.

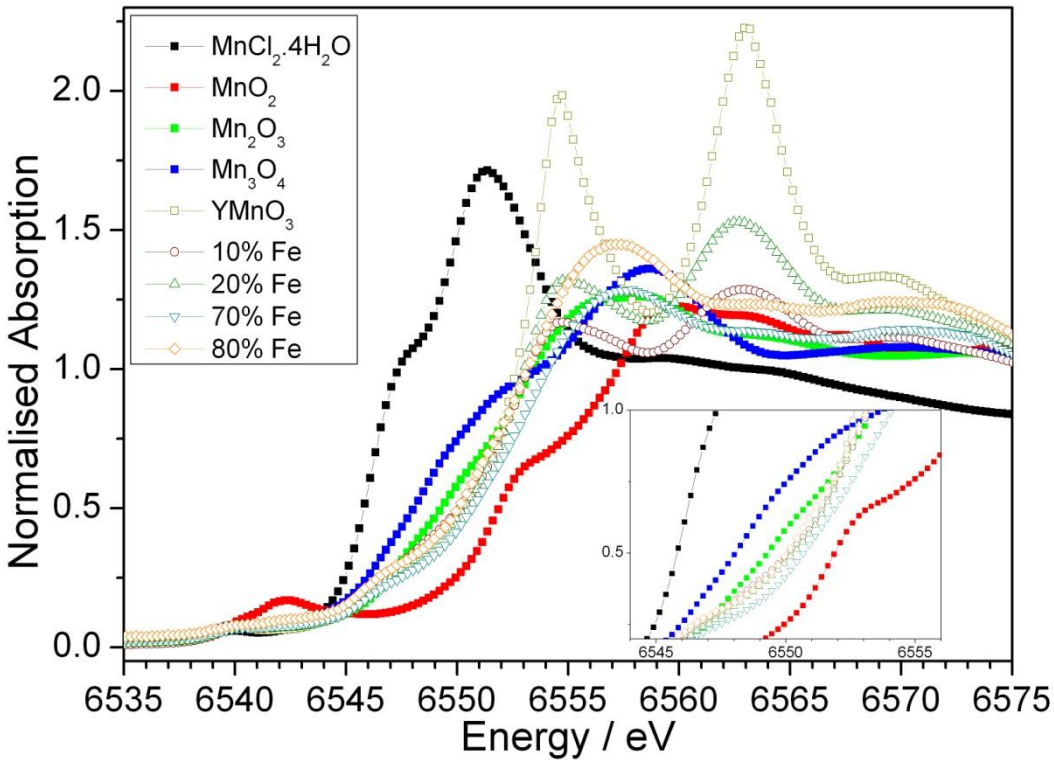

Fig. 5.10 Mn K-edge XANES for $YMn_{1-x}Fe_xO_3$ along with Mn reference materials. The inset shows a zoomed-in view of the edge position

A similar trend is observed in the Fe K-edge XANES (Fig. 5.11). All the $YMn_{1-x}Fe_xO_3$ has similar edge positions and is very close to Fe_2O_3 so it can be concluded that the oxidation state of Fe is close to 3+ as well.

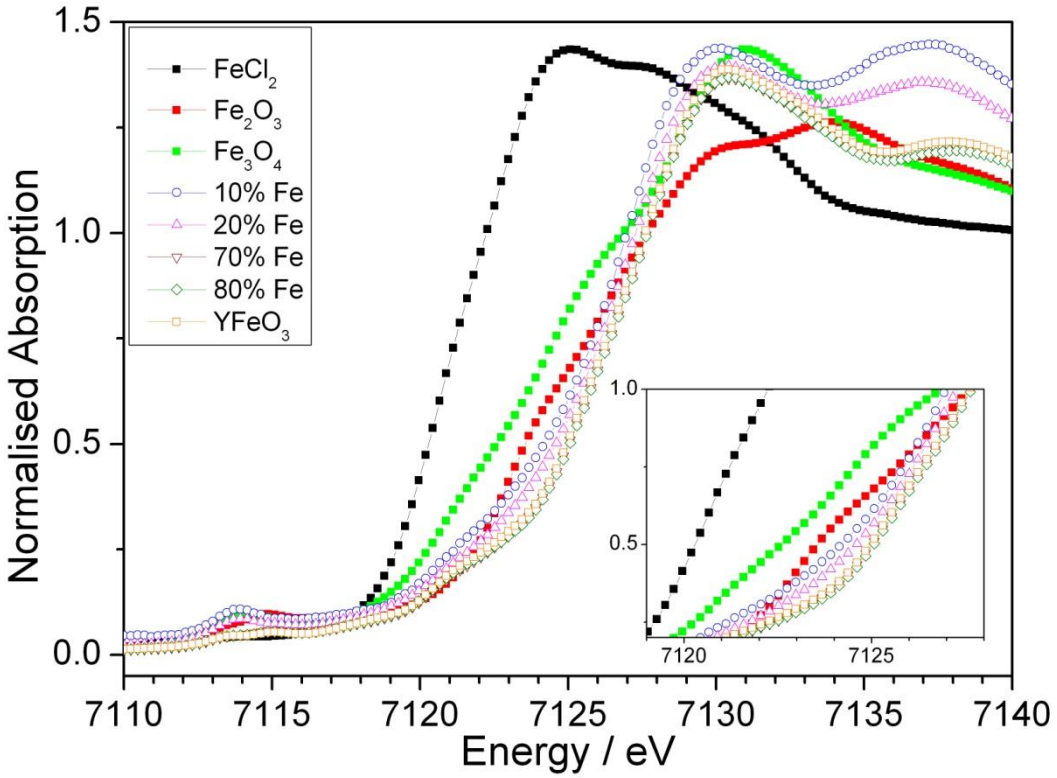

Fig. 5.11 Fe K-edge XANES for $YMn_{1-x}Fe_xO_3$ along with Fe reference materials. The inset shows a zoomed-in view of the edge position

The TGA of $YMn_{1-x}Fe_xO_3$ (Fig. 5.12) shows very little total mass loss at 1000 ^oC, ranging from 0.5% to 3%. Most of the mass is lost by 600 ^oC and is most likely due to removal of surface water or hydroxyl species.

The thermal stability of hexagonal $YMnO_3$ and x = 0.8 was also investigated. The two samples were calcined at 1000 ^oC for 2 hours and the XRD after heating is shown in Fig. 5.13 and Fig. 5.14. Hexagonal $YMnO_3$ still remained after calcination

but peaks due to YMn_2O_5 were also observed. While the x = 0.8 remained stable with no other impurities detected.

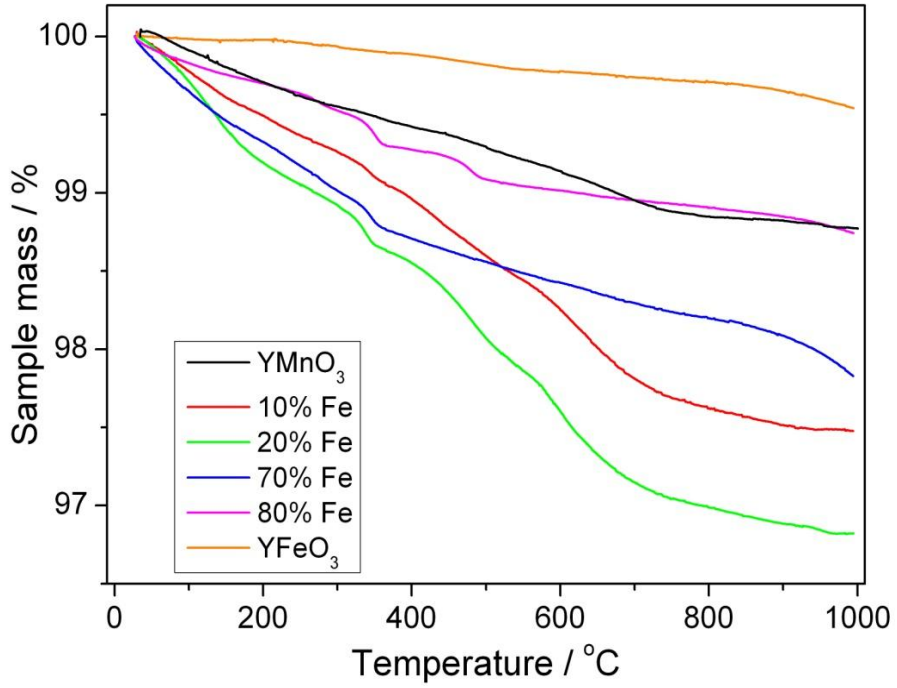

Fig. 5.12 TGA of $YMn_{1-x}Fe_xO_3$ heated from 30 to 1000 °C in air

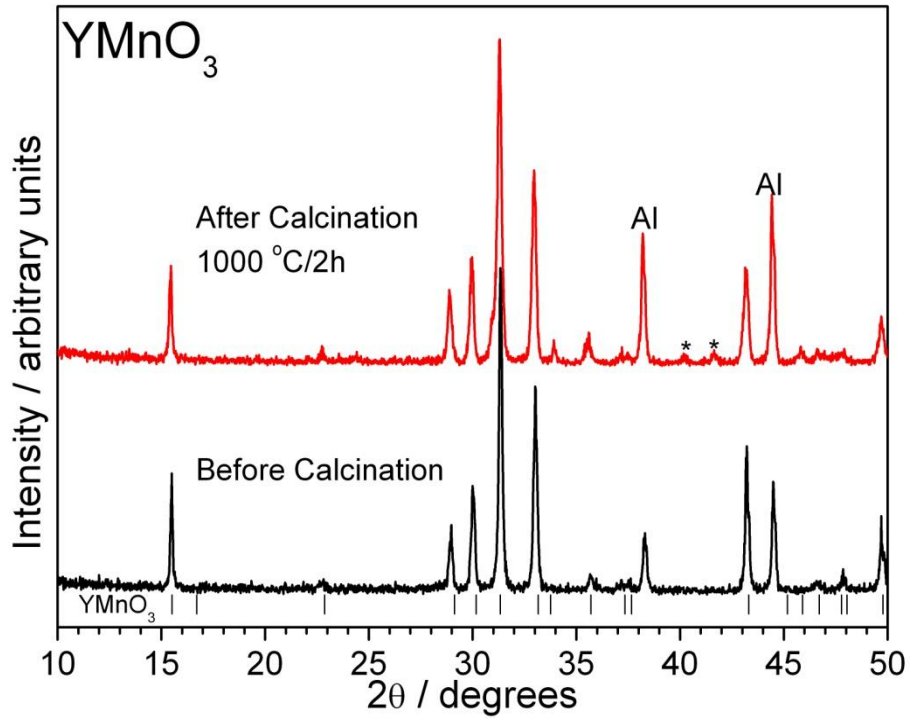

Fig. 5.13 XRD of $YMnO_3$, before and after calcinations at 1000 °C for 2 hours. YMn_2O_5 impurity is labelled with *

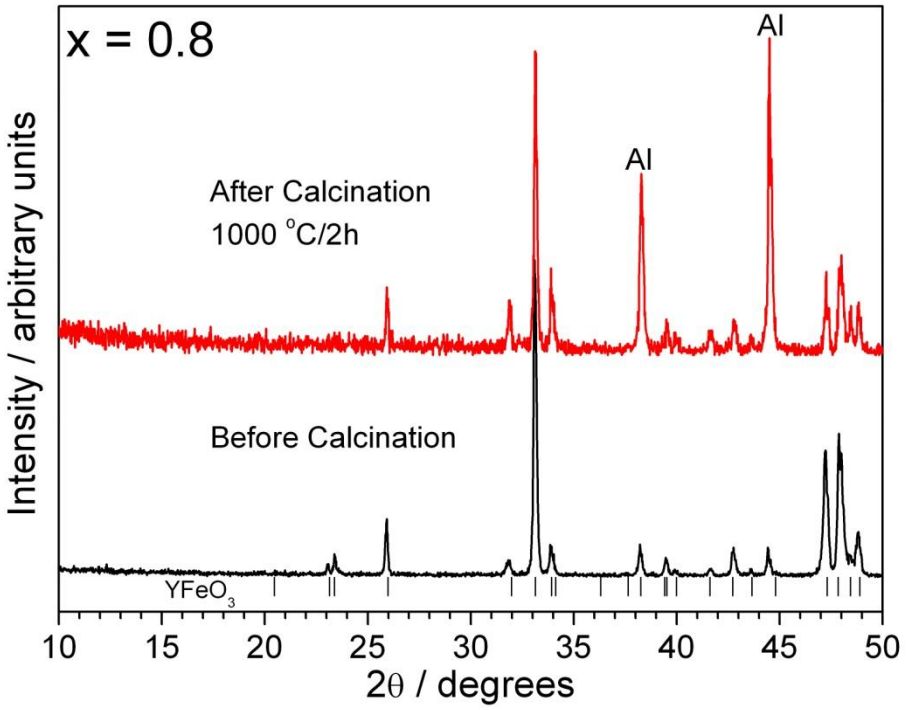

Fig. 5.14 XRD of $YMn_{1-x}Fe_xO_3$, x = 0.8, before and after calcination at 1000 °C for 2 hours

5.3 Conclusion

This chapter has presented a preliminary account of the scope for the synthesis of doped hexagonal perovskites. Pure $YMnO_3$ can be prepared by a comproportionation hydrothermal reaction between MnO_4^- and Mn^{2+}. There is direct evidence for the inclusion of Fe^{3+} for x = 0.1 in place of Mn^{3+} in $YMnO_3$ but above this level, impurity phases are seen. Similarly, pure $YFeO_3$ (an orthorhombic perovskite) can be prepared and the Fe^{3+} can be replaced by Mn^{3+} up to $YMn_{0.3}Fe_{0.7}O_3$. The samples prepared in this chapter are presently being studied for their multiferroic properties by collaborators in Institute of Physics, Chinese Academy of Sciences, Beijing.

5.4 References

(1) Huang, Z. J.; Cao, Y.; Sun, Y. Y.; Xue, Y. Y.; Chu, C. W. *Phys. Rev. B* **1997**, *56*, 2623.

(2) Lee, S.; Pirogov, A.; Han, J. H.; Park, J. G.; Hoshikawa, A.; Kamiyama, T. *Phys. Rev. B* **2005**, *71*, 4.

(3) Medvedeva, J. E.; Anisimov, V. I.; Korotin, M. A.; Mryasov, O. N.; Freeman, A. J. *J. Phys.-Condes. Matter* **2000**, *12*, 4947.

(4) Fiebig, M.; Lottermoser, T.; Frohlich, D.; Goltsev, A. V.; Pisarev, R. V. *Nature* **2002**, *419*, 818.

(5) Fujimura, N.; Ishida, T.; Yoshimura, T.; Ito, T. *Appl. Phys. Lett.* **1996**, *69*, 1011.

(6) Ito, D.; Fujimura, N.; Yoshimura, T.; Ito, T. *J. Appl. Phys.* **2003**, *93*, 5563.

(7) Zhou, J. S.; Goodenough, J. B.; Gallardo-Amores, J. M.; Moran, E.; Alario-Franco, M. A.; Caudillo, R. *Phys. Rev. B* **2006**, *74*, 7.

(8) Munoz, A.; Alonso, J. A.; Martinez-Lope, M. J.; Casais, M. T.; Martinez, J. L.; Fernandez-Diaz, M. T. *Phys. Rev. B* **2000**, *62*, 9498.

(9) Katsufuji, T.; Mori, S.; Masaki, M.; Moritomo, Y.; Yamamoto, N.; Takagi, H. *Phys. Rev. B* **2001**, *64*, 6.

(10) Kimura, T.; Goto, T.; Shintani, H.; Ishizaka, K.; Arima, T.; Tokura, Y. *Nature* **2003**, *426*, 55.

(11) Fiebig, M. *J. Phys. D-Appl. Phys.* **2005**, *38*, R123.

(12) Stampler, E. S.; Sheets, W. C.; Prellier, W.; Marks, T. J.; Poeppelmeier, K. R. *J. Mater. Chem.* **2009**, *19*, 4375.

(13) Zheng, H. W.; Liu, Y. F.; Zhang, W. Y.; Liu, S. J.; Zhang, H. R.; Wang, K. F. *J. Appl. Phys.* **2010**, *107*, 4.

(14) Choi, T.; Lee, J. *Appl. Phys. Lett.* **2004**, *84*, 5043.

(15) Fujimura, N.; Sakata, H.; Ito, D.; Yoshimura, T.; Yokota, T.; Ito, T. *J. Appl. Phys.* **2003**, *93*, 6990.

(16) Sekhar, M. C.; Lee, S.; Choi, G.; Lee, C.; Park, J. G. *Phys. Rev. B* **2005**, *72*, 6.

(17) Nugroho, A. A.; Bellido, N.; Adem, U.; Nenert, G.; Simon, C.; Tjia, M. O.; Mostovoy, M.; Palstra, T. T. M. *Phys. Rev. B* **2007**, *75*, 5.

(18) Asaka, T.; Nemoto, K.; Kimoto, K.; Arima, T.; Matsui, Y. *Phys. Rev. B* **2005**, *71*, 6.

(19) Cao, X. Q.; Kim, C. S.; Yoo, H. I. *J. Am. Ceram. Soc.* **2001**, *84*, 1265.

(20) Veres, A.; Noudem, J. G.; Fourrez, S.; Bailleul, G. *Solid State Sci* **2006**, *8*, 137.

(21) Samal, S. L.; Green, W.; Lofland, S. E.; Ramanujachary, K. V.; Das, D.; Ganguli, A. K. *J. Solid State Chem.* **2008**, *181*, 61.

(22) Han, T. C.; Wu, P. J.; Shih, Y. L. *J. Appl. Phys.* **2012**, *111*.

(23) Ma, Y.; Wu, Y. J.; Lin, Y. Q.; Chen, X. M. *J. Mater. Sci.-Mater. Electron.* **2010**, *21*, 838.

(24) Wu, C. T.; Hsu, Y. Y.; Lin, B. N.; Ku, H. C. *Physica B* **2003**, *329*, 709.

(25) Pinto, H.; Shachar, G.; Shaked, H. *Solid State Commun.* **1970**, *8*, 597.

(26) Ma, Y.; Chen, X. M.; Wu, Y. J.; Lin, Y. Q. *Ceram. Int.* **2010**, *36*, 727.

(27) Wang, Y. W.; Lu, X. Y.; Chen, Y.; Chi, F. L.; Feng, S. H.; Liu, X. Y. *J. Solid State Chem.* **2005**, *178*, 1317.

(28) Spooren, J.; Walton, R. I.; Millange, F. *J. Mater. Chem.* **2005**, *15*, 1542.

(29) Modeshia, D. R.; Walton, R. I. *Chem. Soc. Rev.* **2010**, *39*, 4303.

(30) Shannon, R. D. *Acta Crystallogr. Sect. A* **1976**, *32*, 751.

(31) Katsufuji, T.; Masaki, M.; Machida, A.; Moritomo, M.; Kato, K.; Nishibori, E.; Takata, M.; Sakata, M.; Ohoyama, K.; Kitazawa, K.; Takagi, H. *Phys. Rev. B* **2002**, *66*, 8.

(32) Shen, H.; Xu, J. Y.; Jin, M.; Jiang, G. J. *Ceram. Int.* **2012**, *38*, 1473.

(33) Sundarayya, Y.; Mandal, P.; Sundaresan, A.; Rao, C. N. R. *J. Phys.-Condes. Matter* **2011**, *23*, 7.

(34) Iliev, M. N.; Lee, H. G.; Popov, V. N.; Abrashev, M. V.; Hamed, A.; Meng, R. L.; Chu, C. W. *Phys. Rev. B* **1997**, *56*, 2488.

(35) Fukumura, H.; Matsui, S.; Harima, H.; Kisoda, K.; Takahashi, T.; Yoshimura, T.; Fujimura, N. *J. Phys.-Condes. Matter* **2007**, *19*, 9.

(36) Martin-Carron, L.; de Andres, A.; Martinez-Lope, M. J.; Casais, M. T.; Alonso, J. A. *J. Alloy. Compd.* **2001**, *323*, 494.

(37) Vermette, J.; Jandl, S.; Mukhin, A. A.; Ivanov, V. Y.; Balbashov, A.; Gospodinov, M. M.; Pinsard-Gaudart, L. *J. Phys.-Condes. Matter* **2010**, *22*, 5.

(38) Liu, Y. F.; Wang, B.; Zheng, H. W.; Liu, X. Y.; Gu, Y. Z.; Zhang, W. F. *Chinese Phys. Lett.* **2010**, *27*, 3.

(39) Iliev, M. N.; Abrashev, M. V.; Lee, H. G.; Popov, V. N.; Sun, Y. Y.; Thomsen, C.; Meng, R. L.; Chu, C. W. *Phys. Rev. B* **1998**, *57*, 2872.

(40) Iliev, M. N.; Abrashev, M. V.; Laverdiere, J.; Jandl, S.; Gospodinov, M. M.; Wang, Y. Q.; Sun, Y. Y. *Phys. Rev. B* **2006**, *73*, 6.

(41) Zhang, M. F.; Liu, J. M.; Liu, Z. G. *Appl. Phys. A-Mater* **2004**, *79*, 1753.

(42) Takahashi, J.; Matsubara, E.; Arima, T.; Hanamura, E. *Phys. Rev. B* **2003**, *68*, 5.

(43) Wu, L.; Yu, J. C.; Zhang, L. Z.; Wang, X. C.; Li, S. K. *J. Solid State Chem.* **2004**, *177*, 3666.

Chapter 6 – Hydrothermal Synthesis and Characterisation of doped TiO_2 materials

6.1 Background

TiO_2, also known as titania, is widely used as a white pigment because of its brightness and high refractive index making it very suitable in applications such as in paint, sunscreen and food colouring.[1-4] TiO_2 has spurred a lot of research interest in the past few decades ever since the discovery of TiO_2 photoassisted electrochemical splitting of water by Fujishima and Honda.[5] It is also very suitable for environmental applications because of its non-toxicity, stability and low cost. Its ability to decompose a large variety of organic compounds into harmless products allows it to be used in various applications such as the purification of wastewaters, protective coatings and self-cleaning materials.[6-10]

TiO_2 exists in a number of crystalline forms including rutile, anatase and brookite. In recent years, the hydrothermal synthesis for these phases has been reported. Each of these phases exhibit different physical properties making them suitable for different applications. As the two most investigated phases of TiO_2, anatase is widely reported to be more photocatalytically active than rutile, while rutile is the thermodynamically stable form of TiO_2 and is stable in highly acidic or basic environments. It also has a high dielectric constant and better photo-absorption property in the visible light wavelength range.

Generally, rutile is prepared by calcination at high temperatures. However, such conditions results in the formation of large particle sizes which is undesirable

for photocatalytic activity. Most of the techniques adopted for the synthesis of TiO_2 generally produce anatase at low temperatures. Hence, it is a challenge to obtain highly crystalline rutile TiO_2 with small particle sizes at low temperatures, since the anatase or other polymorphs tend to crystallise from solution.

Recently, Aryanpour *et al.* had published a theoretical paper investigating the structural and electronic properties of W(IV)-doped TiO_2.[11] They outlined the possibility of W doped TiO_2 in replacing conventional carbon black in catalyst support applications. The requirements for a catalyst support are: (i) must be conductive by more than 1 Scm^{-1}, (ii) stable up to 1.5 V with respect to the standard hydrogen electrode and (iii) stable in acidic environments.[11] Rutile TiO_2 easily fulfills the stability requirements but unfortunately, it is an insulator. However, conductivity can be acquired by doping rutile TiO_2 with a suitable dopant such as W since the ionic radius of W^{4+} (0.66 Å, 6 coordination) is similar to Ti^{4+} (0.605 Å, 6 coordination).[12] WO_2 can conduct electricity and has a rutile-like structure with distorted WO_6 octahedra.[13-14] The model made by Aryanpour *et al.* for a 50% W(IV) doped TiO_2 showed that the levels around the Fermi level is mainly made up of W 5d states and the material is a conductor.[11] They also concluded that this conductivity is retained even at low doping levels (10%).

The synthesis of rutile W-TiO_2 has been reported using high temperature methods. Peters *et al.* reported single crystals of rutile $Ti_{0.54}W_{0.46}O_2$ prepared by CO_2-laser technique where high temperatures above 1500 ^oC were used.[15] Whereas Subban *et al.* reported the synthesis of $Ti_{0.7}W_{0.3}O_2$ in the rutile structure via sol-gel technique.[16] The high temperature used resulted in W^{4+} being oxidised to W^{6+} so to reduce the W, they calcined the sample with stoichiometric amount of Zr foil at

750 ^{o}C for 2 days. The Zr formed ZrO_2 and the W^{6+} was reduced to W^{4+}. However, no results confirming the oxidation state of W were shown.

Currently, the majority of W-doped TiO_2 prepared via hydrothermal synthesis have been reported to have the anatase structure and W oxidation state of +6. For example, Kim *et al.* have hydrothermally synthesised W(VI) doped TiO_2 from $H_3PW_{12}O_{40}$ and TiO_2 in NaOH solution at 250 ^{o}C for 3 days.[17] Putta *et al.* prepared W-doped anatase TiO_2 hydrothermally from Na_2WO_4 and tetra(n-butoxyl) titanium at 200 ^{o}C for 10 hours and reported an improved photocatalytic activity compared to pure TiO_2.[18] While Tian *et al.* used $Ti(SO_4)_2$ instead and prepared W doped TiO_2 at a lower temperature and shorter reaction time (120 ^{o}C / 3 hours).[19] The literature also suggests that the introduction of tungsten oxide makes anatase more stable than rutile.[20-21]

Sn doping has also been reported to improve the photocatalytic activity of TiO_2.[22-24] Sn-TiO_2 materials are also of interest in the field of gas sensing, where they give enhanced response to H_2 and CO compared to the pure binary oxides.[25-28] Both TiO_2 and SnO_2 have the rutile structure so they can form a solid solution across the whole compositional range. However, studies carried out by Naidu *et al.* and Hirata *et al.* reported that although the $Sn_xTi_{1-x}O_2$ solid solution can be formed over the whole range, only TiO_2 rich and the SnO_2 rich phases are thermodynamically stable at room temperature.[29-30] The compositions close to x = 0.5 require high temperatures to allow their formation. Hirata *et al.* prepared $Sn_xTi_{1-x}O_2$ by the solid state reaction technique (1500 ^{o}C) intervals of x = 0.1 but samples with Sn concentration of x = 0.3, 0.4, 0.5 and 0.6 phase separated to SnO_2 and TiO_2.[30] However, Uchiyama *et al.* successfully prepared a solid solution of $Sn_xTi_{1-x}O_2$ at

intervals of x = 0.2 via a sol-gel method using $TiOSO_4$ and SnF_2.[31] They did not observe any phase separation in the XRD pattern in the x = 0.4 and 0.6 samples.

Sn-TiO_2 has also been prepared hydrothermally. Li *et al.* obtained Sn-rich Sn-TiO_2 nanospheres from TiF_4 and SnF_4 at 180 ^oC for 2–8 hours.[32] The size of the nanospheres can be controlled by varying the reaction time and temperature. Duan *et al.* prepared Sn-TiO_2 with anatase structure from tetrabutyl titanate and tin *tert*-butoxide in a mixture of solvents.[33] Trotochaud *et al.* performed solvothermal reactions using Ti isopropoxide and $SnCl_4$ in benzyl alcohol, however, mixture of anatase and rutile were observed in the XRD pattern for Ti rich samples.[34] The use of microwave-hydrothermal synthesis was reported by Yang *et al.* where they obtained solid solutions of Sn-TiO_2 nanoparticles in a very short period of time (200 ^oC for 10 min).[35]

Lanthanide metals such as Ce have been found to enhance visible-light photoactivity of TiO_2.[36-37] The Ce dopant can introduces states within the band gap of TiO_2 thus allowing better absorption of photons in the visible spectrum. Cerium doping have also received much interest since the 3+ and 4+ oxidation state allow cerium oxide to shift between CeO_2 and Ce_2O_3 under oxidising and reducing conditions.[38] The two oxidation state also exhibit different optical and photocatalytic properties. Cerium oxides have also been used in catalytic systems owing to their remarkable redox property and oxygen storage capacity.[39-40]

Tong *et al.* prepared Ce-TiO_2 by controlled hydrolysis of titanium tetrabutoxide with water generated via an esterification reaction between ethanol and acetic acid, followed by hydrothermal treatment.[41] The products consisted of spherical particles with a single anatase phase. Xue *et al*. prepared Ce-TiO_2

nanotubes by first preparing TiO_2 nanotubes hydrothermally and then Ce was introduced by an impregnation method. Liu *et al.* obtained Ce-TiO_2 nanosheets from $Ce(NO_3)_3$ solution and TiO_2 at 130 ^oC for 3 hours.[42] However, the as-prepared materials were a mixture of anatase and rutile phases. Wang *et al.* prepared mesoporous Ce-TiO_2 via sol-gel and hydrothermal reaction, using tetrabutyl orthotitanate and $Ce(NO_3)_3$ as the starting materials,[43] whereas Xiao *et al.* reacted cetyltrimethylammonium bromide, $Ti(SO_4)_2$ and $Ce(NO_3)_3$ hydrothermally to make mesoporous Ce-TiO_2.[44]

In this chapter, the hydrothermal synthesis of TiO_2 and Ce doped TiO_2 along with other materials exhibiting the rutile structure is explored. The initial aim was to prepare W^{4+}-doped TiO_2 with the rutile structure since this phase was reported to have useful properties for catalytic applications. It also presented a synthetic challenge since low temperature techniques have usually produced the anatase phase. Hence, more research needs to be done on W (IV) doped rutile TiO_2 and especially its preparation via hydrothermal route. This chapter also describes the preparation of other metal doped TiO_2, particularly Sn and Ce, in a single step hydrothermal reaction. These materials were characterised with several techniques and the photocatalytic property of the Ce-TiO_2 materials was investigated.

6.2 Hydrothermal synthesis of W-doped TiO_2

6.2.1 Synthesis

Attempted hydrothermal synthesis of W-doped TiO_2 (rutile) was performed based on the method published by Tomita *et al.* for TiO_2.[45] Ti powder (Alfa, 99%)

and W powder (Alfa, 99.9%) were weighed according to the values shown in Table 6.1. The mixture of powders were then dissolved in an ice cold 4 : 1 mixture of H_2O_2 (Aldrich, 30 wt. % in H_2O) and aqueous NH_3 solution (Aldrich, 35%). After 2-3 hours, a yellow solution was obtained and glycolic acid was added. The solution was then heated to 80 ^oC to remove the excess H_2O_2 until a yellow gel was obtained. The yellow gel was then dissolved in 10 mL distilled water to get a yellow solution. A slight modification to the procedure was made after this step, whereby the yellow solution was passed through a filter paper to remove any undissolved powder. The solution was then transferred to a ~20 mL Teflon liner. The Teflon liner was then sealed in a steel autoclave and placed in an oven pre-heated at 240 ^oC. After heating for 24 hours, the autoclaves were left to cool to room temperature. The solid products were recovered by suction filtration, washed thoroughly with warm water and dried overnight at 70 ^oC in a drying oven. The product was then ground into powder for further characterisation.

Table 6.1 Amounts of starting materials used for W-TiO_2 synthesis

W conc./%	Ti/g	W/g	H_2O_2/mL	NH_3/mL	Glycolic acid/g
0	0.4788	-	40	10	2
1	0.4738	0.0184			
5	0.4549	0.0919			
10	0.4309	0.1838			
20	0.3830	0.3677			
30	0.3352	0.5516			
40	0.2873	0.7354			
50	0.2394	0.9193			
70	0.1436	1.2869			
100	-	1.8385			

6.2.2 Characterisation

Powder XRD was used to determine the phase purity of the W-TiO_2 samples prepared. The XRD in Fig. 6.1 showed that TiO_2 was successfully prepared hydrothermally using the 'glycolic acid' method and the observed pattern matched the simulated pattern for rutile TiO_2. The sharp peaks indicated that the sample was crystalline with large particle sizes. This rutile phase was still observed upon addition of 1% W and the colour changed from white (undoped TiO_2) to light grey. The absence of any other peaks suggested that the doping was successful and the W was incorporated into the structure.

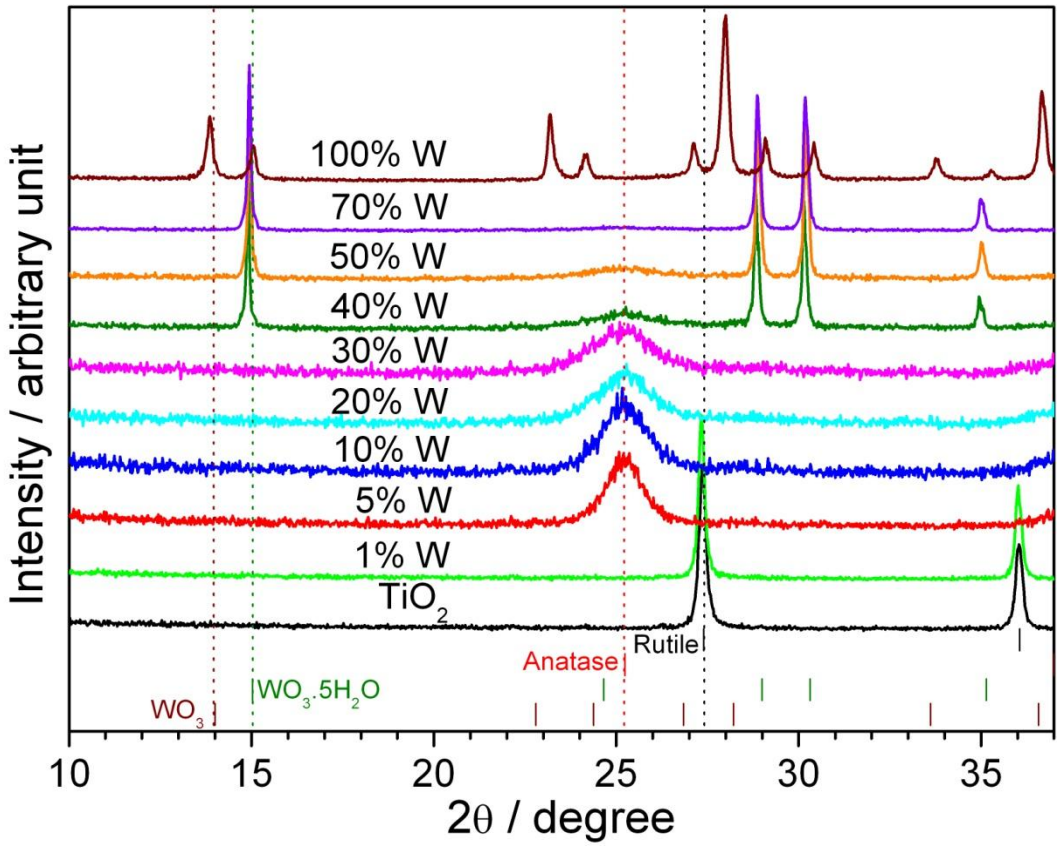

Fig. 6.1 Powder XRD of W-TiO_2, where the tick marks correspond to rutile TiO_2, anatase TiO_2, $WO_3 \cdot 5H_2O$ and WO_3. The dotted line shows the position of the main peak for each material

At 5% W, the rutile phase disappeared and replaced with poorly crystalline anatase TiO_2 instead. This anatase phase persisted up to 30% W. Other studies on W-TiO_2 also reported a preference for the anatase phase over rutile in W-TiO_2 even in W doping as low as 1% W.[46] At 40 to 70% W, peaks corresponding to $WO_3 \cdot 5H_2O$ were observed in the XRD pattern while the anatase TiO_2 peak intensity decreased. When the synthesis was carried out with only W (100% W), without the presence of Ti, a mixture of WO_3 and $WO_3 \cdot 5H_2O$ was obtained.

The XRD patterns for undoped TiO_2 and 1% W were refined with the rutile structure model, space group $P4_2/mnm$ (Fig. 6.2). The Al peaks at 38^o and 44^o were also fitted with cubic $Fm3m$ model. The XRD patterns for 5 to 30% W were fitted with the anatase structure model, space group $I4_1/amd$. The summary of the refinement and the lattice parameters obtained are shown in Table 6.2.

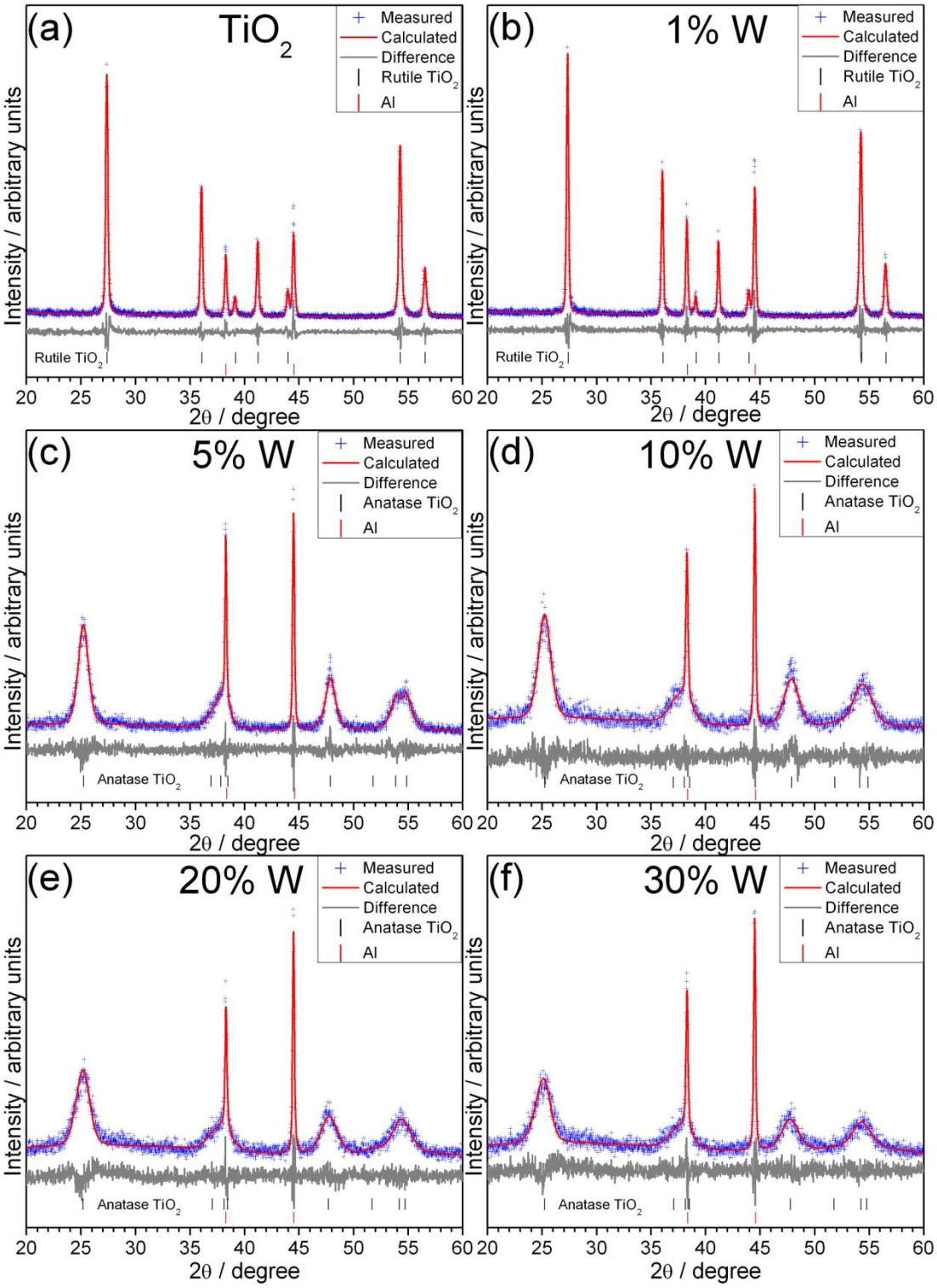

Fig. 6.2 Pawley refinement of XRD for a) TiO_2, b) 1% W, c) 5% W, d) 10% W, e) 20% W and f) 30% W. Al peaks were due to the Al sample holder used

Table 6.2 Summary of Pawley refinement of W-TiO_2 from XRD

W conc. / %	Space group	*a* / Å	*b* / Å	*c* / Å	Cell volume / $Å^3$	R_{wp}	R_p	gof
0	$P4_2/mnm$	4.598(1)	4.598(1)	2.957(1)	62.53(1)	23.157	16.011	1.188
1		4.600(1)	4.600(1)	2.957(1)	62.59(1)	22.508	16.250	1.209
5	$I4_1/amd$	3.797(2)	3.797(2)	9.511(6)	137.19(15)	18.251	13.927	1.074
10		3.797(3)	3.797(3)	9.458(28)	136.41(46)	17.961	13.871	1.117
20		3.809(3)	3.809(3)	9.436(42)	136.94(64)	16.533	12.918	1.099
30		3.805(3)	3.805(3)	9.428(45)	136.55(68)	15.756	12.441	1.109

The lattice parameters obtained from Pawley refinement for rutile TiO_2 and 1% W (Fig. 6.3) showed very little change which is almost within the error of the calculation. On the other hand, the cell volume of anatase W-TiO_2 ranges from 136.5 and 137 $Å^3$ with no clear trend. The *c* lattice parameter decreased upon increasing W concentration while the *a* lattice parameter increased instead. The ionic radius of W^{4+} (0.66 Å, 6 coordination) is bigger than Ti^{4+} (0.605 Å, 6 coordination)[12] so it is expected that the lattice parameter will increase upon successful incorporation of W^{4+}. However, since the cell volume did not increase, then W^{4+} doped TiO_2 was not achieved or W^{6+} (0.6 Å, 6 coordination) was incorporated into TiO_2 instead.

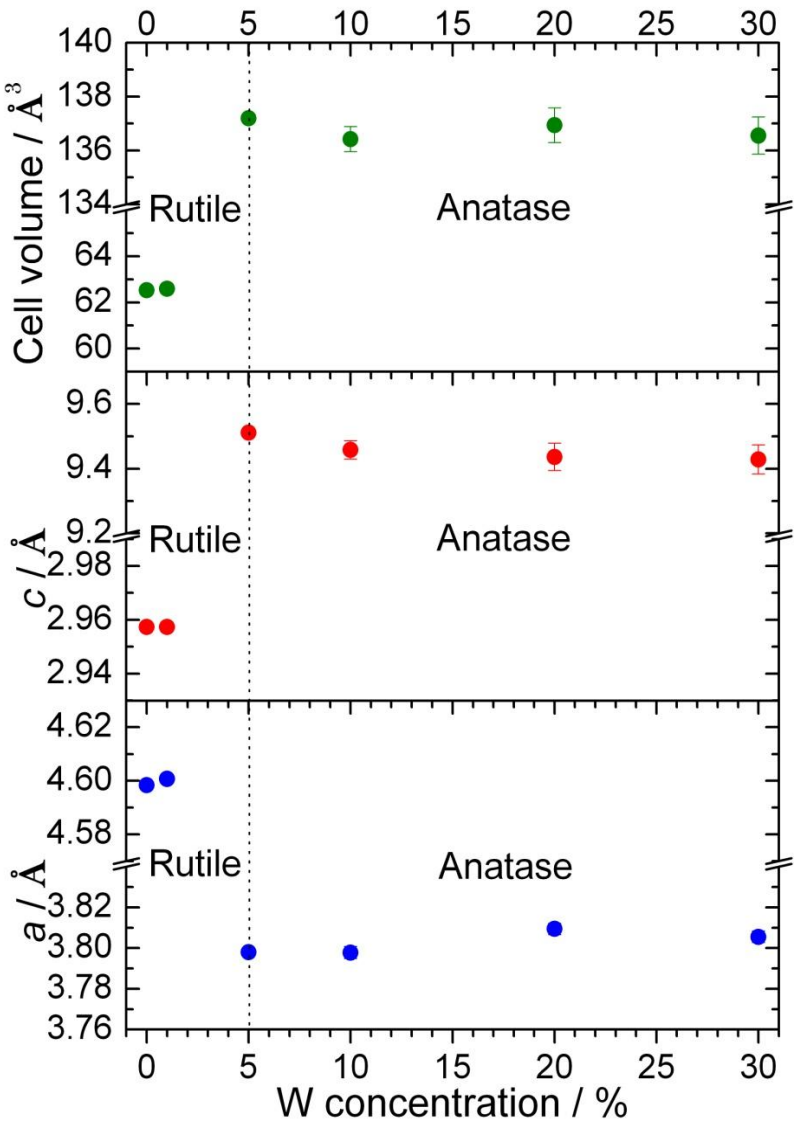

Fig. 6.3 Lattice parameters of W-TiO_2 series obtained from Pawley refinement of XRD data

The Raman spectra of undoped TiO_2 and 1% W-TiO_2 showed three broad bands at about 235, 444 and 608 cm^{-1} and a small band at 143 cm^{-1} (Fig. 6.4). Rutile TiO_2 with space group $P4_2/mnm$ has four Raman active modes, A_{1g} + B_{1g} + B_{2g} + E_g.[47-48] The broad band at 235 cm^{-1} has been assigned to a combination band[47,49] while the bands at 143, 444 and 608 cm^{-1} have been assigned to B_{1g}, E_g and A_{1g} mode respectively. The band at 444 cm^{-1} shifted to 436 cm^{-1} upon 1% W doping.

Although this shift may be related to a change in particle size, Cheng *et al.* observed a shift to lower values for both the E_g and A_{1g} band, instead of just one band, as the particle size of rutile becomes smaller.[50] On the other hand, the Raman spectra for W-TiO_2 samples between 5 and 20% W were similar to the Raman spectrum of anatase TiO_2.[51-52] The main band was observed at 153 cm^{-1} and assigned to the E_g mode. Smaller bands at 395 (B_{1g}), 517 (A_{1g}) and 635 cm^{-1} (E_g) are also characteristic of anatase TiO_2.

The Raman spectra of 40% W-TiO_2 displays the anatase band at 153 cm^{-1} but the three smaller anatase bands disappeared and replaced with a broad band between 600 and 800 cm^{-1}, which resulted from hydrated WO_3.[53] From the XRD pattern, this sample consisted of a mixture of anatase TiO_2 and $WO_3 \cdot 5H_2O$. A similar Raman spectrum was observed for the 70% W but the intensity of the broad band between 200 and 350 cm^{-1} increased significantly. At 100% W, the Raman spectra agree well with reported spectra of WO_3. The broad band between 200 and 350 cm^{-1} can be attributed to the W-O-W bending mode of the bridging oxygen. The bands at 730 and 790 cm^{-1} are related to O-W-O stretching modes, while the bands above 900 cm^{-1} was assigned to terminal W=O bond.[53-54]

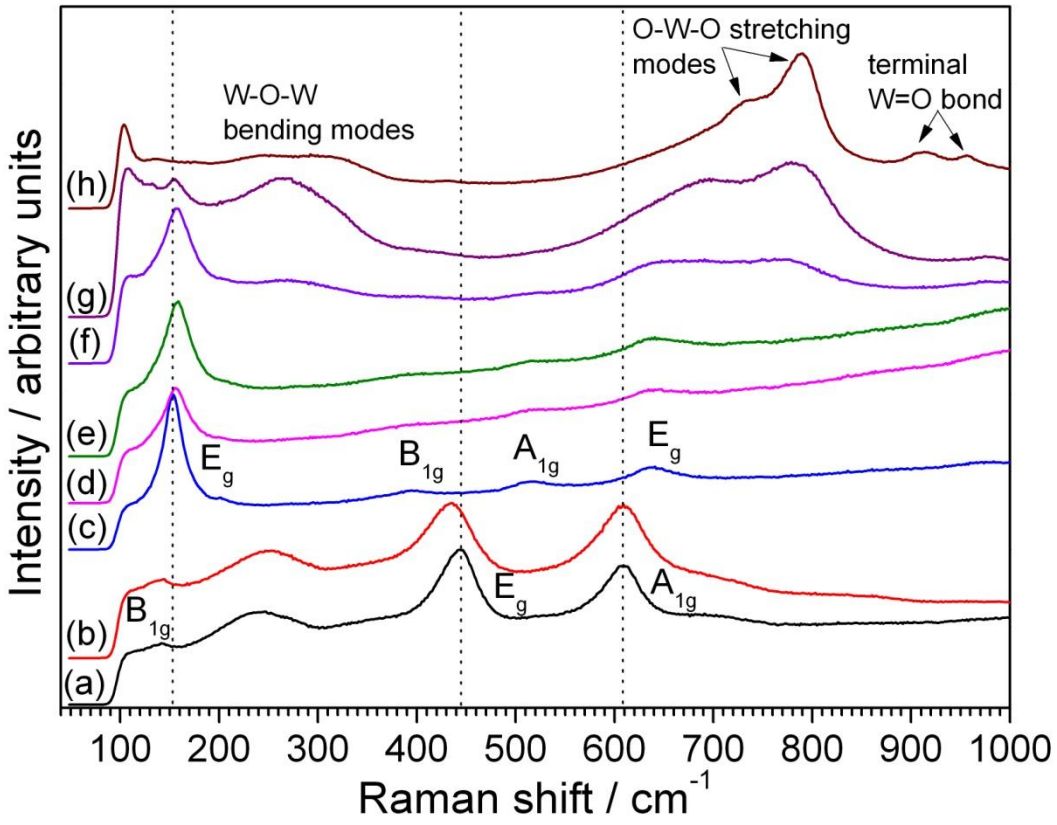

Fig. 6.4 Raman spectra of W-TiO_2 samples, a) TiO_2, b) 1% W, c) 5% W, d) 10% W, e) 20% W, f) 40% W, g) 70% W, h) 100% W

The introduction of W into TiO_2 changed the morphology of the particles. The SEM image of TiO_2 (Fig. 6.5a) showed rod-like particles which were clustered together. Upon the addition of 1% W, the rod-like shapes were lost and spherical particles were obtained. At 10% W, smaller particles were obtained as expected from the broad peaks observed in the XRD pattern. At 50% W and above, the particle size increased. The atomic compositions of the samples obtained from EDXA were close to the expected values (Table 6.3).

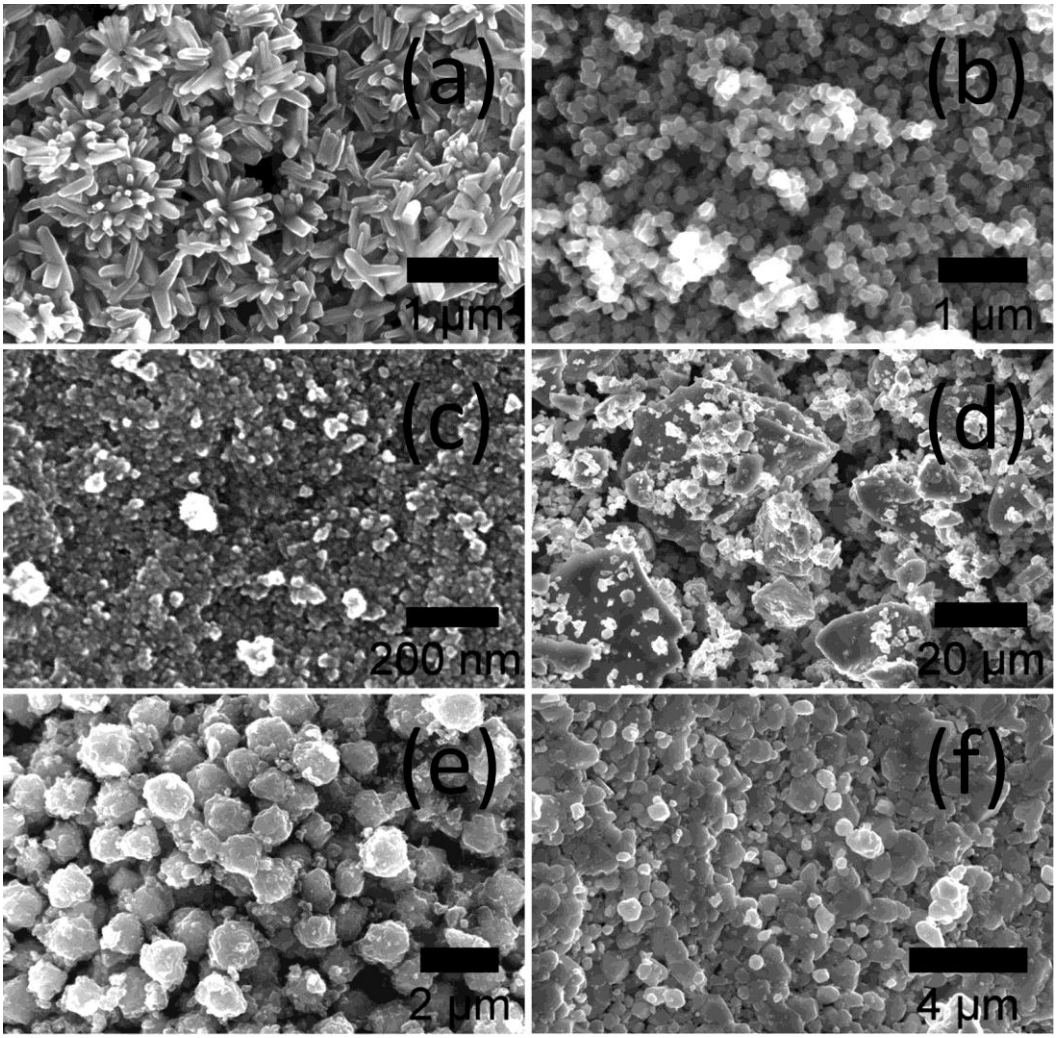

Fig. 6.5 SEM images of W-TiO_2 series: a) TiO_2, b) 1% W, c) 10% W, d) 50% W, e) 70% W, f) WO_3

Table 6.3 Atomic composition of W-TiO_2 obtained from EDXA. Expected values from synthesis are in brackets. *Note: W concentration = [W / (W + Ti)] x 100

W conc. (Expected value) / %	W / %	Ti / %	O / %	W conc.* / %
1	0.6 (0.3)	35.3 (33.3)	64.1 (66.7)	1.7
5	2.5 (1.7)	30.0 (31.7)	67.5 (66.7)	7.7
10	5.4 (3.3)	33.6 (30)	61.0 (66.7)	13.8
30	10.2 (10)	31.3 (23.3)	58.5 (66.7)	24.6
40	14.9 (13.3)	24.7 (20)	60.4 (66.7)	37.6
50	19.5 (16.7)	17.2 (16.7)	63.3 (66.7)	53.1
70	28.5 (23.3)	9.9 (10)	61.5 (66.7)	74.0

The X-ray photoelectron spectra (XPS) of W-TiO_2 samples were collected to determine the oxidation state of W. A typical survey scan of 10% W-TiO_2 is shown in Fig. 6.6, where the main peaks corresponded to W, Ti, O and C. The carbon peaks were due to adventitious carbon contamination on the surface of the samples. Along with the survey scan, a more detailed scan in the binding energy range between 50 and 25 eV were also collected to study the W 4f region for five W-TiO_2 samples and two reference samples, WO_2 and WO_3. The W-TiO_2 spectra were calibrated by setting the position of the C 1s peak to be 284.8 eV.

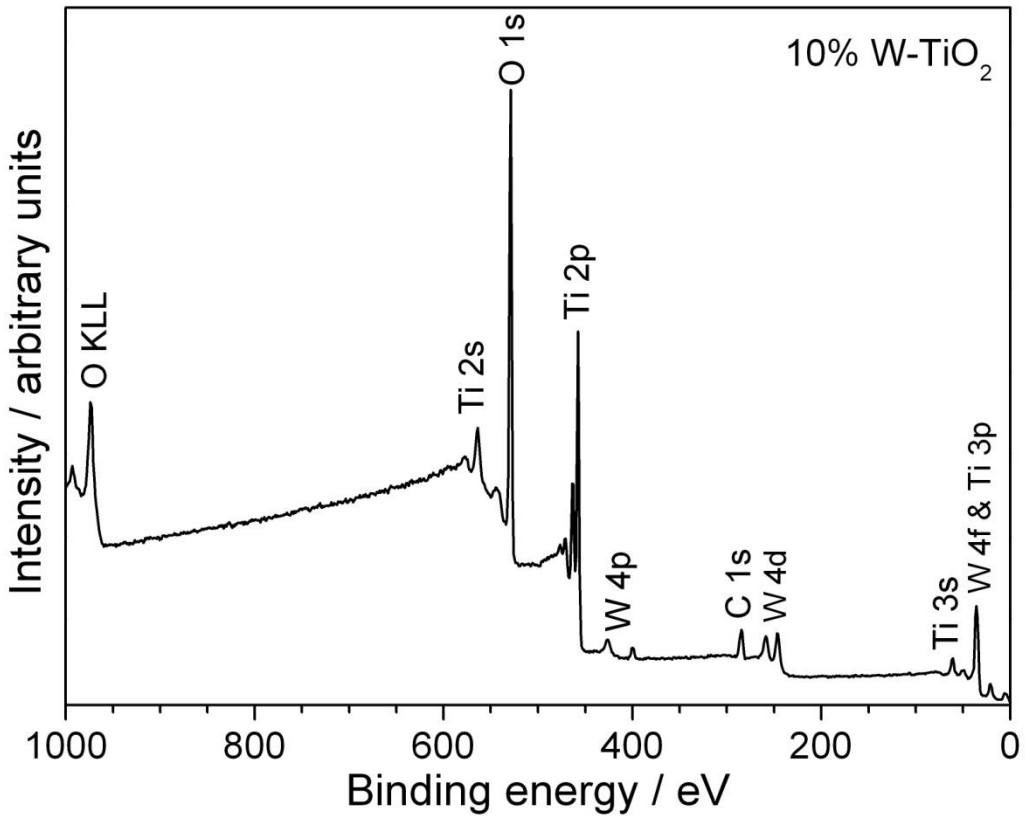

Fig. 6.6 XPS survey scan of 10% W-TiO_2

The longer scans on W 4f for WO_3 showed a doublet band located at 37.5 and 35.5 eV corresponding to the W $4f_{5/2}$ and W $4f_{7/2}$ signals respectively (Fig. 6.7). WO_2 on the other hand has an extra peak at 32.8 eV. This shows that some of the

WO_2 has been surface oxidised to WO_3 causing the W^{6+} doublet to appear. The spectra for W-TiO_2 were made complicated with the overlap of one of the W 4f doublet with a Ti 3p peak positioned at 37.3 eV. So only the W $4f_{7/2}$ peak was observed at 35.5 eV where the intensity of the peak increases going from 5 to 30% W. The position of the W 4f in the W-TiO_2 samples are similar to those of WO_3 so it is clear that the oxidation state of W in the W-TiO_2 samples is 6+.

There was no evidence for the presence of any W metal (expected at 31.1 eV[55]) which may remain from the starting material. If any metallic tungsten was present in the sample, it is probable that at the surface level, all the W metal has been oxidised or it was present in such a low level that it was not detected by XPS.

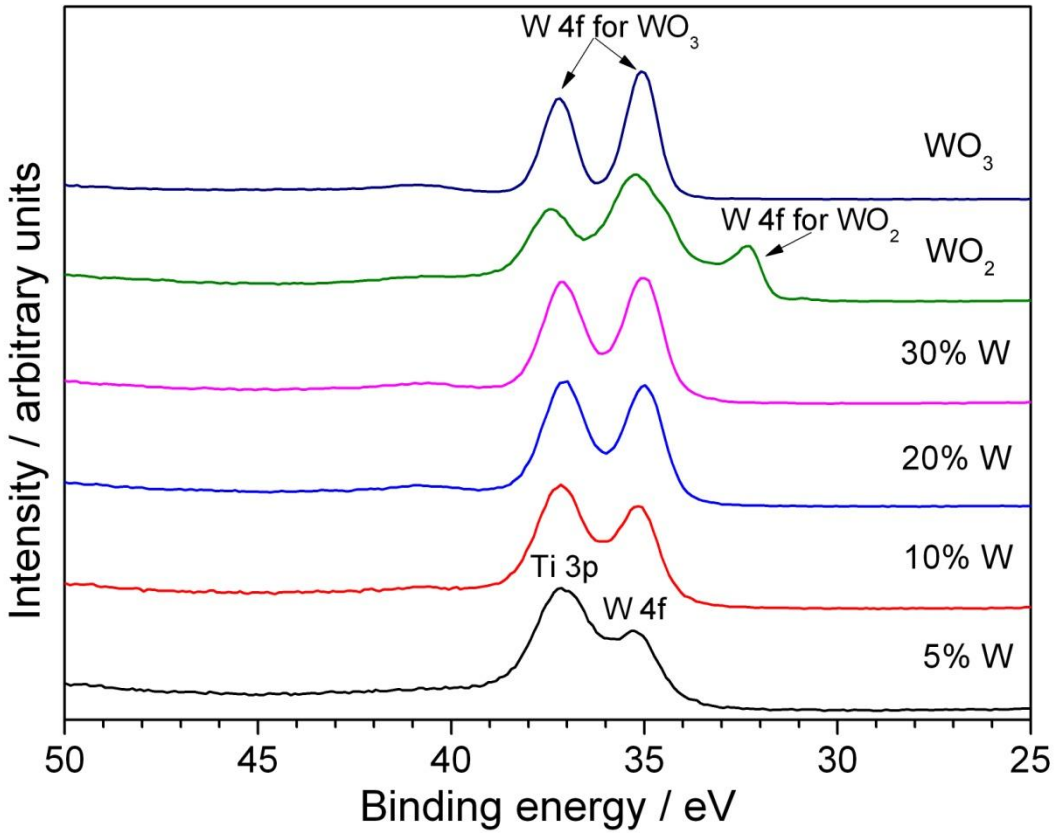

Fig. 6.7 XPS of W-TiO_2 samples along with WO_2 and WO_3 as references

The XPS peaks were fitted to determine the positions of the individual peaks as shown in Fig. 6.8. The backgrounds were fitted with a Shirley-type background and the spectra were deconvoluted into their components with mixed Gaussian-Lorentzian shape lines using CasaXPS software. The position of the Ti 3p peak was kept constant at 37.3 eV[55] while the area ratio of the W $4f_{5/2}$: $W4f_{7/2}$ peaks were set to 3 : 4 and the FWHM ratio was set to 1 : 1. A summary of the peak positions is shown in Table 6.4.

The W 4f spectrum for WO_2 was deconvoluted into two doublet peaks at position 37.5 and 35.5 eV corresponding to W (VI) and at position 34.6 and 32.8 eV for W (IV). The W 4f spectrum for WO_3 was fitted with only one set of doublets with peak positions 37.5 and 35.4 eV corresponding to W (VI). For W-TiO_2 samples, the positions of the W 4f doublet were at about 37.5 and 35.5 eV for the W (VI) $4f_{5/2}$ and $W_{7/2}$ respectively, which were similar to the WO_3 reference sample. Thus the oxidation state of the W found on the surface of the doped TiO_2 samples was 6+.

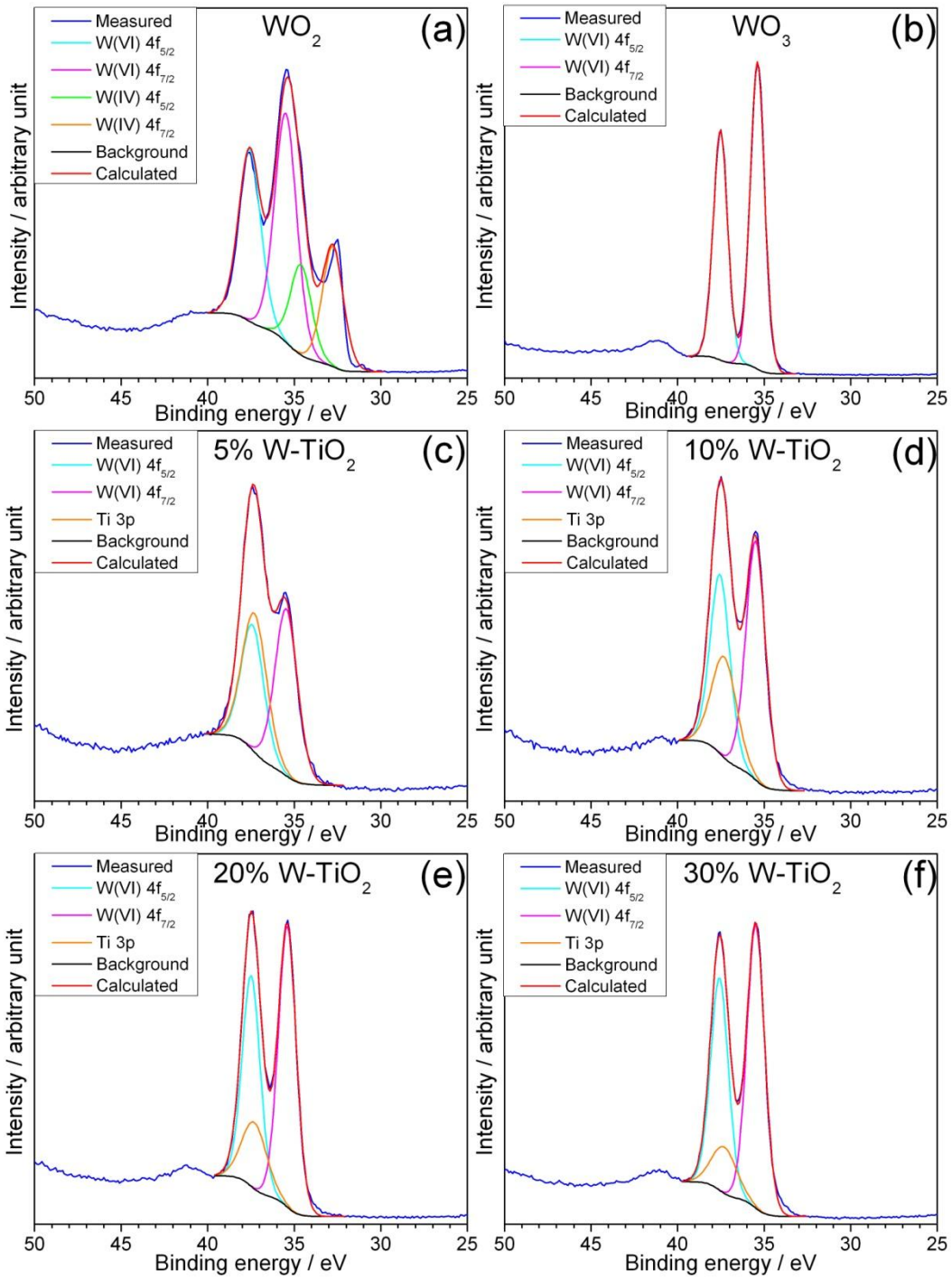

Fig. 6.8 XPS peak fitting for W4f peaks of a) WO_2, b) WO_3, c) 5% W, d) 10% W, e) 20% W and f) 30% W

Table 6.4 Summary of W4f peak positions for W-TiO_2

Sample	Ti 3p	W(VI) $W4f_{5/2}$	W(VI) $W4f_{7/2}$	W(IV) $W4f_{5/2}$	W(IV) $W4f_{7/2}$
WO_2	-	37.57	35.49	34.61	32.77
WO_3	-	37.53	35.39	-	-
5% W	37.3	37.41	35.46	-	-
10% W	37.3	37.55	35.49	-	-
20% W	37.3	37.49	35.40	-	-
30% W	37.3	37.58	35.48	-	-

Fig. 6.9 shows the XPS spectra of Ti 2p for the W-TiO_2 samples. A doublet at positions 464.5 and 458.8 eV was observed and can be attributed to Ti $2p_{1/2}$ and Ti $2p_{3/2}$ for Ti^{4+} respectively. No significant change was observed in the Ti 2p peaks upon increasing addition of W.

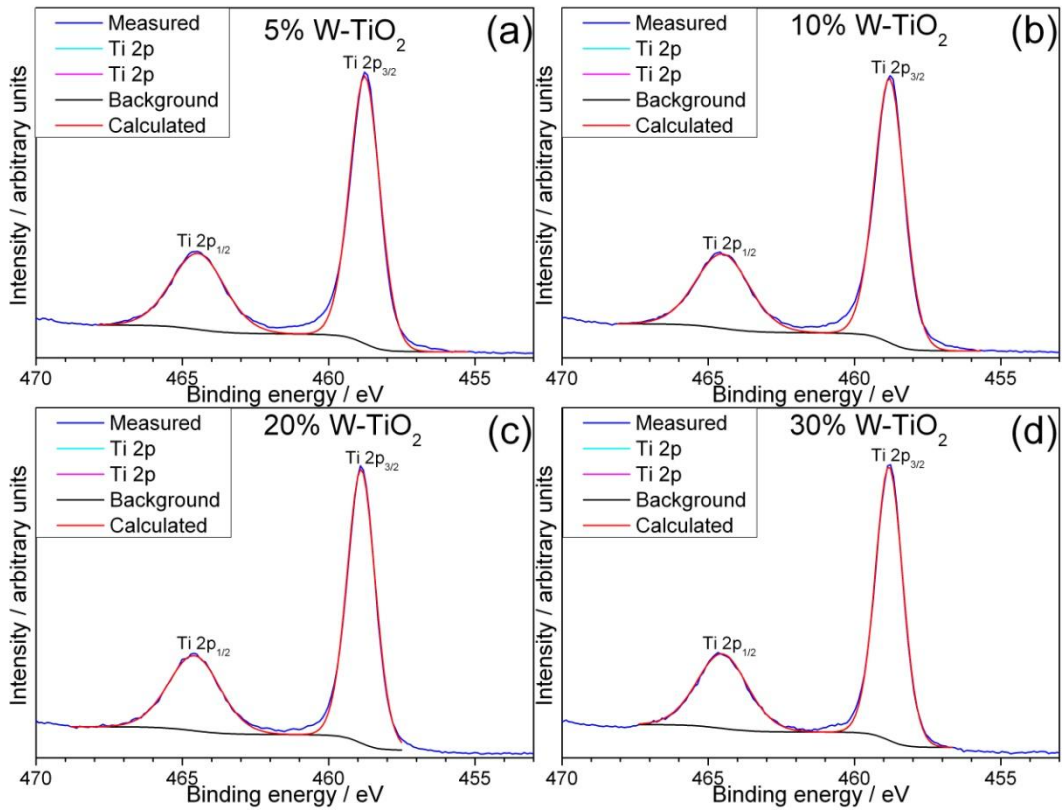

Fig. 6.9 XPS peak fitting for Ti 2p peaks of a) 5% W, b) 10% W, c) 20% W and d) 30% W

The XPS spectra for O 1s for all the samples (Fig. 6.10) composed of a main peak at 530 eV and a shoulder peak at 531 eV. The main peak is due to oxygen bound to Ti while the shoulder peak mainly originates from oxygen in surface hydroxyl groups.[46]

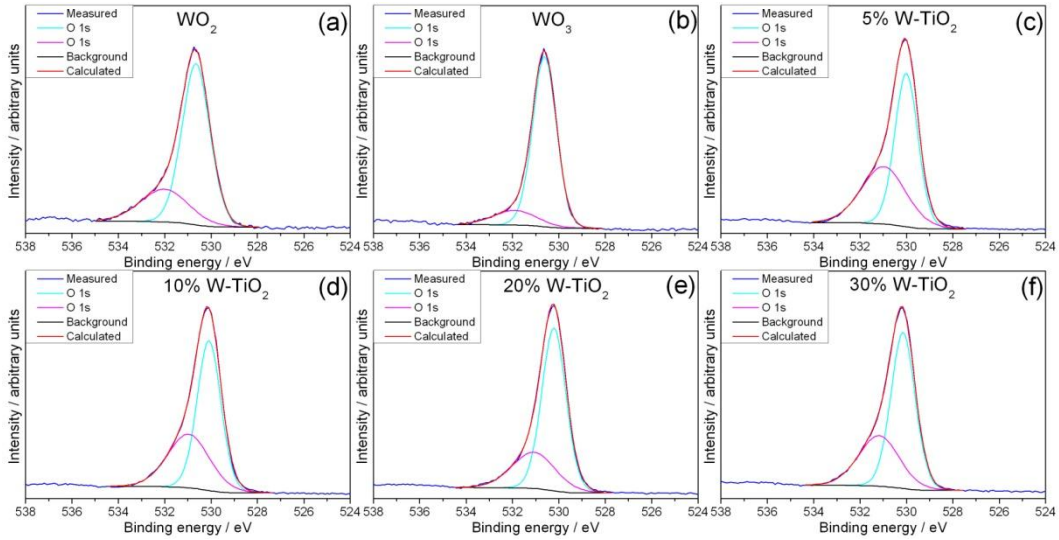

Fig. 6.10 XPS Peak fitting for O 1s peaks of a) WO_2, b) WO_3, c) 5% W, d) 10% W, e) 20% W and f) 30% W

The atomic composition of the surface of W-TiO_2 was also calculated from the XPS data (Table 6.5). The calculated W concentration is slightly higher than the nominal value except for the 30% W. This suggests that more W is on the surface of the sample than expected.

Table 6.5 Atomic composition of W-TiO_2 obtained from XPS. *Note: W concentration = [W/(W+ Ti)] x 100

Sample	W / At.%	Ti / At.%	O / At.%	W conc.* / %
5% W	1.64	20.80	57.44	7.3
10% W	3.36	20.25	58.29	14.2
20% W	4.82	17.15	54.55	21.94
30% W	5.35	14.91	54.73	26.4

6.3 Hydrothermal synthesis of Sn-doped TiO_2

6.3.1 Synthesis

The method used to prepare Sn-doped TiO_2 hydrothermally was by using titanium bisammonium lactato dihydroxide (TiBALD) as the Ti precursor, based on work published by Kandiel *et al.* for pure TiO_2.[56] Stoichiometric amounts of TiBALD solution (Aldrich, 50 wt% in H_2O) and Sn acetate (Alfa-Aesar), as shown in Table 6.6, was mixed in 9 mL H_2O and the solution stirred for 1 hour in a ~20 mL Teflon liner. The Teflon liner was then sealed in a steel autoclave and placed in an oven pre-heated at 240 ^oC. After heating for 24 hours, the autoclaves were left to cool to room temperature. The solid products were recovered by suction filtration, washed thoroughly with warm water and dried overnight at 70 ^oC in a drying oven. The white solid product was then ground into powder for further characterisation.

Table 6.6 Amounts of starting materials used for Sn doped TiO_2 synthesis

Sn conc./%	TiBALD/mL	Sn acetate/g	H_2O/mL
0	0.96	-	9
20	0.77	0.1419	
50	0.48	0.3549	
80	0.19	0.5678	
100	-	0.7096	10

6.3.2 Characterisation

Powder XRD of Sn-TiO_2 series (Fig. 6.11) showed that all the samples have rutile structure. The XRD pattern of TiO_2 has sharp peaks showing that the sample was crystalline. Doping Sn into TiO_2 resulted with a broadening of the XRD peaks, indicating a decrease in the particle size. The peaks also clearly shifted to lower 2θ values and were more obvious at higher angles. Pawley refinement of the XRD

patterns with the tetragonal $P4_2/mnm$ model (space group corresponding to rutile) are shown in Fig. 6.12. A summary of the refinements and the lattice parameters calculated are provided in Table 6.7. The XRD pattern of Sn-TiO_2 fits well when refined with the rutile space group $P4_2/mnm$. However, for the 20% Sn, the peak at 35^o and 53^o were not fitted properly due to the presence of a shoulder peak.

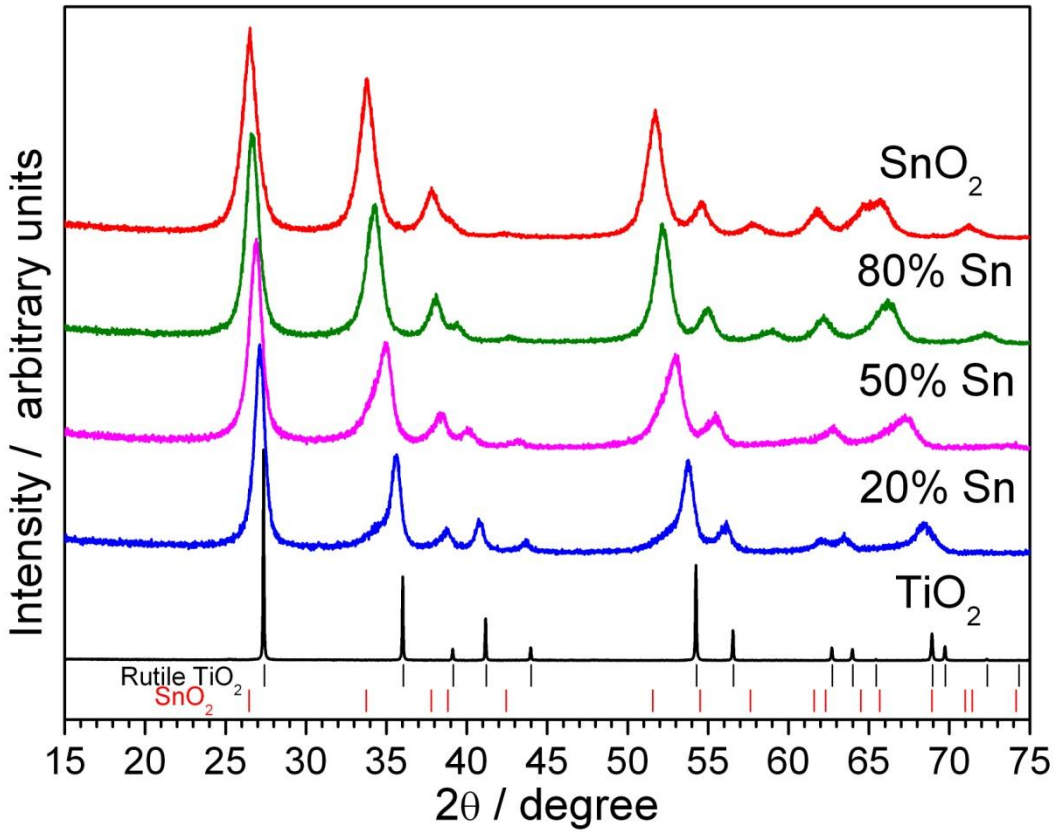

Fig. 6.11 High resolution powder XRD of Sn-TiO_2 samples, where the tick marks correspond to rutile TiO_2 and SnO_2

The lattice parameters obtained from the refinement of the XRD pattern showed a linear increase upon increasing Sn concentration (Fig. 6.13).This confirmed the incorporation of Sn as the ionic radius of Sn (0.69 Å, 6 coordination) is bigger than Ti (0.605 Å, 6 coordination).[12] The crystallite size dimensions of the

Sn-TiO_2 samples calculated from a Scherrer analysis of the XRD data showed a reduction of the particle size from 90 to 7 nm with increasing Sn concentration.

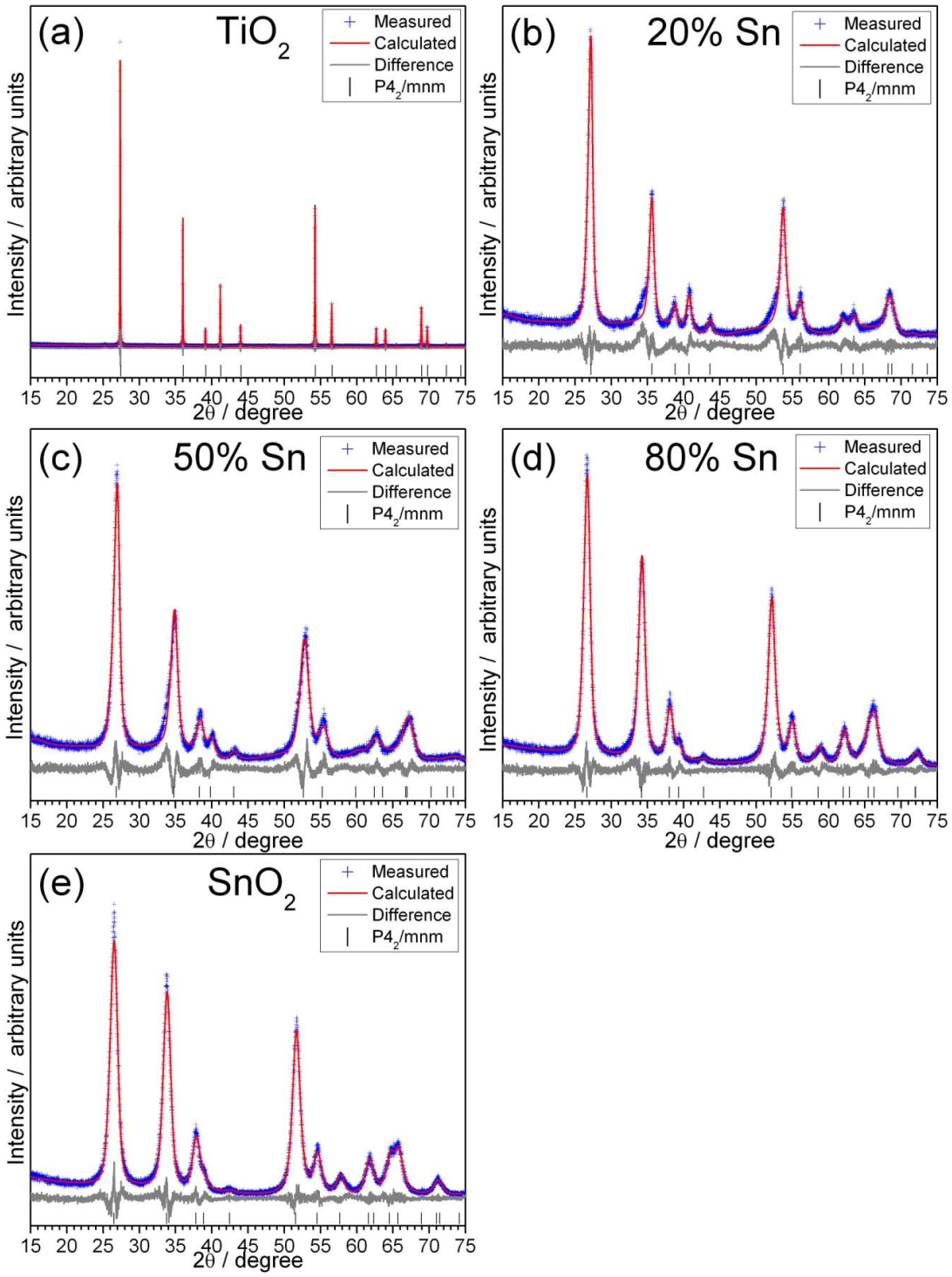

Fig. 6.12 Pawley refinements of XRD for a) TiO_2, b) 20% Sn, c) 50% Sn, d) 80% Sn and e) SnO_2 with the *P*4_2/*mnm* model

Table 6.7 Summary of Pawley refinement of Sn-TiO_2

Sn conc./% (Expected value)	*a*/Å	*c*/Å	Cell volume/Å^3	*c*/*a*	Crystallite size/nm	R_{wp}	R_p	gof
0	4.5968(0)	2.9601(0)	62.548 (1)	0.644	90 ± 41	9.315	7.826	1.409
20	4.6353(8)	3.0014(5)	64.492 (24)	0.648	10 ± 2	12.262	9.131	1.627
50	4.6991(11)	3.0887(6)	68.202 (33)	0.658	9 ± 2	11.887	9.340	1.616
80	4.7288(6)	3.1501(4)	70.441 (20)	0.666	8 ± 2	10.046	7.515	1.382
100	4.7578(6)	3.1961(4)	72.347 (19)	0.672	7 ± 1	9.189	6.859	1.299

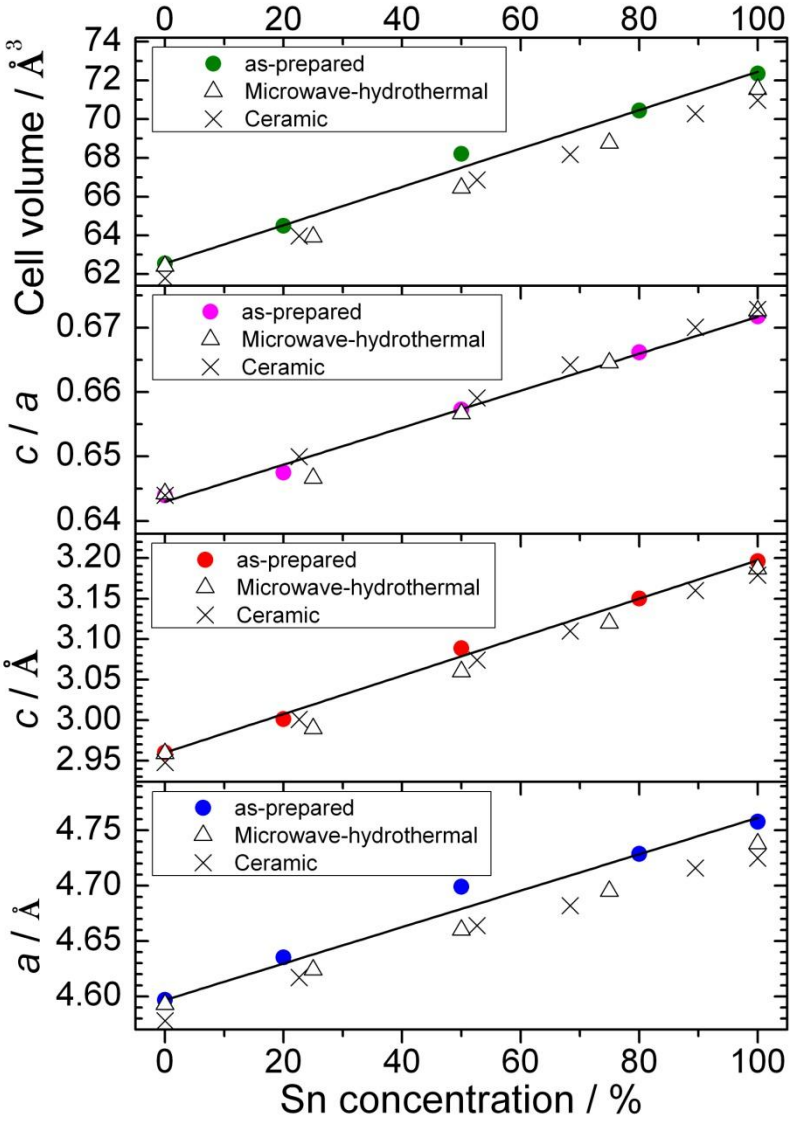

Fig. 6.13 Lattice parameters of Sn-TiO_2 series obtained from Pawley refinement of XRD data. Literature values from Sn-TiO_2 made by microwave-hydrothermal synthesis and ceramic method[35,57]

Both rutile TiO_2 and SnO_2 have the space group $P4_2/mnm$ and display four Raman active modes, $A_{1g} + B_{1g} + B_{2g} + E_g$.[47,58] The Raman spectra of undoped TiO_2 (Fig. 6.14) showed bands at 143, 235, 447 and 610 cm^{-1}. The broad band at 235 cm^{-1} was reported to be a combination band[47,49] while the bands at 143, 446 and 610 cm^{-1} can be assigned to the B_{1g}, E_g and A_{1g} mode respectively. The B_{2g} mode, which was expected at 826 cm^{-1}, was not observed due to its weak intensity.[30] No characteristic bands of anatase TiO_2 were observed, confirming the purity of the as-prepared sample. On the other hand, the Raman spectra of SnO_2 had a high background with a broad band visible at ~570 cm^{-1} and a sharp band at 632 cm^{-1}. The broad band at ~570 cm^{-1} has been reported in the literature to be from amorphous SnO_2.[59-60] The band at 632 cm^{-1} is assigned to the A_{1g} mode. The other 3 modes of SnO_2, expected at 123 (B_{1g}), 475 (E_g) and 773 cm^{-1} (B_{2g}) were not observed due to their weak intensity and high background from the sample.[61]

The Raman spectra of the Sn doped samples resembled that of TiO_2. The band at 446 cm^{-1} (E_g) shifted with increasing Sn concentration but not in a linear way. The band shifted to lower values up to 50% Sn but then returns to higher values at 80% Sn. In contrast, the band at 610 cm^{-1} (A_{1g}) did not show any significant shift until 80% Sn where it shifted slightly to higher values. These trends are identical to the results reported by Hirata *et al.* for TiO_2-SnO_2 samples prepared by solid state synthesis.[30]

The Sn-TiO_2 samples were calcined at 800 ^oC for 3 hours in order to improve the crystallinity and possibly remove the high background in the Raman spectra. The Raman spectra of the calcined samples (Fig. 6.15) showed a similar trend to the as-prepared samples. The E_g band showed a splitting for the 80% Sn sample similar to

the spectra reported by Hirata *et al*.[30] The high background in the 80% Sn and SnO_2 samples were removed and the E_g and B_{2g} bands were clearly observed at 475 and 775 cm^{-1} respectively.

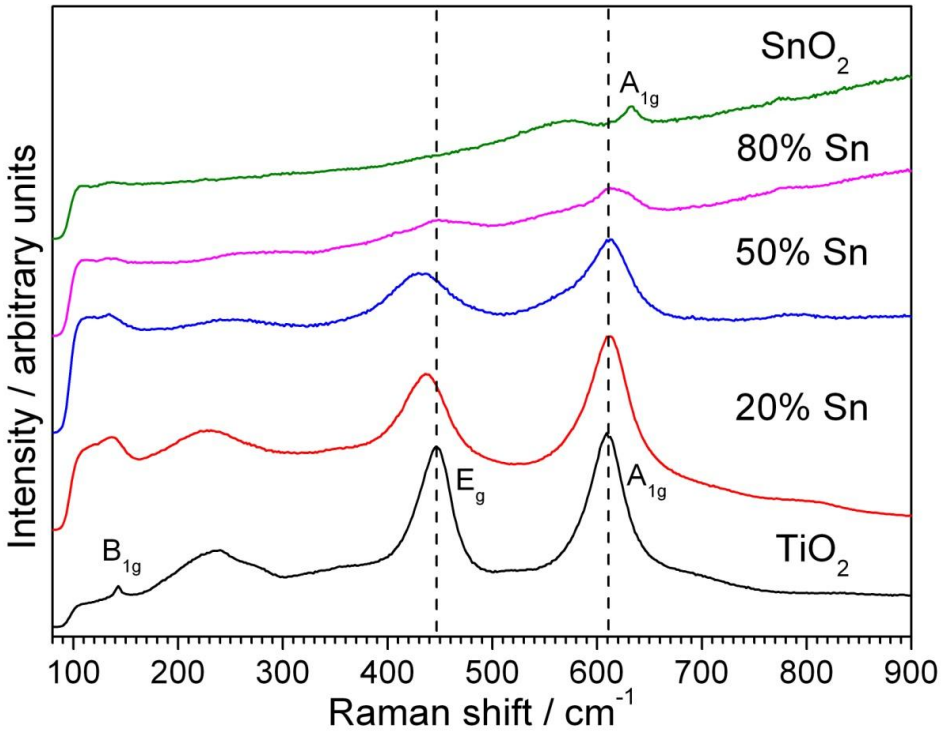

Fig. 6.14 Raman spectra of as-prepared Sn-TiO_2

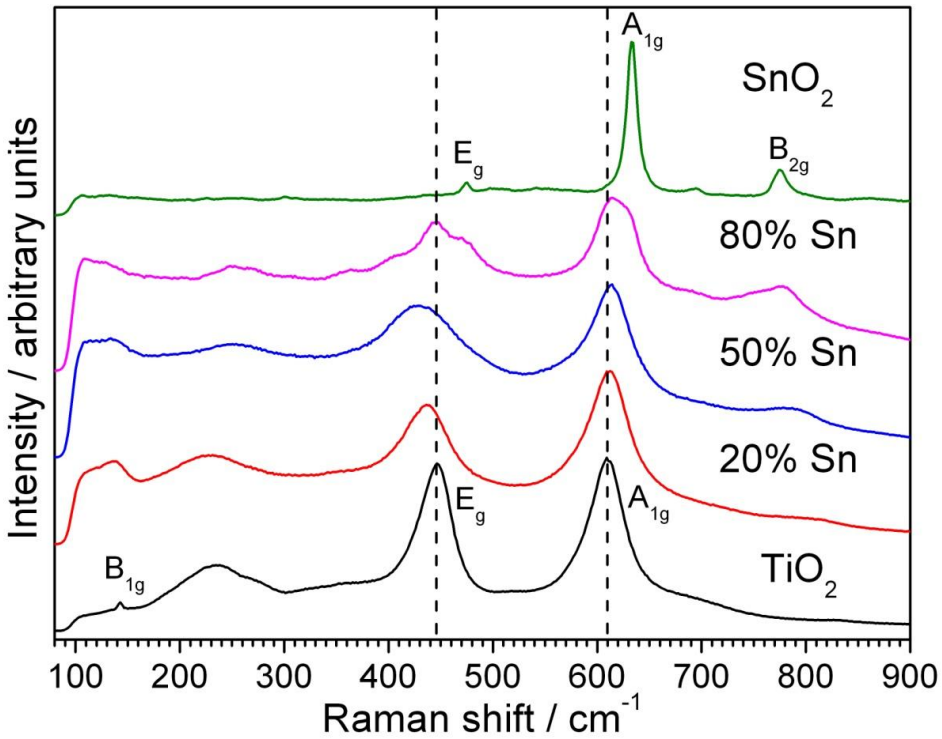

Fig. 6.15 Raman spectra of Sn-TiO_2 after being calcined in air at 800 ^oC for 3 hours

The rutile TiO_2 made from TiBALD (Fig. 6.16) has a different morphology than the TiO_2 made from the 'glycolic acid' method in Section 6.2. The particles consisted of a mixture of rod-shaped particles and polyhedral particles with well-defined corners. The rod shaped morphology was reported in the original work by Kandiel *et al.*,[56] although they used a lower reaction temperature of 200 ^{o}C. This morphology disappears upon addition of Sn, where much smaller, irregular particles were obtained. Upon increasing the Sn concentration from 20% to 100% Sn, there was little change in the morphology. This result agrees with the XRD data where the Sn doped TiO_2 exhibit much broader peaks compared to TiO_2. The atomic compositions of the Sn-TiO_2 samples were also confirmed by EDXA (Table 6.8). In each case, the calculated Sn concentration is slightly higher than the nominal value.

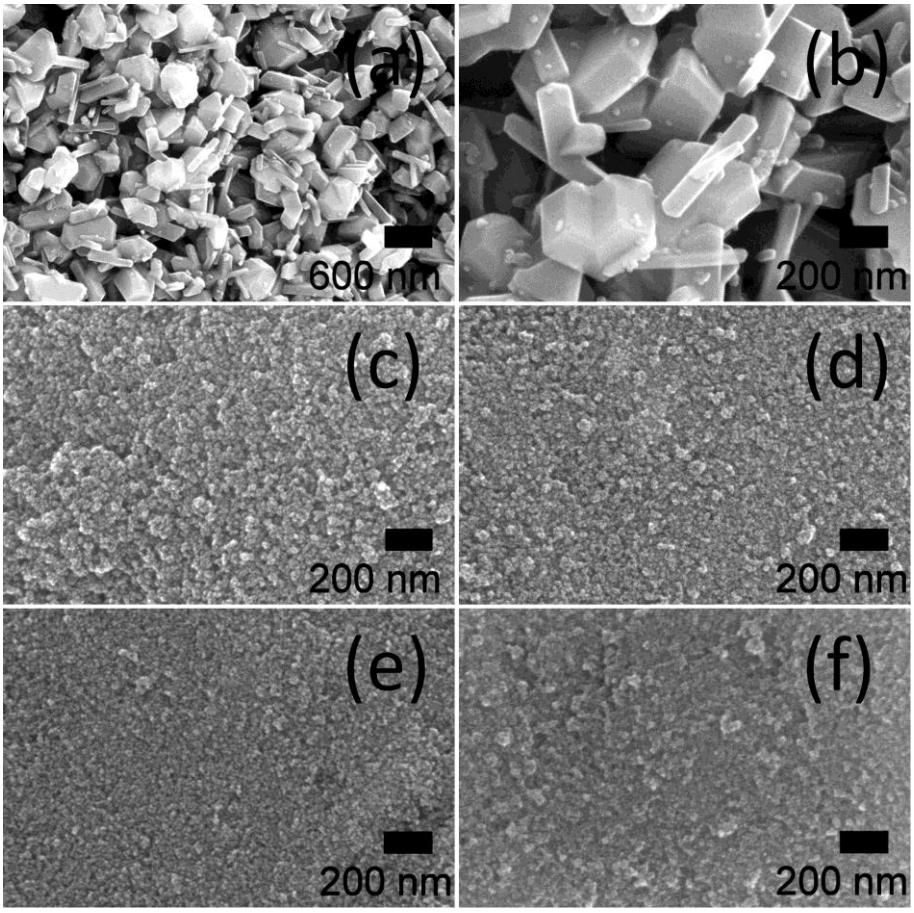

Fig. 6.16 SEM images of a-b) TiO_2, c) 20% Sn, d) 50% Sn, e) 80% Sn and f) SnO_2

Table 6.8 Atomic composition of Sn-TiO_2 obtained from EDXA. Expected values from synthesis are in brackets. *Note: Sn concentration = [Sn / (Sn + Ti)] x 100

Sn conc. (Expected value)/%	Sn/%	Ti/%	O/%	Sn conc.*/%
20	8.5 (6.7)	28.1 (26.7)	63.4 (66.7)	23.2
50	18.1 (16.7)	13.7 (16.7)	68.1 (66.7)	56.9
80	28.1 (26.7)	5.0 (6.7)	66.9 (66.7)	84.9

TEM images of the 50% and 80% Sn-TiO_2 confirmed the small crystallite sizes to be around 10 nm (Fig. 6.17).

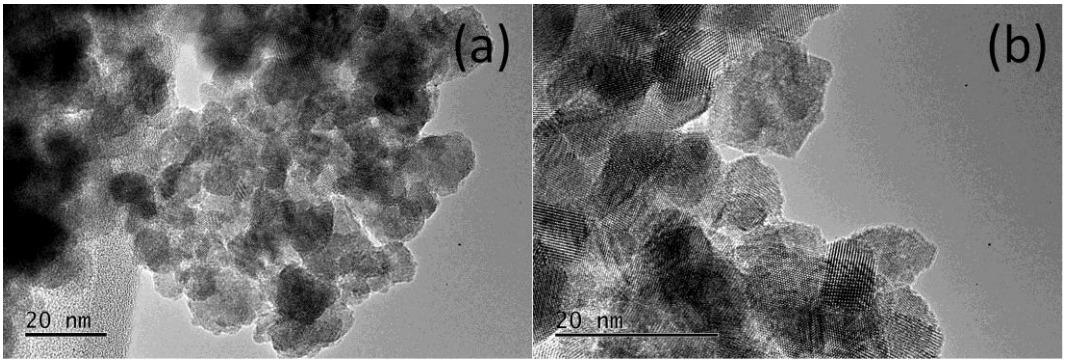

Fig. 6.17 TEM images of a) 50% Sn and b) 80% Sn-TiO_2

In-situ XRD of 20% Sn-TiO_2 (Fig. 6.18) showed that the sample phase separated upon heating to 900 ^{o}C. The XRD pattern of 20% Sn-TiO_2 at 30 ^{o}C, 900 ^{o}C and after cooling back to 30 ^{o}C is shown in Fig. 6.19. The shoulder peak at 35^{o} and 53^{o} appeared to increase in intensity upon heating, suggesting that phase separation has occurred. However, peaks due to the ceramic sample holder were also observed in those positions in the XRD pattern.

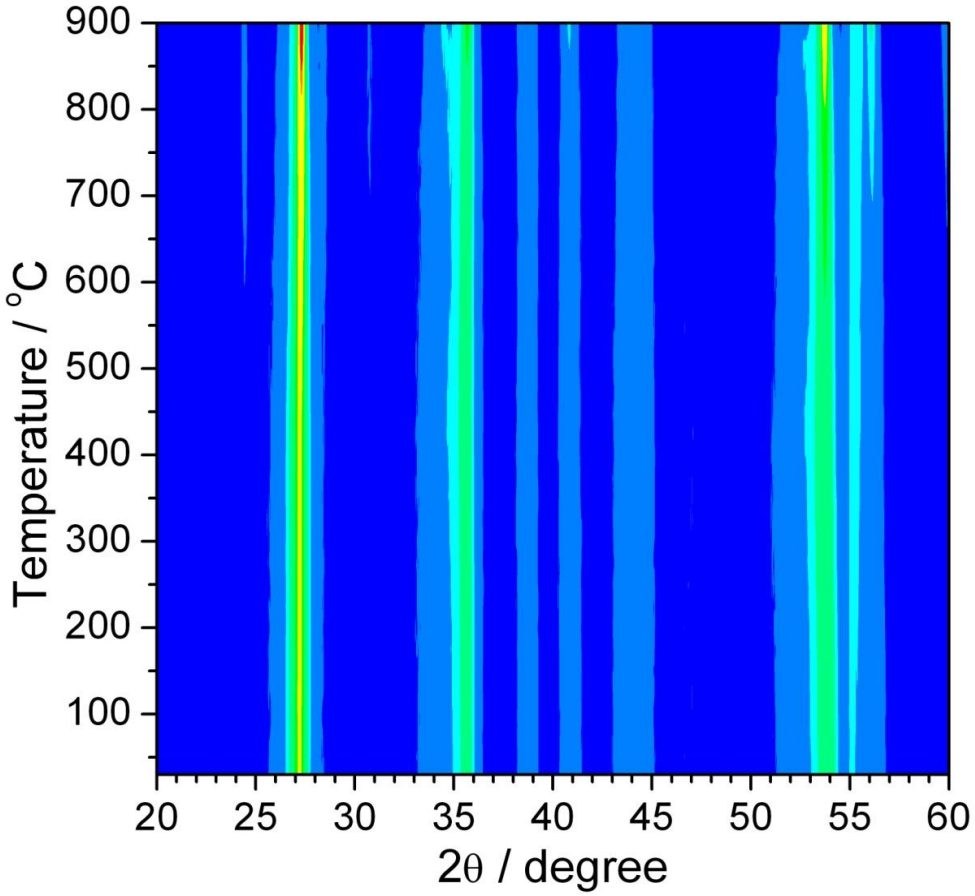

Fig. 6.18 *In-situ* XRD of 20% Sn-TiO_2 heated from 30 °C to 900 °C in air

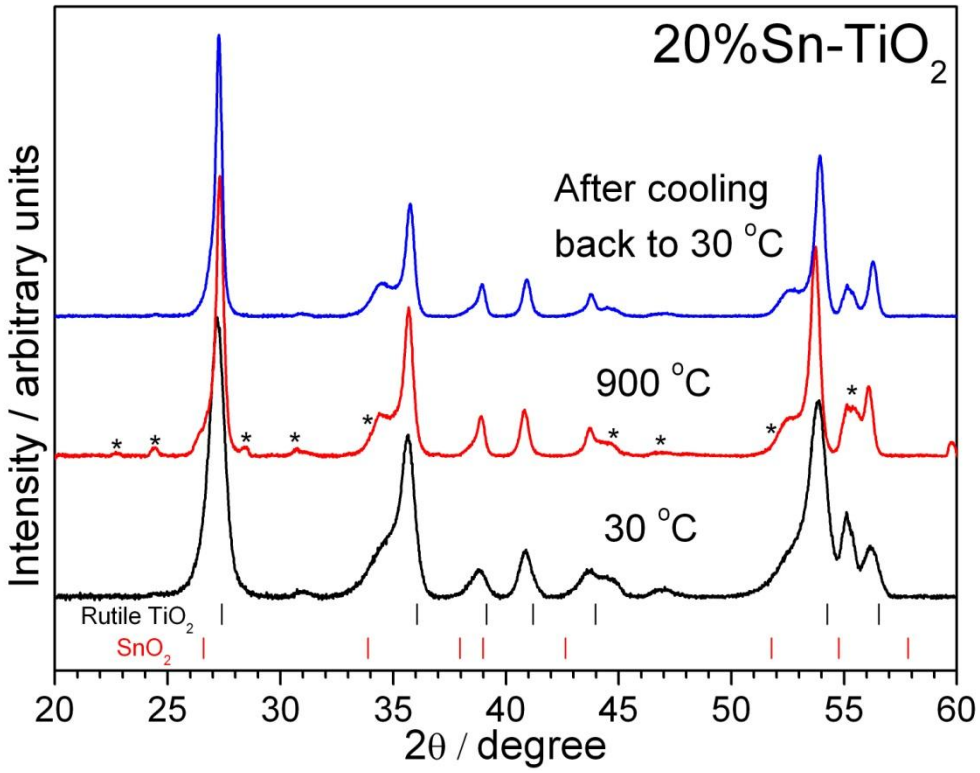

Fig. 6.19 XRD of 20% Sn-TiO_2 at 30 °C, 900 °C and after cooling back to 30 °C. Peaks due to ceramic sample holder are labelled with *

In-situ XRD of 50% Sn-TiO_2 (Fig. 6.20) showed that the rutile phase remained stable and the peaks became sharper when the sample was heated to 900 ^oC. However, the peak at 35^o and 53^o shifted upon heating. It may be possible that amorphous SnO_2 was present in the as-prepared sample and a solid-state reaction occurred with the sample upon heating. The XRD pattern of 50% Sn-TiO_2 at 30 ^oC, 900 ^oC and after cooling back to 30 ^oC is shown in Fig. 6.21.

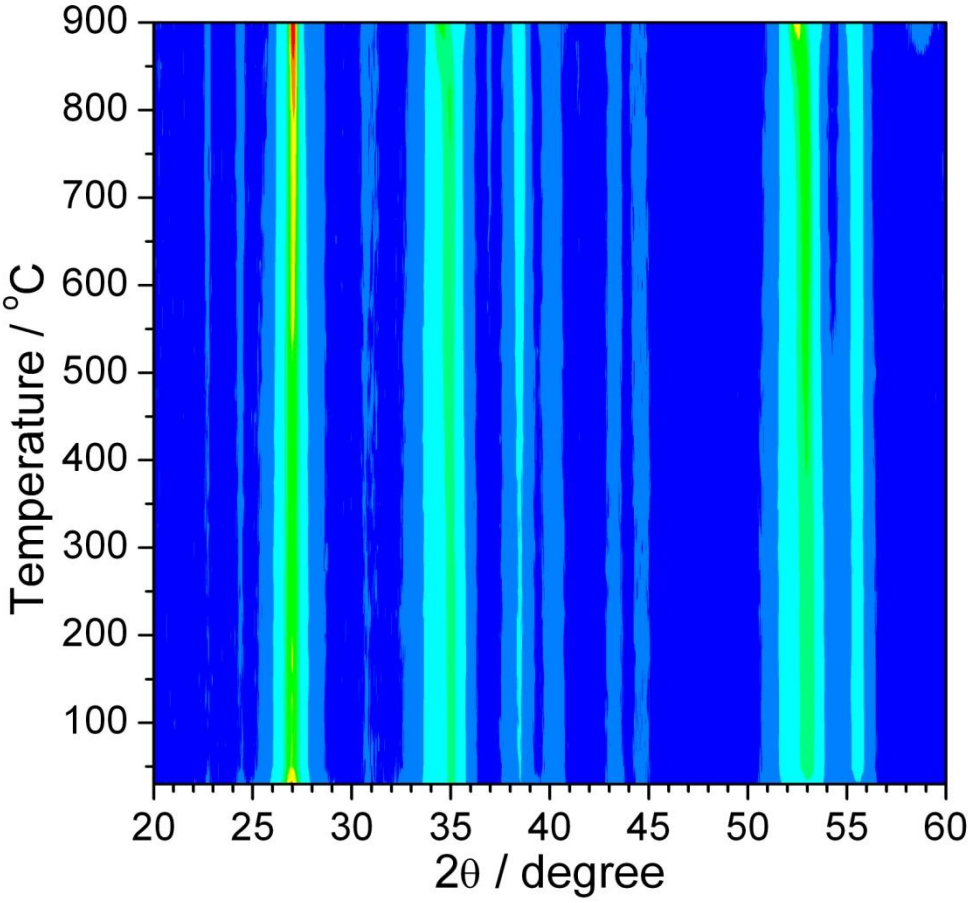

Fig. 6.20 *In-situ* XRD of 50% Sn-TiO_2 heated from 30 ^oC to 900 ^oC in air

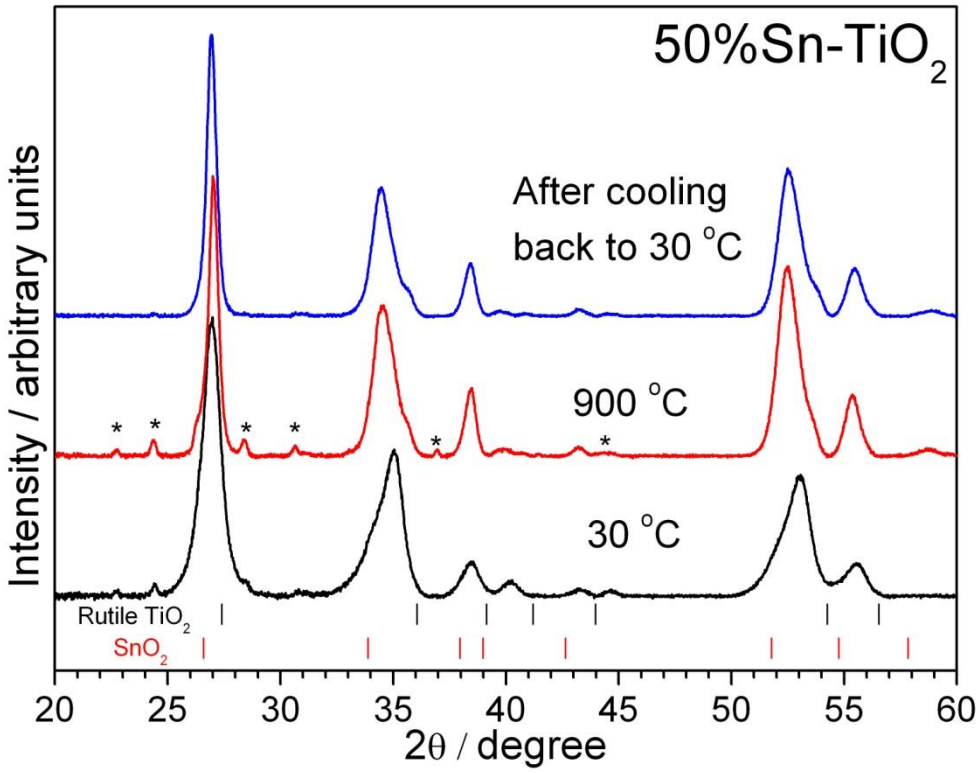

Fig. 6.21 XRD of 50% Sn-TiO_2 at 30 ^oC, 900 ^oC and after cooling back to 30 ^oC.. Peaks due to ceramic sample holder are labelled with *

In-situ XRD of 80% Sn-TiO_2 (Fig. 6.22) showed that the rutile phase remained stable when heated to 900 ^oC. The peaks became sharper upon heating and no other phases were detected. The XRD pattern of 80% Sn-TiO_2 at 30 ^oC, 900 ^oC and after cooling back to 30 ^oC is shown in Fig. 6.23.

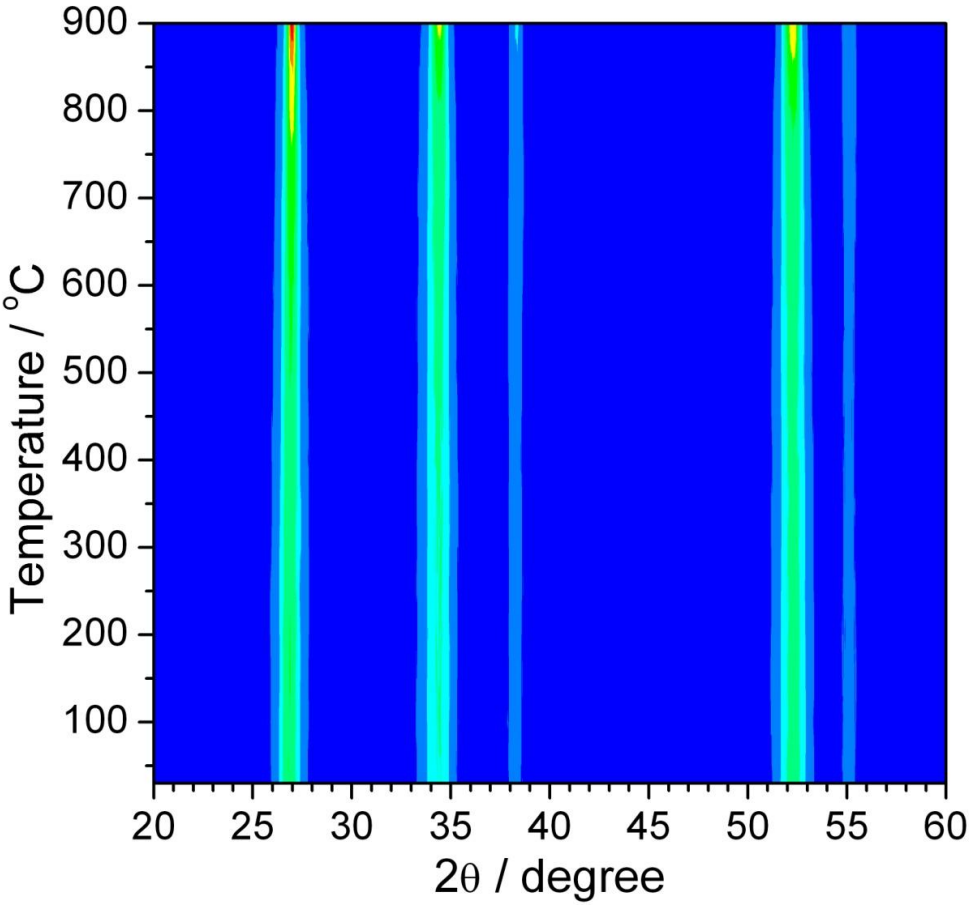

Fig. 6.22 *In-situ* XRD of 80% Sn-TiO_2 heated from 30 °C to 900 °C in air

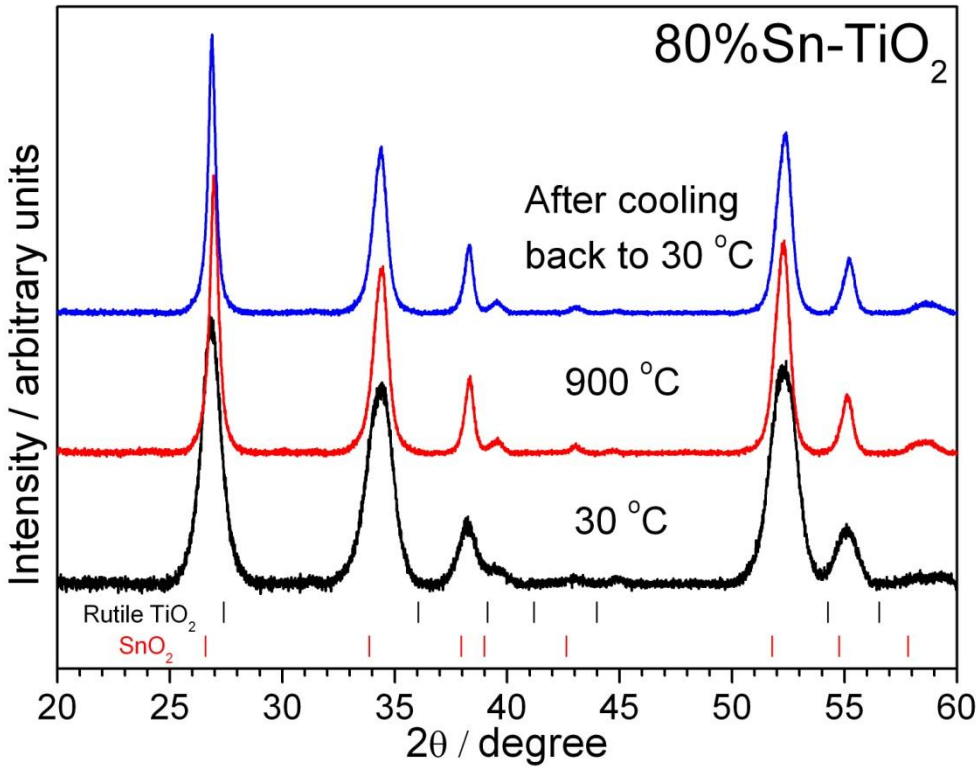

Fig. 6.23 XRD of 80% Sn-TiO_2 at 30 °C, 900 °C and after cooling back to 30 °C

Thermogravimetric analysis of the Sn-TiO_2 was carried out to determine the water content of the as-prepared materials (Fig. 6.24). TiO_2 showed the least mass loss upon heating while the Sn doped TiO_2 showed a mass loss of 4-5% at ~400 ^oC, which can be attributed to the loss of adsorbed water and dehydroxylation of surface attached H_2O and OH groups.[62-63] Above 400 ^oC, no significant mass loss was observed. The water present on the Sn-TiO_2 samples is consistent with the smaller crystallites of these samples.

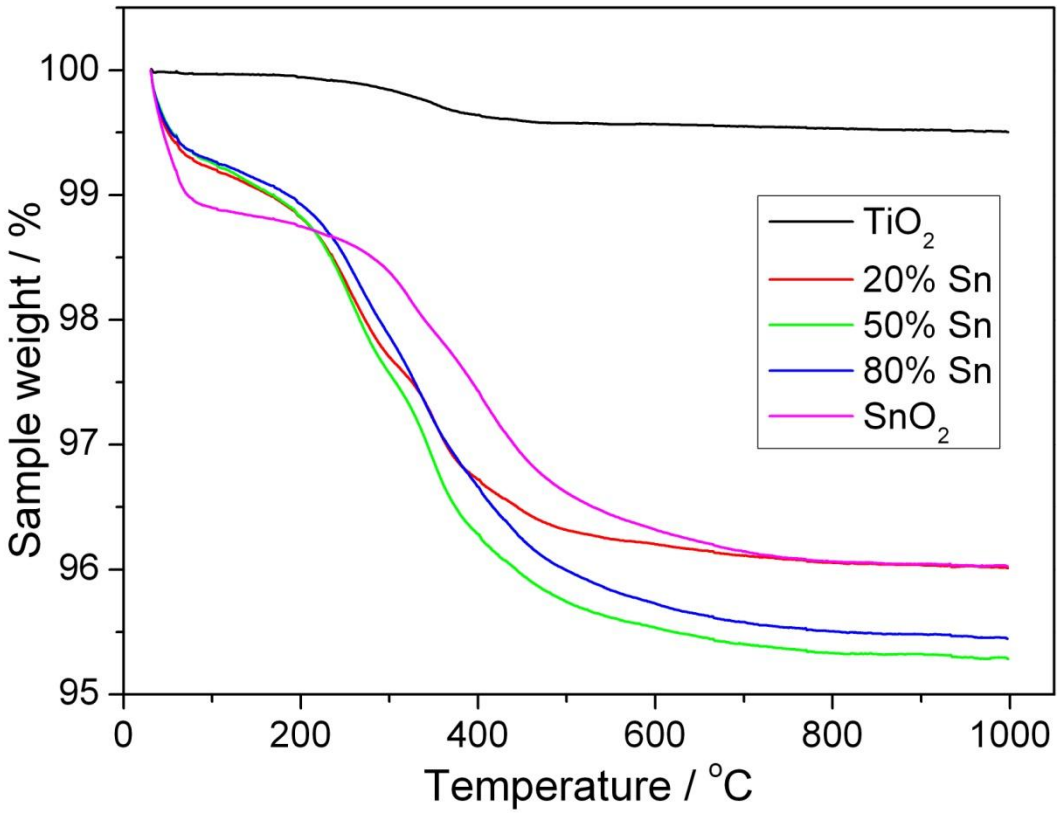

Fig. 6.24 TGA of Sn-TiO_2 heated from 30 ^oC to 1000 ^oC in air

The IR spectra of Sn-TiO_2 are shown in Fig. 6.25. The IR peaks at about 1630 and 3000-3500 cm^{-1} was attributed to surface hydroxyl and adsorbed H_2O respectively.[24,64-65] The most intense peak at 500 cm^{-1} resulted from Ti-O bond in the TiO_2 lattice. The IR spectra showed that there were more surface –OH present in the

Sn-doped samples than in TiO_2, which is in agreement with the TGA data where the mass loss at 200 ^oC is the least for TiO_2. Peaks due to C-O and C-H were observed showing that some organic residues originating from the starting materials may have remained after the hydrothermal reaction.

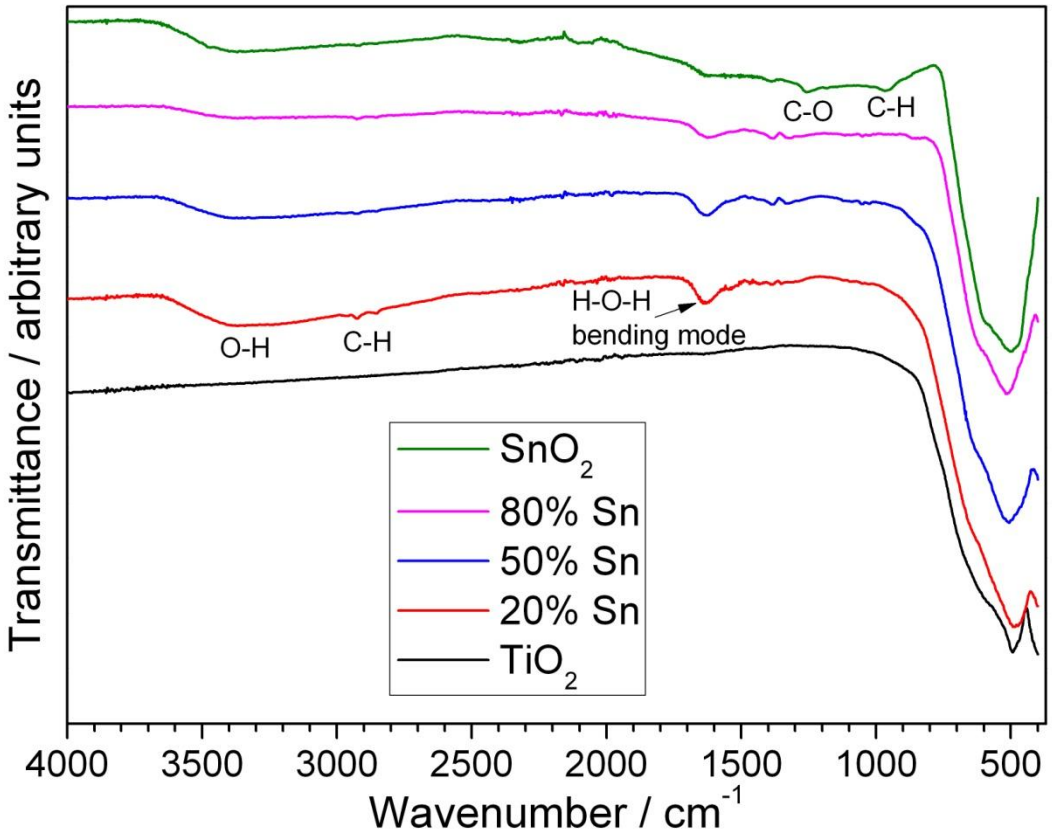

Fig. 6.25 IR of Sn-TiO_2 showing the presence of surface water and organic residue

6.4 Hydrothermal synthesis of Ce doped TiO_2

6.4.1 Synthesis

Hydrothermal synthesis of Ce-doped TiO_2 was typically performed in a ~100 mL Teflon-lined stainless steel autoclaves. The synthesis protocol used here was based on one developed by Dr Juliana Fonseca de Lima.[66] 0.5 M solutions of Ti (IV) isopropoxide and cerium nitrate hexahydrate in ethanol were first prepared. Then, appropriate amounts of the two solutions, as shown in Table 6.9, were mixed according to the desired Ce : Ti ratio to give a total volume of 50 mL. Then, 1 mL lactic acid was added and the mixed solution was left to stir for 1 hour. The Teflon liner was then sealed in a steel autoclave and placed in an oven pre-heated at 240 ^{o}C. After heating for 24 hours, the autoclaves were left to cool to room temperature. The solid products were recovered by suction filtration, washed thoroughly with ethanol and dried overnight at 70 ^{o}C in a drying oven. The products were then ground into powder for further characterisation.

Table 6.9 Amounts of starting materials used for Ce-TiO_2 synthesis

Ce conc./%	$Ce(NO_3)_3.6H_2O$ in ethanol (0.5 M)/mL	Ti isopropoxide in ethanol (0.5M)/mL	Lactic acid/mL
0	-	50	1
0.5	0.25	49.75	
1	0.5	49.5	
5	2.5	47.5	
10	5	45	
15	7.5	42.5	

6.4.2 Characterisation

The powder XRD of TiO_2 and Ce doped TiO_2 in Fig. 6.26 showed that they have the anatase structure as the peaks matched with anatase TiO_2. No rutile TiO_2 phase or impurity peaks were observed. The XRD peaks of undoped TiO_2 are broad indicating small particle size and upon increasing Ce doping, the peaks sharpened and the individual peaks are more visible for the 10% and 15% Ce. This behaviour is different to the Sn-TiO_2 rutile materials where addition of Sn to TiO_2 gave smaller crystallites. The XRD patterns of Ce-TiO_2 were refined with the space group $I4_1/amd$ to determine the lattice parameters (Fig. 6.27).

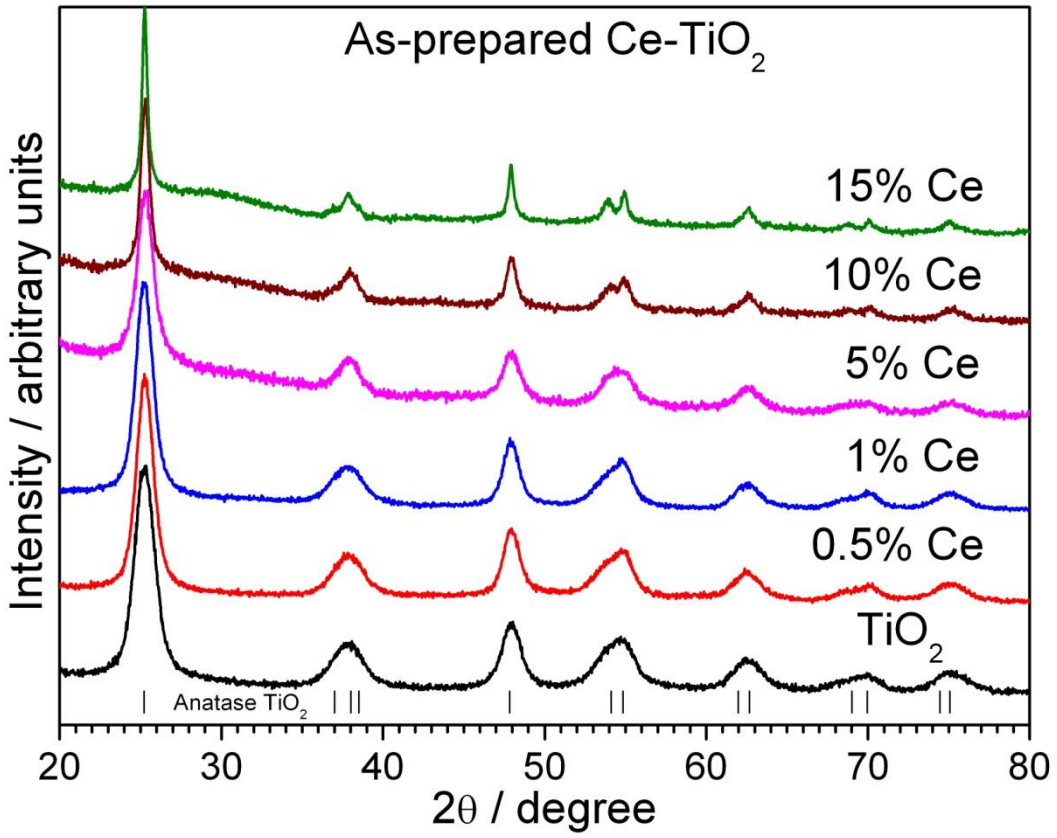

Fig. 6.26 Powder XRD of as-prepared Ce-TiO_2

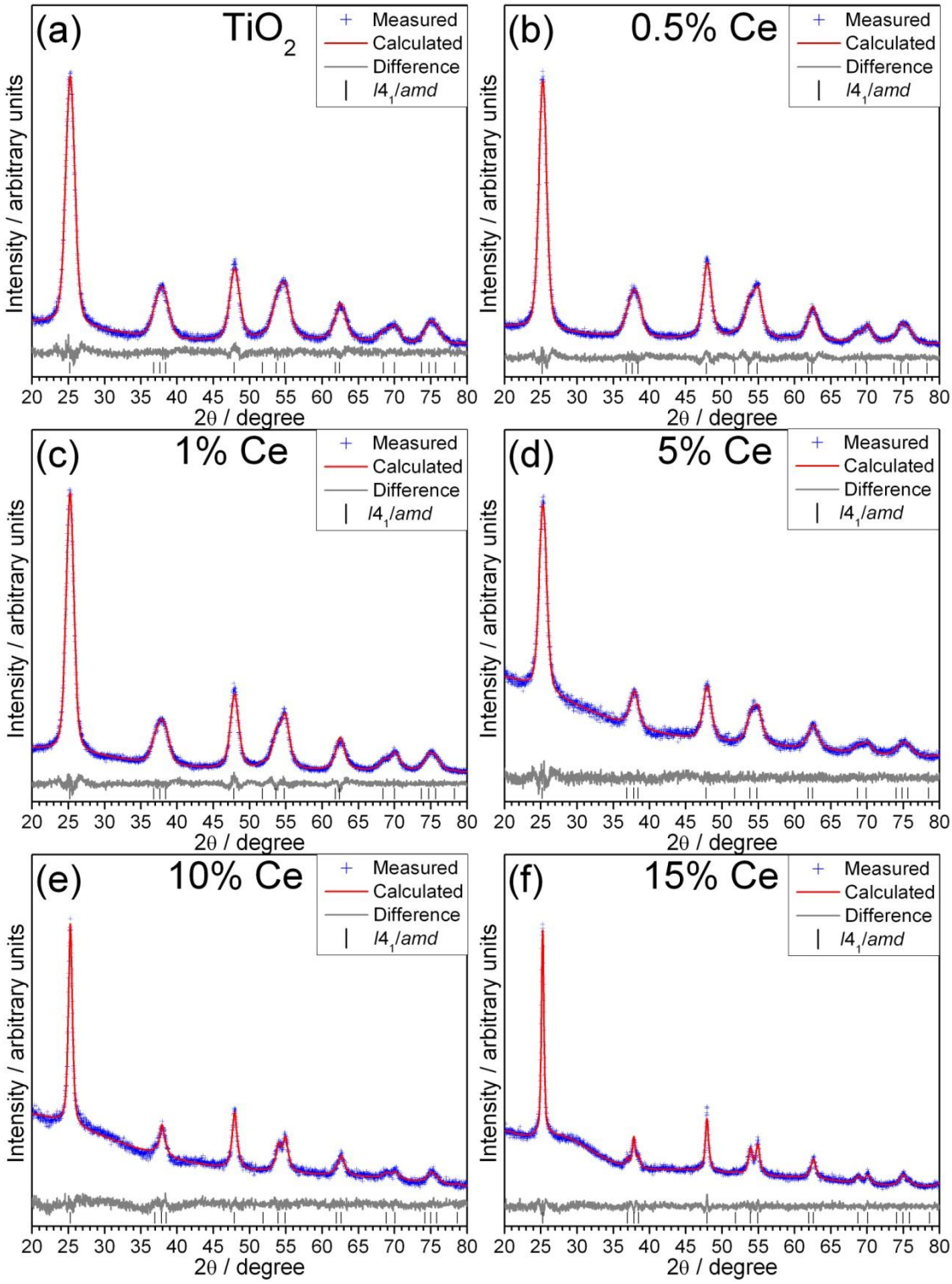

Fig. 6.27 Pawley refinements of XRD for as-prepared a) TiO_2, b) 0.5% Ce, c) 1% Ce, d) 5% Ce, e) 10% Ce and f) 15% Ce with the $I4_1/amd$ model

A summary of the refinement from the XRD patterns is shown in Table 6.10. The lattice parameters obtained from the refinement of these XRD patterns (Fig. 6.28) showed that at low Ce doping level (≤ 1%) the unit cell volume increased slightly but further Ce doping resulted in a reduction of the cell volume. This is different from the expected trend in cell volume where a linear increase with increasing Ce concentration should be seen since the ionic radii of both Ce^{3+} and Ce^{4+} (1.01 Å and 0.87 Å respectively) in a 6 coordinate environment are higher than the ionic radius of Ti^{4+} (0.605 Å, 6 coordination).[12] Since Ce is much larger than Ti, it is difficult for Ce to enter the TiO_2 lattice. Although Ce substitution can still occur, it may be possible that some of the Ce ions are instead dispersed on the surface of TiO_2. Li *et al.* reported an increasing trend in the a lattice parameter and a decrease in the *c* parameter upon Ce doping up to 2%Ce,[67] while Zhao *et al*. observed an increasing trend for both parameters up to 10% Ce.[68] The limit for Ce substitution has also been reported to be at 2.5% for samples prepared by solution combustion method[69] and 10% using sol-gel method[68]. Above this limit, CeO_2 was also formed in both studies.

Table 6.10 Refined structural parameters and *R*-factors of as-prepared Ce-TiO_2 from powder XRD

Ce conc./% (Expected value)	*a*/Å	*c*/Å	Cell volume/Å^3	R_{wp}	R_p	Gof
0	3.8005(10)	9.5519(72)	137.97(17)	4.507	3.468	1.223
0.5	3.8008(12)	9.5554(41)	138.04(9)	3.883	3.068	1.213
1	3.8012(9)	9.5593(34)	138.12(7)	3.919	3.079	1.293
5	3.7992(15)	9.5056(76)	137.20(24)	3.168	2.549	1.114
10	3.7962(18)	9.4980(83)	136.87(20)	3.504	2.761	1.205
15	3.7945(12)	9.5079(58)	136.89(14)	3.199	2.529	1.148

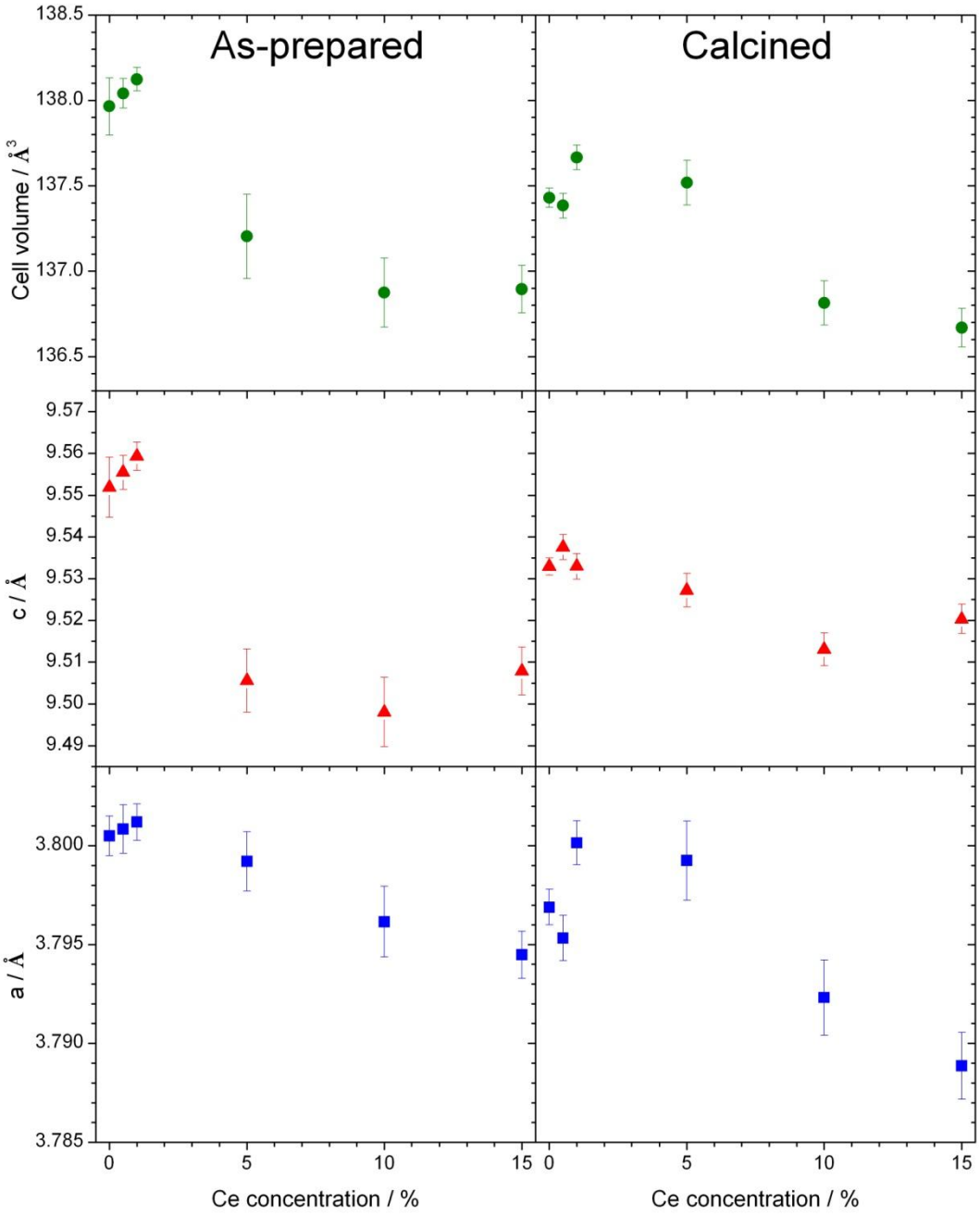

Fig. 6.28 Trend of the lattice parameters of as-prepared and calcined Ce-TiO_2

The samples were also calcined at 400 ^oC for 4 hours, to remove any organic material that may remain from the reaction. The XRD pattern, shown in Fig. 6.29, still has broad peaks although the splitting in some peaks was clearer. The XRD patterns of calcined Ce-TiO_2 were also refined with the tetragonal $I4_1/amd$ model

(Fig. 6.30) and the refinement summary is shown in Table 6.11. The general trend in the lattice parameter (Fig. 6.28) was very similar to the as-prepared samples where the cell volume increased up to 1% Ce but above 5% Ce content, the cell volume decreased. However, between 0 and 1% Ce, the cell volume does not show a linear increase like that of as-prepared Ce-TiO_2. Also, at low Ce concentration (≤ 1), the cell volume of the calcined samples are lower than the as-prepared ones, suggesting that more Ce^{4+} was present since the ionic radius of Ce^{4+} is smaller than Ce^{3+}.

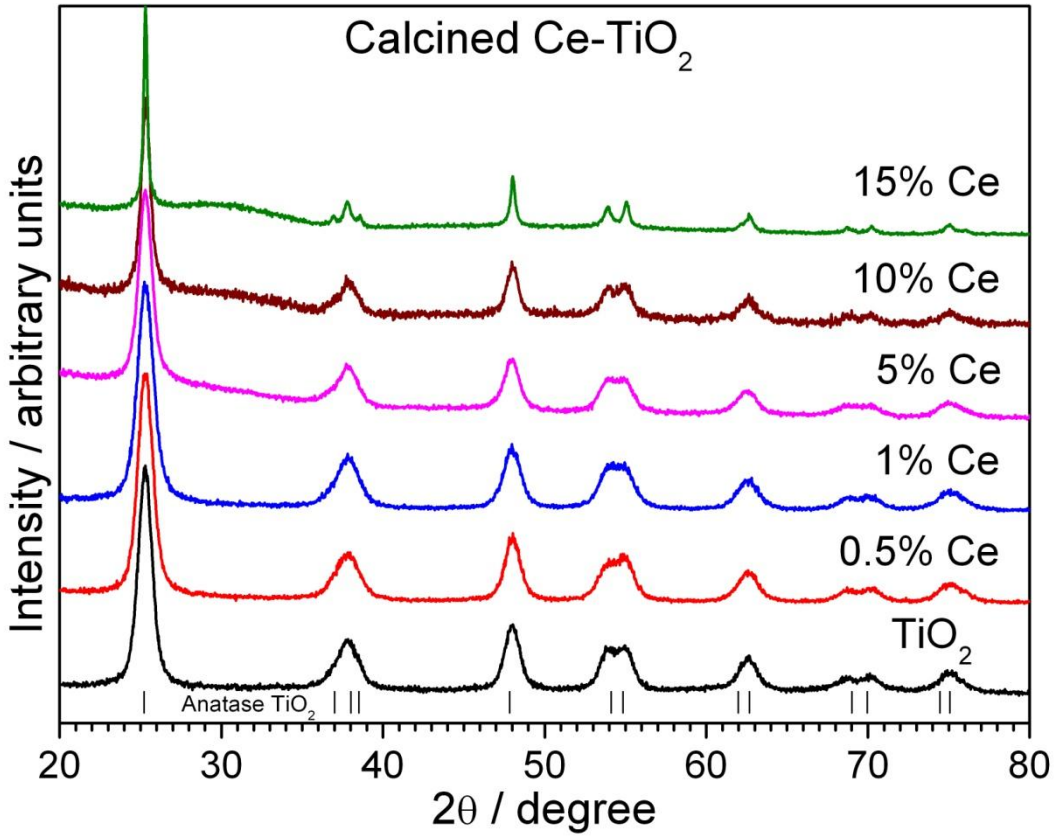

Fig. 6.29 Powder XRD of Ce-TiO_2 after being calcined at 400 ^oC for 4 hours

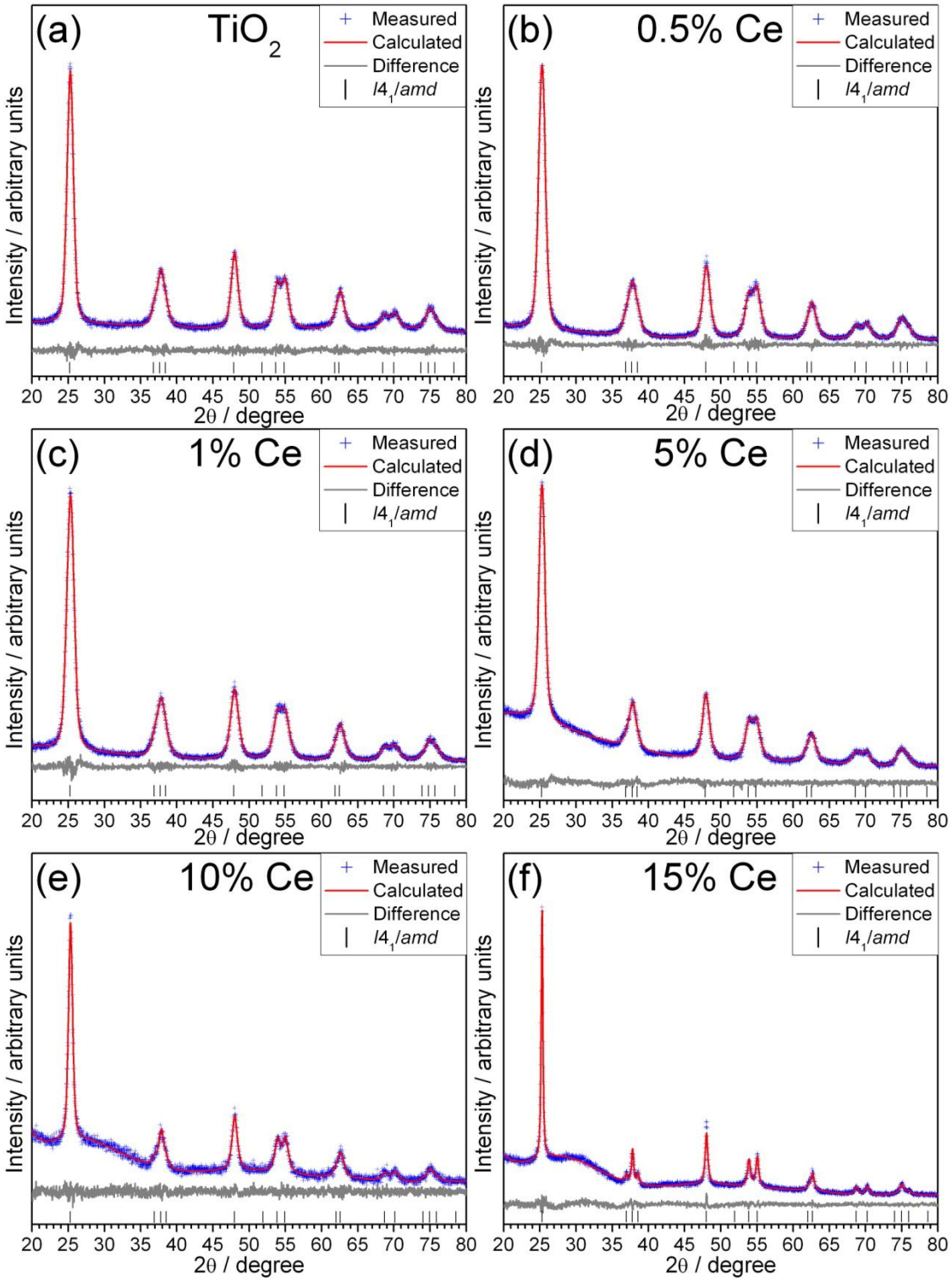

Fig. 6.30 Pawley refinements of XRD for calcined a) TiO_2, b) 0.5% Ce, c) 1% Ce, d) 5% Ce, e) 10% Ce and f) 15% Ce with the $I4_1/amd$ model

Table 6.11 Refined structural parameters and *R*-factors of calcined Ce-TiO_2 from powder XRD

Ce conc./% (Expected value)	*a*/Å	*c*/Å	Cell volume/Å^3	R_{wp}	R_p	Gof
0	3.7969(9)	9.5329(21)	137.43(6)	5.374	4.110	1.116
0.5	3.7953(11)	9.5375(30)	137.384(7)	7.644	5.508	1.097
1	3.8002(11)	9.5329(31)	137.68(7)	7.652	5.626	1.099
5	3.7993(20)	9.5273(40)	137.52(13)	2.847	2.235	1.254
10	3.7923(19)	9.5131(39)	136.81(13)	4.987	3.924	1.076
15	3.7888(17)	9.5203(35)	136.67(11)	6.061	4.702	1.299

The atomic composition of Ce-TiO_2 was determined from ICP analysis (Table 6.12) and the calculated Ce concentrations matched well with the expected values.

Table 6.12 Atomic composition of Ce-TiO_2 samples from ICP analysis. Note: Ce concentration = [Ce / (Ce+Ti)] X 100

Ce concentration (Expected value) / %	Ce / at. %	Ti / at. %	Ce conc. / %
0.5	0.14 (0.17)	28.67 (33.17)	0.49
1	0.30 (0.33)	28.44 (33)	1.05
10	2.08 (3.33)	19.16 (30)	10.86
15	3.38 (5)	20.32 (28.33)	14.26

The thermal stability of the Ce-TiO_2 samples was studied using *in-situ* XRD, where the samples were heated to 900 ^oC and the XRD pattern recorded at intervals of 25 ^oC. The *in-situ* XRD of TiO_2 (Fig. 6.31) showed the anatase peaks sharpened upon heating and the structure remained stable up to 825 ^oC. Above 825 ^oC, the rutile phase started to appear. However, even at 900 ^oC, not all the anatase phase was changed to rutile. The XRD of TiO_2 at 30 ^oC, 900 ^oC and after cooling back to 30 ^oC (Fig. 6.32) showed the peaks sharpened upon heating and rutile phase appeared.

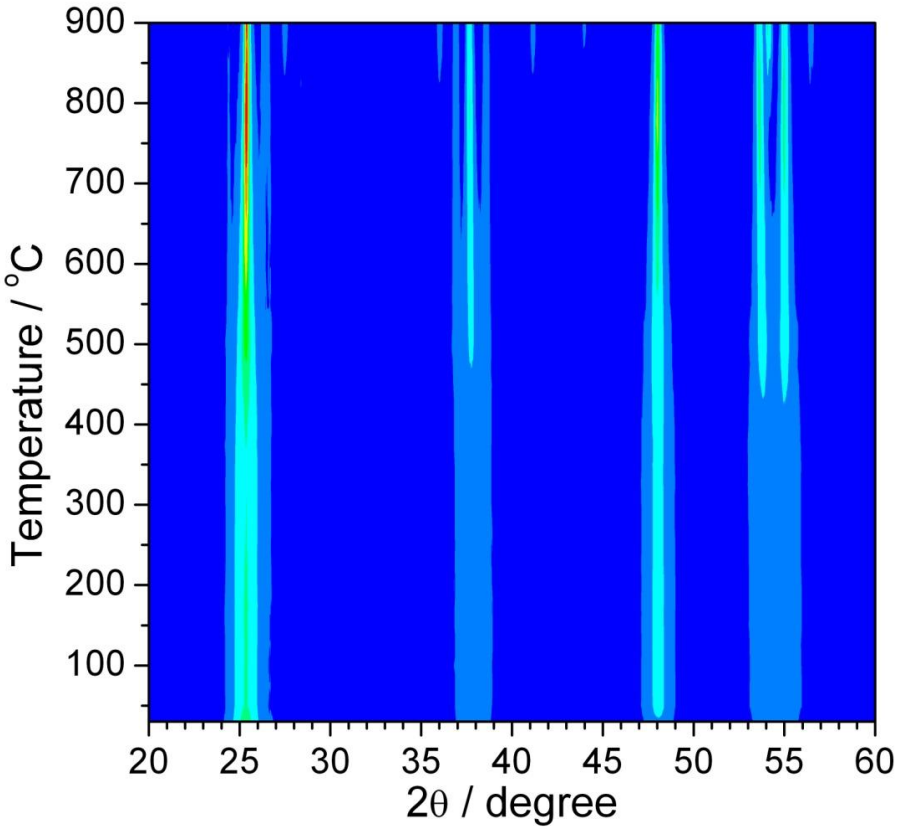

Fig. 6.31 *In-situ* XRD of undoped TiO_2 heated from 30 °C to 900 °C in air

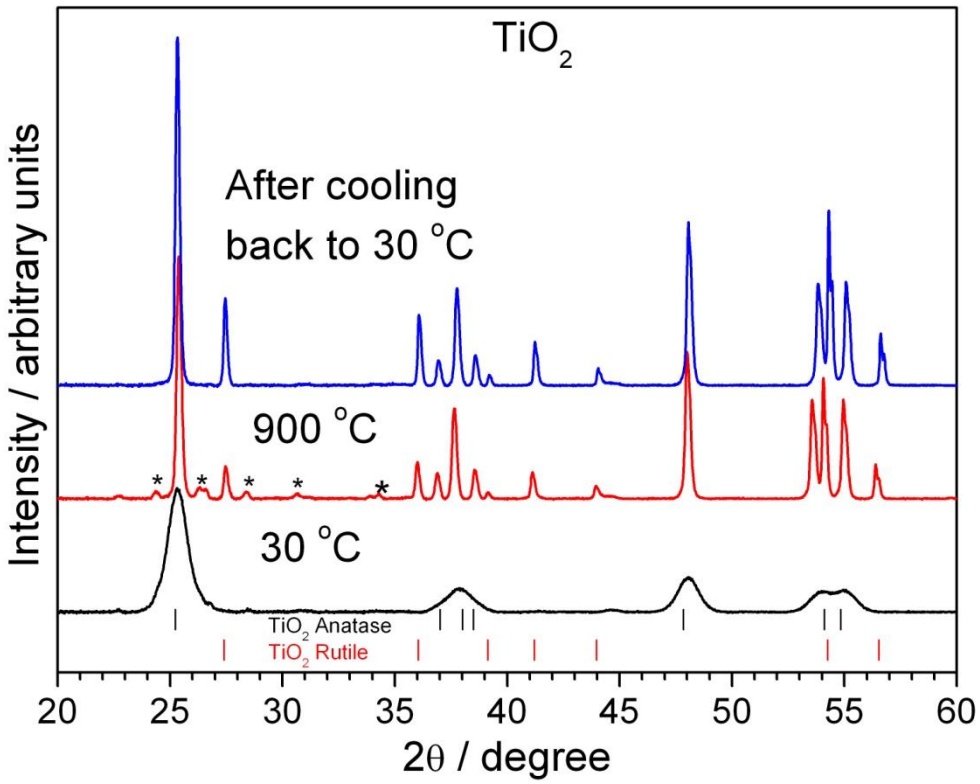

Fig. 6.32 XRD of TiO_2 at 30 °C, 900 °C and after cooling back to 30 °C. Peaks due to ceramic sample holder are labelled with *

The *in-situ* XRD of 0.5% Ce (Fig. 6.33) showed the anatase structure remained stable up to 900 ^{o}C. The XRD of 0.5% Ce at 30 ^{o}C, 900 ^{o}C and after cooling back to 30 ^{o}C showed the peaks sharpened upon heating and the rutile phase was not detected even at 900 ^{o}C (Fig. 6.34).

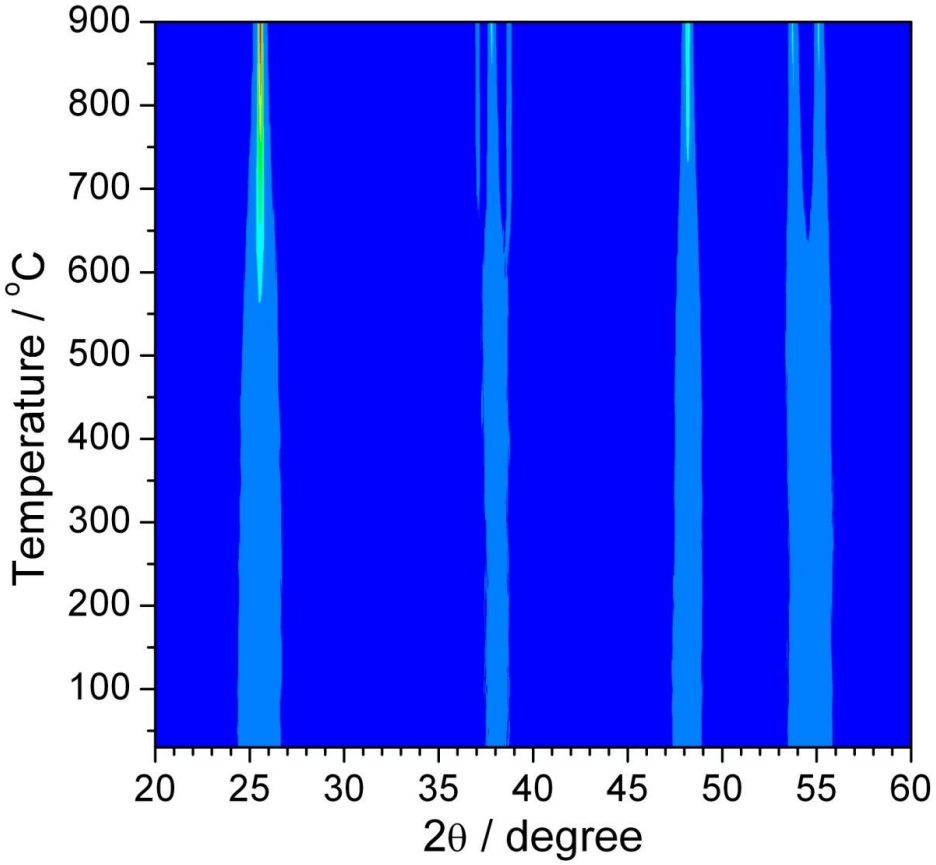

Fig. 6.33 *In-situ* XRD of 0.5% Ce-TiO_2 heated from 30 ^{o}C to 900 ^{o}C in air

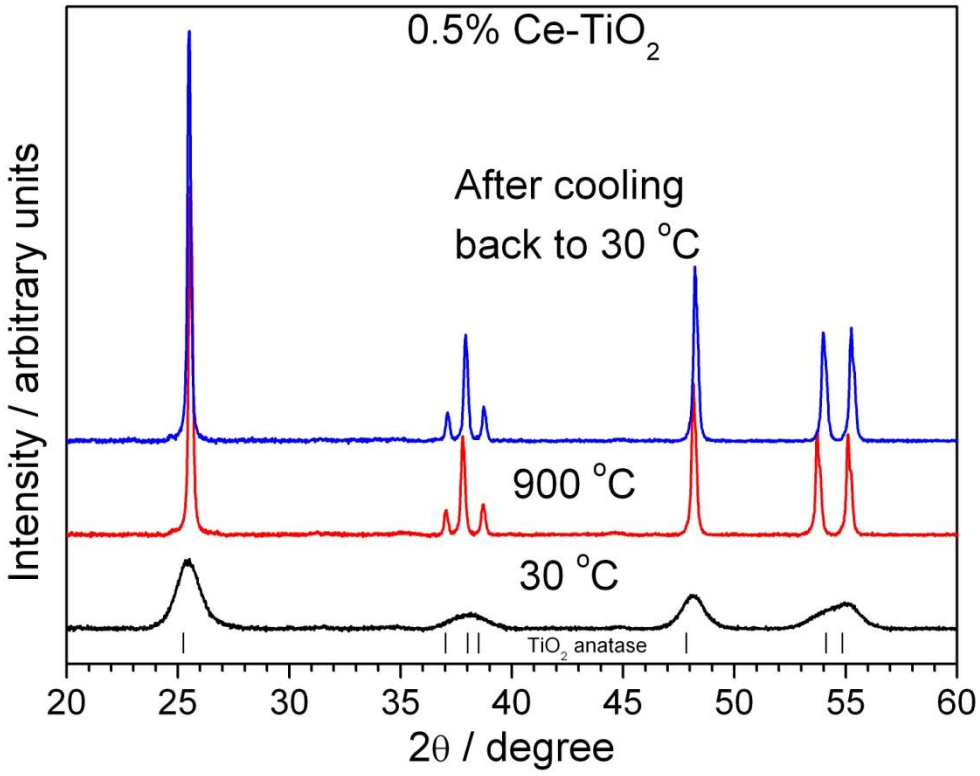

Fig. 6.34 XRD of 0.5% Ce-TiO_2 at 30 °C, 900 °C and after cooling back to 30 °C

The *in-situ* XRD of 15% Ce-TiO_2 (Fig. 6.35) showed the anatase structure remained stable up to 725 °C. Above 725 °C, the sample started to break down and $Ce_4Ti_9O_{26}$ (which contained only Ce(III)) was formed (Fig. 6.36). Interestingly, no rutile phase was formed even at 900 °C. Undoped anatase TiO_2 changed its structure to the more thermodynamically stable rutile upon heating to 825 °C. However, both the in-situ XRD of 0.5% and 15% Ce did not result in rutile formation. This strongly suggests that either the Ce must be incorporated into the lattice instead of being in a separate phase or present as a surface coating. This Ce incorporation prevents the anatase TiO_2 from converting to rutile. This agrees well with the lattice parameters obtained from powder XRD, where the values changed with Ce content, thus a significant amount of Ce must be within the lattice.

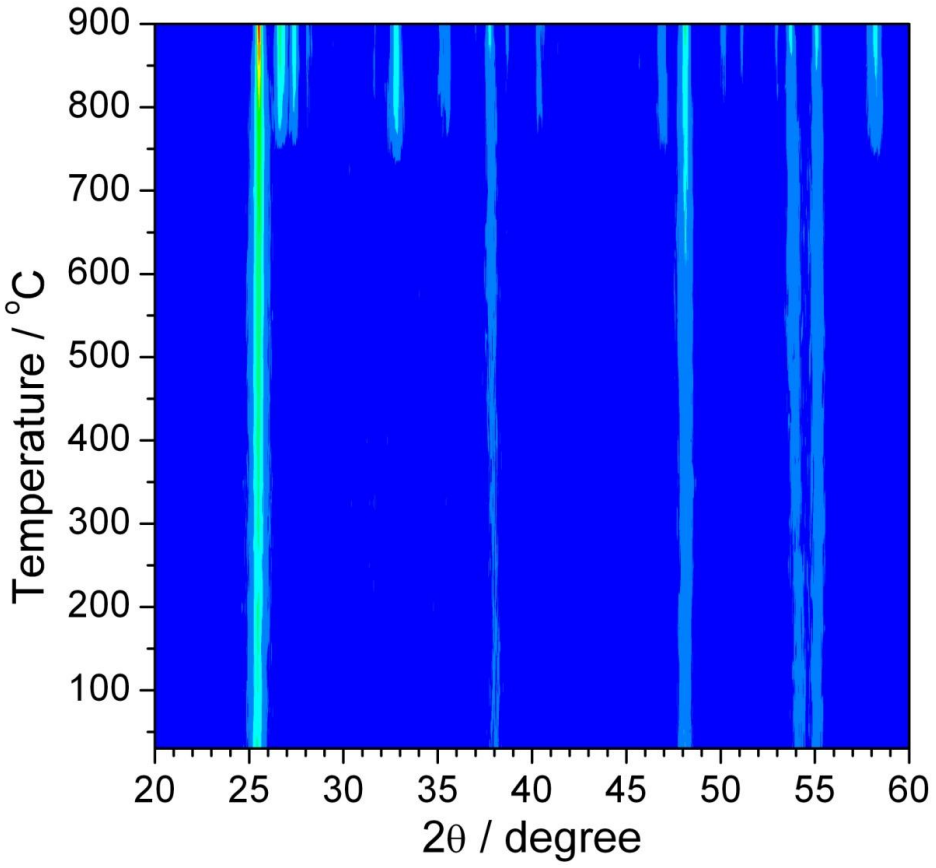

Fig. 6.35 *In-situ* XRD of 15% Ce-TiO_2 heated from 30 °C to 900 °C in air

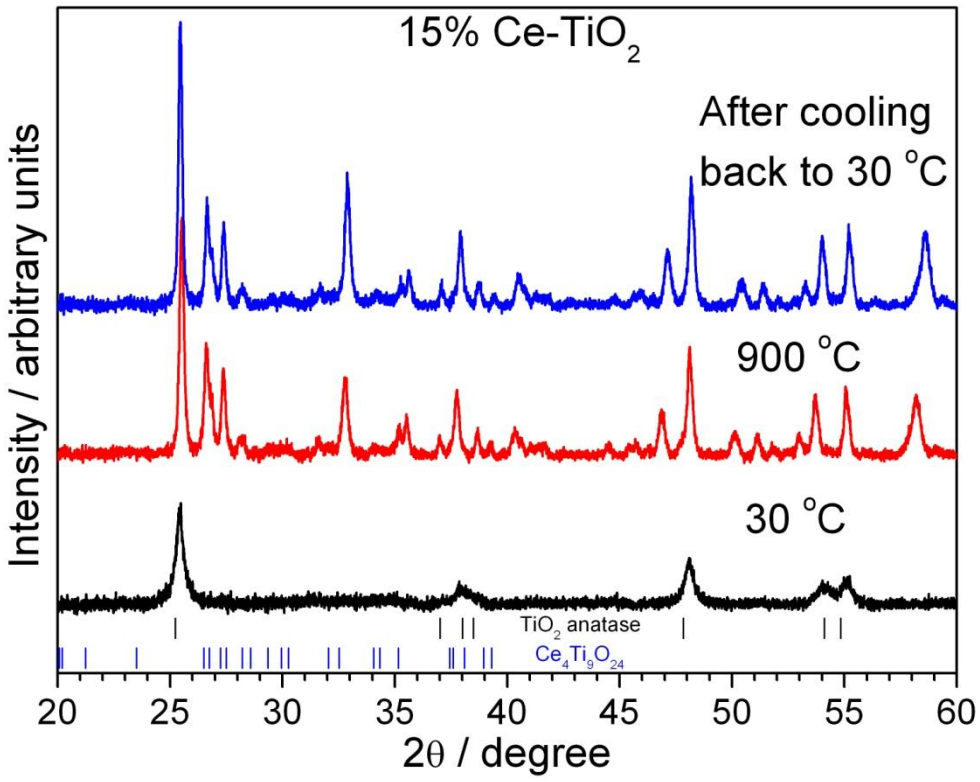

Fig. 6.36 XRD of 15% Ce-TiO_2 at 30 °C, 900 °C and after cooling back to 30 °C

The TGA of Ce-TiO_2 (Fig. 6.37) showed that there are two steps of mass loss. The first step was at ~200 ^oC and the second step was at ~400 ^oC. No further change in the mass was observed above 500 ^oC. The total mass loss at 1000 ^oC varies between 7% and 17%, with the 5% Ce sample showing the least mass loss. The mass loss is likely to be from surface water and organic materials.

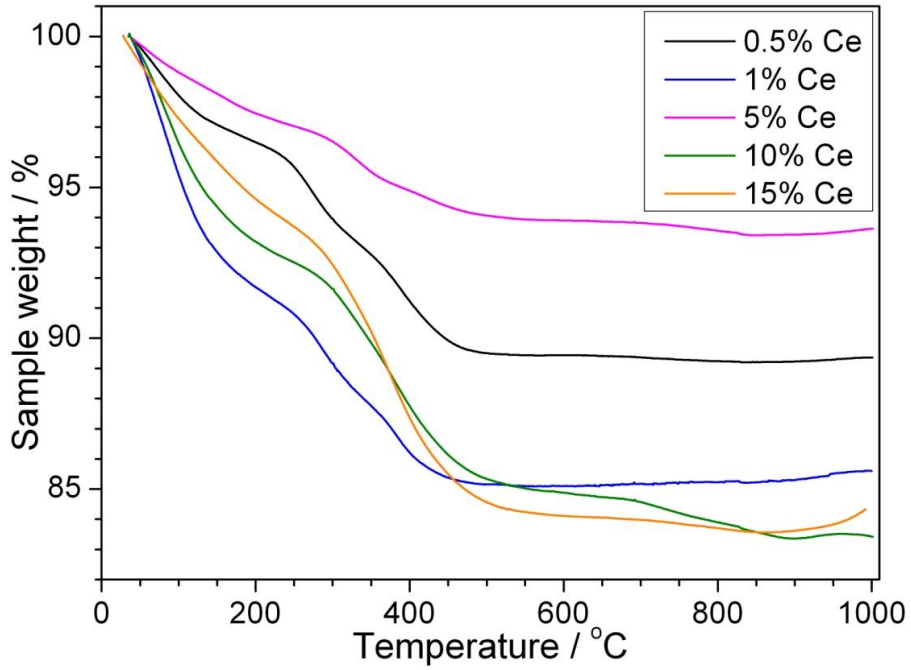

Fig. 6.37 TGA of Ce-TiO_2 series heated from 30 ^oC to 1000 ^oC

The Raman spectra of Ce-TiO_2 (Fig. 6.38) matched with anatase TiO_2 reported in the literature.[48,51-52] The main peaks were at 146, 395, 514 and 641 cm^{-1}, which can be attributed to the Raman active modes of anatase phase with the symmetries of E_g, B_{1g}, A_{1g} and E_g respectively.[51-52] The peak at 146 cm^{-1} shifted to higher values but the other peaks did not exhibit any significant shift. Fang *et al.* also observed a shift of this peak to higher values with increasing Ce content.[70] No other Raman peaks, such as for CeO_2 at 460 cm^{-1},[71-73] was observed thus confirming the purity of the samples. The Raman of calcined Ce-TiO_2 samples (Fig. 6.39) were also measured and no significant change were observed.

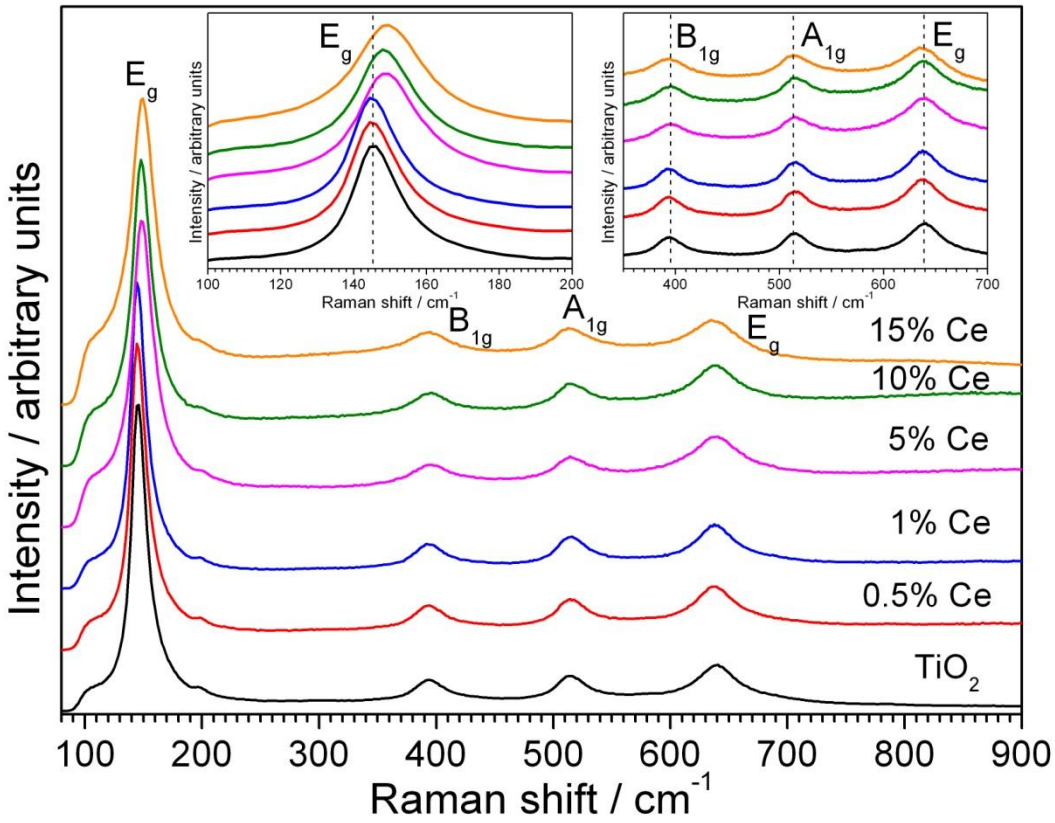

Fig. 6.38 Raman spectra of as-prepared Ce-TiO_2 series. The insets shows the zoomed-in view of each peaks

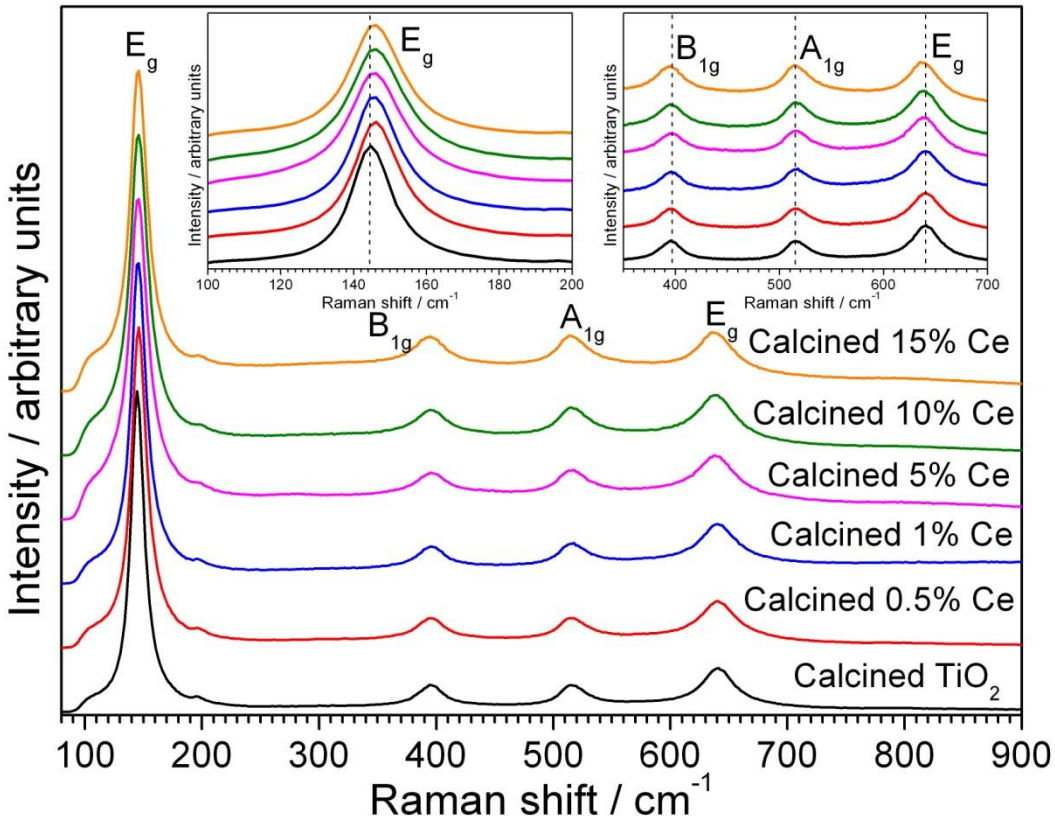

Fig. 6.39 Raman spectra of Ce-TiO_2 series after being calcined at 400 ^oC for 4 hours. The insets shows the zoomed-in view of each peaks

The oxidation state of Ce in Ce-TiO_2 for the as-prepared (Fig. 6.40) and calcined (Fig. 6.41) samples was determined by XANES spectroscopy at the CeL_{III} edge. $CeCl_3 \cdot 7H_2O$ (which contains 7-coordinate Ce^{3+}) and CeO_2 were used as the reference material for Ce^{3+} and Ce^{4+} respectively. A 1 : 1 mixture of $CeCl_3 \cdot 7H_2O$ and CeO_2 was also made as a reference material. $CeCl_3 \cdot 7H_2O$ only has a single peak at 5726 eV while CeO_2 has a characteristic double feature in the near-edge region. The spectra for the 1 : 1 mixture combines both those features and has an edge step that lies in between $CeCl_3 \cdot 7H_2O$ and CeO_2. The as-prepared Ce-TiO_2 samples have a peak at the same position as $CeCl_3 \cdot 7H_2O$ but samples with higher Ce content also have a second peak at 5739 eV. On the other hand, all the calcined samples have double peaks similar to CeO_2.

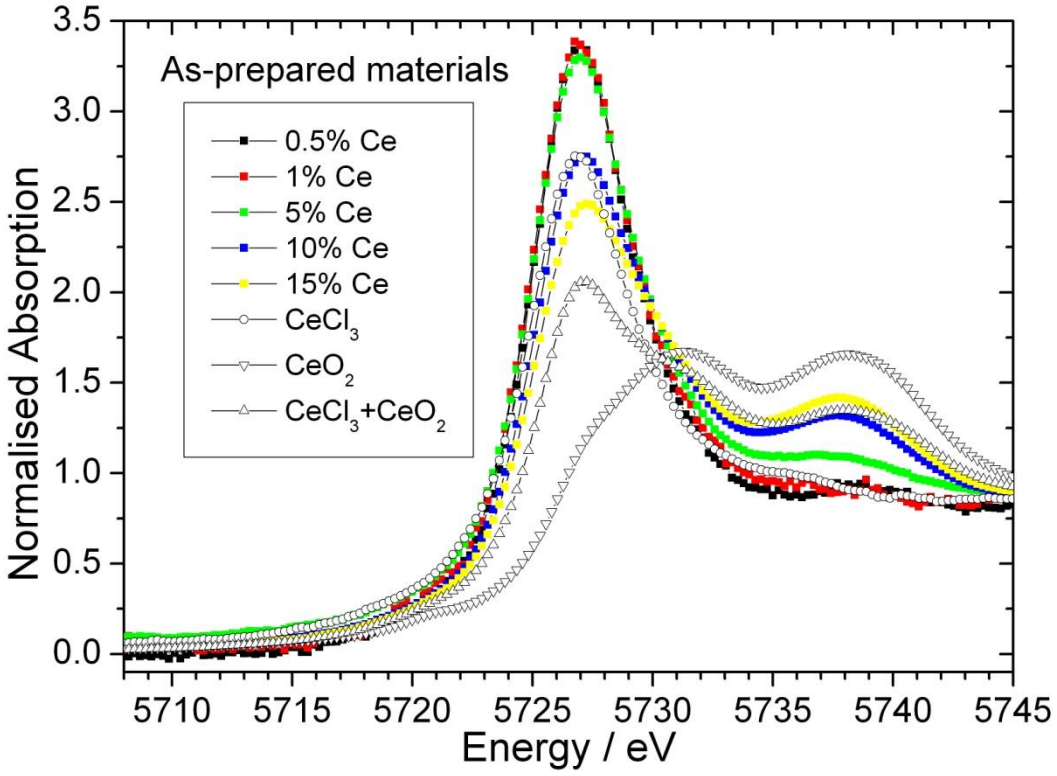

Fig. 6.40 Ce L_{III}-edge XANES of as-prepared Ce-TiO_2 samples

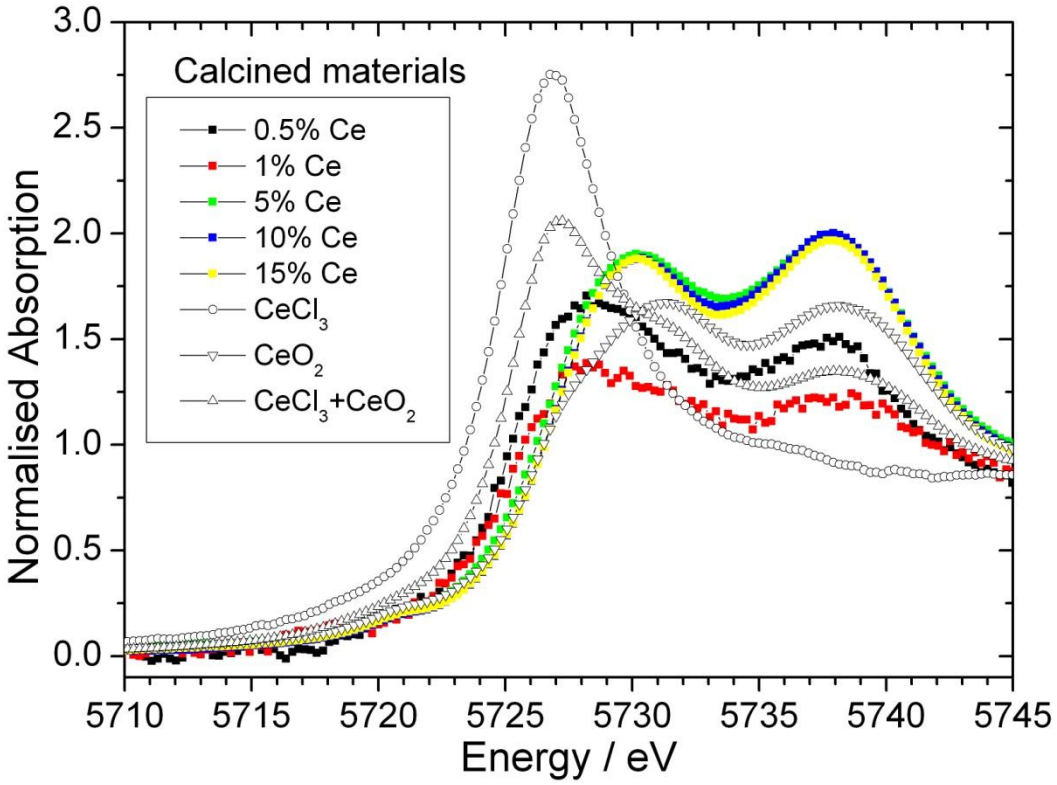

Fig. 6.41 Ce L_{III}-edge XANES of calcined Ce-TiO_2 samples

The energy which corresponds to 50% of the edge step was taken to be the edge position. A plot correlating the oxidation state and the edge position was then used to determine the oxidation state of each sample (Fig. 6.42). The as-prepared samples have an oxidation state between 3.1 and 3.4 suggesting that the samples mainly contain Ce^{3+} but higher Ce doping generally resulted in more Ce^{3+} being oxidised to Ce^{4+}. The double peak feature and the average oxidation state determined from the edge position of the calcined samples showed that most of the Ce has been oxidised to Ce^{4+}.

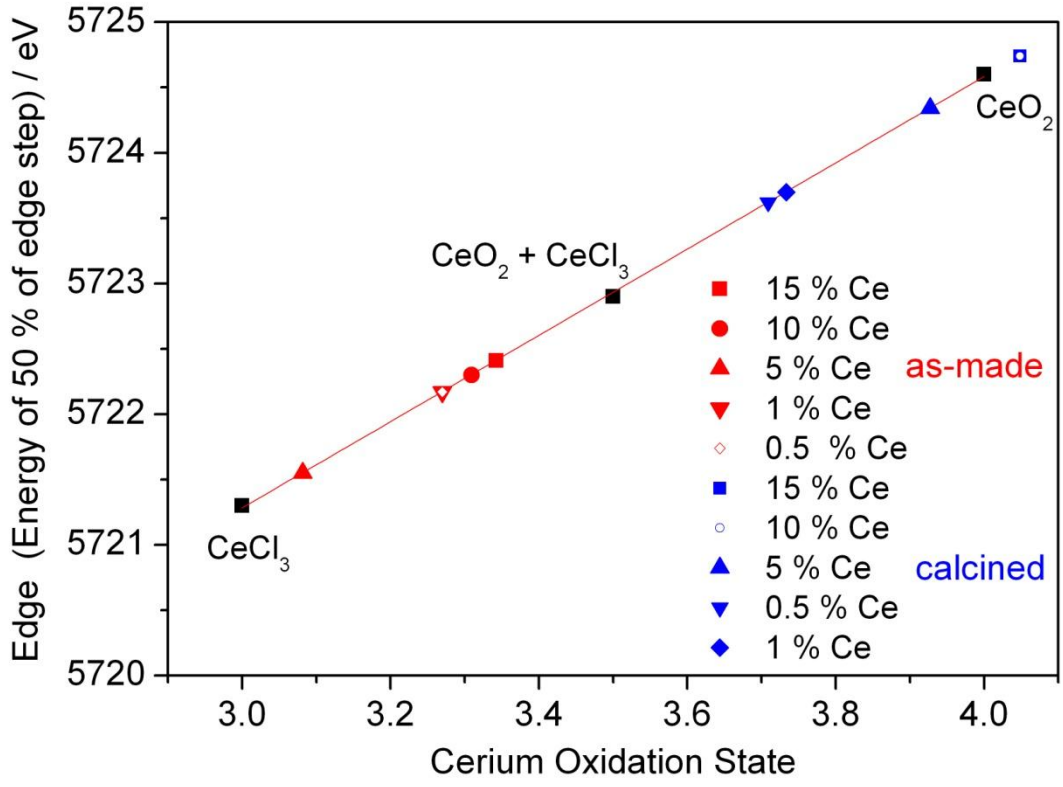

Fig. 6.42 The correlation between oxidation state and edge position, with deduced average oxidation states of the Ce-TiO_2 samples

XPS was also used to determine the oxidation state of Ce in the Ce-TiO_2 samples. Unlike XANES which gives the average oxidation state of Ce in the bulk of the sample, XPS is more sensitive to the oxidation state of Ce present on the surface. A typical survey scan for 15% Ce-TiO_2 is shown in Fig. 6.43.

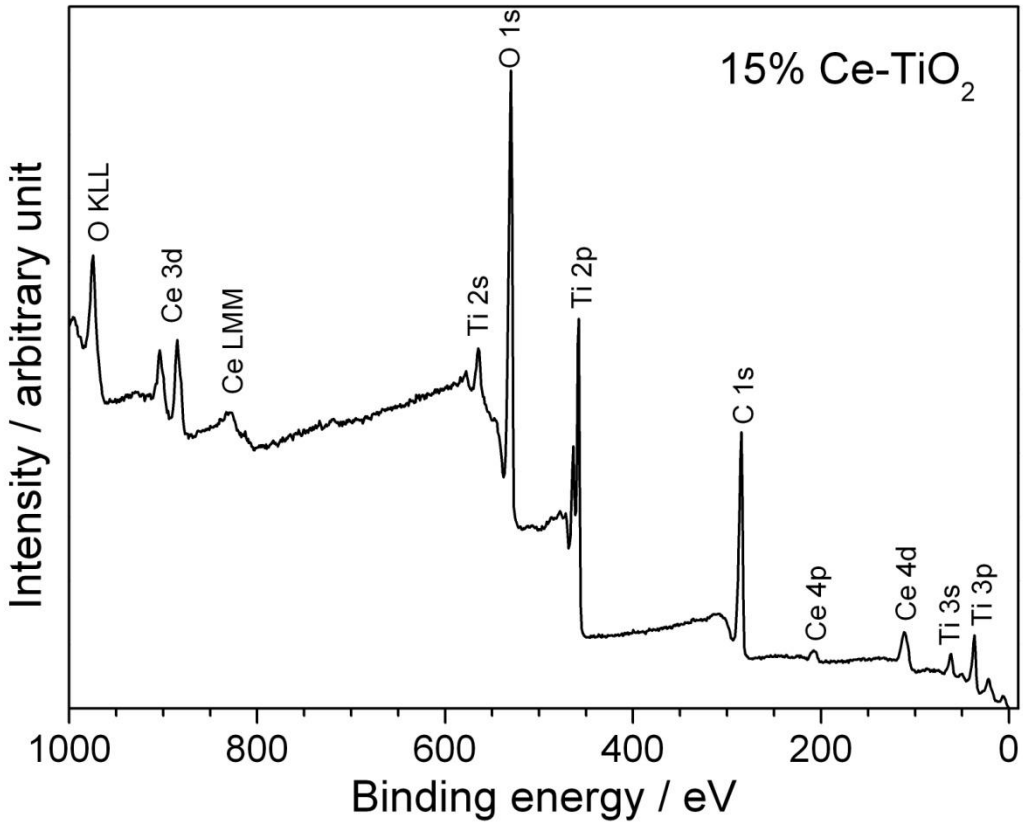

Fig. 6.43 XPS survey scan of 15% Ce-TiO_2

More detailed scans were also collected, particularly for Ce 3d (Fig. 6.44). The labels used to describe the Ce 3d XPS spectra follow the convention established by Burroughs *et al.* in which u and v refer to the $3d_{3/2}$ and $3d_{5/2}$ spin orbital components respectively.[74] In Ce(IV) oxides, particularly CeO_2, the Ce 3d XPS spectrum is composed of three pairs of spin-orbit doublets. The three doublets are located at 901.3 (u), 882.7 (v), 907.3 (u"), 888.5 (v"), 916.9 (u'") and 898.3 (v'"). The peaks referred to as v, v" and v'" are the result of Ce(IV) ($3d^9 4f^2$) O ($2p^4$), Ce(IV) ($3d^9 4f^1$) O ($2p^5$) and Ce(IV) ($3d^9 4f^0$) O ($2p^6$) final states respectively. The same peak assignment is applied to the corresponding u peaks. The highest binding energy peak (u'") at 916.9 eV is characteristic of the presence of tetravalent Ce^{4+} in Ce compounds.[75] On the other hand, the Ce 3d spectra of Ce(III) oxides consists of only

two pairs of spin-orbit doublets located at 899.1 (u^0), 880.9 (v^0), 903.4 (u') and 885.2 (v'). The peaks v^0 and v' are the result of Ce(III) ($3d^9 4f^2$) O ($2p^5$) and Ce(III) ($3d^9 4f^1$) O ($2p^6$) respectively.

The Ce 3d for as-prepared Ce-TiO_2 is characteristic of a Ce(III) oxide with only two pairs of doublets present (u^o, v^o, u' and v'). The spectra were deconvoluted using a peak fitting process to determine the position of each peak (Fig. 6.45). Table 6.13 gives a summary of the peak positions. The absence of u''' at ~916.9 eV showed that no Ce^{4+} was present on the surface of the samples.

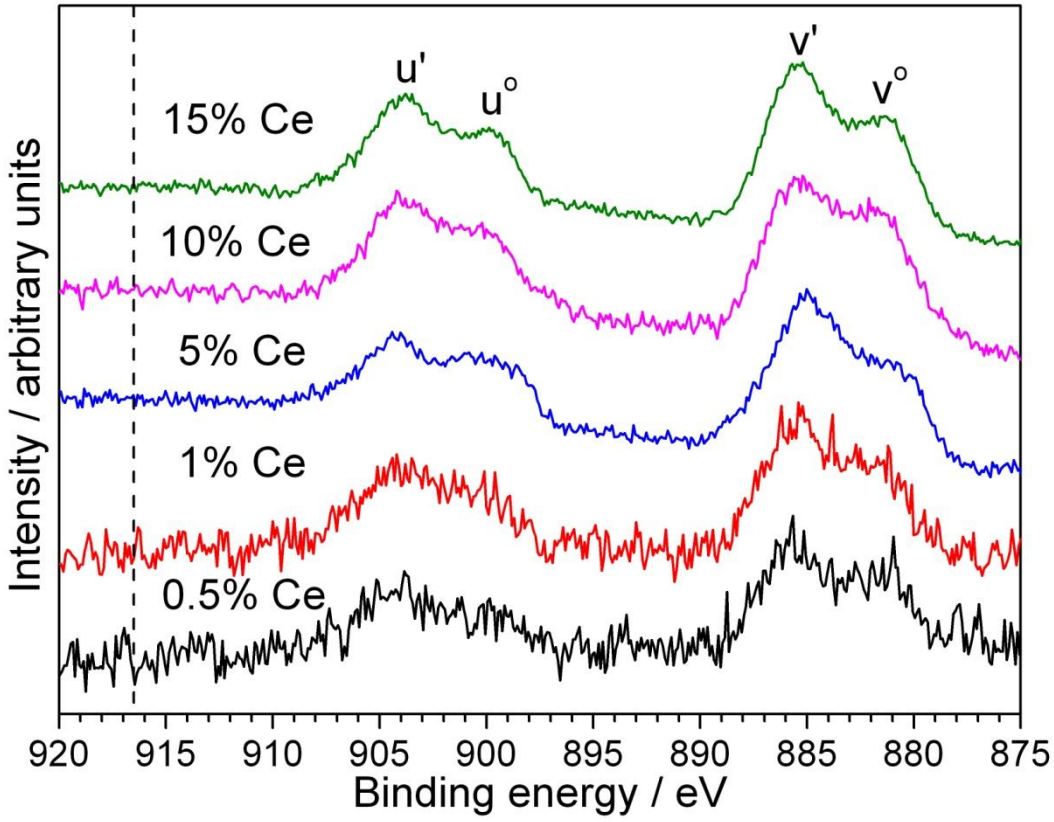

Fig. 6.44 XPS of Ce 3d for as-prepared Ce-TiO_2

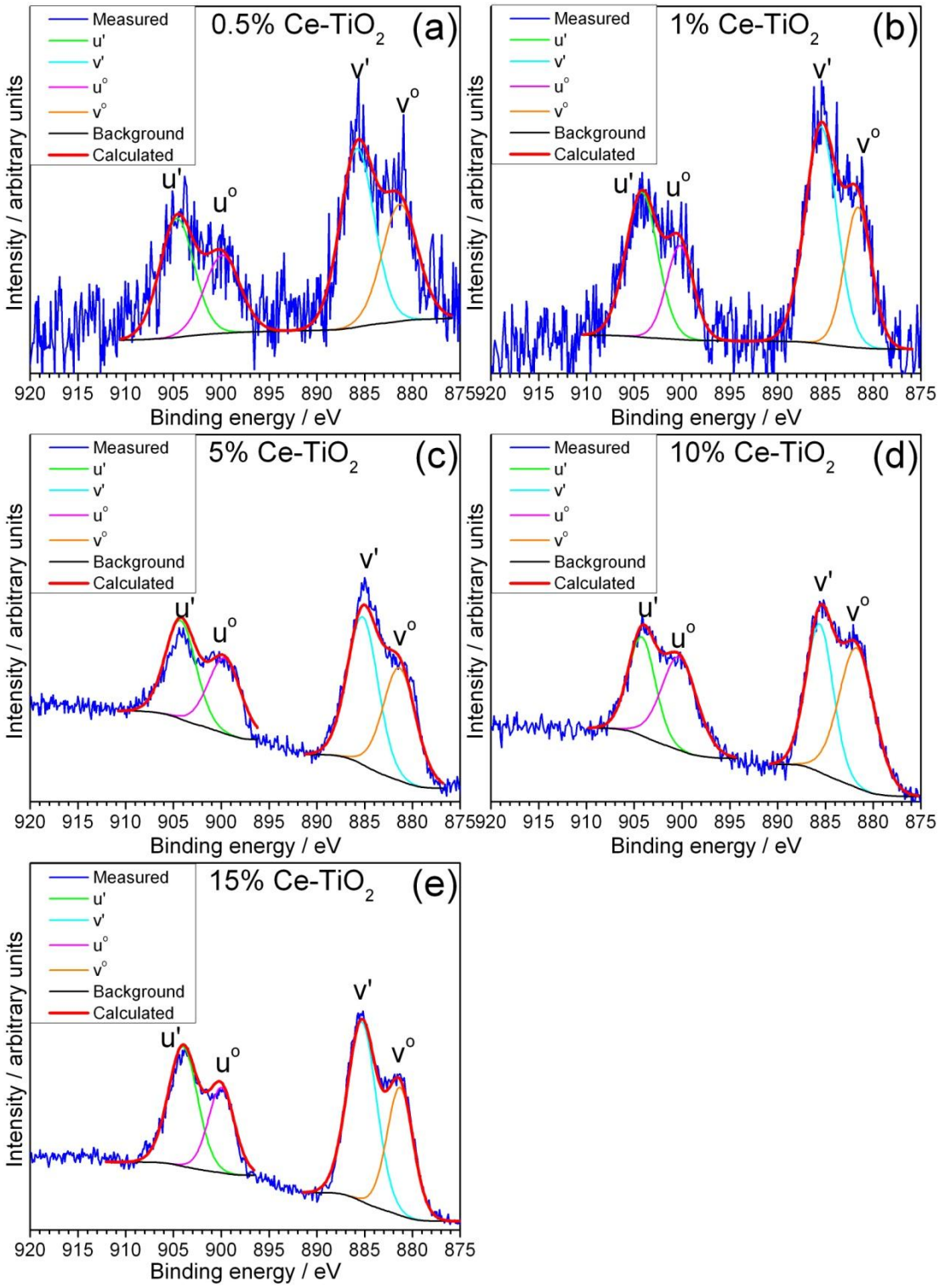

Fig. 6.45 XPS Peak fitting of Ce 3d for as-prepared Ce-TiO_2, a) 0.5% Ce, b) 1% Ce, c) 5% Ce, d) 10% Ce and e) 15% Ce

Table 6.13 Peak positions of fitted XPS data for as-prepared Ce-TiO_2

Ce conc./%	u' / eV	v' / eV	u^o / eV	v^o / eV
0.5	904.7	885.8	899.9	881.3
1	904.2	885.5	900.2	881.6
5	904.3	885.2	899.7	881.4
10	904.2	885.6	900.3	881.7
15	904.0	885.3	900.0	881.3

The XPS spectra of Ti 2p for as-prepared Ce-TiO_2 are shown in Fig. 6.46. From the literature, the binding energies of Ti $2p_{1/2}$ and $2p_{3/2}$ in undoped TiO_2 are at 464.4 and 458.8 eV respectively.[76] The XPS spectra of Ti 2p for Ce-TiO_2 were fitted with two main peaks at 464.3 and 458.7 eV, which are the Ti 2p doublet for Ti^{4+}. At 1% Ce and above, two additional peaks at binding energies 457 and 455 eV was also observed. These two peaks can be attributed to Ti^{3+} and Ti^{2+} respectively.[38,77-78] This reduction of Ti on the surface of the Ce-TiO_2 has also been reported in other studies carried out on Ce doped TiO_2 and is thought to be due to a charge imbalance caused by the cerium ion being localised in the octahedral interstitial sites.[38,77,79]

The O 1s of the 0.5% Ce-TiO_2 were fitted with three peaks, one main peak at 529.7 and two shoulder peaks on each side located at 531.2 and 528.1 eV (Fig. 6.47). At 1% and above, another peak started to appear at 526.8 eV. The O 1s peak at 529.7 can be assigned to oxygen bound to Ti^{4+}.[78,80] The intensity of the shoulder peak at 528.1 eV increased with higher Ce concentration and is assigned to oxygen bound to Ce while the peak at 531.2 was due to surface hydroxyl groups.[70] The peak at 526.8 eV may likely be due oxygen bound to Ti^{3+} as the intensity changes of this O 1s peak was similar to the Ti^{3+} peak.

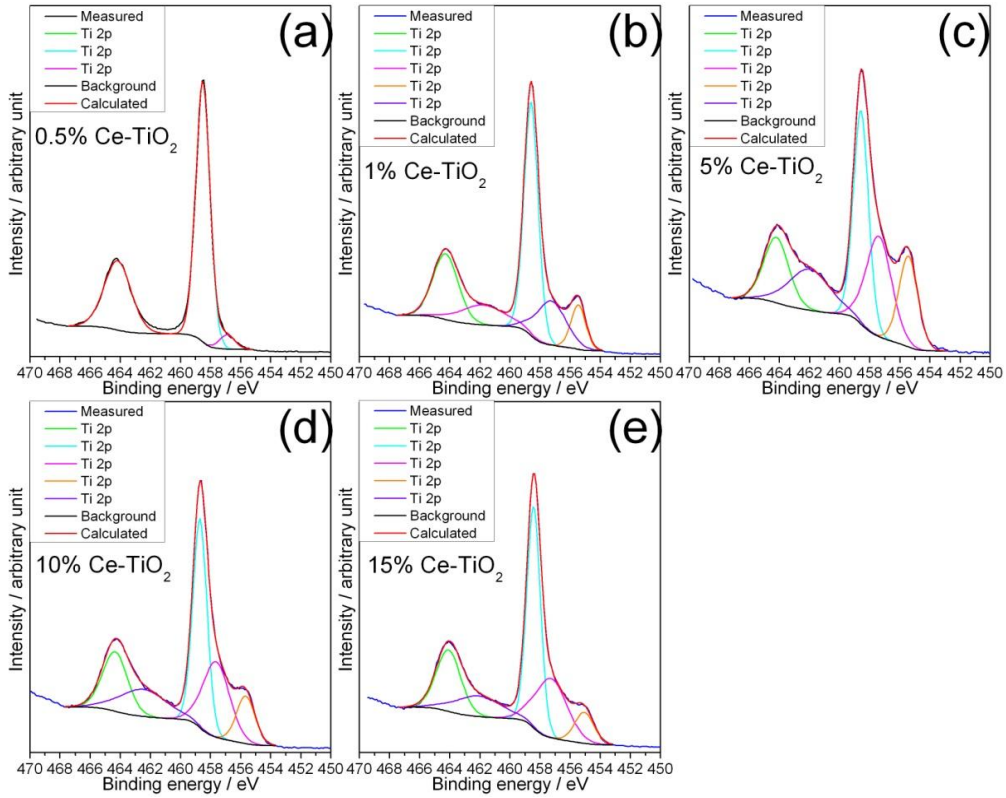

Fig. 6.46 XPS Peak fitting of Ti 2p for Ce-TiO_2, a) 0.5% Ce, b) 1% Ce, c) 5% Ce, d) 10% Ce and e) 15% Ce

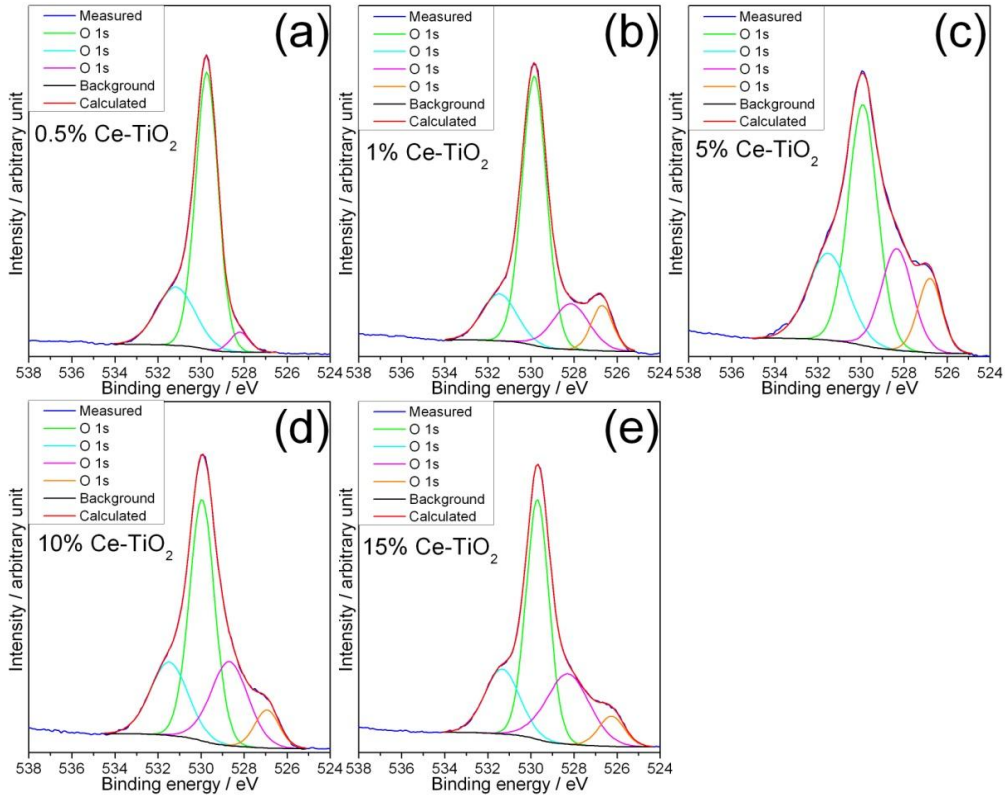

Fig. 6.47 XPS Peak fitting of O 1s for Ce-TiO_2, a) 0.5% Ce, b) 1% Ce, c) 5% Ce, d) 10% Ce and e) 15% Ce

The XPS spectra for calcined Ce-TiO_2 were also collected (Fig. 6.48). The peaks assigned to u', v', u^o and v^o were still observed with positions similar to the as-prepared samples. However, for 5% Ce and above, a peak at ~916.9 eV was also observed, which corresponded to u''' in Ce(IV) oxides. Hence, some of the Ce on the surface has been oxidised during the calcination. For the 0.5% and 1% Ce sample, the u''' peak was absent but this may be due to the low concentration of Ce in these samples. A peak fitting process was also performed (Fig. 6.49) to determine the peak positions, shown in (Table 6.14).

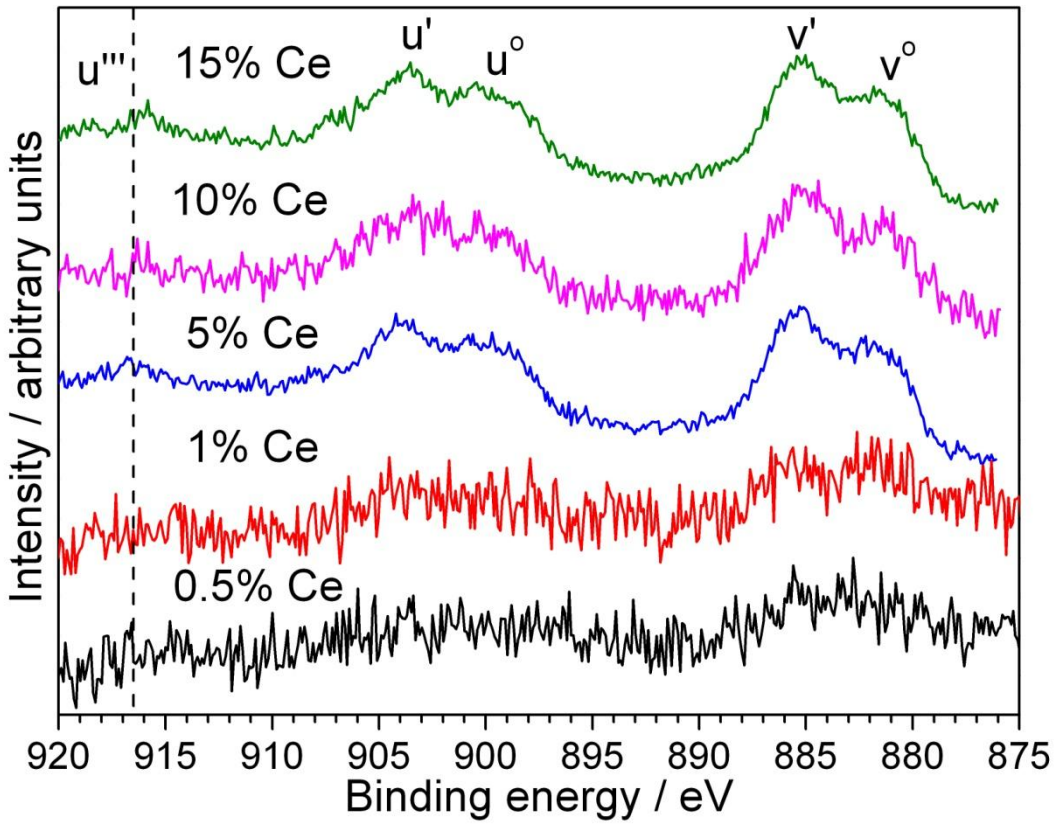

Fig. 6.48 XPS of Ce 3d for Ce-TiO_2 after being calcined at 400 ^oC for 4 hours

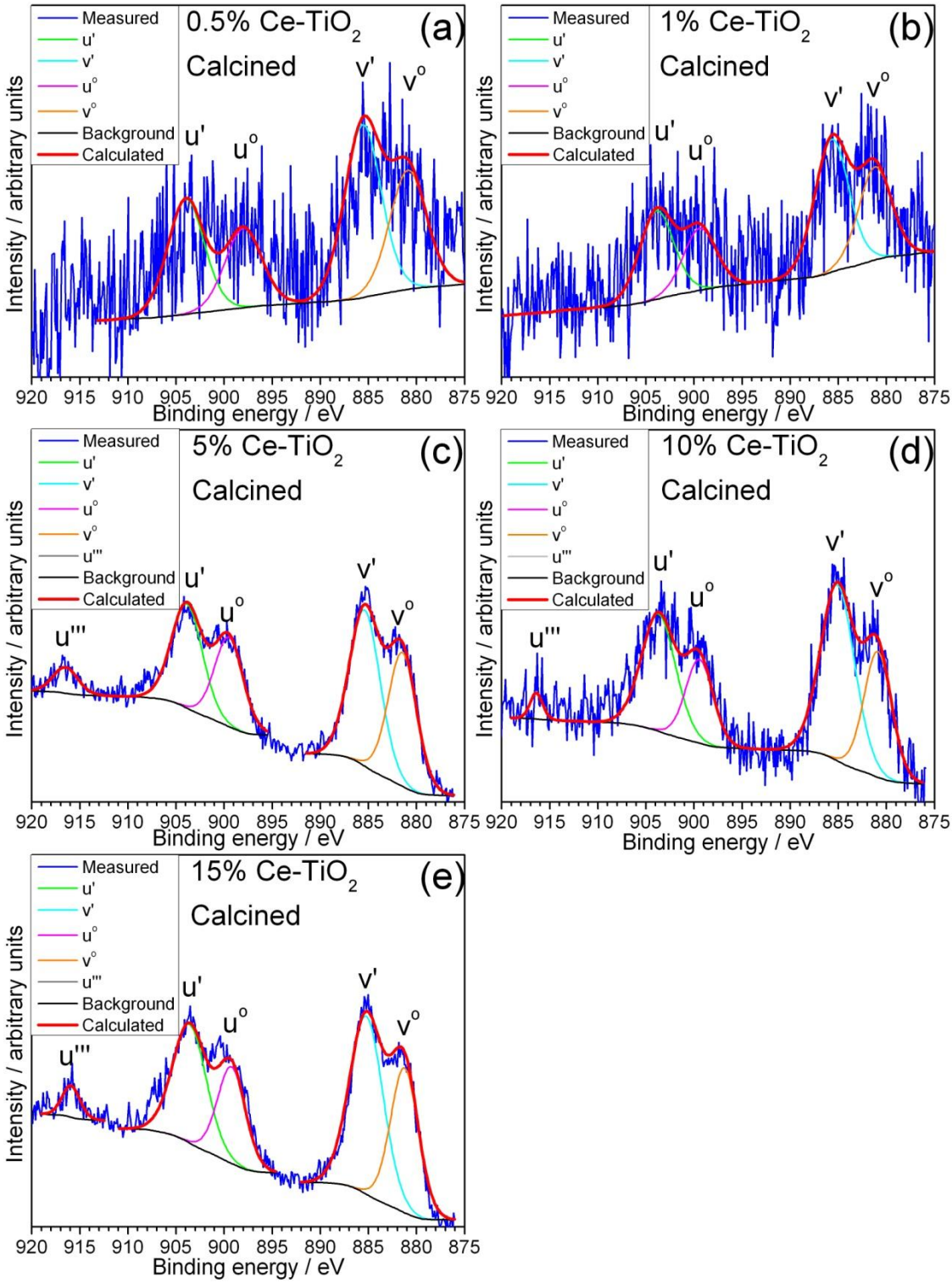

Fig. 6.49 XPS Peak fitting of Ce 3d for calcined Ce-TiO_2, a) 0.5% Ce, b) 1% Ce, c) 5% Ce, d) 10% Ce and e) 15% Ce

Table 6.14 Peak positions of fitted XPS data for calcined Ce-TiO_2

Ce conc./%	u' / eV	v' / eV	u^0 / eV	v^0 / eV	u''' / eV
0.5	904.0	885.6	898.0	880.9	-
1	903.9	885.7	899.4	881.2	-
5	903.9	885.4	899.5	881.5	916.5
10	903.7	885.1	899.4	880.9	916.4
15	903.6	885.2	898.2	881.2	915.9

The XANES results showed that Ce in the as-prepared Ce-TiO_2 samples are mostly Ce^{3+} but from the XPS data, all the Ce on the surface has oxidation state of +3. This suggests that any Ce^{4+} present was within the structure. Possibly at low Ce concentrations, most of the Ce present was Ce^{3+} and was incorporated in the lattice. Thus, this explains the increase in the cell volume seen by powder XRD at low Ce content. Upon further doping, more Ce^{4+} was incorporated into the lattice while Ce^{3+} remained on the surface. Hence, the cell volume dropped at higher Ce doping level.

The IR of Ce-TiO_2 is shown in Fig. 6.50. The most intense peak at 440 cm^{-1} results from Ti-O bond in the TiO_2 lattice. This peak is at a lower value when compared to the IR spectra of Sn-TiO_2 (Fig. 6.25) or other TiO_2 in the literature.[44,65,68,81-82] Ma *et al.* observed a peak shift from 514 cm^{-1} to 486 cm^{-1} when TiO_2 is doped with 2% Ce, which they suggest to be due to the formation of a Ti-O-Ce bond.[83] However, in this case, no significant peak shift was observed upon Ce doping. The IR peaks at 1630 and 3000-3500 cm^{-1} are attributed to surface hydroxyl and adsorbed H_2O.[24,64-65] Peaks relating to lactic acid were observed showing that some organic material remained in the as-prepared samples.[84-85]

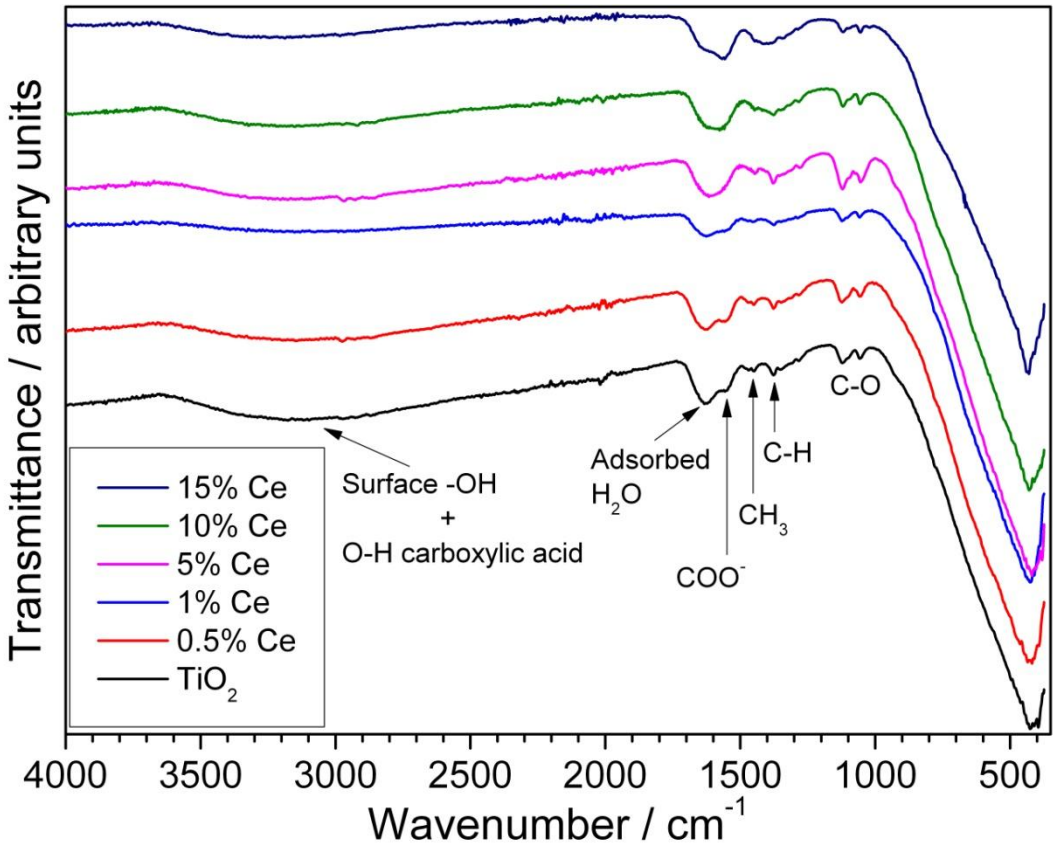

Fig. 6.50 IR of as-prepared Ce-TiO_2 showing the presence of surface water and organic residue

6.4.3 Photochemical water splitting

Photochemical water splitting measurements (Fig. 6.51) were carried out by monitoring the amount of O_2 and H_2 evolved when the as-prepared Ce-TiO_2 materials were suspended in an aqueous solution and exposed to UV and visible light. This work was performed by David Martin and Dr Junwang Tang of University College London. The amount O_2 and H_2 evolved was used to determine their capacity to catalyse a water splitting process. For oxygen evolution, the Ce-TiO_2 materials were mixed with silver nitrate solution, while for hydrogen evolution Pt was deposited on the particles. The results are summarised in Table 6.15, including the surface area measurements obtained from BET. Under visible light,

none of the samples exhibit O_2 or H_2 gas evolution. When the samples were exposed to UV light, O_2 gas evolution was observed at a rate of 56 μmol h^{-1} g^{-1} for anatase TiO_2. At 0.2% and 0.5% Ce, the rate drops to ~ 40 μmol h^{-1} g^{-1}. Further Ce doping up to 10% did not exhibit any O_2 gas evolution. In contrast, the H_2 gas evolution rate is much higher under UV light. Low Ce doping improves the photochemical water splitting. The maximum rate was observed for 0.5% Ce-TiO_2, where the rate was increased by three fold compared to undoped TiO_2. Above 1% doping, the rate starts to decrease but unlike O_2, H_2 evolution was still observed at 10% Ce.

Interestingly, the surface area of the 0.5% Ce-TiO_2 is actually lower than undoped TiO_2. This provides evidence that the improvement in the H_2 gas evolution rate is due to the presence of Ce and irrespective of the surface area of the doped sample.

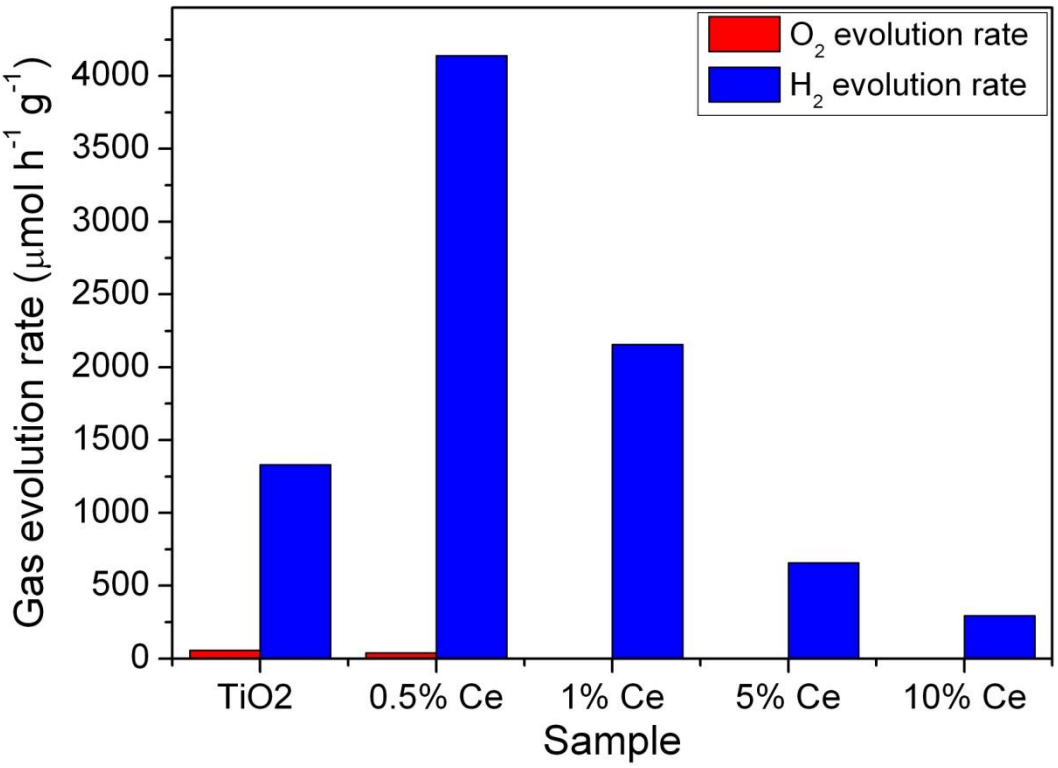

Fig. 6.51 Gas evolution rate by Ce-TiO_2 samples exposed to UV light

Table 6.15 Photochemical water splitting measurements by Ce-TiO_2 samples

Ce conc./%	O_2 in visible light/µmol h^{-1} g^{-1}	O_2 in UV light/µmol h^{-1} g^{-1}	H_2 in visible light/µmol h^{-1} g^{-1}	H_2 in UV light/µmol h^{-1} g^{-1}	Crystallite size/nm	Surface area/m^2 g^{-1}
0	-	56	-	1331	5.6	229.59
0.5	-	40	-	4138	6.6	197.87
1	-	-	-	2155	6.6	210.02
5	-	-	-	657	6.9	236.58
10	-	-	-	296	12.9	291.20
15					23.5	277.59

6.5 Conclusions

In conclusion, TiO_2 doped with W, Sn and Ce have been prepared hydrothermally and characterised with several techniques. In the case of W, the target material of W^{4+} doped TiO_2 in the rutile structure was only achieved at 1% W doping. Higher doping level resulted in formation of anatase. The oxidation state of W was also confirmed to be 6+ on the surface by XPS. On the other hand, a solid solution of Sn-TiO_2 in the rutile phase was achieved where the lattice parameter increasing linearly with increasing Sn concentration. The morphology of TiO_2 was changed with Sn doping followed by a decreased in particle size. There is some evidence of phase separation at some compositions, but the samples appear more homogeneous than others reported in the literature.

Ce-doped TiO_2 was prepared hydrothermally as pure anatase phase as confirmed by powder XRD and RAMAN spectroscopy. The addition of 0.5% Ce improved the stability of the anatase phase up to 900 ^oC, while the 15% Ce-TiO_2 samples breaks down at 725 ^oC and $Ce_4Ti_9O_{26}$ was formed. The Ce was mainly present as Ce^{4+} in the bulk of the sample while Ce^{3+} was mainly found on the surface. Doping 0.5% Ce significantly improved the ability of TiO_2 to photocatalyse

the splitting of water despite it having a lower surface area. The photocatalytic properties are currently under further investigation.

6.6 References

(1) Weir, A.; Westerhoff, P.; Fabricius, L.; Hristovski, K.; von Goetz, N. *Environ. Sci. Technol.* **2012**, *46*, 2242.

(2) Farrokhpay, S. *Adv. Colloid Interfac* **2009**, *151*, 24.

(3) Braun, J. H.; Baidins, A.; Marganski, R. E. *Prog. Org. Coat.* **1992**, *20*, 105.

(4) Barker, P. J.; Branch, A. *Prog. Org. Coat.* **2008**, *62*, 313.

(5) Fujishima, A.; Honda, K. *Nature* **1972**, *238*, 37.

(6) Mills, A.; Davies, R. H.; Worsley, D. *Chem. Soc. Rev.* **1993**, *22*, 417.

(7) Hoffmann, M. R.; Martin, S. T.; Choi, W. Y.; Bahnemann, D. W. *Chem. Rev.* **1995**, *95*, 69.

(8) Carp, O.; Huisman, C. L.; Reller, A. *Prog. Solid State Chem.* **2004**, *32*, 33.

(9) Parkin, I. P.; Palgrave, R. G. *J. Mater. Chem.* **2005**, *15*, 1689.

(10) Watanabe, T.; Nakajima, A.; Wang, R.; Minabe, M.; Koizumi, S.; Fujishima, A.; Hashimoto, K. *Thin Solid Films* **1999**, *351*, 260.

(11) Aryanpour, M.; Hoffmann, R.; DiSalvo, F. J. *Chem. Mater.* **2009**, *21*, 1627.

(12) Shannon, R. D. *Acta Crystallogr. Sect. A* **1976**, *32*, 751.

(13) Jones, F. H.; Egdell, R. G.; Brown, A.; Wondre, F. R. *Surf. Sci.* **1997**, *374*, 80.

(14) Gulino, A.; Parker, S.; Jones, F. H.; Egdell, R. G. *J. Chem. Soc. Faraday T.* **1996**, *92*, 2137.

(15) Peters, E.; MullerBuschbaum, H. *Z. Naturforsch., B: Chem. Sci.* **1996**, *51*, 29.

(16) Subban, C. V.; Zhou, Q.; Hu, A.; Moylan, T. E.; Wagner, F. T.; DiSalvo, F. J. *J. Am. Chem. Soc.* **2010**, *132*, 17531.

(17) Kim, D. S.; Yang, J. H.; Balaji, S.; Cho, H. J.; Kim, M. K.; Kang, D. U.; Djaoued, Y.; Kwon, Y. U. *Crystengcomm* **2009**, *11*, 1621.

(18) Putta, T.; Lu, M. C.; Anotai, J. *J. Environ. Manage.* **2011**, *92*, 2272.

(19) Tian, H.; Ma, J. F.; Li, K.; Li, J. J. *Mater. Chem. Phys.* **2008**, *112*, 47.

(20) Komornicki, S.; Radecka, M.; Sobas, P. *J. Mater. Sci.-Mater. Electron.* **2004**, *15*, 527.

(21) Yang, H.; Zhang, D.; Wang, L. *Mater. Lett.* **2002**, *57*, 674.

(22) Tu, Y. F.; Huang, S. Y.; Sang, J. P.; Zou, X. W. *J. Alloy. Compd.* **2009**, *482*, 382.

(23) Harunsani, M. H.; Oropeza, F. E.; Palgrave, R. G.; Egdell, R. G. *Chem. Mater.* **2010**, *22*, 1551.

(24) Jing, L. Q.; Fu, H. G.; Wang, B. Q.; Xin, B. F.; Li, S. D.; Sun, J. Z. *Appl. Catal. B-Environ.* **2006**, *62*, 282.

(25) Zakrzewska, K.; Radecka, M.; Rekas, M. *Thin Solid Films* **1997**, *310*, 161.

(26) Radecka, M.; Zakrzewska, K.; Rekas, M. *Sensor Actuat. B-Chem.* **1998**, *47*, 194.

(27) Tai, W. P.; Oh, J. H. *Sensor Actuat. B-Chem.* **2002**, *85*, 154.

(28) Carotta, M. C.; Gherardi, S.; Guidi, V.; Malagu, C.; Martinelli, G.; Vendemiati, B.; Sacerdoti, M.; Ghiotti, G.; Morandi, S.; Bismuto, A.; Maddalena, P.; Setaro, A. *Sensor Actuat. B-Chem.* **2008**, *130*, 38.

(29) Naidu, H. P.; Virkar, A. V. *J. Am. Ceram. Soc.* **1998**, *81*, 2176.

(30) Hirata, T.; Ishioka, K.; Kitajima, M.; Doi, H. *Phys. Rev. B* **1996**, *53*, 8442.

(31) Uchiyama, H.; Imai, H. *Chem. Commun.* **2005**, 6014.

(32) Li, J.; Zeng, H. C. *J. Am. Chem. Soc.* **2007**, *129*, 15839.

(33) Duan, Y. D.; Fu, N. Q.; Liu, Q. P.; Fang, Y. Y.; Zhou, X. W.; Zhang, J. B.; Lin, Y. *J. Phys. Chem. C.* **2012**, *116*, 8888.

(34) Trotochaud, L.; Boettcher, S. W. *Chem. Mater.* **2011**, *23*, 4920.

(35) Yang, Y. L.; Hu, C. C.; Hua, C. C. *Crystengcomm* **2011**, *13*, 5638.

(36) Xu, Y. H.; Chen, H. R.; Zeng, Z. X.; Lei, B. *Appl. Surf. Sci.* **2006**, *252*, 8565.

(37) Silva, A. M. T.; Silva, C. G.; Drazic, G.; Faria, J. L. *Catal. Today* **2009**, *144*, 13.

(38) Li, F. B.; Li, X. Z.; Hou, M. F.; Cheah, K. W.; Choy, W. C. H. *Appl. Catal., A* **2005**, *285*, 181.

(39) Zhang, J.; Peng, W. Q.; Chen, Z. H.; Chen, H.; Han, L. Y. *J. Phys. Chem. C.* **2012**, *116*, 19182.

(40) Gao, X.; Jiang, Y.; Fu, Y. C.; Zhong, Y.; Luo, Z. Y.; Cen, K. F. *Catal. Commun.* **2010**, *11*, 465.

(41) Tong, T. Z.; Zhang, J. L.; Tian, B. Z.; Chen, F.; He, D. N.; Anpo, M. *J. Colloid Interface Sci.* **2007**, *315*, 382.

(42) Liu, Y.; Fang, P. F.; Cheng, Y. L.; Gao, Y. P.; Chen, F. T.; Liu, Z.; Dai, Y. Q. *Chem. Eng. J.* **2013**, *219*, 478.

(43) Wang, C.; Xi, H.; Wang, R. D. *Chem. Lett.* **2004**, *33*, 20.

(44) Xiao, J. R.; Peng, T. Y.; Li, R.; Peng, Z. H.; Yan, C. H. *J. Solid State Chem.* **2006**, *179*, 1161.

(45) Tomita, K.; Petrykin, V.; Kobayashi, M.; Shiro, M.; Yoshimura, M.; Kakihana, M. *Angew. Chem. Int. Ed.* **2006**, *45*, 2378.

(46) Riboni, F.; Bettini, L. G.; Bahnemann, D. W.; Selli, E. *Catal. Today* **2013**, *209*, 28.

(47) Porto, S. P. S.; Fleury, P. A.; Damen, T. C. *Phys. Rev.* **1967**, *154*, 522.

(48) Balachandran, U.; Eror, N. G. *J. Solid State Chem.* **1982**, *42*, 276.

(49) Ma, H. L.; Yang, J. Y.; Dai, Y.; Zhang, Y. B.; Lu, B.; Ma, G. H. *Appl. Surf. Sci.* **2007**, *253*, 7497.

(50) Cheng, H. M.; Ma, J. M.; Zhao, Z. G.; Qi, L. M. *Chem. Mater.* **1995**, *7*, 663.

(51) Ohsaka, T.; Izumi, F.; Fujiki, Y. *J. Raman Spectrosc.* **1978**, *7*, 321.

(52) Tompsett, G. A.; Bowmaker, G. A.; Cooney, R. P.; Metson, J. B.; Rodgers, K. A.; Seakins, J. M. *J. Raman Spectrosc.* **1995**, *26*, 57.

(53) Daniel, M. F.; Desbat, B.; Lassegues, J. C.; Gerand, B.; Figlarz, M. *J. Solid State Chem.* **1987**, *67*, 235.

(54) Frey, G. L.; Rothschild, A.; Sloan, J.; Rosentsveig, R.; Popovitz-Biro, R.; Tenne, R. *J. Solid State Chem.* **2001**, *162*, 300.

(55) Fiedor, J. N.; Proctor, A.; Houalla, M.; Hercules, D. M. *Surf. Interface Anal.* **1995**, *23*, 204.

(56) Kandiel, T. A.; Dillert, R.; Feldhoff, A.; Bahnemann, D. W. *J. Phys. Chem. C.* **2010**, *114*, 4909.

(57) Ma, Y. Y.; Navrotsky, A. *J. Am. Ceram. Soc.* **2010**, *93*, 3432.

(58) Peercy, P. S.; Morosin, B. *Phys. Rev. B* **1973**, *7*, 2779.

(59) Ristic, M.; Ivanda, M.; Popovic, S.; Music, S. *J. Non-Cryst. Solids* **2002**, *303*, 270.

(60) Yu, K. N.; Xiong, Y. H.; Liu, Y. L.; Xiong, C. S. *Phys. Rev. B* **1997**, *55*, 2666.

(61) Sato, K.; Yokoyama, Y.; Valmalette, J. C.; Kuruma, K.; Abe, H.; Takarada, T. *Cryst. Growth Des.* **2013**, *13*, 1685.

(62) Oliveira, M. M.; Schnitzler, D. C.; Zarbin, A. J. G. *Chem. Mater.* **2003**, *15*, 1903.

(63) Alemany, L. J.; Banares, M. A.; Pardo, E.; Martin-Jimenez, F.; Blasco, J. M. *Mater. Charact.* **2000**, *44*, 271.

(64) Nag, M.; Basak, P.; Manorama, S. V. *Mater. Res. Bull.* **2007**, *42*, 1691.

(65) Yan, M. C.; Chen, F.; Zhang, J. L.; Anpo, M. *J. Phys. Chem. B* **2005**, *109*, 8673.

(66) Fonseca de Lima, J., Personal Communication.

(67) Li, G. Q.; Liu, C. Y.; Liu, Y. *Appl. Surf. Sci.* **2006**, *253*, 2481.

(68) Zhao, X. P.; Yin, J. B. *Chem. Mater.* **2002**, *14*, 2258.

(69) Nagaveni, K.; Hegde, M. S.; Madras, G. *J. Phys. Chem. B* **2004**, *108*, 20204.

(70) Fang, J.; Bi, X. Z.; Si, D. J.; Jiang, Z. Q.; Huang, W. X. *Appl. Surf. Sci.* **2007**, *253*, 8952.

(71) Graham, G. W.; Weber, W. H.; Peters, C. R.; Usmen, R. *J. Catal.* **1991**, *130*, 310.

(72) Weber, W. H.; Hass, K. C.; McBride, J. R. *Phys. Rev. B* **1993**, *48*, 178.

(73) Kosacki, I.; Suzuki, T.; Anderson, H. U.; Colomban, P. *Solid State Ionics* **2002**, *149*, 99.

(74) Burroughs, P.; Hamnett, A.; Orchard, A. F.; Thornton, G. *J. Chem. Soc. Dalton* **1976**, 1686.

(75) Beche, E.; Charvin, P.; Perarnau, D.; Abanades, S.; Flamant, G. *Surf. Interface Anal.* **2008**, *40*, 264.

(76) Mayer, J. T.; Diebold, U.; Madey, T. E.; Garfunkel, E. *J. Electron. Spectrosc. Relat. Phenom.* **1995**, *73*, 1.

(77) Watanabe, S.; Ma, X. L.; Song, C. S. *J. Phys. Chem. C.* **2009**, *113*, 14249.

(78) Carley, A. F.; Chalker, P. R.; Riviere, J. C.; Roberts, M. W. *J. Chem. Soc. Farad. T. 1* **1987**, *83*, 351.

(79) Liu, C.; Tang, X.; Mo, C.; Qiang, Z. *J. Solid State Chem.* **2008**, *181*, 913.

(80) Dake, L. S.; Lad, R. J. *Surf. Sci.* **1993**, *289*, 297.

(81) Mohammadi, M. R.; Fray, D. J. *Sensor Actuat. B-Chem.* **2010**, *150*, 631.

(82) Dvoranova, D.; Brezova, V.; Mazur, M.; Malati, M. A. *Appl. Catal. B-Environ.* **2002**, *37*, 91.

(83) Ma, T. Y.; Cao, J. L.; Shao, G. S.; Zhang, X. J.; Yuan, Z. Y. *J. Phys. Chem. C.* **2009**, *113*, 16658.

(84) Garlotta, D. *J. Polym. Environ.* **2001**, *9*, 63.

(85) Chen, Y. K.; Lin, Y. F.; Peng, Z. W.; Lin, J. L. *J. Phys. Chem. C.* **2010**, *114*, 17720.

Chapter 7 – Conclusions and future work

The broad aim of this work, which was to prepare new mixed metal oxides via hydrothermal synthesis, has been achieved. The materials have been characterised using various techniques and control over their particle size, morphology and phase purity have been demonstrated. The materials are all examples of complex, multi-element oxides, either doped systems or solid solutions and they provide examples of how hydrothermal synthesis can be used to prepare functional materials for use in practical applications.

A reproducible synthesis route to complex perovskites with up to three different A-site cations was achieved hydrothermally. The $NaCe_{1-x}La_xTi_2O_6$ series, over the whole compositional range, were assigned the $R\bar{3}c$ space group. The lattice parameter showed a linear increase with increasing La concentration thus confirming a solid solution was achieved. The particle size and morphology was changed by varying the solvents used and the NaOH concentration. ^{23}Na NMR gives a novel way of confirming that the materials produced are a genuine solid solution, where the effect of paramagnetic Ce^{3+} proves the intimate mixing of the A-site metals. The presence of defects in the structure was investigated using ^{2}H NMR, where D_2O or OD^- was found to be present in the perovskite lattice. XANES showed that some of the Ce^{3+} in all the materials was oxidised to Ce^{4+} and this may provide a possible means of balancing the charge of A-site defects. This work has been published in *Journal of Solid State Chemistry*.[1] Further work on these materials may involve making the structure more complex, by adding a fourth metal on the A-site and examining whether a solid solution can still be obtained. This is important since many of the real materials currently proposed as lead-free ferroelectrics are such

multi-element perovskites, with both A and B site dopants. Another perovskite that should be studied in more detail is $NaHoTi_2O_6$ since its synthesis also proved possible when TiF_3 was used as the precursor, and this material contains a magnetic Ho^{3+} cation so may have interesting physical properties.

B-site substituted perovskites, in particular, $NaLa(Ti_{1-x}Zr_x)_2O_6$ were prepared for the compositional range $0 \leq x \leq 0.5$. These series were assigned the space group $R\bar{3}c$ following the end member $NaLaTi_2O_6$. The samples with composition x = 0.2-0.4, showed splitting in the XRD peaks which may result from the presence of two separate phases, one proposed to be Na rich and another being Na deficient. Despite the presence of two phases, the particles observed in the SEM images appeared homogeneous and they exhibit interesting flower-shaped morphology. The morphology can be easily changed to cubes or spheres by increasing the NaOH concentration and using an ethylene glycol / water mixture as the solvent. For future work, more study could be done to gain a better understanding on the formation of these different morphologies. The effect of using other solvents and also different mixtures of solvents on the morphology could be undertaken. Analysis using high resolution TEM, with selected area EDXA and electron diffraction, could be done to determine whether the flower shaped morphologies arise from the material being two separate phases.

Another B-site substituted perovskite prepared hydrothermally was $NaBi(Ti_{1-x}Zr_x)_2O_6$. A much lower Zr doping level ($0 \leq x \leq 0.1$) was achieved for these materials and the series were assigned the space group *R*3*c* following the end member $NaBiTi_2O_6$. The lattice parameter of $NaBi(Ti_{1-x}Zr_x)_2O_6$, obtained from refinement of XRD patterns, increased with increasing Zr concentration confirming

that the Zr has been incorporated into the perovskite structure. Their SEM images showed that cubic particles were obtained. The presence of F defects was deduced by ^{19}F NMR for the x = 0 and 0.01 sample and their ferroelectric and piezoelectric properties were also investigated. The d_{33} value of $NaBiTi_2O_6$ in this work was much higher than one made by another hydrothermal method. The addition of Zr at x = 0.01 was found to improve the piezoelectric property of $NaBiTi_2O_6$, but higher Zr doping degrades them. The work showed the potential hydrothermal synthesis has for making complex solid solutions of ferroelectric perovskites for real applications. Further work on these materials could involve optimisation of the piezoelectric properties. Zr doping between x = 0.01 and 0.05 could be studied and also use different precursors to see whether the limit of Zr substitution could be increased.

Preliminary studies on the synthesis of doped hexagonal perovskites were carried out. Pure hexagonal $YMnO_3$ was successfully prepared by a comproportionation hydrothermal reaction between MnO_4^- and Mn^{2+}. XANES confirmed the oxidation state of both the Mn and Fe to be 3+. There is direct evidence for the inclusion of Fe^{3+} for x = 0.1 in place of Mn^{3+} in $YMnO_3$ but above this level, impurity phases are seen. Similarly, pure orthorhombic $YFeO_3$ can be prepared and the Fe^{3+} can be replaced by Mn^{3+} up to $YMn_{0.3}Fe_{0.7}O_3$. Further work on these materials is presently being undertaken where their multiferroic properties are being studied by collaborators in the Institute of Physics, Chinese Academy of Sciences, Beijing. Further work could also be carried out on the possibility of substituting Y with other metals such as magnetic lanthanide cations.

Rutile TiO_2 was successfully prepared from Ti metal based on the work by Tomita *et al.*[2] This method was then modified to include W with the aim of

preparing W^{4+} doped TiO_2 in the rutile structure. However, this material was only achieved at 1% W doping. Higher doping level resulted in formation of anatase. The oxidation state of W was also confirmed to be 6+ on the surface by XPS. Further work could be done to modify this synthesis route to include other metals.

Rutile TiO_2 was also successfully prepared from TiBALD based on the work by Kandiel *et al*.[3] By modifying this method to include Sn acetate, a solid solution of Sn-TiO_2 in the rutile phase was achieved where the lattice parameter increasing linearly with increasing Sn concentration. The morphology of TiO_2 was changed with Sn doping followed by a decreased in particle size. There is some evidence of phase separation at some compositions, but the samples appear more homogeneous than others reported in the literature. This work has been submitted for publication.[4] Future work on this material could involve solvothermal reactions, effect of reaction time or the use of a different Sn precursor. This method could also be modified to prepare other metal doped TiO_2.

Ce-doped TiO_2 was prepared hydrothermally as pure anatase phase. The addition of 0.5% Ce improved the stability of the anatase phase up to 900 ^{o}C, while the 15% Ce-TiO_2 samples breaks down at 725 ^{o}C and $Ce_4Ti_9O_{26}$ was formed. XANES confirmed that the Ce was mainly present as Ce^{4+} in the bulk of the sample while XPS showed that Ce^{3+} was mainly found on the surface. Doping 0.5% Ce significantly improved the ability of TiO_2 to photocatalyse the splitting of water despite it having a lower surface area. Further work on the photocatalytic properties are currently undertaken by collaborators at University College London.

7.1 References

(1) Harunsani, M. H.; Woodward, D. I.; Peel, M. D.; Ashbrook, S. E.; Walton, R. I. *J. Solid State Chem.* **2013**.

(2) Tomita, K.; Petrykin, V.; Kobayashi, M.; Shiro, M.; Yoshimura, M.; Kakihana, M. *Angew. Chem. Int. Ed.* **2006**, *45*, 2378.

(3) Kandiel, T. A.; Dillert, R.; Feldhoff, A.; Bahnemann, D. W. *J. Phys. Chem. C.* **2010**, *114*, 4909.

(4) Burnett, D. L.; Harunsani, M. H.; Kashtiban, R. J.; Playford, H. Y.; Sloan, J.; Hannon, A. C.; Walton, R. I. *Submitted for publication* **2013**.